

Investigation of Acceleration Dependent Nonlinear Lubricated Friction in Hydraulic Actuation Systems

A Thesis Submitted to the College of
Graduate Studies and Research
in Partial Fulfillment of the Requirements
for the Degree of Doctor of Philosophy
in the Department of Mechanical Engineering
University of Saskatchewan
Saskatoon

By
Scott Li

© Copyright Scott Li, January, 2016. All rights reserved.

PERMISSION TO USE

In presenting this thesis in partial fulfillment of the requirements for a Postgraduate degree from the University of Saskatchewan, I agree that the Libraries of this University may make it freely available for inspection. I further agree that permission for copying of this thesis in any manner, in whole or in part, for scholarly purposes may be granted by the professor or professors who supervised my thesis work or, in their absence, by the Head of the Department or the Dean of the College in which my thesis work was done. It is understood that any copying or publication or use of this thesis or parts thereof for financial gain shall not be allowed without my written permission. It is also understood that due recognition shall be given to me and to the University of Saskatchewan in any scholarly use which may be made of any material in my thesis.

Requests for permission to copy or to make other use of material in this thesis in whole or part should be addressed to:

Head of the Department of Mechanical Engineering
University of Saskatchewan
57 Campus Drive
Saskatoon, Saskatchewan, S7N 5A9
Canada

ABSTRACT

Lubricated friction issues are central to all hydraulic actuation systems undergoing motion and any in-depth understanding of the nature of lubricated friction will advance future component design. The classic friction models of hydraulic actuation systems under steady state conditions and their dependency on velocity and temperature have been studied extensively over the past years. A model which is commonly employed to represent the characteristics of friction is that of Stribeck in which the dependency of the friction force is based on velocity alone. However, experimentally, it has been found that lubricated friction is dependent on acceleration. Thus, the Stribeck model can be considered as a subset of a dynamic friction model in which acceleration is zero. Thus, it can be concluded that the Stribeck model is best applied to cases when the change rate of the velocities is very small.

This thesis considers the dependency of lubricated friction on acceleration when pressure and temperature changes are relatively constant. As such, the basic hypothesis for this study was proposed as follows: “Lubricated friction in hydraulic actuation systems is not only a function of velocity, but is also a function of both velocity and acceleration”.

In this thesis several terms are defined which facilitate the description under which friction models are developed. For example, the term non-steady state friction is used to account for the effect of acceleration on lubricated friction force while in motion. Further, the lubricated friction models are divided into two groups: steady state friction models and non-steady state friction models.

Nonlinear friction modeling and measuring methods are reviewed in this dissertation. This review also includes nonlinear lubricated friction modeling in hydraulic actuation systems. A conclusion from this review was that limited research has been done in documenting and explicitly demonstrating the role of acceleration on lubricated friction.

The research first introduced a methodology to experimentally measure friction as a function of acceleration and to demonstrate this dependency in the form of a three dimensional graph. A novel technique to experimentally obtain data for the lubricated friction model was introduced. This allowed the lubricated friction forces to be measured as a function of velocity in a continuous manner, but with acceleration being held constant as a family parameter. Two different valve controlled hydraulic actuation systems (VCHAS) were studied under a wide variety of accelerations at constant temperature and pressure. To enable repeatable data collection for the

different friction conditions and to accommodate for the effect of hysteresis, a periodic parabolic displacement waveform was chosen which enabled the acceleration to be a family parameter.

The second phase of the research introduced a method of representing the data (lubricated friction model) in a lookup table form. The relationship of lubricated friction (in this work, pressure differential, ΔP , across the actuator) as a function of velocity and acceleration was presented in a unique semi-empirical 2D lookup table (2D LUT). Limitations of this experimental approach were identified, but the dependency on acceleration was clearly established.

The last phase of the study implemented this 2D LUT model into a practical software model of an actuator and demonstrated its accuracy when compared to its experimental counterpart. The semi-empirical model (2D LUT) was experimentally verified by implementing the semi-empirical and Stribeck models into a real time simulation of an actuator and by comparing the experimental outputs against simulated outputs for a common sinusoidal input. A sinusoidal actuator displacement input was chosen to test the simulations as it was not used in the collection of the original data. The output of the simulation was compared to the experimental results and it was evident that for the range in which data could be collected in developing the model, the proposed 2D LUT model predicted an output that was superior to a model which used a standard Stribeck model. It was concluded that the semi-empirical model could be integrated into a simulation environment and predict outputs in a superior fashion when compared to the Stribeck friction model.

Thus it was concluded that the stated hypothesis is consistent with the experimental evidence shown by all hydraulic actuators considered. Further, it was also observed that the traditional Stribeck form (steady state dynamic friction) does change with increasing acceleration to the point that the standard breakaway friction almost disappears.

It is evident that the 2D LUT is a viable tool for modeling the non-steady state friction of hydraulic actuation systems. The semi-empirical 2D LUT model so developed is a more global representation of hydraulic actuator lubricated friction. In this research, only linear hydraulic actuators were considered; however, the novel nonlinear semi-empirical 2D LUT lubricated friction model can be applied to any actuator (linear and rotary) and provides a new way in which the dynamic friction can be viewed and modeled.

ACKNOWLEDGMENTS

I would like to express my sincere gratitude to my supervisor, Professor Richard Burton, for his guidance, suggesting ideas to work with, asking challenging questions and “criticism” and encouragement and patience, for offering the freedom to develop my own research style, and for concerning himself with my wellbeing in general. His insights on this research have been invaluable in keeping me on the right track. It would not have been possible to write this thesis without his help and support.

Special thanks to Mr. Doug Bitner for his enthusiastic participation and essential technical assistance during all phases of the research and also writing of this thesis. I would like thank Professors Reza Fotouhi, Chris Zhang, Daniel Chen and Ramakrishna Gokaraju for serving on my advisory committee. I am grateful for the time and inputs that they have given to my research. I would also like to thank my former advisor Professor Saeid Habibi for his supports during the first three years of my PhD research. I would like also thank Professor Fangxiang Wu for providing me the guidance of the nonlinear system identification theory.

Financial assistance provided by my supervisors in the form of a research assistantship and also from the University of Saskatchewan in the form of a teaching assistantship is greatly acknowledged.

Finally, I wish to express a lot of thanks to my family and friends for their supports during the preparation of this thesis.

DEDICATION

To my wife, Jenny and our children, Steven and Andrew, whose supports, encouragements and love made this research and this thesis possible.

TABLE OF CONTENTS

PERMISSION TO USE	i
ABSTRACT	ii
ACKNOWLEDGMENTS	iv
DEDICATION	v
LIST OF TABLES	11
LIST OF FIGURES	xii
NOMENCLATURE	xxv
CHAPTER 1: BACKGROUND AND INTRODUCTION	1
1.1 Research Background	1
1.2 Brief Introduction of Friction	5
1.2.1 Classical Friction Models	5
1.2.2 Experimental Techniques to Measure Friction	10
1.3 Limitations of the Stribeck Model	12
1.3.1 Acceleration Effect on Friction	12
1.4 Hypothesis of the Research.....	14
1.5 Objectives and Scope of Thesis	14
1.6 Outline of Thesis	15
CHAPTER 2: LITERATURE REVIEW OF LUBRICATED FRICTION MEASUREMENTS AND MODELING.....	17
2.1 Introduction	17
2.2 Lubricated Friction in Hydraulic Actuation Systems.....	17
2.2.1 The Effect of Seals.....	18
2.2.2 The Effect of Pressure.....	19
2.2.3 The Effect of Viscosity	19
2.2.4 The Effect of Velocity	20
2.2.5 The Effect of Temperature.....	24
2.2.6 Summary.....	24
2.3 Measurements of Lubricated Friction.....	24

2.3.1	Indirect Approach	25
2.3.2	Direct Approach.....	27
2.3.3	Discussion.....	27
2.4	Representation of Experimental Lubricated Friction as a Function of Velocity.....	27
2.4.1	Discrete Measurement Based Model: Stribeck Model.....	28
2.4.2	Continuous Measurements Based Models	29
2.4.3	Discontinuity of the Friction Model as a Function of Velocity	32
2.5	Discrete vs Continuous Based Models: Some Issues.....	33
2.5.1	Hysteresis of Lubricated Friction.....	33
2.5.2	Discussion on the Stribeck Effect and Limit Cycles.....	35
2.5.2.1	Limit Cycles.....	35
2.5.2.2	Stribeck Effect of Stribeck Model	36
2.5.3	Velocity History and Acceleration.....	37
2.5.4	Lubricated Film Thickness vs Acceleration.....	38
2.6	Summary.....	38

CHAPTER 3: LUBRICATED FRICTION MEASUREMENT WITH ACCELERATION EFFECT 40

3.1	Introduction	40
3.2	Definitions	40
3.3	Lubricated Friction in Different Motion Conditions and Quadrants.....	46
3.4	Experimental Apparatus	50
3.4.1	Selection of Hydraulic Actuators.....	51
3.4.2	Hydraulic Circuit Configuration and Instrumentation	52
3.5	Experimental Procedures	55
3.5.1	Steady State Dynamic Friction Measurement.....	56
3.5.2	Non-Steady State Dynamic Friction Measurement.....	60
3.6	Experimental Limitations	63
3.6.1	Limitation of Velocity and Acceleration Sensors	63
3.6.2	Limitation of the Velocity Triangular Waveform Approach	67
3.6.3	Limitations of the Experimental Systems	71
3.7	Experimental Results	74
3.7.1	Experimental Results of VCHAS1	75
3.7.1.1	Steady State Friction by Increasing Velocities Only	75
3.7.1.2	Steady State Friction by Increasing and Decreasing Velocities.....	76
3.7.1.3	Non-Steady State Friction.....	77
3.7.2	Experimental Results of VCHAS2	78
3.7.2.1	Steady State Friction.....	78
3.7.2.2	Non-Steady State Friction.....	80
3.7.3	Discussion.....	80
3.7.4	Repeatability and Stability of Experimental Results	81
3.7.4.1	Repeatability of VCHAS1	82
3.7.4.2	Repeatability of VCHAS2	84
3.7.5	Pressure Effect Consideration.....	86

3.8	Summary.....	89
-----	--------------	----

CHAPTER 4: DEVELOPMENT OF A SEMI-EMPIRICAL FRICTION MODEL WITH ACCELERATION EFFECT 90

4.1	Introduction	90
4.2	Model Development	90
4.2.1	Lookup Table Model Approach.....	92
4.2.2	Analysis of Experimental Data	95
4.2.3	Preprocessing of Experimental Data.....	99
4.2.3.1	Development of the Sampling Point Index Number (SPIN).....	99
4.2.3.2	Selection of Start Point (<i>Sp</i>) and End Point (<i>Ep</i>) in Each Quadrant	99
4.2.3.3	Complexity Associated with the Start Point	100
4.2.3.4	From Time Domain to Velocity Domain.....	101
4.2.4	Velocity Range Specification	102
4.2.5	Universal Velocity Set and Universal Acceleration Set	103
4.2.6	Data Interpolation Process	105
4.3	3D Visualization of the 2D LUT Model.....	108
4.3.1	3D Plot of 2D LUT of VCHAS1	109
4.3.2	3D Plot of 2D LUT of VCHAS2	110
4.3.3	Alternative Views of 3D Data	112
4.4	Model Verification.....	113
4.5	Summary.....	116

CHAPTER 5: MODEL VALIDATION AND IMPLEMENTATION 117

5.1	Introduction	117
5.2	Model Validation	118
5.2.1	Model Validation Strategy.....	118
5.2.2	Causality Issues	120
5.2.3	Design of Input Signal of Model Validation.....	121
5.2.4	Experimental Data – ΔP_E	124
5.2.4.1	Experiment of Sinusoidal Accelerations.....	124
5.2.4.2	Selection of a Stable Period of Experimental Data	126
5.2.4.3	Estimation of Sinusoidal Velocity and Acceleration by Curve Fitting	127
5.2.4.4	Selection of Start Point (<i>Sp</i>) and End Point (<i>Ep</i>)	130
5.2.4.5	Determination of No Model Data Zone	131
5.2.5	2D LUT Data – ΔP_L – Meshing Technique	139
5.2.6	Stribeck Data – ΔP_S – Stribeck Lookup Table.....	144
5.2.7	Model Validation of 2D LUT of VCHAS1	144
5.3	Discussion and Summary	150

CHAPTER 6: CONCLUSIONS AND FUTURE WORKS 152

6.1	Summary.....	152
6.2	Outcomes	153

6.3	Discussion on the Limitations of the Triangular Velocity Waveform	155
6.4	Important Contributions.....	155
6.5	Conclusions	156
6.6	Future Research Recommendations.....	157
6.6.1	Increase the Cylinder Stroke.....	157
6.6.2	Use Other Types of Input Signals.....	157
6.6.3	Use Adaptive Sampling Rates	158
6.6.4	Use Parameter Estimation for Curve Fitting for Analytical Modeling	158
6.6.5	Use Neural Networks to Replace the Lookup Table (LUT)	159
6.6.6	Extend to Rate-Dependent Model of Static and Dynamic Friction	159
	LIST OF REFERENCES.....	160
	APPENDIX A: ASME 2007 INTERNATIONAL MECHANICAL ENGINEERING CONGRESS AND EXPOSITION (IMECE) PAPER.....	168
	APPENDIX B1: ASME/BATH 2010 POWER TRANSMISSION AND MOTION CONTROL (PTMC) CONFERENCE PAPER	178
	APPENDIX B2: CANCAM 2013 CANADIAN CONGRESS OF APPLIED MECHANICS CONFERENCE PAPER.....	193
	APPENDIX C: CALIBRATION INFORMATION.....	199
	APPENDIX D: FREQUENCY CONTROL FOR DESIRED CONSTANT VELOCITIES AND DESIRED CONSTANT ACCELERATIONS	203
	APPENDIX E: DEVELOPMENT OF VELOCITY AND ACCELERATION LISTS.....	209
	APPENDIX F: DESIGN OF AN INNOVATIVE PERIODIC PARABOLIC INPUT SIGNAL WHICH RESULTS IN A CONSTANT ACCELERATION.....	219
	APPENDIX G: ADDITIONAL MODEL VERIFICATION AND VALIDATION RESULTS	224
	APPENDIX H: EXPERIMENTAL LIMITATION ANALYSIS.....	245
	APPENDIX I: ADDITIONAL 3D VISUALIZATIONS OF THE 2D LUT OF VCHAS1 AND VCHAS2.....	254
	APPENDIX J: ALGORITHM FOR DETERMINING THE START POINTS AND END POINTS.....	262

LIST OF TABLES

Table 3.1 Parameters of two hydraulic actuators selected	52
Table 3.2 Instrumentation of VCHAS1 and VCHAS2	54
Table 3.3 Maximum velocity (v_{\max}) ranges and maximum acceleration (a_{\max}) ranges of VCHAS1 and VCHAS2	72
Table 3.4 Minimum velocity (v_{\min}) ranges and minimum acceleration (a_{\min}) ranges of VCHAS1 and VCHAS2	73
Table 4.1 Universal Velocity Set intervals	104
Table 4.2 Universal Velocity Set	105

LIST OF FIGURES

Figure 1.1 Categorization of hydraulic actuation systems (HAS)	1
Figure 1.2 Schematic of a typical valve controlled hydraulic actuation system (VCHAS)	2
Figure 1.3 Schematic of a pump controlled hydraulic actuation system (PCHAS). This is an example of a closed hydraulic system because the flow from the actuator is directed back to the inlet of the pump. A schematic of the symmetrical actuator is shown in Figure 1.4	2
Figure 1.4 Design of a single rod, symmetric actuator by Habibi et al. [3]. Note the “third” chamber C3 which allows the effective areas of the pistons to be equal; that is A1, the working area (in a circular shape) of the “first” chamber C1 is designed to be equal to A2, the working area (in a ring disc shape) of the “second” chamber C2. Therefore, the inlet flow Q_1 of opening O1 equals to the outlet flow Q_2 of opening O2. The openings O3 and O4 allow draining of fluid from Chamber C3. Opening O5 is provided to allow pressurization of Chamber C3 for special applications	3
Figure 1.5 Simulated step response of the EHA (with Stribeck model)	4
Figure 1.6 Experimental step response of the EHA [6]	4
Figure 1.7 Friction is always against the applied force in the pre-sliding phase and always against the sliding motion direction in the sliding phase	6
Figure 1.8 Friction in the pre-sliding and sliding conditions. In the pre-sliding condition, dry or lubricated friction is equal to the applied force (but in the opposite direction). In general breakaway friction for dry friction is larger than for lubricated friction. Once the system breaks away, the system starts to move (the sliding condition) and lubricated friction is a function of velocity (Stribeck friction) whereas dry friction is approximately independent of velocity (Coulomb friction).....	7
Figure 1.9 Coulomb friction	8
Figure 1.10 Viscous friction which is a linear function of the velocity.....	8
Figure 1.11 Coulomb friction plus viscous friction	9
Figure 1.12 A typical Stribeck model	10
Figure 1.13 Discrete friction vs. velocity curves under steady state conditions.....	11
Figure 1.14 Typical friction result for increasing velocity in one direction for the EHA. (Reproduced with permission from the ASME/Bath symposium [24]). Please note: Acc refers to acceleration, units are m/s^2	13

Figure 2.1 The Stribeck model with four regimes of the hydrodynamic lubrication of hydraulic actuation systems; this form assumes that values of friction were obtained under steady state conditions (Details are provided in Section 2.4.1).....	21
Figure 2.2 Four Coulomb friction types in lubricated friction models: Coulomb A, Coulomb B, Coulomb C and Coulomb D.....	23
Figure 2.3 Unsteady state lubricated friction of the experimental results in [12]. Reprinted from Mechatronics, Vol. 18 (7), H. Yanada and Y. Sekikawa, Modeling of dynamic behaviors of friction, pp. 330-339. Copyright 2008, with permission from Elsevier	31
Figure 2.4 The lubricated friction-velocity relation observed in [46]. The lubricated friction force is lower for decreasing velocities than for increasing velocities. The hysteresis loop becomes wider as the velocity change rates become larger.	34
Figure 2.5 Time relation between a change in velocity and the corresponding change in friction [73].	34
Figure 2.6 Hysteretic effects of dry friction: contact compliance [86].....	35
Figure 3.1 An example of four quadrants for a “parabolic” piston motion cycle.....	44
Figure 3.2 Motion condition coordinate system and four quadrants used in this research, NSSC=Non-Steady State Condition, SSC=Steady State Condition, SC=Static Condition... ..	45
Figure 3.3 Friction ($F_f(v, a)$) measured at a motion condition point (v, a)	45
Figure 3.4 Piston positions in a cylinder for non-steady state conditions, L is the stroke of a cylinder. Q_1 = Quadrant 1, Q_2 = Quadrant 2, Q_3 = Quadrant 3, Q_4 = Quadrant 4	47
Figure 3.5 A typical velocity – time (v - t) plot of a piston motion in a cylinder.....	48
Figure 3.6 A typical example of the lubricated friction measured in four quadrants under non-steady state conditions at acceleration $a = 0.25 \text{ m/s}^2$ of VCHAS1	49
Figure 3.7 An example of the lubricated friction of VCHAS1 measured in four quadrants under non-steady state conditions at acceleration $a= 0.25 \text{ m/s}^2$ in four views – front view (friction-velocity), top view (acceleration-velocity), side view (friction-acceleration) and isometric view (friction-velocity and acceleration)	50
Figure 3.8 Schematic of a double-acting and double-rod end linear hydraulic actuator (The stroke is limited by the ends of the each cylinder housing).....	51
Figure 3.9 Schematic of the valve controlled hydraulic actuation system (VCHAS) [2]. The two experimental systems used in this study were located in the fluid power research lab in the College of Engineering at the University of Saskatchewan.....	53

Figure 3.10 Schematic of closed loop control of the piston position (proportional controller) for VCHAS1 and VCHAS2.....	55
Figure 3.11 EHA input ramp displacement signal (blue line) for steady state friction measurements.....	57
Figure 3.12 A cycle of input triangular displacement signal (x) (periodic) to the VCHAS1 and VCHAS2 for steady state friction (SSF) measurements and the expected actuator velocity (v) and acceleration (a).	58
Figure 3.13 An example of a cycle of measured differential pressure (ΔP) and measured displacement (x) in both directions. Please note: Velocity and acceleration were not measured but were obtained by differentiating the position (x) once for velocity (v). No filtration of any signal was required.....	60
Figure 3.14 A typical one cycle of the input parabolic displacement signal (x) to the VCHAS1 and VCHAS2 and the expected actuator triangular velocity (v) and square acceleration (a). NSSF refers to non-steady state friction.	61
Figure 3.15 An example of measured differential pressure (ΔP) and measured displacement (x) in all four quadrants. Please note: velocity and acceleration were not measured but were obtained by differentiating the “curve fitted” position (x) once for velocity (v) and then once again for acceleration(a). No filtration of any signal was required.....	62
Figure 3.16 A typical parabolic curve fitting of the measured displacement at acceleration = 5 m/s ²	64
Figure 3.17 A typical parabolic curve fitting of the measured displacement at acceleration = 1.5 m/s ²	65
Figure 3.18 A typical parabolic curve fitting of the measured displacement at acceleration = 0.001 m/s ²	65
Figure 3.19 The measured position (x), the velocity (v) from the first derivative of the measured position (x), and acceleration a for the second devative of position are shown in green lines. The red lines are theoretical based on an optimal fit of a parabolic curve shown superimposed on the position curve (x), using experimental data and by differentiating a best fit curve (x _f) to the position signal (x) to get velocity (v _f) and acceleration (a _f). No filtration of any signal was made	66
Figure 3.20 Boundary lines of displacement (x), maximum velocities (v _{max}) and accelerations (a) for parabolic displacement inputs. Regions above the maximum values indicate where data cannot be physically collected due to the limited stroke of the actuator. Please note: Acc refers to acceleration, units are m/s ²	68
Figure 3.21 Expanded view of Zoom Windows of Figure 3.20 at high accelerations	68

Figure 3.22 Maximum velocity boundary lines of four quadrants. Outside the boundary lines (areas in red) experimental data cannot be collected using the parabolic displacement signal waveform approach. Details are provided in Appendix H.....	69
Figure 3.23 VCHAS1 & VCHAS2: the measured position follows the desired position very well when $a = 0.001 \text{ m/s}^2$	71
Figure 3.24 VCHAS1 & VCHAS2: the measured position follows the desired position but a small distortion is introduced, when $a = 5 \text{ m/s}^2$ for VCHAS1 and $a = 2 \text{ m/s}^2$ for VCHAS2. This established the upper limits for acceleration (a_{\max}).....	72
Figure 3.25 Physical limits (red boxes) of VCHAS1. Please note: the zoom view shows the minimum physical limit box	73
Figure 3.26 Physical limits (red boxes) of VCHAS2. Please note: the zoom view shows the minimum physical limit box	74
Figure 3.27 Stribeck curve of VCHAS1 – a list of discrete calculated friction points (steady state dynamic friction in both directions). There is no data near the velocity zero from -0.003 m/s to 0.003 m/s (see the zoom view for details)	75
Figure 3.28 Curve fitting of Stribeck curve of VCHAS1 (steady state dynamic friction in both directions). An extrapolation technique is needed to estimate the break-away frictions. The breakaway friction of VCHAS1 in the forward direction is around 202.9 N and the breakaway friction of VCHAS1 in the reverse direction is around 288.6 N (See zoom view for details)	76
Figure 3.29 Superimposed steady state friction of VCHAS1 of increasing and decreasing velocities (see zoom view for details).....	77
Figure 3.30 Acceleration dependent non-steady state dynamic friction curves of VCHAS1 – four quadrants at three different accelerations.....	78
Figure 3.31 Stribeck curve of VCHAS2 – a list of discrete measured friction points (steady state dynamic friction in both directions). There is no data near the velocity zero from -0.001 m/s to 0.001 m/s (see the zoomed in view for details).....	79
Figure 3.32 Curve fitting of Stribeck curve of VCHAS2 (steady state dynamic friction in both directions). An extrapolation technique is needed to estimate the break-away frictions. The breakaway friction of VCHAS2 is around 150 N (See the zoomed in view for details)	79
Figure 3.33 Acceleration dependent non-steady state dynamic friction curves of VCHAS2 – four quadrants at three different accelerations.....	80
Figure 3.34 Stribeck curve (in red markers) and non-steady state friction curve at acceleration $a = 0.001 \text{ m/s}^2$ (in blue line) of VCHAS1 as an example. NSSF refers to non-steady state friction. SSF refers to steady state friction which essentially is the Stribeck curve	81

Figure 3.35 Repeatability of VCHAS1 – an envelope of three measured differential pressures (ΔP) acceleration conditions. Although small deviations are noted, the trends are maintained	82
Figure 3.36 Repeatability of VCHAS1 – an envelope of three measured differential pressure (ΔP) at medium acceleration conditions. Although small deviations are noted, the trends are maintained	83
Figure 3.37 Repeatability of VCHAS1 – an envelope of three measured differential pressures (ΔP) high acceleration conditions. Although small deviations are noted, the trends are maintained	83
Figure 3.38 An example of measured differential pressure (ΔP) and displacement (x) at acceleration $a = 1.5 \text{ m/s}^2$. Data was collected for the lookup table (LUT) modelling at the 18 th cycle (in red)	84
Figure 3.39 Repeatability of VCHAS2 – an envelope of three measured differential pressures (ΔP) at low acceleration conditions. Although small deviations are noted, the trends are maintained	85
Figure 3.40 Repeatability of VCHAS2 – an envelope of three measured differential pressures (ΔP) at medium acceleration conditions. Although small deviations are noted, the trends are maintained	85
Figure 3.41 Repeatability of VCHAS2 – an envelope of three measured differential pressures (ΔP) at high acceleration conditions. Although small deviations are noted, the trends are maintained	86
Figure 3.42 Measured pressure drop across the seals versus velocity at a constant acceleration of 2 m/s^2 (two masses) for VCHAS1	87
Figure 3.43 Equivalent friction versus velocity at a constant acceleration of 2 m/s^2 (two masses) for VCHAS1	87
Figure 3.44 Measured pressure drop across the seals versus velocity at a constant acceleration of 4 m/s^2 (two masses) for VCHAS1	88
Figure 3.45 Equivalent friction versus velocity at a constant acceleration of 4 m/s^2 (two masses) for VCHAS1	88
Figure 4.1 Friction lookup table (LUT) with two inputs v, a and its output friction (F_f)	92
Figure 4.2 Differential pressure ΔP LUT with two inputs v, a and its output differential pressure (ΔP)	92
Figure 4.3 A 2D LUT layout which illustrates the requirements for such a table	94
Figure 4.4 2D LUT layout in a 3D presentation	94

Figure 4.5 Representation of actuator velocities at three constant accelerations (a_1, a_2 and a_3). a_1 represents low acceleration, a_2 represents median acceleration and a_3 represents high acceleration ($a_1 \ll a_2 \ll a_3$). For the same sampling interval (Δt), the change in velocity over the interval is not the same ($\Delta v_{a1} \ll \Delta v_{a2} \ll \Delta v_{a3}$). v_{max_a} is a function of acceleration a ($v_{max_a1}, v_{max_a2}, v_{max_a3}$)	96
Figure 4.6 An example of superimposed measured differential pressures ($\Delta P_1, \Delta P_2, \Delta P_3$) versus velocity (v) at three accelerations (a_1, a_2, a_3). Note how the data is spread out because of different Δv_a at a constant sampling time (Δt). (Please note: the data is greatly exaggerated for clarity).....	97
Figure 4.7 Sampling point index numbers (SPIN) vs. sampling time	99
Figure 4.8 An example of start point(Sp) and end point (Ep) of each quadrant at acceleration $a = 1.5 \text{ m/s}^2$ (See zoom view for details)	100
Figure 4.9 An example of the start point of the 18 th cycle measured ΔP determined at acceleration $= 5 \text{ m/s}^2$	101
Figure 4.10 An example of four quadrants of ΔP separated by start and end points at $a = 5 \text{ m/s}^2$ (See zoom view for details). SPIN was used to develop these curves.	102
Figure 4.11 An example of velocity range specifications at three representative accelerations (a_1, a_2, a_3).....	103
Figure 4.12 An example of Universal Velocity Set (UVS) of three representative accelerations	104
Figure 4.13 Nomenclature used for the interpolation process under a constant acceleration condition (a). v_i is an Universal Velocity Set (UVS) point	106
Figure 4.14 Nomenclature for when Universal Velocity set points fall within the ΔP (friction) data points. v_{i1}, v_{i2}, v_{i3} are points in the Universal Velocity Set (UVS)	107
Figure 4.15 An example of interpolation in the Universal Velocity Set (UVS) which is a plot of pressure differential as a function of the Universal Velocity Set at three accelerations (a_1, a_2, a_3).....	108
Figure 4.16 3D visual plot for all 4 quadrants of VCHAS1	109
Figure 4.17 3D visual plot for Quadrant 1 of VCHAS1	110
Figure 4.18 3D visual plot for all 4 quadrants of VCHAS2	111
Figure 4.19 3D visual plot for Quadrant 1 of VCHAS2.....	111
Figure 4.20 Top view of the 3D plot of ΔP 2D LUT model for VCHAS1. Note the cyan region in which no experimental data exists	112

Figure 4.21 Top view of the 3D plot ΔP 2D LUT model for VCHAS2. Note the cyan region in which no experimental data exists	113
Figure 4.22 Model verification of the 2D LUT under constant acceleration levels	114
Figure 4.23 Model verification of the 2D LUT at $a = 0.001 \text{ m/s}^2$	115
Figure 4.24 Model verification of the 2D LUT at $a = 1.2 \text{ m/s}^2$	115
Figure 4.25 Model verification of the 2D LUT at $a = 5 \text{ m/s}^2$	116
Figure 5.1 Model validation strategy - error comparisons of the 2D LUT model and Stribeck model.....	119
Figure 5.2 A possible Matlab formulation of the model in which ΔP_{Ap} (hydraulic force) is the input. The term 2D LUT is already defined.	120
Figure 5.3 A possible Matlab formulation of the model in which x , v and a are the inputs and ΔP (hydraulic force) the output.	121
Figure 5.4 An example of an input sinusoidal displacement signal (x) to the VCHAS and the expected actuator velocity (v) and acceleration (a)	122
Figure 5.5 An example of motion condition (v , a) in the sinusoidal velocity (v), acceleration (a) and v - a curve. The v - a curve is an ellipse and is dependent on frequency (or period) of the sinusoidal signal	124
Figure 5.6 An example of a selected cycle of measured differential pressure (ΔP) and measured displacement (x) at frequency $f = 1.22 \text{ Hz}$. Please note: velocity and acceleration were not measured, but were obtained by differentiating the curve fitted position (x) once for velocity (v) and once again for acceleration (a) (see Section 5.2.4.3 for details)	126
Figure 5.7 An example of a selected cycle of the measured differential pressure (ΔP) under non-steady state conditions by a sinusoidal signal at frequency $f = 1.22 \text{ Hz}$ in four views – front view (ΔP vs. v), top view (a vs. v), side view (ΔP vs. a) and isometric view (ΔP vs. v , a)... ..	126
Figure 5.8 An example of measured differential pressure (ΔP) and displacement (x) at a frequency of 0.73 Hz . Data was collected for model validation at the 18th cycle (in red). ..	127
Figure 5.9 Sinusoidal curve fitting of the measured displacement at frequency $f = 0.02 \text{ Hz}$..	128
Figure 5.10 Sinusoidal curve fitting of the measured displacement at frequency $f = 0.73 \text{ Hz}$..	128
Figure 5.11 Sinusoidal curve fitting of the measured displacement at frequency $f = 1.22 \text{ Hz}$..	129
Figure 5.12 Sinusoidal curve fitting of the measured displacement at frequency $f = 1.48 \text{ Hz}$..	129

Figure 5.13 An example of start point(Sp) and end point (Ep) of a selected cycle of the sinusoidal signal at frequency $f = 0.73$ Hz.....	130
Figure 5.14 An example of the start point (Sp) of the 18th cycle measured ΔP determined at frequency $f = 0.73$ Hz	130
Figure 5.15 v-a curves of sinusoidal signals for low, medium, high and extreme high frequencies (0.02Hz (see the zoom view for details), 0.73 Hz, 1.22 Hz and 1.48 Hz), the background (red hatched region) shows the limits of the parabolic signals.....	132
Figure 5.16 The intersection point (v, a) of the elliptical curve (v-a) of sinusoidal signal and physical limit boundary line in Quadrant 1	134
Figure 5.17 Sinusoidal signal for model validation at low frequency $f = 0.02$ Hz (see the zoom view for details). The experimental physical limitations are provided by red lines. The different colors in the elliptical paths of velocity, acceleration and ΔP curves of one cycle represent the model data availability. Derivation of the data ranges is given in Appendix H. (Red solid: Limitations of 2D LUT; Green: Model validation zone; Blue dash: Extrapolation data).....	136
Figure 5.18 Sinusoidal signal for model validation at medium frequency $f = 0.73$ Hz. The experimental physical limitations are provided by red lines. The different colors in the elliptical paths of velocity, acceleration and ΔP curves of one cycle represent the model data availability. Derivation of the data ranges is given in Appendix H. (Red solid: Limitations of 2D LUT; Green: Model validation zone; Red dash: No model data zone).....	137
Figure 5.19 Sinusoidal signal for model validation at high frequency $f = 1.22$ Hz. The experimental physical limitations are provided by red lines. The different colors in the elliptical paths of velocity, acceleration and ΔP curves of one cycle represent the model data availability. Derivation of the data ranges is given in Appendix H. (Red solid: Limitations of 2D LUT; Green: Model validation zone; Red dash: No model data zone).....	138
Figure 5.20 Sinusoidal signal for model validation at extreme high frequency $f = 1.48$ Hz. The experimental physical limitations are provided by red lines. The different colors in the elliptical paths of velocity, acceleration and ΔP curves of one cycle represent the model data availability. Derivation of the data ranges is given in Appendix H. (Red solid: Limitations of 2D LUT; Green: Model validation zone; Red dash: No model data zone).....	139
Figure 5.21 Meshing technique which employs double interpolation of an operating point (v, a)	140
Figure 5.22 Flow chart of the meshing technique for determining single or double interpolation.	141
Figure 5.23 Single Interpolation algorithm. $\Delta P(v, a)$ is the calculated pressure differential (friction) value at input estimated velocity (v) and acceleration (a). All other terms are	

defined in Figure 5.2. Note that v_1 , v_2 and v are part of the Universal Velocity Set and a_1 , a_2 and a are part of the Universal Acceleration Set.....	141
Figure 5.24 Double interpolation (or meshing) algorithm. $\Delta P(v, a)$ is the calculated pressure differential (friction) value at input estimated velocity (v) and acceleration (a). All other terms are defined in Figure 5.21. Note that v_1 , v_2 and v are part of the Universal Velocity Set and a_1 , a_2 and a are part of the Universal Acceleration Set.....	142
Figure 5.25 Interpolation limitation between two accelerations due to the 2D LUT model boundaries (Please note: the data in this figure is greatly exaggerated for clarity. Also Green circles can represent experimental data whereas red circles do not.).....	143
Figure 5.26 An example of the interpolated underestimation of ΔP predicated by the 2D LUT near the boundary lines at frequency $f = 0.07$ Hz.....	143
Figure 5.27 The 3D experimentally obtained Stribeck ΔP LUT for VCHAS1 which is used in the model comparison study (Red for Quadrant 1, Green for Quadrant 2, Blue for Quadrant 3, and Magenta for Quadrant 4.	144
Figure 5.28 Model validation of the 2D LUT at a low sinusoidal frequency $f = 0.02$ Hz by superimposing the ΔP measured, ΔP from the 2D LUT and ΔP from the Stribeck model (Refer to Figure 5.17 for details of the regions (indicated by asterisks) with no model data of the 2D LUT at sinusoidal frequency $f = 0.02$ Hz)	146
Figure 5.29 Model validation of the 2D LUT at a medium sinusoidal frequency $f = 0.73$ Hz by superimposing the ΔP measured, ΔP from the 2D LUT, and ΔP from the Stribeck model (Refer to Figure 5.18 for details of the regions (indicated by circles) with no model data of the 2D LUT at sinusoidal frequency $f = 0.73$ Hz). Stri LUT refers to the Stribeck model lookup table.....	147
Figure 5.30 Model validation of the 2D LUT at a sinusoidal frequency $f = 1.22$ Hz by superimposing the ΔP measured, ΔP from the 2D LUT, and ΔP from the Stribeck model (Refer to Figure 5.19 for details of the regions (indicated by circles) with no model data of the 2D LUT at sinusoidal frequency $f = 1.22$ Hz). Stri LUT refers to the Stribeck model lookup table.....	148
Figure 5.31 Model validation of the 2D LUT at a sinusoidal frequency $f = 1.48$ Hz by superimposing the ΔP measured, ΔP from 2D LUT, and ΔP from Stribeck model (Refer to Figure 5.20 for details of the regions (indicated by asterisks and circles) with no model data of the 2D LUT at sinusoidal frequency $f = 1.48$ Hz). Stri LUT refers to the Stribeck model lookup table.....	149
Figure C.1 The pressure-voltage relationship of the pressure transducer of VCHAS1. The data was measured in psi and hence the graph is presented in this form. The sensitivities and calibration data can be converted to metric using the usual conversion equations.....	200

Figure C.2 The pressure-voltage relationship of the pressure transducer of VCHAS2. The data was measured in psi and hence the graph is presented in this form. The sensitivities and calibration data can be converted to metric using the usual conversion equations.....	201
Figure D.1 A cycle of the displacement curve with constant velocity for each direction; the period of the signal is P, the amplitude of the signal is A. Please note, L is the stroke of the piston. The amplitude A is half of the actuator stroke $A = L/2$	204
Figure D.2 A cycle of the velocity curve with constant velocity for each direction; the period of the signal is P, and the amplitude of the signal is the desired constant velocity v.....	204
Figure D.3 A cycle of the displacement curve to produce constant acceleration for each quadrant: the period of the signal is P, the amplitude of the signal is A where $A = L/2$. Please note, L is the stroke of the piston.	206
Figure D.4 A cycle of the resulting velocity curve; the period of the signal is P, the amplitude of the triangular waveform is the maximum velocity (v_{a_max}) the piston can achieve under constant acceleration (a) within the stroke of system.	206
Figure D.5 A cycle of the acceleration curve with constant acceleration for each quadrant; the period of the signal is P, and a is the amplitude of the signal which is the desired constant acceleration.	207
Figure E.1 16 positive velocity points were chosen for the Velocity list for VCHAS1. Note that the velocity intervals at lower velocity points are very small to accommodate measurements in which steady state friction (SSF) dominated.	210
Figure E.2 A total 32 velocity points (including the negative side) was chosen for the Velocity list for VCHAS1. SSF refers to steady state friction.	210
Figure E.3 Velocity vs Frequency of steady state friction measurement of VCHAS1.....	211
Figure E.4 15 positive velocity points were chosen for the Velocity list for VCHAS2. SSF refers to steady state friction.	212
Figure E.5 A total of 30 velocity points (including the negative side) were chosen for the Velocity list for VCHAS2. SSF refers to the steady state friction.	212
Figure E.6 Velocity vs Frequency of VCHAS2.....	213
Figure E.7 58 positive acceleration points were chosen for the Acceleration list for VCHAS1. NSSF refers to the non-steady state friction.	214
Figure E.8 A total of 116 acceleration points (including the negative side) of VCHAS1 for non-steady state friction (NSSF).	215
Figure E.9 Acceleration vs Frequency of VCHAS1	216

Figure E.10 41 positive acceleration points for VCHAS2 were chosen for the Acceleration list. NSSF refers to non-steady state friction	217
Figure E.11 A total 82 acceleration points (including the negative side) of VCHAS2 for non- steady state friction (NSSF)	218
Figure E.12 Acceleration vs Frequency of VCHAS2. NSSF refers to non-steady state friction	218
Figure F.1 A cycle of a periodic square wave S with amplitude (A), and period P	220
Figure F.2 A cycle of the adjusted square wave S with amplitude (A/2), and period P	220
Figure F.3 A cycle of a triangular wave obtained by integrating the square wave of Figure F.2	221
Figure F.4 A cycle of the adjusted triangular wave (M) of Figure F.3 with no bias	221
Figure F.5 A cycle of the parabolic wave T with amplitude ($AP^2/64$) and period (P)	222
Figure F.6 A cycle of the parabolic wave X with amplitude (A) and period (P)	222
Figure F.7 The Simulink © code to generate the periodic parabolic wave with period P, amplitude A	223
Figure G.1 Parabolic curve fitting of the measured displacement at acceleration = 4.8 m/s^2	224
Figure G.2 Parabolic curve fitting of the measured displacement at acceleration = 4.6 m/s^2	225
Figure G.3 Parabolic curve fitting of the measured displacement at acceleration = 4.4 m/s^2	225
Figure G.4 Parabolic curve fitting of the measured displacement at acceleration = 3.4 m/s^2	226
Figure G.5 Parabolic curve fitting of the measured displacement at acceleration = 2.2 m/s^2	226
Figure G.6 Parabolic curve fitting of the measured displacement at acceleration = 1.2 m/s^2	227
Figure G.7 Parabolic curve fitting of the measured displacement at acceleration = 0.2 m/s^2	227
Figure G.8 Parabolic curve fitting of the measured displacement at acceleration = 0.01 m/s^2 ..	228
Figure G.9 Sinusoidal curve fitting of the measured displacement at frequency $f = 0.98 \text{ Hz}$..	229
Figure G.10 Sinusoidal curve fitting of the measured displacement at frequency $f = 0.3 \text{ Hz}$..	230
Figure G.11 Sinusoidal curve fitting of the measured displacement at frequency $f = 0.07 \text{ Hz}$	230
Figure G.12 Sinusoidal curve fitting of the measured displacement at frequency $f = 0.03 \text{ Hz}$	231
Figure G.13 Model verification of the 2D LUT at $a = 0.01 \text{ m/s}^2$	232

Figure G.14 Model verification of the 2D LUT at $a = 0.2 \text{ m/s}^2$	232
Figure G.15 Model verification of the 2D LUT at $a = 1.2 \text{ m/s}^2$	233
Figure G.16 Model verification of the 2D LUT at $a = 2.2 \text{ m/s}^2$	233
Figure G.17 Model verification of the 2D LUT at $a = 3.4 \text{ m/s}^2$	234
Figure G.18 Model verification of the 2D LUT at $a = 4.4 \text{ m/s}^2$	234
Figure G.19 Model verification of the 2D LUT at $a = 4.6 \text{ m/s}^2$	235
Figure G.20 Model verification of the 2D LUT at $a = 4.8 \text{ m/s}^2$	235
Figure G.21 Sinusoidal signal for model validation at medium frequency $f = 0.03 \text{ Hz}$. The experimental physical limitations are provided by red lines. The different colors in the elliptical paths of velocity, acceleration and ΔP curves of one cycle represent the model data availability. Derivation of the data ranges was given in Appendix C.2.4. (Red solid: Limitations of 2D LUT; Green: Model validation zone; Red dash: No model data zone)..	237
Figure G.22 Model validation of the 2D LUT at frequency $f = 0.03 \text{ Hz}$. Stri LUT refers to the Stribeck lookup table.....	238
Figure G.23 Sinusoidal signal for model validation at medium frequency $f = 0.07 \text{ Hz}$. The experimental physical limitations are provided by red lines. The different colors in the elliptical paths of velocity, acceleration and ΔP curves of one cycle represent the model data availability. Derivation of the data ranges is given in Appendix C.2.4. (Red solid: Limitations of 2D LUT; Green: Model validation zone; Red dash: No model data zone)..	239
Figure G.24 Model validation of the 2D LUT at frequency $f = 0.07 \text{ Hz}$. Stri LUT refers to the Stribeck lookup table.....	240
Figure G.25 Sinusoidal signal for model validation at medium frequency $f = 0.3 \text{ Hz}$. The experimental physical limitations are provided by red lines. The different colors in the elliptical paths of velocity, acceleration and ΔP curves of one cycle represent the model data availability. Derivation of the data ranges is given in Appendix C.2.4. (Red solid: Limitations of 2D LUT; Green: Model validation zone; Red dash: No model data zone)..	241
Figure G.26 Model validation of the 2D LUT at frequency $f = 0.3 \text{ Hz}$. Stri LUT refers to the Stribeck lookup table.....	242
Figure G.27 Sinusoidal signal for model validation at medium frequency $f = 0.98 \text{ Hz}$. The experimental physical limitations are provided by red lines. The different colors in the elliptical paths of velocity, acceleration and ΔP curves of one cycle represent the model data availability. Derivation of the data ranges is given in Appendix C.2.4. (Red solid: Limitations of 2D LUT; Green: Model validation zone; Red dash: No model data zone)..	243

Figure G.28 Model validation of the 2D LUT at frequency $f = 0.98$ Hz. Stri LUT refers to the Stribeck lookup table.....	244
Figure H.1 The four intersection points (in circles) (v_1, a_1) , (v_2, a_2) , (v_3, a_3) , and (v_4, a_4) of the elliptical curve (v - a) of the sinusoidal signal and physical limit boundary lines in all quadrants	248
Figure H.2 The four time points t_1, t_2, t_3, t_4 correspond to the four intersection points (v_1, a_1) , (v_2, a_2) , (v_3, a_3) , and (v_4, a_4) of Section H.2.3	250
Figure H.3 The four intersection points (in asterisks) (v_1, a_1) , (v_2, a_2) , (v_3, a_3) , and (v_4, a_4) of the elliptical curve (v - a) of the sinusoidal signal and maximum/ minimum acceleration lines in all quadrants	251
Figure H.4 The four time points t_1, t_2, t_3, t_4 correspond to the four intersection points (v_1, a_1) , (v_2, a_2) , (v_3, a_3) , and (v_4, a_4) of Section H.2.5	252
Figure I.1 3D visual plot for Quadrant 2 of VCHAS1.....	254
Figure I.2 3D visual plot for Quadrant 3 of VCHAS1 viewing from the bottom up (note, the sign of ΔP (kPa) is negative).....	255
Figure I.3 3D visual plot for Quadrant 4 of VCHAS1 viewing from the bottom up (note, the sign of ΔP (kPa) is negative).....	255
Figure I.4 3D visual plot for Quadrant 2 of VCHAS2.....	256
Figure I.5 3D visual plot for Quadrant 3 of VCHAS2 viewing from the bottom up (note, the sign of ΔP (kPa) is negative).....	256
Figure I.6 3D visual plot for Quadrant 4 of VCHAS2 viewing from the bottom up (note, the sign of ΔP (kPa) is negative).....	257
Figure I.7 Isometric View of the 2D LUT of VCHAS1	258
Figure I.8 Front View of the 2D LUT of VCHAS1.....	259
Figure I.9 Side View of the 2D LUT of VCHAS1	259
Figure I.10 Isometric view of 2D LUT of VCHAS2	260
Figure I.11 Front view of the 2D LUT of VCHAS2.....	260
Figure I.12 Side view of the 2D LUT of VCHAS2	261
Figure J.1 Start points and end points of each quadrant of a selected cycle.....	262

NOMENCLATURE

a	Acceleration	[m s ⁻²]
a_0	Initial acceleration	[m s ⁻²]
a_1	1 st acceleration – low	[m s ⁻²]
a_2	2 nd acceleration – medium	[m s ⁻²]
a_3	3 rd acceleration 3 – high	[m s ⁻²]
a_n	n th acceleration	[m s ⁻²]
a_f	Double Derivative of Curve fitted displacement	[m s ⁻²]
a_{ini}	Initial acceleration	[m s ⁻²]
a_{max}	Maximum acceleration	[m s ⁻²]
a_{min}	Minimum acceleration	[m s ⁻²]
a_{sim}	Predicted acceleration	[m s ⁻²]
A_1	Effective piston area of chamber 1	[m ²]
A_2	Effective piston area of chamber 2	[m ²]
A_p	Effective piston area	[m ²]
A	Amplitude of piston displacement	[m]
e	Euler's number	[-]
e_{EL}	Error between measured and predicted ΔP from 2D LUT model	[kPa, psi]
e_{ES}	Error between measured and predicted ΔP from Stribeck model	[kPa, psi]
F	Applied force	[N]
F_c	Coulomb friction force	[N]
F_{c_A}	Coulomb friction force – Type A	[N]
F_{c_B}	Coulomb friction force – Type B	[N]
F_{c_C}	Coulomb friction force – Type C	[N]
F_{c_D}	Coulomb friction force – Type D	[N]
F_b	Breakaway friction force	[N]
F_d	Dynamic friction force	[N]

F_f	Friction force	[N]
F_s	Static friction force	[N]
F_{stri}	Stribeck friction force	[N]
F_v	Viscous friction force	[N]
F_0	Static friction force	[N]
F_1	Difference between the static friction and the kinetic friction	[N]
f	Frequency of the signal	[Hz]
f_s	Sampling frequency	[Hz]
f_{sig}	Signal frequency	[Hz]
K_v	Viscous Coefficient	[Nmrad ⁻¹ s ⁻¹]
L	Actuator stroke	[m]
M_c	Total mass of VCHAS1	[kg]
M_e	Extra mass	[kg]
M_h	Total mass of VCHAS2	[kg]
M	Mass	[kg]
N_s	Number of sampling points	[-]
N_v	Number of velocity points	[-]
n	Index	[-]
n_1	Index1	[-]
n_2	Index 2	[-]
P	Instantaneous absolute pressure	[MPa]
P_1	Pressure of chamber 1	[kPa, psi]
P_2	Pressure of chamber 2	[kPa, psi]
ΔP	Differential pressure between chambers	[kPa, psi]
ΔP_E	Measured differential pressure	[kPa, psi]
ΔP_L	Predicted differential pressure by 2D LUT	[kPa, psi]
ΔP_S	Predicted differential pressure by Stribeck Model	[kPa, psi]
ΔP_{exp}	Measured differential pressure	[kPa, psi]
ΔP_{sim}	Predicted differential pressure	[kPa, psi]

Q_1	Flow into the actuator	$[\text{m}^3 \text{s}^{-1}]$
Q_2	Flow out of the actuator	$[\text{m}^3 \text{s}^{-1}]$
$Q1$	Quadrant 1	[-]
$Q2$	Quadrant 2	[-]
$Q3$	Quadrant 3	[-]
$Q4$	Quadrant 4	[-]
t	Time	[s]
t_s	Sampling rate	[s]
t_{sig}	Signal period	[s]
Δt	The sampling time	[s]
T	Instantaneous temperature	$[\text{°C}]$
v	Velocity	$[\text{m s}^{-1}]$
v_i	Velocity at i point	$[\text{m s}^{-1}]$
v_s	Stribeck Velocity	$[\text{m s}^{-1}]$
v_{ini}	Initial velocity	$[\text{m s}^{-1}]$
v_{sim}	Predicted velocity	$[\text{m s}^{-1}]$
v_0	Characteristic velocity at which the system transitions to kinetic friction	$[\text{m s}^{-1}]$
v_1	Velocity 1	$[\text{m s}^{-1}]$
v_2	Velocity 2	$[\text{m s}^{-1}]$
v_{max}	Max velocity	$[\text{m s}^{-1}]$
v_{max_a}	Max velocity under acceleration a	$[\text{m s}^{-1}]$
v_{max_a1}	Max velocity under 1 st acceleration a_1	$[\text{m s}^{-1}]$
v_{max_a2}	Max velocity under 2 nd acceleration a_2	$[\text{m s}^{-1}]$
v_{max_a3}	Max velocity under 3 rd acceleration a_3	$[\text{m s}^{-1}]$
Δv_a	The velocity interval for any constant acceleration (a)	$[\text{m s}^{-1}]$
Δv_{a1}	1 st velocity interval for any constant acceleration (a_1)	$[\text{m s}^{-1}]$
Δv_{a2}	2 nd velocity interval for any constant acceleration (a_2)	$[\text{m s}^{-1}]$
Δv_{a3}	3 rd velocity interval for any constant acceleration (a_3)	$[\text{m s}^{-1}]$

v_f	Derivative of Curve fitted displacement	[m s ⁻¹]
x	Displacement	[m]
x_{exp}	Measured displacement	[m]
x_{sim}	Predicted displacement	[m]
x_{max}	Maximum displacement	[m]
x_f	Curve fitted displacement	[m]
z	Average deflection of the bristles	[m]
α	Size of active region	[-]
β	Amplitude gain	[-]
w	Complement of the average dynamic z	[m]
ω	Angular frequency of the input signal	[rad/s]

CHAPTER 1: BACKGROUND AND INTRODUCTION

1.1 Research Background

Industrial applications increasingly require hydraulic actuation systems that offer a combination of high force (torque) output, large stroke, variable velocity and high accuracy. Some traditional approaches to accomplish this make use of hydraulic actuation systems in which a fixed displacement pump and valve, or a closed circuit variable displacement pump modulate flow to a linear or rotary actuator (In this research, only linear hydraulic actuators are considered). In general, hydraulic actuation systems can be categorized as valve controlled hydraulic actuation systems (VCHAS) and pump controlled hydraulic actuation systems (PCHAS). This categorization is illustrated in Figure 1.1 [1].

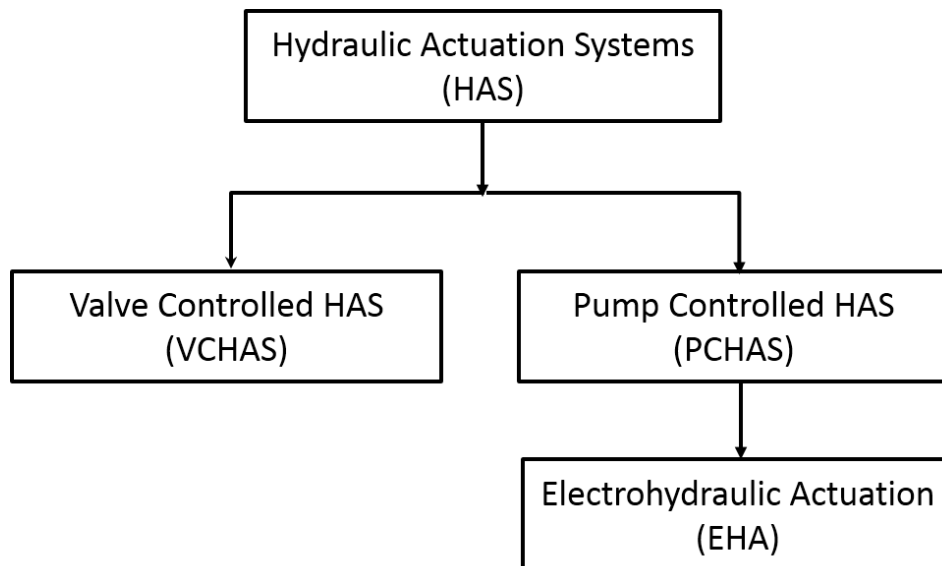


Figure 1.1 Categorization of hydraulic actuation systems (HAS)

With reference to Figure 1.2, in the VCHAS configuration, a hydraulic power supply (a pressure compensated pump, for example) delivers “demand” flow to a proportional valve (in Figure 1.2, an electrohydraulic servovalve) which in turn, modulates flow to a linear actuator. In some cases, these systems use feedback (e.g. position or velocity feedback) for control purposes, but because a pressure drop across the valve is required to modulate the flow, power losses occur which reduce the efficiency of the system significantly [2].

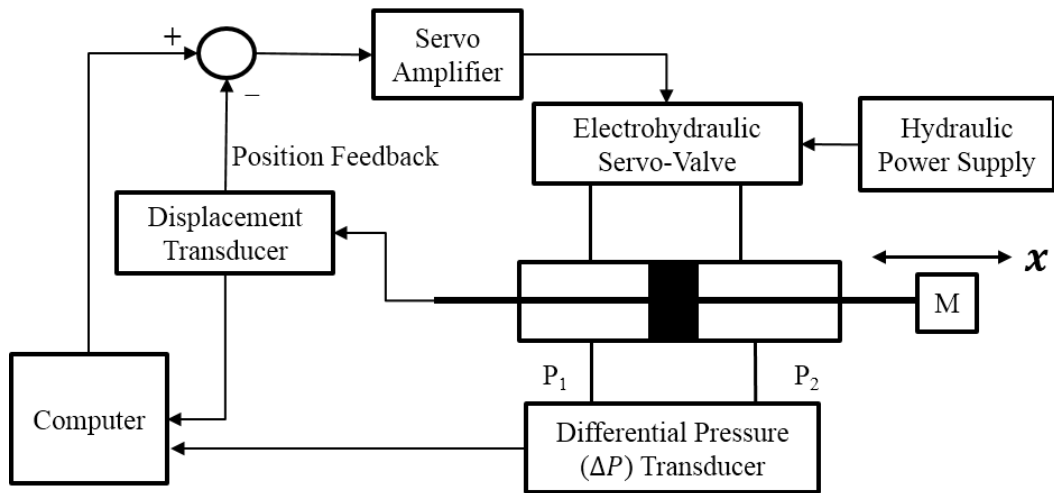


Figure 1.2 Schematic of a typical valve controlled hydraulic actuation system (VCHAS)

The PCHAS configuration uses a variable displacement pump which ports the output flow from the actuator directly back to the inlet of the pump (closed system, see Figure 1.3) or in some cases, back to the system reservoir if the load is primarily resistive (open system).

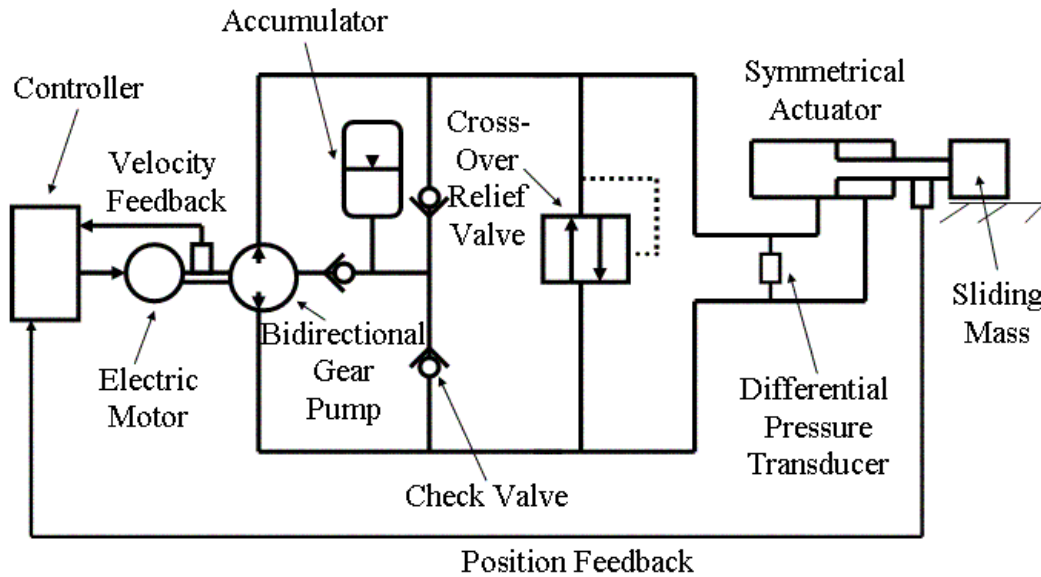


Figure 1.3 Schematic of a pump controlled hydraulic actuation system (PCHAS). This is an example of a closed hydraulic system because the flow from the actuator is directed back to the inlet of the pump. A schematic of the symmetrical actuator is shown in Figure 1.4

Movement of the actuator is controlled by varying the amount of flow that comes from the pump which in turn is controlled by changing the pump swash plate angle or the angular speed of the pump driving motor. If the system is closed, the actuator must be symmetric and thus for

linear single rod actuation, special actuators have to be designed. Closed or open systems of this form are highly desirable because they do not require valves to modulate the flow which increases the system efficiency [3]. These systems are often labelled as hydrostatic or electrohydraulic actuation (EHA) systems [4, 5].

Consider the pump controlled electrohydraulic actuation system (PCHAS) shown in Figure 1.3. A special version of the PCHAS was designed by Habibi et al which could position a 20 kg linear load to a positional accuracy of 50 ± 25 nm which was quite unprecedented for such systems [3]. Habibi labelled this system as an electrohydraulic actuator (EHA) [4]. This accuracy was a secondary (and indeed, unexpected) outcome of the design, the primary outcome being an EHA system which could control a single rod actuator (Figure 1.4) in a closed form.

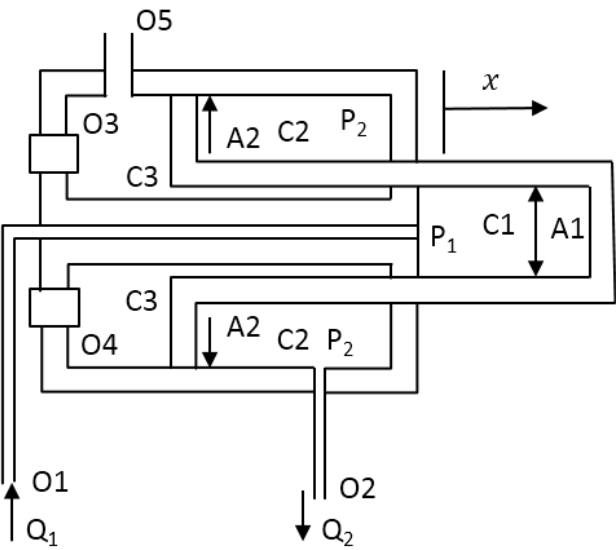


Figure 1.4 Design of a single rod, symmetric actuator by Habibi et al. [3]. Note the “third” chamber C3 which allows the effective areas of the pistons to be equal; that is A1, the working area (in a circular shape) of the “first” chamber C1 is designed to be equal to A2, the working area (in a ring disc shape) of the “second” chamber C2. Therefore, the inlet flow Q_1 of opening O1 equals to the outlet flow Q_2 of opening O2. The openings O3 and O4 allow draining of fluid from Chamber C3. Opening O5 is provided to allow pressurization of Chamber C3 for special applications

To better understand why this positional accuracy was possible, a study was undertaken by Li et al (which is presented in Appendix A) to model the EHA based on well-established equations and behavioral characteristics (such as “classical” actuator friction) directly measured from the EHA [6].

An unexpected result arose from this study: the predicted position output from a simulation of the EHA under certain circumstances demonstrated limit cycles whereas the actual output from the experimental system show a damped response. The simulated results of a step response of the EHA assuming a Stribeck model for friction (to be discussed) is shown in Figure 1.5. Figure 1.6 shows the experimental step response of the EHA using the same input.

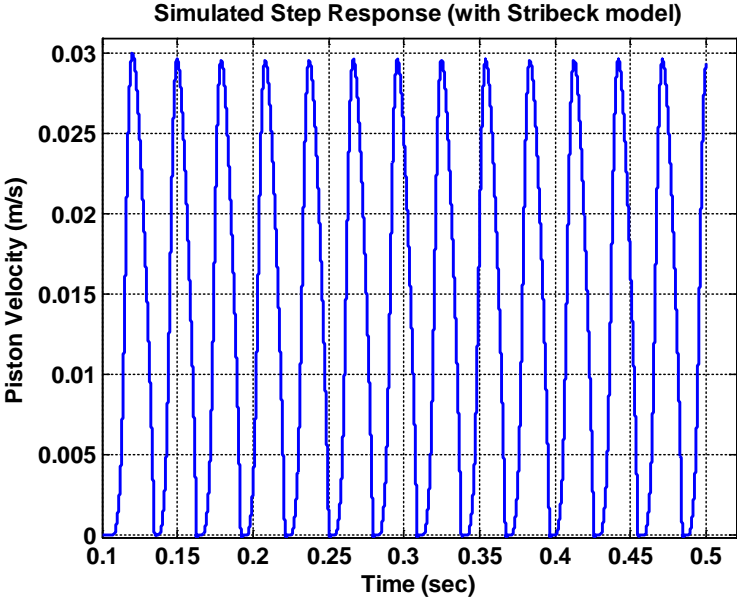


Figure 1.5 Simulated step response of the EHA (with Stribeck model)

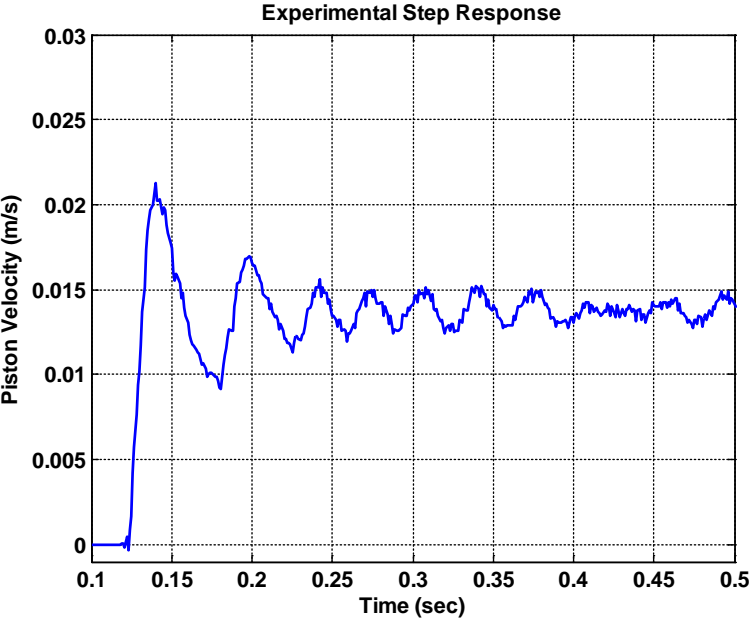


Figure 1.6 Experimental step response of the EHA [6]

This result was surprising because the equations used in the model were well established for this system in previous studies [4, 7]. Further, careful measurements of system properties and behavioral characteristics such as nonlinear lubricated friction were conducted. Thus, the question of “what was the underlying reason for the observed discrepancy” arose and indeed, became the motivation for this research. After examining various possibilities for this issue, it was proposed that nonlinear lubricated friction in the actuator might be the cause. The model assumed the standard Stribeck formulation of friction [7] (to be expanded upon in the next section and Chapter 2) whose form was substantiated experimentally using well accepted experimental techniques [2, 8]. This was concluded because a sensitivity study on the model showed that if the friction of the EHA was assumed to be purely viscous as opposed to a Stribeck formulation of friction, limit cycles did not appear. Subsequently, it was hypothesized that the assumed form of friction using the Stribeck model was not appropriate for the conditions experienced in the simulation studies. Thus, nonlinear lubricated friction in linear hydraulic actuators became the main focus of this thesis.

1.2 Brief Introduction of Friction

1.2.1 Classical Friction Models

A literature review of lubricated friction and its effect on hydraulic actuation systems will be presented in Chapter 2. This section will briefly present a review of the classical friction models including the traditional Stribeck model and how the characteristics are traditionally represented.

In hydraulic systems, friction exists between the piston and the cylinder in which it resides. To prevent leakage across the piston lands (or externally between the piston rod and outside sleeves), seals of various sorts are employed. In some applications such as servovalves, the clearances between the piston lands and sleeves are very small and hence no physical seals are required. In most “working” actuators, however, seals of some sort are required.

In the traditional sliding surface sense, there are two main types of friction: static (from pre-sliding to breakaway) friction and dynamic (sliding) friction [9]. Static friction is the friction between two contact surfaces without relative motion; it is also referred to as a pre-sliding condition. Static friction is always equal to the applied force but is in the opposite direction as illustrated in Figure 1.7. The maximum value of static friction is defined as breakaway

friction (F_b). This break-away friction occurs between two contact surfaces which are just about to slip. Note, break-away friction is commonly referred to as static friction in the literature [10]. Dynamic friction (F_d), also known as kinetic friction, is defined as the friction between two contact surfaces with relative motion (essentially a sliding condition). The term dynamic friction applies to both dry and lubricated conditions. Generally, friction is always against the applied force in the pre-sliding phase and always against the sliding motion direction in the sliding phase (Figure 1.7). A graphical representation of these friction types is given in Figure 1.8.

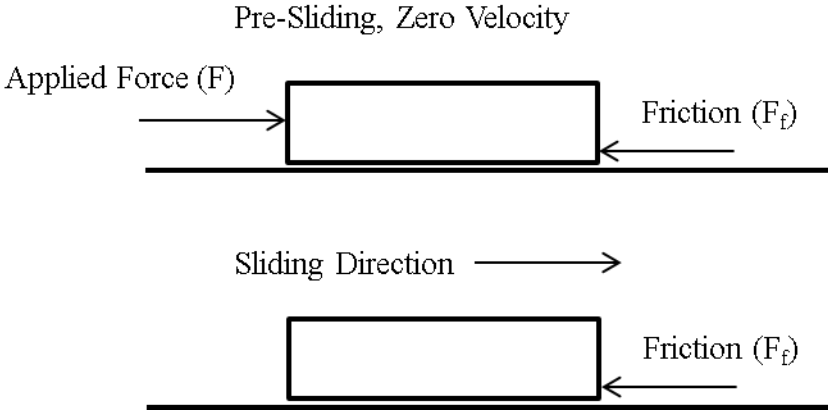


Figure 1.7 Friction is always against the applied force in the pre-sliding phase and always against the sliding motion direction in the sliding phase

Based on the physical conditions of the contact surfaces, friction can be placed into two categories: dry friction and lubricated friction [10]. Dry friction refers to the friction between two unlubricated solid surfaces, whereas, lubricated friction refers to the friction between moving surfaces that are separated by a partial or complete layer of fluid or some solid. Figure 1.8 illustrates that in the pre-sliding condition, dry friction and lubricated friction display similar behavior, that is, static friction matches the applied force until reaching the breakaway point. Usually, the static coefficient of dry friction is larger than that for lubricated friction; therefore, the breakaway friction of dry friction is larger than that of lubricated friction.

After the break-away point, sliding occurs; dry friction is nearly independent of the sliding velocity [11] whereas lubricated friction is primarily a function of velocity. In this study, lubricated friction in hydraulic actuation systems (specifically linear actuators) was the main concern and hence for the most part, discussion is focused on lubricated friction only.

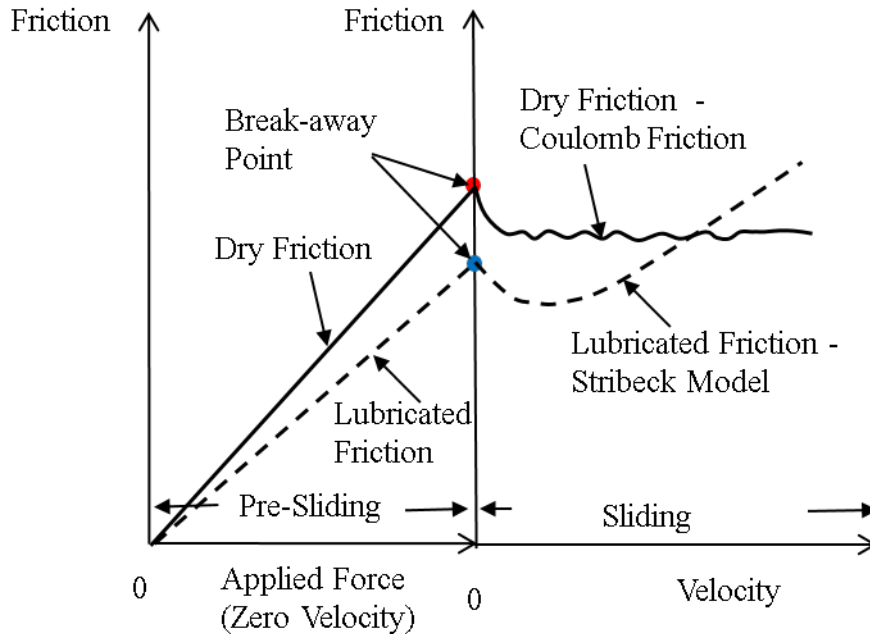


Figure 1.8 Friction in the pre-sliding and sliding conditions. In the pre-sliding condition, dry or lubricated friction is equal to the applied force (but in the opposite direction). In general breakaway friction for dry friction is larger than for lubricated friction. Once the system breaks away, the system starts to move (the sliding condition) and lubricated friction is a function of velocity (Stribeck friction) whereas dry friction is approximately independent of velocity (Coulomb friction).

There are four types of classical friction models used in the modeling and simulation of hydraulic actuation systems which are usually presented graphically or mathematically as a function of velocity [12]: Coulomb friction, viscous friction, Coulomb friction plus viscous friction and Stribeck friction.

Coulomb friction is a constant friction force (does not vary with velocity) and is discontinuous at zero velocity. Coulomb friction represents friction associated with mechanical surfaces rubbing together and includes bearing friction, friction in flight control surface hinges, and so on. The most prevalent physical explanation for Coulomb friction is that it is a “dry” friction, and is independent of the velocity of sliding (see Figure 1.9).

However, in the literature, the term Coulomb friction has often been used for any friction which is independent of velocity, which includes lubricated conditions [13]. Thus the term Coulomb friction is applied to both dry and lubricated conditions.

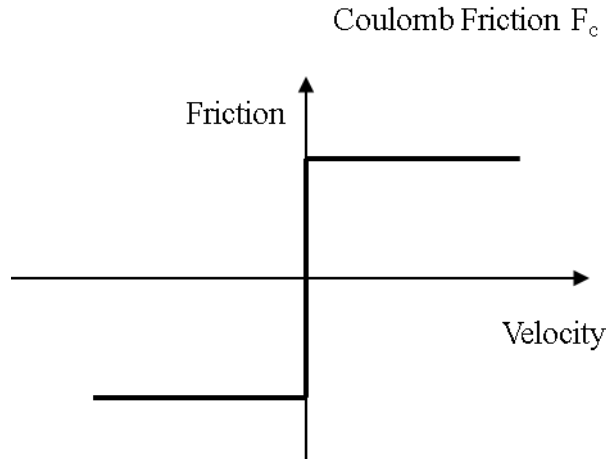


Figure 1.9 Coulomb friction

Viscous friction is that force required to move one surface with respect to another in which the fluid in-between undergoes a shearing action. Viscous friction is a linear function of the velocity as illustrated in Figure 1.10. The shearing action on the fluid is velocity (and viscosity) dependent and mathematically is given by the relationship $F_v = K_v v$ which is linearly proportional to the sliding velocity, where F_v is viscous friction, K_v the viscous coefficient, and v the sliding velocity. Viscous friction is continuous at zero velocity.

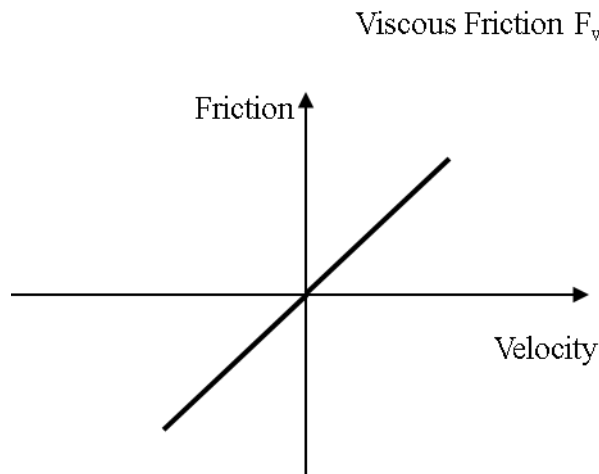


Figure 1.10 Viscous friction which is a linear function of the velocity

It is interesting to note that even for hydraulic actuators in which sealing between the piston and cylinder is achieved through the use of rubber or metal seals, viscous friction can still dominate at high velocities beyond the “Stribeck velocity” (to be defined).

The Coulomb friction plus viscous friction model illustrated in Figure 1.11 is a popular model used for the modeling and simulation in hydraulic actuation systems. As its name suggests, this is the combination of the first two models. The model is discontinuous at zero velocity, but it still is not a true representation of the lubricated friction at low velocities.

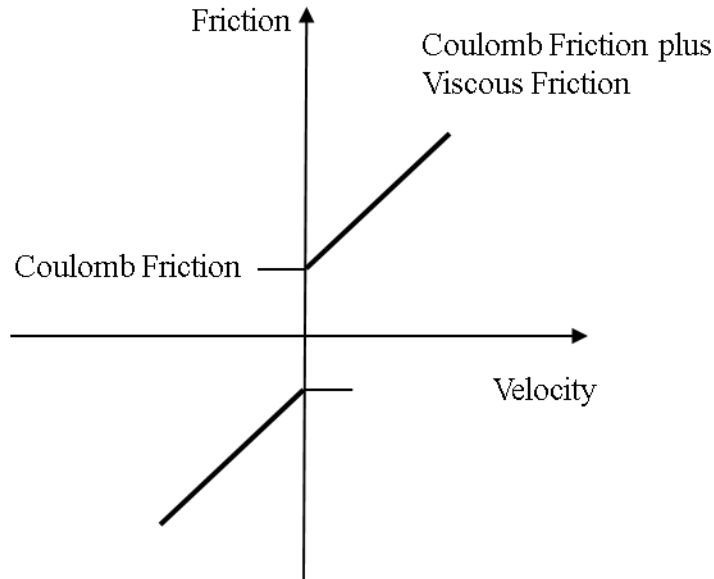


Figure 1.11 Coulomb friction plus viscous friction

A third type of model is called the Stribeck model and is associated with breakaway friction in which the contact between the piston (or seal) and the cylinder housing is “broken” before the piston can move. It is similar to static (breakaway) friction in mechanical systems except there is a transition to the Coulomb and viscous states. This results in a “negative” viscous friction (the slope of the friction velocity curve) at velocities less than the “Stribeck velocity” as shown in Figure 1.12. The model is also discontinuous at zero velocity.

Consider Figure 1.12. It is necessary to clearly define some terms which have appeared in the literature in various forms and have provided much confusion when trying to discuss lubricated friction. As mentioned above, the transition between the breakaway friction and Coulomb and viscous friction is called the “Stribeck friction”. The point where the transition ends and Coulomb and viscous friction dominate is called the “Stribeck velocity”. Beyond the Stribeck velocity, the friction is dominated by Coulomb and/or viscous friction. As illustrated in Figure 1.11, the offset of viscous friction is sometimes called Coulomb friction (see Figure 1.11). More details about this subject will be provided in Chapter 2. The full curve which shows the Stribeck

friction, the Coulomb friction and the viscous friction is called the “Stribeck model”. In the literature, the term “Stribeck Effect” is often used to describe the consequences of the Stribeck model. This thesis then will adopt the aforementioned terminology throughout.

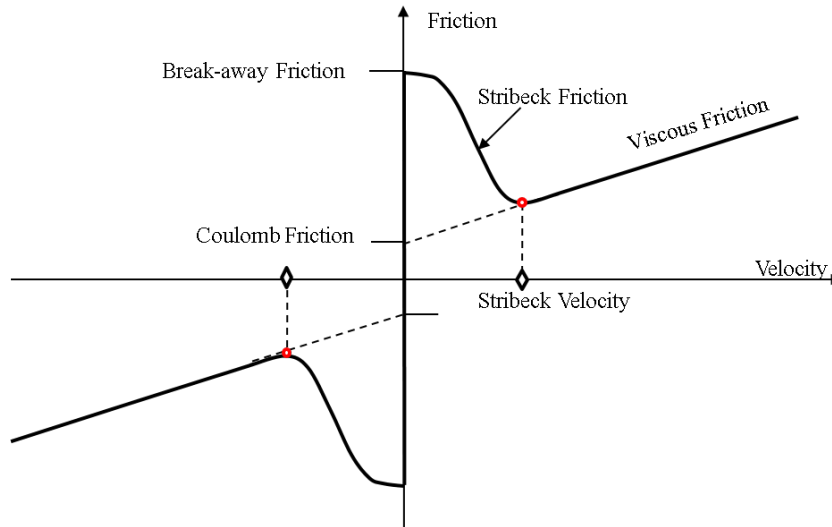


Figure 1.12 A typical Stribeck model

With reference to Figure 1.12, note how the Stribeck model has a minimum value and is dominated by the Stribeck friction at velocities less than the Stribeck velocity and by viscous friction at velocities higher than the Stribeck velocity. It is also noteworthy that Coulomb friction simply raises or lowers the total friction curve. Determining the Coulomb Friction term creates its own challenges as it is also defined several ways in the literature. However, further discussion is deferred to Chapter 2.

Any friction represents wasted energy that is dissipated as heat within the actuator. Therefore, friction reduces overall actuator efficiency especially at higher velocities. Normally, it is desirable to keep friction in any moving parts low. However, there are tradeoffs in the potential for leakage and seals to wear prematurely if friction levels are designed too high [14].

1.2.2 Experimental Techniques to Measure Friction

As mentioned previously, the Stribeck model shown in Figure 1.12 is most often assumed in fluid power studies. It is important to this thesis, however, to illustrate how this model has been obtained experimentally. Since lubricated friction is plotted as a function of velocity, the experimental system requires a method of measuring force on a piston at discrete velocities. Such

an approach has been used by Burton 1975 [15], Armstrong-Helouvry 1991[16] and Chinniah 2004 [8], amongst others, using an experimental system similar to that shown in Figure 1.2. Some other techniques that have been used to measure friction will be discussed in Chapter 2.

With reference to Figure 1.2, the differential pressure ($\Delta P = P_1 - P_2$) across the linear actuator is measured and used to determine the friction force by using Newton’s second law. The actuator and valve system is a closed loop system (as opposed to a closed system) in which velocity or position feedback is employed. If velocity is the controlled variable, then a square wave input is used; if the feedback is position, then a triangular input signal is used. In both cases, the output velocity is a square wave. The amplitude of the velocity signal is changed (or the slope of the ramp of the triangular waveform in the position feedback case) and at some steady state part of the output curve, the pressure difference is measured. This is usually considered as a “discrete type” of measurement because the transients must settle before a measurement can be made. It is important to note that temperature must be carefully controlled in this experimental approach to obtain repeatability and to rule out the temperature effects on the measurements.

A typical lubricated friction (F_f) versus velocity (v) curve for one of the valve controlled hydraulic actuators (VCHAS1) under steady state condition in the fluid power laboratory at the University of Saskatchewan is shown in Figure 1.13. Details of the definition of steady state condition and the procedure to generate this curve are given in Chapter 3. It is quite apparent that this friction under steady state conditions follows a Stribeck model form.

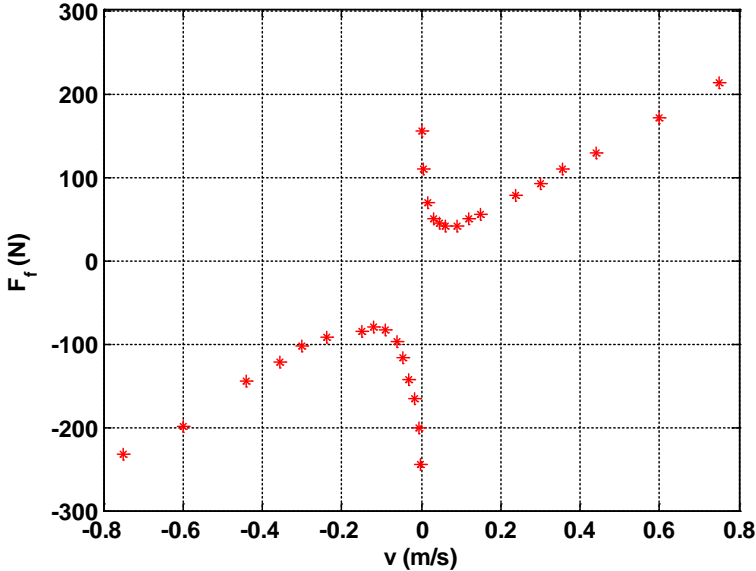


Figure 1.13 Discrete friction vs. velocity curves under steady state conditions

1.3 Limitations of the Stribeck Model

There have been many studies conducted on lubricated friction of hydraulic actuation systems and methods of overcoming the Stribeck friction portion of the Stribeck model [12, 14, 17-19]. A more detailed literature review of this subject is presented in Chapter 2, but a few important studies are briefly considered in this section. Sugimura et al. [20] did basic lubrication research by placing a lubricated ball under a rotating disk which was accelerating or decelerating. They observed that the Elasto-Hydro-Dynamic film thickness between the contacts of the ball and disk was highly acceleration (and deceleration) dependent, and that film thickness decreased with positive acceleration, but increased with negative acceleration (deceleration) in a linear fashion. Further, they established that the film thickness under acceleration or deceleration conditions were different from the film thickness under the constant velocity condition (acceleration = 0).

It is known that lubricated friction is very sensitive to the thickness of the lubrication film [21]. It was therefore postulated by the author of this thesis that perhaps lubricated friction would be also sensitive to the acceleration effect. Some of the results that other researchers found tended to support this idea. For example, the research work of Owen et al. [22] showed that the Stribeck effect can be eliminated and the friction in the axial direction and the hysteresis effect can be reduced by rotating the piston and rod while moving in the axial direction. In addition, they found that the Stribeck friction region of the friction–velocity curve is avoided under rotation and the axial friction opposing the piston movement is approximately linearized. The research work of Harnoy et al. [23] indicated that friction is not only a function of the velocity at that instant, but rather a function of the “past history” of the motion; however, since the “past history” of the motion was not well defined in this paper, improvement to the Stribeck model was not made.

1.3.1 Acceleration Effect on Friction

As briefly discussed in Section 1.1, in some early modeling studies on Habibi’s high precision EHA [4], it was observed that under certain conditions, limit cycles were predicted in the step response of the output actuator velocity, but were not observed physically even though the parameters used in the modeling were based on experimental measurements. A major question arose from this observation: why do the results of the simulation of the high precision electrohydraulic actuation system using a traditional Stribeck model, not correlate well with the

experiment results even though the most relevant parameters were measured from the experimental system? It was suspected that the measured (and subsequently modeled) friction characteristics of the actuator obtained under a set of constant velocities may not be physically representative of friction under high acceleration conditions and thus be part of the reason for this discrepancy.

To determine if the acceleration did play a role in friction, an initial study (using a unique input signal to the aforementioned EHA and which will be expanded upon in a later Chapter) was conducted. The friction characteristics for increasing velocity in one direction were obtained and are shown in Figure 1.14 in which acceleration was held constant for each test over the effective velocity ranges (The unit of acceleration is m/s^2). Clearly, the friction-velocity curves varied and did show a dependency on acceleration. A paper based on this preliminary work was submitted and presented at the ASME / Bath conference [24] and an updated version in CANCAM 2013 [25] and are presented in Appendix B1 and B2.

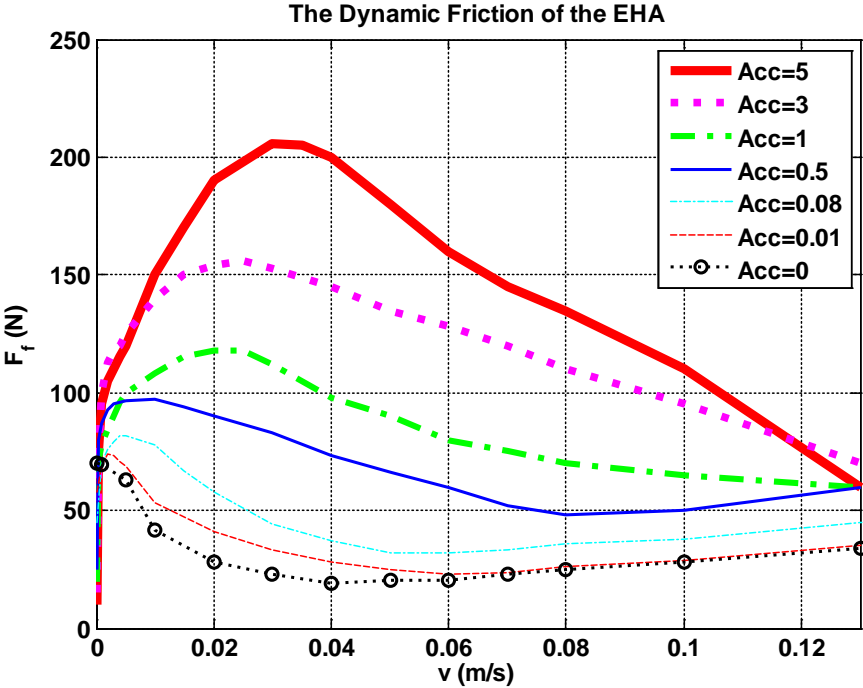


Figure 1.14 Typical friction result for increasing velocity in one direction for the EHA. (Reproduced with permission from the ASME/Bath symposium [24]). Please note: Acc refers to acceleration, units are m/s^2

A critical question was raised at the ASME/Bath conference about how universal was this type of result as it was only applied to a single EHA system and only in one direction. It then

became the objective at this stage to expand the study on the EHA to include other conditions, where the actuator increased and decreased its velocity in both directions. Unfortunately, the EHA system experienced a critical electronic hardware failure which could not be fixed in a reasonable time frame. Thus, it was recognized that the study had to be expanded to other system configurations so that the lubricated friction of other types of actuators could be examined systematically.

1.4 Hypothesis of the Research

Based on the observations presented in the above discussion, the following hypothesis is forwarded.

Lubricated friction in hydraulic actuation systems is not only a function of velocity, but is also a function of both velocity and acceleration.

1.5 Objectives and Scope of Thesis

The primary objective was to experimentally prove the stated hypothesis for hydraulic actuation systems; specifically, to determine whether the acceleration of the sliding piston of a hydraulic actuation systems plays an important role in nonlinear friction modeling. Specific sub-objectives include the following:

- To conduct a literature review on nonlinear lubricated friction modeling in hydraulic actuation systems ;
- To experimentally investigate acceleration dependent nonlinear lubricated friction in hydraulic actuation systems ;
- To develop a semi-empirical model of acceleration dependent nonlinear lubricated friction;
- To experimentally verify the semi-empirical model by implementing a semi-empirical and Stribeck model into a real time simulation of an actuator and by comparing the experimental outputs against simulated outputs for a common sinusoidal input.

This scope of this study will focus on the effect of system acceleration on the nonlinear lubricated friction in linear hydraulic actuation systems. As stated in Section 1.3.1, preliminary results of the EHA indicated that lubricated friction did show some dependency on acceleration,

but the study needed to be substantially expanded to other hydraulic actuation systems. In addition, these preliminary tests were conducted for a simple case where the velocity increased only in one direction. It was deemed necessary to extend the tests to cases where the actuator increased and decreased its velocity in both directions. Thus this research focused on two other hydraulic actuation systems commonly found in fluid power industrial applications. Although temperature effects on friction are important, temperature was assumed to be (and made to be experimentally) approximately constant in this study. In addition it was assumed that the load variations were sufficiently small such that pressure effects on friction would also be minimized. The reliability or the uncertainty of the position and pressure measurements of the hydraulic actuation systems were not considered. The methodology used in this study included both experimental and numerical modeling components.

1.6 Outline of Thesis

The thesis consists of six chapters, plus references and appendices. A brief description of each chapter is given below.

Chapter 1 briefly reviews friction modeling and measurements, introduces the hypothesis and main objectives of the study and presents the background information for the study.

Chapter 2 comprehensively reviews the relevant literature related to nonlinear lubricated friction modeling in hydraulic actuation systems and provides a detailed review of the past research related to this new acceleration dependent modeling approach.

Chapter 3 describes the experiment design, setup and data collection of the measurements of position and differential pressures to determine the changes of nonlinear lubricated friction dynamic characteristics due to the acceleration effect. The experimental results used for developing a semi-empirical model are presented here.

Chapter 4 describes the development and verification of the innovative non-linear friction models (2D LUT) based on the experimental data from Chapter 3. Simulation-ready semi-empirical models for increasing and decreasing velocities in both directions under different constant accelerations for two different hydraulic actuation systems are developed.

Chapter 5 describes the model validation and implementation process. The validation is done by comparing both the new semi-empirical and the Stribeck model's predicted results with the experimental results of VCHAS1. The new semi-empirical model is to be validated for

increasing and decreasing velocities in both directions under different constant accelerations for both hydraulic actuation systems under consideration.

Chapter 6 presents the contributions and conclusions of the study and recommendations for future research.

CHAPTER 2: LITERATURE REVIEW OF LUBRICATED FRICTION MEASUREMENTS AND MODELING

2.1 Introduction

In Chapter 1, a brief review of classic friction models and experimental friction measurement techniques was presented. In this Chapter, a literature review on topics specific to this study will be considered. Several reviews on friction and related topics have been published and do provide an “encyclopedic” overview of some areas pertinent to this research [13, 19, 26-29]. This approach will not be followed in this Chapter; indeed, the review that follows will focus on friction which occurs under lubricated conditions such as experienced in hydraulic actuation systems. For consistency and clarity, friction under lubricated conditions has been defined in this Chapter as “lubricated friction”. The background and measurement techniques both direct and indirect associated with lubricated friction are reviewed. In addition, studies which involve lubricated friction and its “velocity history factor” will be considered. Because of its importance, a brief history of the Stribeck model is reviewed; further, problems of using this model for all operating conditions are also provided. The dynamic model called the LuGre model (which is an extension to the Stribeck model), will be introduced in the Chapter.

2.2 Lubricated Friction in Hydraulic Actuation Systems

Friction in hydraulic actuation systems occurs under lubricated conditions (verses dry conditions) [1] and is more complex than dry friction. In [13], Olsson et al states that “the friction interfaces in most engineering applications are lubricated. Friction models have therefore been derived using hydrodynamics. Viscous friction is a simple example, but other models also exist”. In [30], Lischinsky suggested that the dynamic properties of lubricated friction can be defined as:

- “Stick-slip” motion which is a process of no movement (presliding) followed by a sudden slip effect. It is often associated with limit cycle oscillation at low velocities. (Please note: the term “Stick-slip” is often found in the literature when referring to lubricated friction. However, because lubricated friction is also a function of velocity, the term “Stribeck model” is more appropriate than “Stick-slip” [31]. “Stick-slip” in some literature is called as “Slip-stick”, but basically they are same concepts, just a different way of labelling it [32]).

- Presliding displacement in which lubricated friction shows spring like characteristics in a region where the applied force is less than the break-away force.
- Frictional lag in which lubricated friction is not consistent with the sign of the velocity change (hysteresis).

Based on these properties, it is evident that lubricated friction is indeed, a complex phenomenon. In a review of the literature, lubricated friction is influenced by many factors such as: type of seals used (if applicable), fluid pressure, viscosity, temperature, and velocity but other factors come into play as well. Some of these are now considered.

2.2.1 The Effect of Seals

As previously mentioned, hydraulic actuation systems can be both linear and rotary; however, linear systems are more dominant application wise, and are the focus of this study. Seals in hydraulic actuation systems can be categorized as rod seals and piston seals. Rod seals guard against external leakage whereas piston seals or piston rings are used for fluid sealing between two cylinder chambers [18, 33]. While the piston seal is designed to isolate the two chambers, it is also deliberately designed to introduce some minor leakage to provide lubrication between the seal and cylinder surface in which the piston and piston rod moves [34]. If there was a perfect seal without any leakage, the friction between the seal and cylinder would be essentially dry friction and the seal could be compromised very quickly. Rod and piston seals are usually made of rubber, polytetrafluoroethylene or reinforced Teflon but some piston seals are metal [35].

Even though hydraulic seals are very important components in hydraulic actuation systems, their presence usually “appear” in systems models in the form of leakage paths and/or classic friction models [35]. Modeling of seal friction based on a physical principles is very difficult to do. Friction effects due to all seals are usually lumped together based on the type of the seals and type of the cylinders [36]. This approximation to lubricated friction is reasonably acceptable when the velocity of the piston is low, or the lubrication condition is minimal between the seal and cylinder. This is because the seals are subjected to mixed lubrication (where the velocity is around the Stribeck velocity (v_s), see Chapter 1), and hence, the seal roughness plays a major role. But as the velocity increases, full film lubrication theory plays a major role, and the seal effect on lubricated friction will be reduced [37]. In short, the seal type has a major effect on the static and the Stribeck friction at low velocities (below the Stribeck velocity (v_s)).

It must be noted that lubricated friction of hydraulic actuation systems is a summation of the lubricated friction of the piston seal against cylinder, and the lubricated friction of all the rod seals.

2.2.2 The Effect of Pressure

In a typical hydraulic actuation system, a differential hydraulic pressure across the piston is required to overcome lubricated friction, inertial forces and external forces in order to perform its functions. The differential pressure can be quite substantial (depending on the loading conditions) and can have the effect of increasing lip seal friction [38]. When pressure is applied across the piston seals, deformation occurs, and a large contact surface results between the piston and the cylinder surface. As a result, the normal force increases; consequently, the lubricated friction force will also increase and will be a function of the pressure. In the case of the metal piston rings, the deformation is minimal and the normal force (hence the lubricated friction force) dependency on pressure is minimal [39, 40].

The effect of system pressure on lubricated friction was observed by many researchers. Yanada's research indicated that "Coulomb friction" of the hydraulic cylinder increased as the pressure increased [41]. However, pressure did not show a significant effect on viscous friction. This result was not consistent with the findings of Lewis et al. who pointed out that the viscosity of liquids (and indirectly, viscous friction) increased with increasing pressure, in particular at high pressures [42]. In a study by Blau et al, the authors concluded that for hydraulic actuation systems, the effect of pressure on lubricated friction is very complex. They also concluded that the dependency of lubricated friction on contact pressure and load cannot be generalized for all cases [9].

2.2.3 The Effect of Viscosity

Viscosity is an important property of the fluid and is essential for lubrication purposes. Low viscosity in general, reduces the lubricity of the fluid but additives often offset this issue. High viscosity fluids reduce leakage but shearing forces increase and hence increase viscous friction effects [42]. Viscous friction at the hydraulic actuator arises because a force is needed to shear the lubrication fluid. It is well-known that viscous friction is linearly proportional to the fluid viscosity [14], but as mentioned in Section 2.2.1, this effect is minimal at low velocities

[43]. In order to reduce viscosity type friction, it is desirable to use a low viscosity fluid; however, a low viscosity will increase leakage, which affects the volumetric efficiency of the actuator. Thus, choice of a fluid is a trade-off decision [44]. A secondary effect is that viscosity is a function of both pressure and temperature (Section 2.2.5) which makes system modeling a very complex task [45]. Further, lower viscosity oil results in a smaller difference between the accelerating and decelerating portion of the friction-velocity curve [46].

In summary, fluid viscosity has a significant effect on viscous friction in hydraulic actuation systems.

2.2.4 The Effect of Velocity

In practical simulation models, lubricated friction is often modeled as a force which is dependent solely on velocity and assumes pressure effects are minimal if temperature is held constant (within an acceptable tolerance). This has given rise to one of the most well used models for lubricated friction and as discussed in Chapter 1, been labelled in this thesis as the “Stribeck model” [47]. In this model, lubricated friction force is normally plotted (evaluated) as a function of velocity.

Early studies identified that velocity had an important influence on lubricated friction [48]. The reason is related to hydrodynamic lubrication; specifically, the status of the lubrication film between two sliding surfaces under different sliding velocities. Figure 2.1 shows a typical friction force as a function of increasing velocity of a hydraulic actuator when moving in one direction giving rise to the aforementioned Stribeck model. In reality, the friction force should be shown as a function of increasing velocity in both forward and reverse directions of the actuator movement. When both directions are considered, the full Stribeck curve is often assumed to be symmetrical; however, the following discussion will focus on the case where velocity is increasing in one direction only.

With reference to Figure 2.1, there are four regions which describe the lubrication conditions in the Stribeck model. In the first region, there is no motion between two surfaces (presliding), and is called a static friction regime (Regime I). When the sliding velocity is below the Stribeck velocity, the lubricated condition is referred to as a “boundary lubrication regime” (Regime II). When the sliding velocity is at or around the Stribeck velocity, the lubricated condition is referred as a “mixed or partial lubrication regime” (Regime III). When the sliding

velocity is larger than the Stribeck velocity, the lubricated condition is referred as a hydrodynamic (or full fluid lubrication) regime (Regime IV). In this regime, the two sliding surfaces are fully separated. In the literature, the friction in the regions which are less than or equal to the Stribeck velocity has been labeled as “Stribeck friction”.

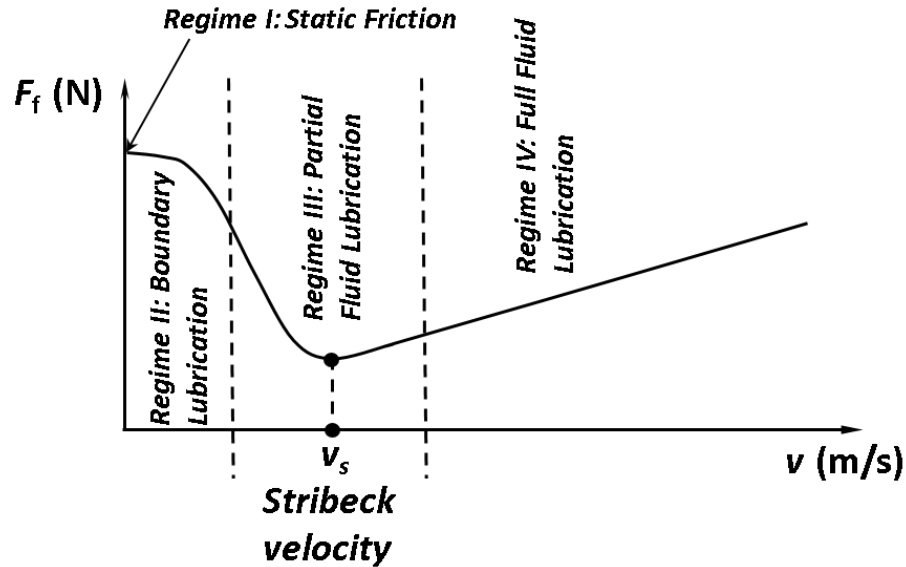


Figure 2.1 The Stribeck model with four regimes of the hydrodynamic lubrication of hydraulic actuation systems; this form assumes that values of friction were obtained under steady state conditions (Details are provided in Section 2.4.1)

Before the Stribeck model was proposed, many other models were developed which related lubricated friction forces as a function of velocity [13]. Some of these include a Coulomb friction model (a model in which the friction force is constant and independent of velocity and is mathematically similar to dry dynamic friction, but with different physical meaning), viscous friction (in which the friction force is a linear function of velocity only), and models which are a combination of both. All of these models were briefly introduced in Chapter 1. These models are usually experimentally based and simplified for lubricated friction prediction or estimation in simulation type studies [13].

More recent studies have considered the friction forces in the presence of lubrication. In [16] it was found that lubricated friction increased as the sliding velocity increased (when velocity was larger than the Stribeck velocity). As a result, a popular simplified model known as the viscous friction model was developed in which the lubricated friction was linearly proportional to the velocity; that is $F_f = \text{sgn}(v) * K_v$, where K_v is the viscous coefficient. For velocities

beyond the Stribeck velocity, this is a reasonable approximation although many experimental studies have shown that a linear relationship of lubricated friction to velocity only occurs at extremely high velocities [25]. Of more importance, though, is the fact that experimental results indicate that the linear viscous model does not reflect the real physical mechanism of lubricated friction at low velocities [12]. It should be clarified that low velocity (which is below or around the Stribeck velocity) implies that the lubrication film thickness at this velocity is on the order of the surface roughness dimensions or less [47]. High velocity implies that the velocity is much higher than the Stribeck velocity [49] and the system is well in the lubricated regime.

The history of friction studies is of interest in understanding how various models of friction have evolved. In the “early” days, lubrication was rarely integrated into mechanical actuation designs. Thus fundamental friction laws were based on the dry friction phenomenon. One of the earliest dry friction models proposed by Leonardo da Vinci had the friction force depending on normal load and nominal contact area (but being independent of the real contact area) [16, 50]. Nominal contact area is the geometrical contact area between two objects, whereas, the real contact area is the area of elastic-plastic asperity contacts between two objects. Another well-known scientist was Coulomb who modelled dynamic friction (friction under motion condition) based on his observation on dry friction and concluded that “kinetic friction was nearly independent of the sliding speed” [11].

Although research on dry friction has laid a solid foundation for friction modeling, specific studies on lubricated friction are, in fact, influenced by dry friction concepts. For example in some experimental studies, it has been observed that an “offset” exists in the plot of lubricated friction versus velocity (see Figure 1.11). This offset has often been labelled as “Coulomb friction” since mathematically, the offset can be modeled as being independent of the velocity [13].

The literature is somewhat confusing in how various researchers determine and then apply Coulomb friction to models. In this thesis, the author has attempted to clarify this situation by assigning Coulomb friction into four categories: Coulomb A (F_{c_A}), Coulomb B (F_{c_B}), Coulomb C (F_{c_C}) and Coulomb D (F_{c_D}) (Figure 2.2).

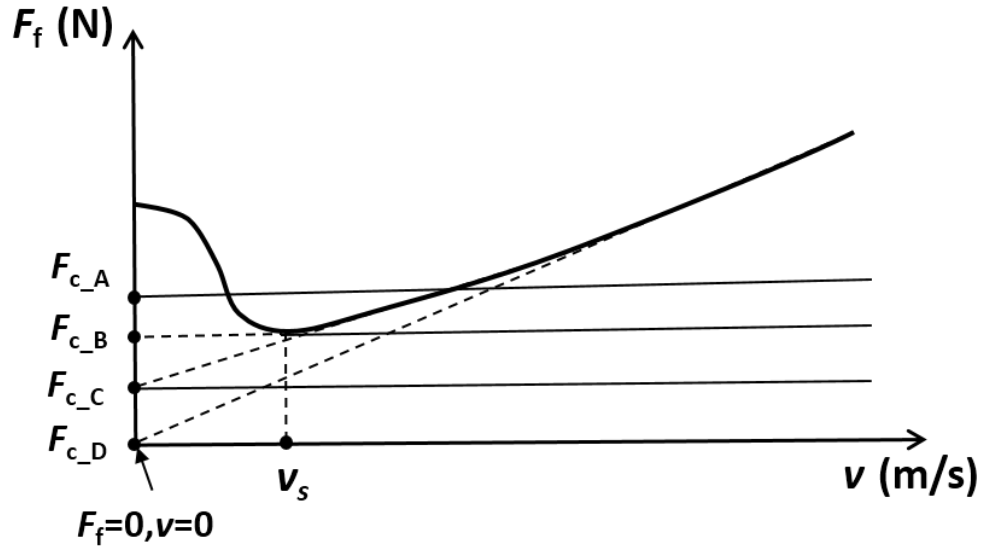


Figure 2.2 Four Coulomb friction types in lubricated friction models: Coulomb A, Coulomb B, Coulomb C and Coulomb D

The traditional form of Coulomb friction based on the kinetic friction of dry surfaces is defined as “Coulomb A (F_{c_A})”. Some researchers such as Lischinsky suggest Coulomb friction is based on the value of force at the Stribeck velocity (v_s), “Coulomb B (F_{c_B})” which he called “Stribeck friction” [30]. This is in contrast to the definition used by others in which Stribeck friction is the friction forces which occur at less than or equal to the Stribeck velocity. Some studies plot friction force versus velocity and then extract a line from the viscous friction data back to the origin (zero velocity), and this is defined as “Coulomb C (F_{c_C})”. Most Stribeck models use “Coulomb C” in the curve fitting models [13, 51, 52]. In many cases, some studies do not use Coulomb friction at all; that is, the Coulomb friction is zero. This is defined as “Coulomb D (F_{c_D})” [11, 31].

It is worth mentioning that Ferreira found that the Coulomb friction (Coulomb C) of the lubricated friction was proportional to the normal force when lubrication was present [53]. This observation may be helpful in explaining why Coulomb friction exists even if the lubrication is in the hydrodynamic regime – that is the regions in which the surfaces are fully separated. Because of the confusion in how Coulomb friction can be determined, it is quite evident that this type of friction is still not completely understood or indeed, defined in a standard manner.

2.2.5 The Effect of Temperature

The operating temperature of a hydraulic actuation system can heavily influence the viscosity of the lubrication fluid; indeed, viscosity decreases with increasing temperature on a logarithmic scale. A lower viscosity fluid in the boundary lubrication region (regime II of Figure 2.1) and partial lubrication region (regime III of Figure 2.1) translates to more surfaces contact or “asperity contact”, which in turn increases the lubricated friction [11]. However, in a full lubrication region (regime IV of Figure 2.1), the lubricated friction is reduced as the oil viscosity decreases [54]. The experimental results of [55] do confirm that the oil temperature does have effect on the Stribeck model. In addition, the basic mechanical properties of hydraulic seals such as hardness, and compressibility all depend strongly on temperature [35].

2.2.6 Summary

Sections 2.2.1 through 2.2.5 have indicated that lubricated friction is a complex phenomenon in that it is dependent on so many system and operating conditions (seal type, pressure, viscosity, temperature, and velocity etc.). Seal type has a major effect on both the lubricated static and dynamic friction at low velocities (below or around Stribeck velocity). Hydraulic pressure influences Coulomb friction. Fluid viscosity and temperature have a significant effect on viscous friction. Furthermore, velocity of the moving surfaces influence lubricated friction giving rise to what is commonly known as the Stribeck model.

The literature reveals that a universal model of lubricated friction which can be used for simulation purposes has not yet been developed.

2.3 Measurements of Lubricated Friction

As mentioned in the previous section, lubricated friction values depend on the normal force and roughness of the surface (which are important considerations for dry friction). But a more significant effect is the relative motion conditions and the lubricating film between the moving surfaces. This representation of lubricated friction force plotted as a function of velocity has become the common approach in most of the literature [12]. However, determining the relationship between lubricated friction force and velocity requires that both be measured at the same time which does create some challenges.

There are a number of different methods which exist for evaluating and quantifying dry friction, such as used in various tribometers. In these approaches the static and dynamic dry friction coefficients are measured [9]. In mechanical design, it is common practice to “look up” in Standard Tables, well-established values of static and dynamic dry friction coefficients for different contact surface materials [56, 57]. However, the measurement of lubricated friction is much more complex and difficult. From the literature review, only one standard was determined for measuring lubricated friction between a piston ring and its liner, ASME G181-11 [58]. This standard requires the use of segments of a piston ring and cylinder liner immersed in a lubricant; both parts are attached to a special test rig and submerged in the oil. The testing procedure uses sinusoidal reciprocating motion to simulate the movement of a piston surface against the cylinder liner. The lubricated friction is measured by a friction force sensor attached directly with the specimens, and the average value over a cycle recorded [59]. It is evident that the ASTM standard (G181-11) is not an appropriate approach for hydraulic actuation systems studied in this research.

In summary, there does not appear to be any specific standard for the measurement of lubricated friction which would be appropriate for a hydraulic actuation system in its normal operating conditions. Therefore, many experimental systems to obtain the force versus velocity relationships are designed to meet specific operating conditions and a one fit for all approach is not available [35]. Overall, experimental test rigs have been proposed to facilitate the measurement of lubricated friction versus velocity and can be categorized as indirect and direct methods. Further both categories can be subdivided into discrete and continuous methods. These experimental approaches are now reviewed.

2.3.1 Indirect Approach

Under constant velocity motion condition, lubricated friction of a symmetrical hydraulic cylinder (such as a double rod actuator) can be indirectly obtained by measuring the differential pressure across an actuator piston and multiplying it by the effective piston area. The lubricated friction of a non-symmetrical hydraulic cylinder (such as single rod hydraulic actuator) can be obtained by measuring upstream pressure times its effective piston area minus downstream pressure times its effective area. In either case, the measurement must be made under conditions in which acceleration is zero and any external forces accounted for and subtracted from the force balance equation [40]. However, under non-constant velocity motion conditions, the inertial force

of mass times the acceleration has to be considered. By simultaneously measuring the velocity, acceleration (if applicable) and pressures, a friction curve of the lubricated friction force versus velocity can readily be determined. Because it uses differential or absolute pressures to calculate the lubricated friction force, it is considered to be an “indirect” approach.

This approach has been successfully used by Burton, and Chinniah to measure lubricated friction characteristics in their hydraulic actuation systems in the Fluid Power Research Lab at the University of Saskatchewan [2, 15]. Their approach was to control the actuator to move at constant velocity (essentially a controlled square velocity waveform) and then record the differential pressure for the symmetrical case or absolute pressures of the upstream and downstream chambers for the asymmetrical case. Specifically, the procedure followed was to measure a point on the velocity-time trace in which the velocity was constant and then determine from the pressure plots, an average value of force. The magnitude of the actuation velocity was changed and the corresponding force recorded. The test was repeated many times at a controlled temperature. A plot consisting of lubricated friction force versus velocity was then used to approximate an average viscous friction value.

This approach by Burton and Chinniah can be considered as a “discrete measurement” in that data was taken at selected points on the data traces after transients had died down. As will be discussed, this type of measurement cannot detect hysteresis. Other researchers have followed a similar approach to Burton and Chinniah [12, 23, 46, 55, 60-64] and all have found that the plot of force versus velocity gives rise to a very nonlinear plot (the Stribeck model). Some researchers make use of a standardized equation form for frictions versus velocity and approximate coefficients by applying curve fitting techniques to these nonlinear friction plots [65, 66]. Others simply use quadratic functions to approximate the lubricated friction characteristics again using curve fitting techniques [2, 67]. In both cases, lubricated friction is approximated as a function of velocity based on the experiment data.

Using the indirect approach, other researchers have measured lubricated friction as a function of velocity using sinusoidal motion (or other periodic waveforms) in the movement of the pistons [46]. This approach is considered as continuous and hence hysteresis effects can be detected. This will be considered in greater detail in Section 2.4.2.

2.3.2 Direct Approach

Direct measurement of the lubricated friction is achieved by placing a force transducer directly on the actuator rod and then using the force transducer itself to induce a constant velocity. This has been shown to be a more difficult approach than the indirect approach because the force transducer must be controlled to create constant velocity or periodic waveform. This approach has been considered as being intrusive since the dynamics and mass of the force transducer must be taken into consideration [17, 40, 51, 60]. It is noted that both discrete and continuous measurements are possible with this approach.

2.3.3 Discussion

Two types of approaches for measuring lubricated friction in a hydraulic actuation system have been introduced: indirect and direct. Both approaches do give rise to the common Stribeck model for the measured system. However, if both approaches use points where the velocities are constant, the method is considered discrete because the measurement is made at discrete points in the velocity trace. Therefore the lubricated friction curve is made up of discrete points and hence is not considered to be a continuous measurement. The reason that this is important is as follows. If hysteresis does exist in the lubricated friction domain, discrete measurements cannot capture it because there is no “frictional memory” of the previous test waveform. On the other hand, if the data is taken from velocity waveforms that are not constant but vary (for example a sinusoidal waveform), the approach is considered to be continuous. As a result, each point on the data is affected by what came before and as such frictional memory exists; consequently, the measurement of hysteresis is possible.

As a last point, this review indicates that the direct lubricated friction measurement method is considered to be intrusive, whereas, the indirect method is not. Therefore, the indirect method is commonly used to approximate friction characteristics in hydraulic actuation research projects.

2.4 Representation of Experimental Lubricated Friction as a Function of Velocity

The following discussions are valid for both indirect and direct measurements in hydraulic actuation systems.

2.4.1 Discrete Measurement Based Model: Stribeck Model

In 1902, Stribeck studied lubricated friction in journal bearings and developed the Stribeck model [48]. The Stribeck model is based on experimental data and has been approximated analytically by several forms. Tustin [68, 69] has studied a particular form given by Equation (2.1). His assumption was that lubricated friction follows an exponential decay from its static value to a high velocity kinetic value. Tustin's model was given by:

$$F(v) = F_0 + F_1(1 - e^{-\frac{v}{v_0}}) \quad (2.1)$$

where, $F(v)$ is the lubricated friction as a function of velocity (v), F_0 is the static friction, F_1 is the difference between the static friction and the kinetic friction, v is the relative velocity between the two surfaces or sliding velocity, v_0 velocity is a constant (m/s) and is the characteristic velocity at which the system transitions to kinetic friction. All parameters must be extracted from experimental data [68, 69].

In 1982, Bo and Pavelescu [70] proposed a revised exponential model to fit the Stribeck model (Equation (2.2)). Since it was a very good fit of characteristics of the Stribeck model, it has become a de facto standard equation ever since. Mathematically this model is given as:

$$F(v) = F_c + (F_b - F_c)e^{-\left|\frac{v}{v_s}\right|^m} + K_v v \quad (2.2)$$

where, F_c is Coulomb friction (Coulomb C in Figure 2.2), F_b the Breakaway friction, v_s the Stribeck velocity, K_v the viscous coefficient. e is Euler's constant, and m is an appropriate exponent (typically, $m = 2$); please refer to Figures 1.8, 1.12 and 2.2 for details. In Equation (2.2), F_c is a constant item in the Equation which is independent of velocity and corresponds to Coulomb C (if $F_c > 0$), or Coulomb D (if $F_c = 0$).

It is of interest to note that in the original form of the Stribeck model, Stribeck friction was a function of a Sommerfeld number (or Hersey number) which is defined as viscosity times velocity divided by the normal load [31, 54]. Later, it was simplified to velocity only by assuming the changes of viscosity and normal load over a particular test were negligible [54]. Because the Stribeck model described the physical nature of lubricated friction so well, it has been used extensively in many simulation studies on hydraulic actuation systems and other actuation systems [55]. In the literature, the phenomenon has been labelled as the Stribeck effect or Stribeck diagram [7] but in this thesis, it has been labelled as the Stribeck model. It should be emphasized

that the Stribeck model can vary for different hydraulic actuation systems, due to the fact that parameters of the Stribeck model are system dependent [11, 30, 31].

As mentioned earlier the experimental technique to measure lubricated friction as a function of velocity using discrete points gives rise to the standard representation of the Stribeck model [71]. Models employing continuous data (which means that hysteresis can be shown) are far and few in-between because of complexity in the resulting describing equations. In many of the papers reviewed, the experimental technique to obtain the lubricated friction as a function of velocity was not explicitly defined. But if the resulting plots of lubricated friction vs velocity did not show hysteresis or the resulting plots were based on certain discrete points, the logical conclusion was that the technique was based on discrete measurements. From an applied point of view, the operation of hydraulic actuation systems is “continuous” rather than being discrete; therefore, friction models based on continuous measurement are closer to the “real life situation”. The Stribeck model was one such model that was obtained from discrete measurements. Several issues arise with this particular discrete friction form, which will be discussed in Section 2.5.

2.4.2 Continuous Measurements Based Models

Recent studies have indicated that lubricated friction vs velocity is not single valued, but is influenced by the motion conditions [46]. This effect gives rise to hysteresis. As mentioned above, the only way that hysteresis can be identified is if the experimental approach uses continuous data. A common approach has been to excite motion between two surfaces using sinusoidal velocity or displacement wave forms [12, 23, 46, 60, 64] in which acceleration varies over the time. In [25], an experimental protocol was established using triangle velocity and parabolic displacement wave forms in which the acceleration was constant for these inputs (and will be detailed in Chapter 3).

The literature has shown that it is difficult to construct a lubricated friction model from physical first principles but there have been some attempts [72]. The Dahl model [73] describes the stiction or breakaway portion as a spring-like behavior (similar to Lischinsky’s approach) in the presliding regime and friction force is modeled as a function of the displacement and the sign of the velocity. The Dahl model did not capture the Stribeck effect, but it was still one of the earliest attempts in modeling friction based on physical principles instead of being based on

experimental data. This established a base for further development of continuous dynamic friction modeling.

One such continuous measurement based model is the LuGre Model (so named to recognize that it originated in a collaboration between the control-groups in Lund and Grenoble [13, 74, 75]). Technically, the LuGre model was an extension of the Dahl model, by assuming that asperities of two lubricated surfaces could be treated as elastic bristles. This was defined as the “bristle concept”. The LuGre model was developed to improve upon the Stribeck model by combining the physical principles (Dahl model) and experimental data (from the Stribeck model). The movement and subsequent forces on these bristles were modelled as:

$$\frac{dz}{dt} = v - \frac{|v|}{g(v)}z \quad (2.3)$$

$$F = \sigma_0 z + \sigma_1 \frac{dz}{dt} + \sigma_2 v \quad (2.4)$$

where, z is the average deflection of the bristles, v the relative velocity between the two surfaces, σ_0 the stiffness of elastic bristles, σ_1 a damping coefficient, σ_2 viscous coefficient, and $g(v)$ is a function to represent the Stribeck effect. $g(v)$ decreases as v increases. $g(v)$ was proposed to be $g(v) = F_c + (F_s - F_c)e^{-\left(\frac{v}{v_s}\right)^2}$ which was taken from the Stribeck model, where F_c is Coulomb friction (Coulomb C in Figure 2.2), F_s the Breakaway friction, v_s the Stribeck velocity. Under steady state conditions, the LuGre model converges to the Stribeck model [75]. The LuGre model is considered to be an improvement to the Stribeck model; however, it only can capture hysteresis in lubricated friction [76] but did not correlate well with experimental results.

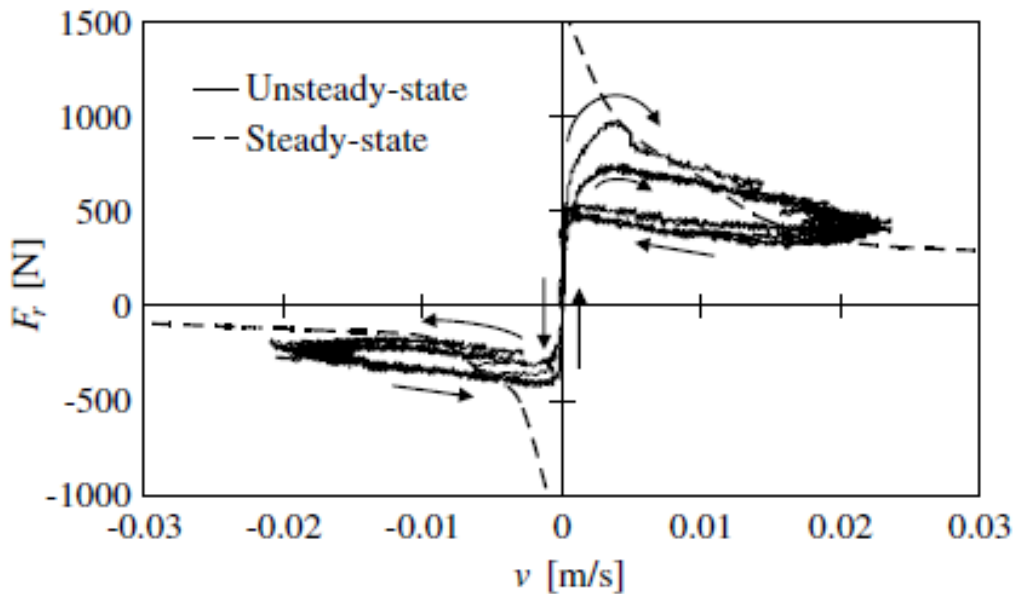


Figure 2.3 Unsteady state lubricated friction of the experimental results in [12]. Reprinted from Mechatronics, Vol. 18 (7), H. Yanada and Y. Sekikawa, Modeling of dynamic behaviors of friction, pp. 330-339. Copyright 2008, with permission from Elsevier

In the paper by Yanada and Sekikawa [12], the LuGre model was evaluated using the parameters from data in which the velocity varied sinusoidally. Some of their experimental results are showing in Figure 2.3. It is evident that hysteresis is present. It is also observed viscous effects were minimal for their system studied. They concluded that “the LuGre Model cannot simulate the real friction characteristics of hydraulic actuators”. Yanada et al developed a modified LuGre model by taking the dynamics of lubricant film formation into consideration instead of the acceleration itself directly [12, 41, 77]. A limited improvement was achieved in the experimental verification. It is noteworthy that their approach was an alternative or indirect way of including acceleration effects.

There were other attempts to improve the LuGre model. For example, Acho et al. established that the LuGre friction model was a first-order model which depended on the internal state z , which denotes the average deflection of the bristles. The LuGre model could be extended from first order to second order model by adding extra dynamic effects (α, β) , (which are the size of the active region (term used in nonlinear oscillator) and amplitude gain respectively). This is shown in Equations (2.5) and (2.6). The second-order LuGre model can be used to account for the internal vibration, a common issue in mechanical systems with nonlinear friction [78].

$$\frac{dw}{dt} = v - f(w); \quad f(w) = \frac{w^3}{\alpha} - w \quad (2.5)$$

$$F = \sigma_0 z + \sigma_1 \frac{dz}{dt} + \sigma_2 (v + \beta w) \quad (2.6)$$

where, z is the average deflection of the bristles, v the relative velocity between the two surfaces, σ_0 is the stiffness of elastic bristles, σ_1 is a damping coefficient, σ_2 is viscous coefficient, α, β are two constant parameters which can be interpreted as the size of the active region and $f(w)$ is a nonlinear function which is common in nonlinear oscillator (this is the special case for the Van der Pol oscillator).

In summary, all the modified LuGre models have some improvements, but they are very much limited by their more complex implementation and identification process because of the large number of parameters that have to be identified experimentally [79].

2.4.3 Discontinuity of the Friction Model as a Function of Velocity

Most friction models which are a function of velocity are discontinuous at zero velocity. The discontinuity creates a common problem for any friction model which uses velocity as the variable. The reality is that friction at zero velocity is no longer a function of the velocity; instead, it is a function of the external applied force [53]. What this means is that when the piston is not moving (presliding condition), the friction force is numerically equal to the applied force. It is only when the external force becomes greater than the breakaway force that sliding motion occurs.

For simulation purposes, this gives rise to causality changes between when the velocity is zero and non-zero. To overcome some of the issues for modeling that arise when such discontinuity exists, various researchers have made approximations. For example, Lischinsky proposed a “presliding displacement” in which friction displays spring like characteristics in a region where the applied force is less than the break-away force [30]. Therefore friction is not discontinuous since it is always matching the applied external force at zero velocity. Other researchers employ a steep slope which passes through zero (force and velocity) and connects to the peak static friction force thus making the relationship continuous in this region [80, 81]. This is different from Lischinsky’s approach.

Another approach has been to build a “zero velocity detection zone” which avoids switching between different state equations of sticking (presliding) and sliding; this has been called the Karnopp model [80, 81]. Physically it is not a true representation because the friction

force is not zero at zero velocity. However, it is an approach that has been satisfactorily used in hydraulic actuation systems simulations when the behavior at low velocities is not a major concern.

2.5 Discrete vs Continuous Based Models: Some Issues

As mentioned previously, the Stribeck model is very popular in modeling lubricated friction. This model can represent other common lubricated friction phenomena, but it cannot explain such things as hysteresis. It is a static model in that the relationship between friction and velocity is independent of the motion condition. This will be expanded upon in Chapter 3. The following sections will present some of the literature that has identified the presence of hysteresis in the friction - velocity relationship.

2.5.1 Hysteresis of Lubricated Friction

In order to study the hysteresis of lubricated friction, it is necessary to understand the general concept of hysteresis. Hysteresis is present in many physical systems and can appear as magnetic hysteresis, ferro-electric hysteresis and friction hysteresis [82, 83]. Alexander defines hysteresis as “the dependence of the output of a system not only on its current input, but also on its history of past inputs. The dependence arises because the history affects the value of an internal state. To predict its future outputs, either its internal state or its history must be known.”[84].

Since lubricated friction is a function of velocity, then this implies that the moving surfaces undergo acceleration or deceleration changes, that is, an increase in velocity in either direction is an acceleration, and a decrease in velocity in either direction is a deceleration. It is quite possible then that such a system can experience hysteresis. Hysteresis of lubricated friction in this sense, is the difference in the lubricated friction force between the acceleration and deceleration (in either direction of the actuator) portion of the friction-velocity curve [85].

Hysteresis of lubricated friction can appear as oscillations in position with continuous sliding, or reciprocal motion. Such phenomenon has been reported for the first time by Hess et al during experiments with a sinusoidal signal velocity with different frequencies [46]. They found that the experimental lubricated friction to velocity relationship appeared as shown in Figure 2.4. This kind of behavior has been observed and reported by many other researchers [12, 23, 46, 60, 64]. The hysteresis was observed as velocity varied in a continuous reciprocal motion. The size

of the loop increased as the velocity variations (essentially acceleration / deceleration) increased [13]. The lubricated friction force was lower for decreasing velocities (deceleration) than increasing velocities (acceleration).

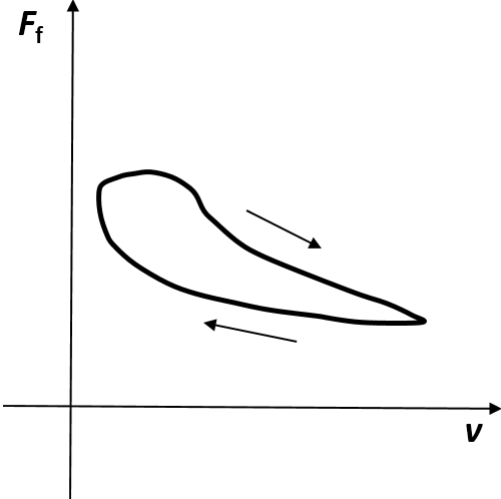


Figure 2.4 The lubricated friction-velocity relation observed in [46]. The lubricated friction force is lower for decreasing velocities than for increasing velocities. The hysteresis loop becomes wider as the velocity change rates become larger.

The dynamic behavior of hysteresis of lubricated friction can be explained by the existence of “frictional memory” caused by a lag in the lubricated friction force [86]. This frictional memory has been defined by Hess et al as “friction lag” and is defined as the pure time delay in the relation between velocity and lubricated friction force (see Figure 2.5) [75].

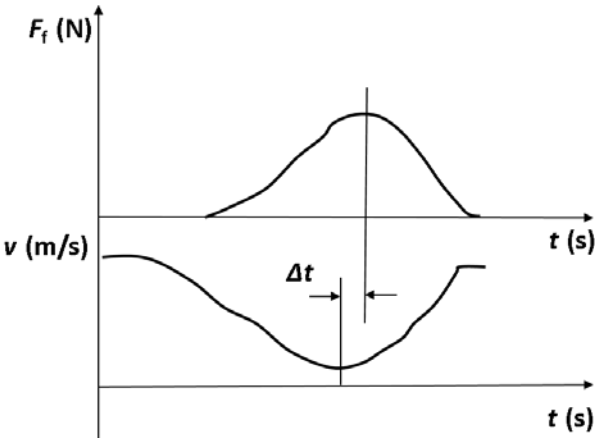


Figure 2.5 Time relation between a change in velocity and the corresponding change in friction [73].

Some researchers believe hysteresis is related to the fluid film thickness [20] while others point out that there is a hysteresis type effect in dry friction as well [86]; however, the hysteresis of the dry friction is concentrated around the zero velocity. As the velocity increases in both directions, the friction force will approach Coulomb friction (Coulomb A in Figure 2.2), which is independent of the velocity. Graphically, this type of hysteresis is represented in Figure 2.6, which is just a narrow hysteresis around the zero relative velocity. Its behavior is certainly different than the hysteresis under lubricated conditions.

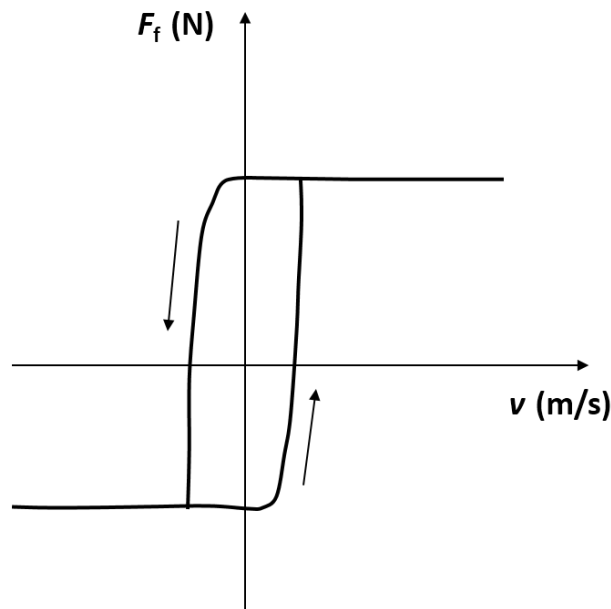


Figure 2.6 Hysteretic effects of dry friction: contact compliance [86]

2.5.2 Discussion on the Stribeck Effect and Limit Cycles

The previous sections have identify various models which related lubricated friction to velocity. It is useful to examine some other phenomena that arises when the Stribeck model is used.

2.5.2.1 Limit Cycles

Hensen et al observed that limit cycling of an actuator, also known as hunting, can be caused by non-linear lubricated friction in hydraulic actuation systems when using a closed-loop controller. They also observed that such limit cycles when excited were not necessarily stable in that their amplitude and frequency could vary in time [87].

With reference to Figure 2.1, the Stribeck model has a negative friction slope for velocities less than the Stribeck velocity which is based on the observation under steady state conditions where the sliding velocity is constant over the time. If the system is operating in these regions, simulations can predict stable limit cycles since essentially the model displays negative damping. The investigation by Radcliffe et al. confirmed that only the negative slope of stick-slip models predicts limit cycle generation [88].

However, this is not always the case. Haessig and Friedland have reported that sometimes the Stribeck model will predict a limit cycle which is not observed experimentally in the laboratory [89]. This indicates that under certain circumstances, limit cycles can be falsely predicted by the chosen lubricated friction model. Canudas de Wit, et al reported that the “Stribeck effect has produced a destabilizing effect at very low velocities”. Some researchers suggested that some other nonlinear factors experimentally may have played the role to damp out the limit cycle [90]. That is why the Coulomb plus viscous friction model could be used to replace the Stribeck model in such unstable simulation situations [26].

In the following section, it will be discussed why the Stribeck effect can be changed. In other words, the “negative” viscous friction in the Stribeck model may be reduced or eliminated under certain conditions which may help to explain the false prediction of limit cycles using the traditional Stribeck effect [75].

2.5.2.2 Stribeck Effect of Stribeck Model

It is well known that the effect of the breakaway portion (or the stick-slip portion) of the Stribeck model can be overcome by external means. For example, a small dither force applied to the piston has been used for years to improve the dynamic performance of spool valves. Indeed, it is a common practice [13]. Dither can be introduced electronically or mechanically by a vibrator, as was done in early auto pilots [13, 91]. Chatterjee et al. conducted research on the effect of high-frequency excitation on a class of mechanical systems with dynamic friction. They found that the low-velocity effective-friction force decreases with the increasing strength of the excitation signal. In addition by proper choice of the dither characteristics, it was possible to completely or partially remove the negative slope in the friction-velocity characteristics [92]. Owen et al, found that by rotating the piston and rod as it moved, the Stribeck effect could be changed and became approximately linearized [22].

It is widely observed that stick-slip can be eliminated by stiffening the mechanism or increasing the stiffness of the system [93]. Stiffness of a system can be interpreted as either a physical stiffness (plant) or a controller parameter (displacement gain) [85].

A major outcome of being able to reduce the Stribeck effect is the implication that this effect is not an inherent property of lubricated friction; instead the Stribeck effect is dependent on the motion conditions. The effect could be changed or eliminated by changing the motion conditions and not just compensated for. This means that some other parameter(s) such as acceleration, can influence lubricated friction behavior and hence this became one of the motivations for this research.

2.5.3 Velocity History and Acceleration

In 1943, Sampson et al. [94] first started to question the Stribeck model based on their limited experimental observations and concluded that lubricated friction may not solely be a function of the velocity, but rather a function of the “past history” of the motion. Unfortunately in their paper, what constitutes past history of the motion was not well defined, and subsequently, the authors did not make an improvement to the Stribeck model. In 1990, Hess et al [46] introduced a novel approach to explore the dynamic friction in the lubricated contact surface by measuring the lubricated friction under oscillating sliding velocities at various frequencies. It was observed that the frequency of velocity variation had a significant effect on the shape and size of the lubricated friction vs. velocity curves. This study put dynamic friction in a new light by recognizing that there was a frequency effect which needed to be accounted for. This frequency effect could be considered as the history of the velocity measurement [46].

Harnoy et al [23, 60, 95-98] continued this approach by developing a unique apparatus to measure lubricated friction in the presence of sinusoidally-varying velocity at various frequencies. Their preliminary findings demonstrated a reduction in the magnitude of the lubricated friction near zero velocity as the frequency of oscillation increased [60]. This echoed Sampson et al’s observation that the lubricated friction was not only a function of the instantaneous velocity, but was also a function of previous velocities. Armstrong found that if the relative velocity changes, the lubricated friction force does not simultaneously change according to the Stribeck model. A time delay is needed to develop the lubricant layer between the surfaces. This affect is called “frictional memory” [16] (see Figure 2.5). Berger in his review of lubricated

friction briefly mentioned the possible role of acceleration in lubricated friction modeling, and indicated that very limited research has been done in the role of acceleration on lubricated friction [85].

2.5.4 Lubricated Film Thickness vs Acceleration

Under the classical hydrodynamic lubrication theory, the lubrication film thickness is a function of velocity. The region of full hydrodynamic lubrication occurs when the sliding velocity is above the minimum critical velocity required to generate a lubrication film thicker than the size of the surface asperities. The thickness of the fluid film is a very important parameter in the analysis of the lubricated friction [53].

As mentioned in section 2.2.5, sliding velocity is a main factor to determine the lubrication film thickness. The film thickness increase as the velocity increases, until the two sliding surfaces are fully separated in the full lubrication regime [54]. However, Sugimura et al. considered film thickness under conditions where the sliding velocity was not constant over time; their results indicated that the film thickness could be influenced by acceleration. Further, they found that the film thicknesses so formed during acceleration were thinner than that formed during deceleration [20]. Therefore, the lubricant film thickness dynamics should be considered when the sliding is in accelerating and decelerating modes [33]. Yanada et al proposed a new model by a modification to the LuGre model taking the lubricant film thickness into consideration, and did make some improvements in model accuracy to some degree; however, the modified LuGre model has only been validated on one type of hydraulic cylinder in the negative resistance (Stribeck friction) regime. The validity of the modified LuGre model has not been investigated in the fluid lubrication regime [12, 41].

2.6 Summary

The review of the literature has indicated that the Stribeck model is one of the most commonly used lubricated friction relationships used for simulation purposes. This model is based on the experimental observation that lubricated friction is a function of velocity. The LuGre model is an improved Stribeck model that captures some dynamics of the lubricated friction. However, other studies have shown that lubricated friction is also a function of the velocity history or acceleration. For modeling of dynamic friction in hydraulic actuation systems applications, it

is deemed very important to include the effects of the acceleration on the Stribeck effect. The literature has shown that very little has been published on acceleration dependence of lubricated friction. Consequently, this lack of information has led to the major objective of this research which is to systematically investigate the acceleration dependency of the nonlinear lubricated friction in hydraulic actuation systems, and to develop an experimentally based lubricated friction model (semi-empirical friction model) which is a function of velocity and acceleration. Details will be presented in Chapters 3, 4 and 5.

CHAPTER 3: LUBRICATED FRICTION MEASUREMENT WITH ACCELERATION EFFECT

3.1 Introduction

To achieve the objectives of this research, an experimental program and a numerical method to determine the effect of acceleration on nonlinear lubricated friction models of hydraulic actuation systems were required.

This Chapter initially introduces some important definitions for clarification purposes, which will be used extensively in the following Sections and Chapters.

A brief introduction to a novel experimental setup of hydraulic actuation systems used to obtain the lubricated friction characteristics under controlled acceleration conditions is given. The data acquisition and instrumentation used in the experimental system are also briefly described followed by a discussion of the data collection process. The input signals to the hydraulic actuation systems to measure the different friction characteristics are presented followed by the experimental friction results so obtained from these special signal formats. An experiment designed to rule out the pressure effect on the lubricated friction measurements is introduced and the results are presented. This Chapter concludes with a discussion on repeatability of the experimental results. The experimental data collected here will be used for developing a three-dimensional (3D) semi-empirical model (which has been labelled as a 2D lookup table or 2D LUT) in Chapter 4.

3.2 Definitions

Lubricated friction issues in systems undergoing motion are central to all hydraulic actuation systems and any in-depth understanding of the nature of lubricated friction will advance future component design. Before proceeding, several definitions are provided to facilitate the discussion of lubricated friction. Some of the definitions introduce new concepts for this study and some have already been mentioned in previous chapters. The objective is to provide clarity and consistency in subsequent discussions.

Because some of the definitions require the use of terms previously defined, the terms are not listed alphabetically.

Static condition:

No motion condition ($v = 0$).

Dynamic condition:

A motion condition ($v \neq 0$).

Duty cycle of actuator:

In a linear hydraulic actuation systems, the midpoint of the cylinder is usually defined as the origin point (zero point) with one direction being defined as the positive direction. In order to take advantage of the full stroke of the cylinder, the piston was relocated to the left end of the cylinder at a start point ($-x_{max}$). A complete work cycle of piston motion within a stroke is defined as a motion which starts from ($-x_{max}$), passes the zero point and reaches the other end (x_{max}). The actuator then changes direction and moves passed the zero point back to the starting point ($-x_{max}$). In implementation of this motion in the experimental systems, ($-x_{max}$) and (x_{max}) are not at the physical ends of the stroke so as to prevent hard collisions between the piston and the end of the cylinder. This is achieved by using position control on the actuator system.

Steady state condition:

This motion condition occurs when the velocity is constant ($a = 0$).

Non-steady state condition:

This motion condition occurs when the velocity changes over time ($a \neq 0$). Note, in some of the literature, a non-Steady State Condition is referred to as an Unsteady State Condition.

Static friction:

Friction which occurs under static conditions; that is, no movement ($v = 0$). Breakaway friction is commonly labelled as Static friction.

Dynamic friction:

Friction which occurs under motion conditions ($v \neq 0$). Note, in some of the literature, Dynamic friction is referred to as Kinetic friction.

Steady state friction

Dynamic friction which occurs under Steady State Conditions($a = 0$). Steady state friction is an abbreviated form of Steady state dynamic friction. Steady state friction is the term that will be adopted in this thesis.

Non-steady state friction:

Dynamic friction which occurs under non-steady state conditions. Non-steady state conditions is an abbreviated form of non-steady state dynamic friction. Note, in some of the literature, non-steady state friction is referred to as unsteady state friction. Non-steady state conditions is the term that will be adopted in this thesis.

Minimum velocity:

The lowest velocity in which the hydraulic actuation systems can sustain a stable motion under steady state conditions.

Maximum velocity:

The highest velocity the system can make before the stable area is too small to collect meaningful data under steady state conditions.

Velocity list:

A list of desired discrete velocities from minimum velocity to maximum velocity used in steady state friction measurements.

Universal Velocity Set:

A list of discrete velocities from minimum velocity to maximum velocity used in lookup table (LUT) modeling.

Minimum acceleration:

The lowest acceleration the hydraulic actuation systems can sustain a stable motion under non-steady state conditions.

Maximum acceleration:

The highest acceleration the system can achieve before the distortion of the output becomes visually noticeable under non-steady state conditions.

Acceleration list:

A list of desired discrete accelerations from minimum acceleration to maximum acceleration used in non-steady state friction measurements.

Universal Acceleration Set:

A list of discrete accelerations from minimum acceleration to maximum accelerations used in lookup table (LUT) modeling.

Static model:

A model which uses “static” maps between real-time velocity and friction force such as a Coulomb model and the Stribeck model. Static models are used for modelling static friction, steady state dynamic dry or lubricated friction and non-steady state dynamic dry friction. It should be noted that Static models have been used for non-steady state dynamic lubricated friction models before their dynamic behavior was established; however, static models are not capable of modelling the Non-steady state dynamic lubricated friction accurately. These models must be dynamic. Static models are just a special case of dynamic models.

Dynamic model:

A model which uses “dynamic” maps between real-time velocity and friction force. This model attempts to capture the dynamics of non-steady state friction behavior (such as the Dahl and LuGre models). Dynamic models are appropriate for non-steady state lubricated friction (NSSF) situations.

Operating motion condition:

Velocity and acceleration conditions (v, a) at any operating point.

Forward direction:

The actuator rod direction in which the sign of velocity is positive.

Reverse direction:

The actuator rod direction in which the sign of velocity is negative.

Operating motion condition plane:

A two dimension surface which consists of operating motion condition points.

Motion condition coordinate system:

A coordinate system of the operating motion condition plane, which consists of velocity as the abscissa and acceleration as the ordinate. Any point on the acceleration axis (including the origin of the motion condition coordinate system) is in a static condition; any point on the velocity axis (excluding the origin of the Motion condition coordinate system) is a steady state condition.

Quadrant:

One of the four regions on the operating motion plane divided by two axis – velocity as the abscissa and acceleration as the ordinate. When the system is in the non-steady state condition, the motion condition has to be in one of four quadrants. All four quadrants are defined in Figures 3.1, 3.2 and 3.3. The defining of quadrants is necessary because the actuator moves in the forward and reverse directions. The sign of v and a dictates the quadrants in which the actuator motion is in. So in common verbiage, a negative “ a ” can imply an acceleration or deceleration, depending on which direction (hence quadrant) the actuator is going.

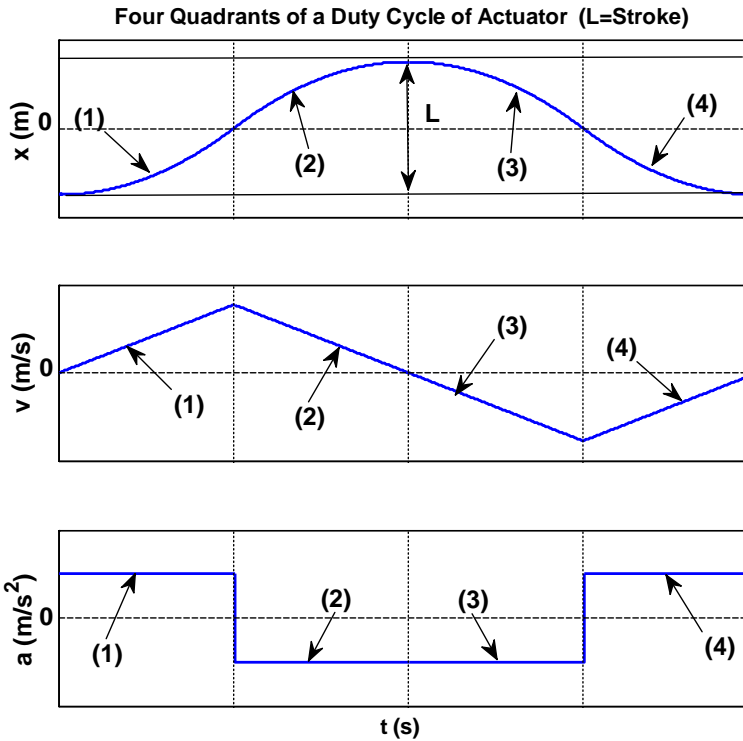


Figure 3.1 An example of four quadrants for a “parabolic” piston motion cycle

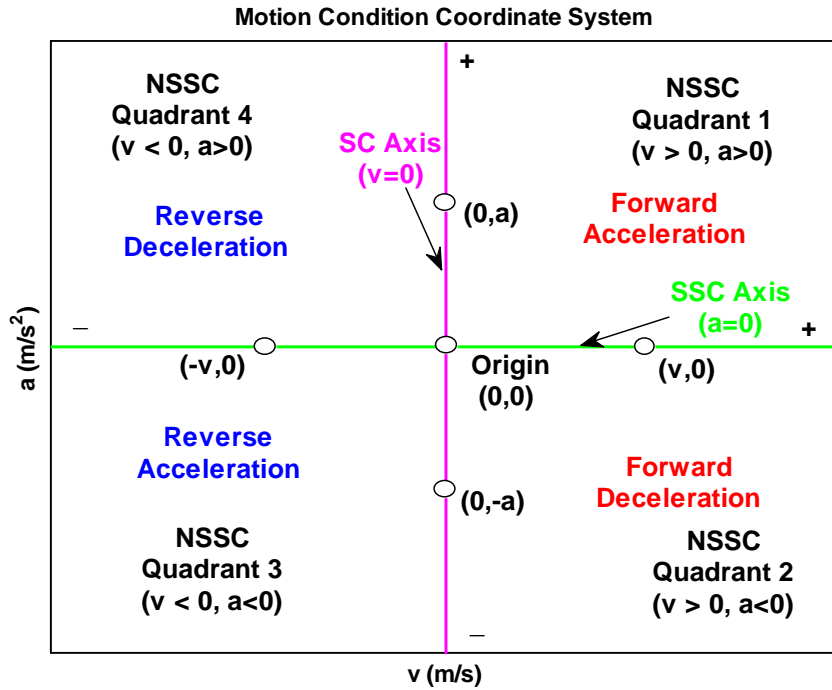


Figure 3.2 Motion condition coordinate system and four quadrants used in this research, NSSC=Non-Steady State Condition, SSC=Steady State Condition, SC=Static Condition

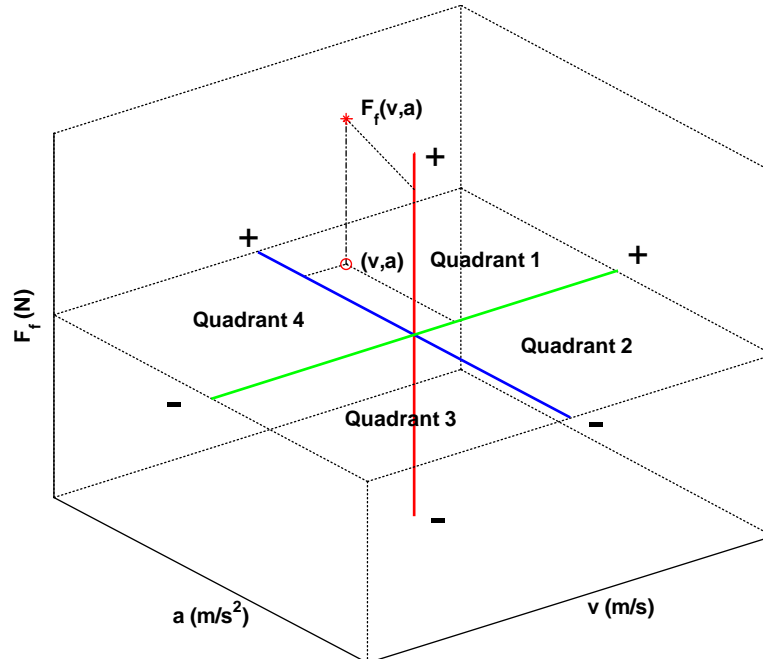


Figure 3.3 Friction ($F_f(v, a)$) measured at a motion condition point (v, a)

Quadrant 1(Q1):

The region of the motion condition coordinate system where $v > 0$ and $a > 0$; in Quadrant 1, the system is “speeding up” (or accelerating) and is moving forward.

Quadrant 2(Q2):

The region of the motion condition coordinate system where $v > 0$ and $a < 0$ (decelerating); in Quadrant 2, the system is “slowing down” (or decelerating, but is still moving in the forward direction.

Quadrant 3(Q3):

The region of the motion condition coordinate system where $v < 0$ and $a < 0$; in Quadrant 3, the system is “speeding up” (or accelerating, but now is moving in the reverse direction).

Quadrant 4(Q4):

The region of the motion condition coordinate system where $v < 0$ and $a > 0$; in Quadrant 4, the system is “slowing down” (or decelerating) and is moving in the reverse direction.

It is evident that the quadrant concept introduced in this thesis is different from the definition used in conventional mathematical quadrants [99] where the quadrants are positioned in the counter clock-wise direction. In the system used here, the quadrants are clock-wise, for example, from Quadrant 1 to Quadrant 4 (physically, the actuator changing directions from forward to reverse). In addition, as mentioned above, a negative acceleration does not necessarily mean the motion is slowing down.

In summary, from these definitions and from the literature review of Chapter 2, it is apparent that static models are not exclusively based on static friction; however, static models can include dynamic friction.

3.3 Lubricated Friction in Different Motion Conditions and Quadrants

When a hydraulic actuation system is in motion, the operating motion condition can be in any point on the operating motion plane. For non-steady state conditions, the piston can operate in all four quadrants. Since the velocities of the piston at both ends are zero, for the input patterns used in this study, the maximum velocities in both directions occur at the midpoint of travel (the position “zero” point). Therefore each quadrant represents half the stroke of the actuator, as shown

in Figure 3.4. It should be noted that for the steady state conditions, the concept of quadrants is not relevant since $a = 0$.

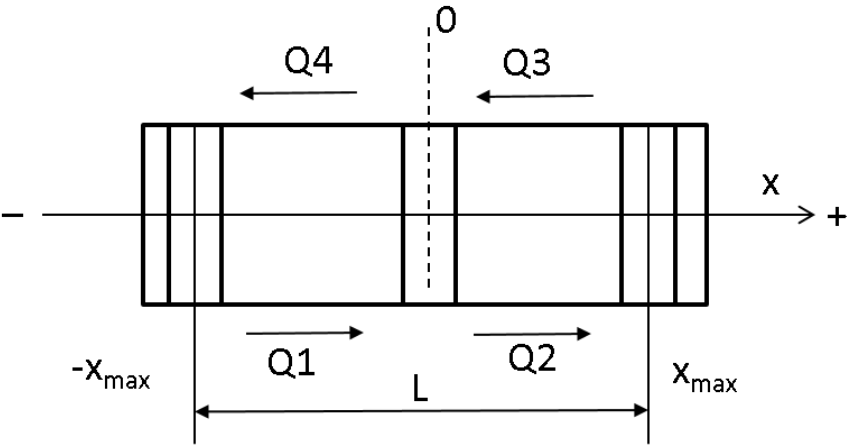


Figure 3.4 Piston positions in a cylinder for non-steady state conditions, L is the stroke of a cylinder. $Q1$ = Quadrant 1, $Q2$ = Quadrant 2, $Q3$ = Quadrant 3, $Q4$ = Quadrant 4

Figure 3.5 shows a typical velocity-time plot for a piston motion in a cylinder. From the shape of the velocity profile, the actuator experiences three different motion conditions over the cycle: static condition, non-steady state condition, and steady state condition. All these motion conditions can be correlated to the motion condition coordinate system, origin, quadrants and axis.

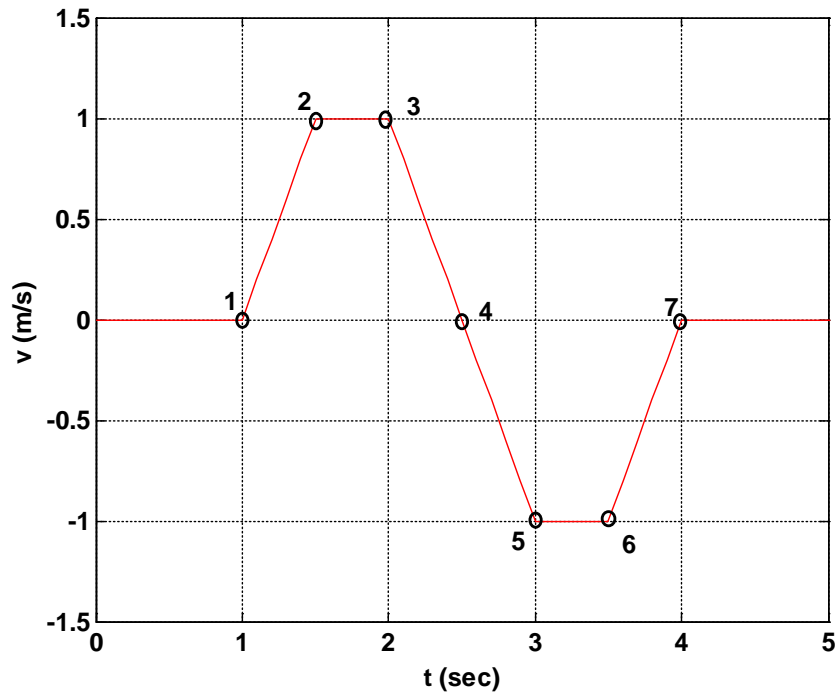


Figure 3.5 A typical velocity – time ($v - t$) plot of a piston motion in a cylinder

1. Static conditions: before the point 1, and after point 7, the velocity of the actuator is zero; therefore it is a static condition ($v = 0$). Friction measured at those regions is static friction.
2. Non-steady state conditions at points 1 to 2, 3 to 4, 4 to 5, and 6 to 7, both velocity and acceleration are not zero ($v \neq 0$ and $a \neq 0$). The actuator experiences acceleration or deceleration, and therefore it is a non-steady state condition. Friction measured in those regions is non-steady state dynamic friction. Each region can be correlated to different quadrants.
3. Steady state conditions: at points 2 to 3 and 5 to 6, the velocity is constant ($a = 0$); therefore the actuator is a steady state condition. Friction measured in those regions is steady state dynamic friction.

In order to fully understand lubricated friction under different motion conditions, lubricated friction can be represented in four quadrants. Consider a typical friction-velocity curve for a hydraulic actuator as shown in Figure 3.6. Curve 1 (red line) represents lubricated friction measured in Quadrant 1, curve 2 (green line) in Quadrant 2, curve 3 (blue line) in Quadrant 3 and curve 4 (magenta line) in Quadrant 4.

From Figure 3.6, lubricated friction in Quadrant 1 and Quadrant 2 have the same velocity range; however, they are measured in different ways. Lubricated friction in Quadrant 1 is measured by increasing the velocity from 0 to a maximum velocity v_{max} , whereas, lubricated friction in Quadrant 2 is measured by decreasing the velocity from the maximum velocity v_{max} back to 0. It is evident that the lubricated friction in “speeding up” and in “slowing down” is different. The same patterns occur in Quadrants 3 and 4.

Figure 3.7 provides a 3D view of lubricated friction in the four quadrants associated with the traces shown in Figure 3.6 with three different projected views: front view, side view and top view. The front view in Figure 3.7 is the same as Figure 3.6 (which is the more traditional way to represent the friction-velocity curves). The side view gives the friction-acceleration curves, the top view gives the acceleration-velocity curves, and the isometric view shows a 3D view of friction-velocity and acceleration curves. These various representations will facilitate discussion of the results and 3D modelling in Chapters 4 and 5.

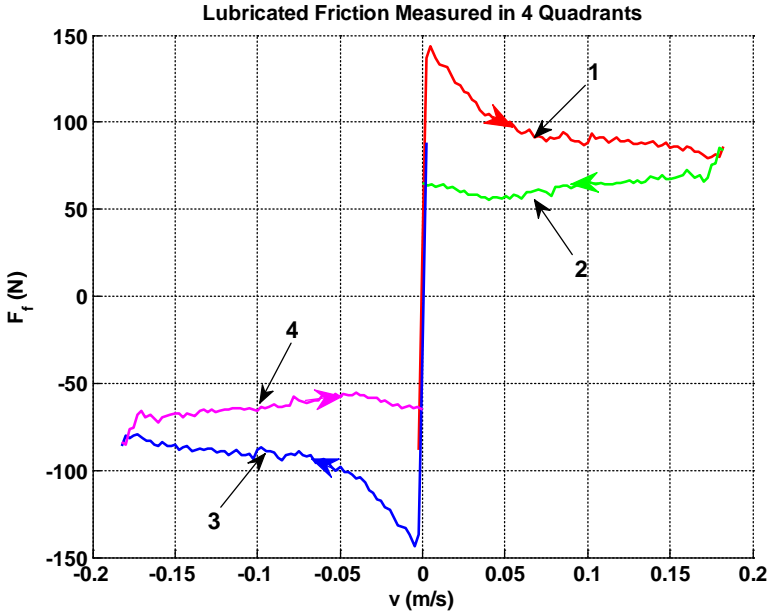


Figure 3.6 A typical example of the lubricated friction measured in four quadrants under non-steady state conditions at acceleration $a = 0.25 \text{ m/s}^2$ of VCHAS1

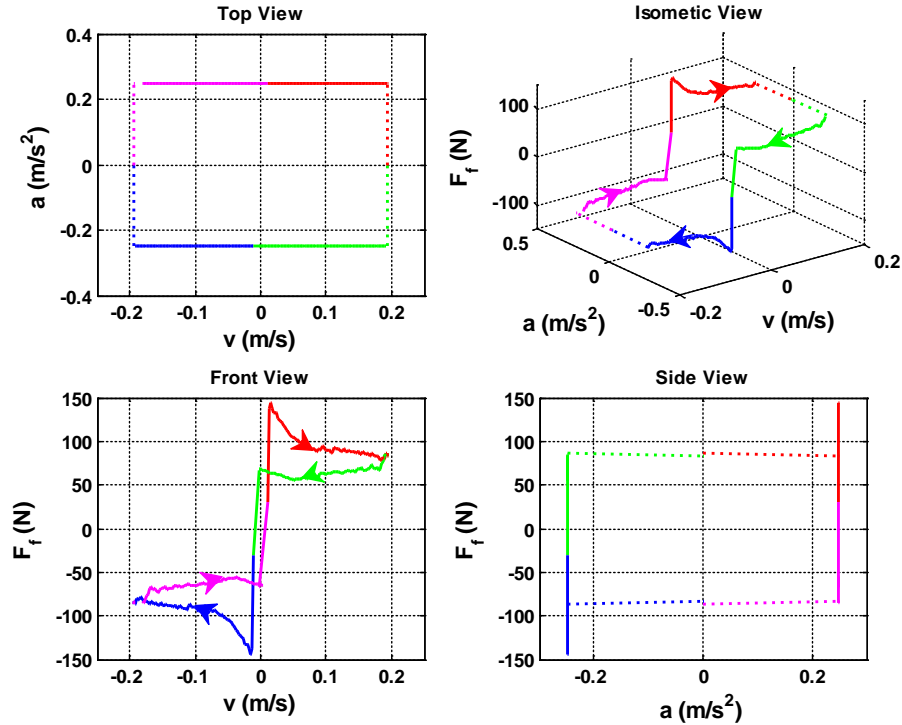


Figure 3.7 An example of the lubricated friction of VCHAS1 measured in four quadrants under non-steady state conditions at acceleration $a = 0.25 \text{ m/s}^2$ in four views – front view (friction-velocity), top view (acceleration-velocity), side view (friction-acceleration) and isometric view (friction-velocity and acceleration)

It is worthwhile to again point out that the piston is moving on the same side of the cylinder (with respect to the midpoint) in Quadrants 1 and 4, and on the opposite side in Quadrants 3 and 2 (Figure 3.4).

3.4 Experimental Apparatus

In Chapter 1, the experimental non-steady state dynamic friction behavior in an EHA system was presented in which the velocity increased in one direction (Quadrant 1 only) under various constant acceleration conditions. The preliminary experimental results indicated that the lubricated friction of the EHA system had a strong dependency on the velocity of the moving surfaces as well as a strong dependency on the acceleration [24]. It was one of the objectives of the research to extend the work to other hydraulic actuation systems to determine if the trends so observed in all quadrants could be applied more universally.

3.4.1 Selection of Hydraulic Actuators

Two hydraulic actuators (sometimes labelled as hydraulic cylinders [34]) were selected for the experimental study of this research. The actuators were linear, double-acting and double-rod end as shown in Figure 3.8. The reason for this particular choice was primarily due to the fact that linear hydraulic actuators are commonly used in research and industry, and are readily reversible, an important consideration in designing an experimental procedure to collect friction data. In addition, because the stroke is limited in linear hydraulic actuators, nonlinear friction at low velocities becomes more dominant. It must be recalled that the objective was to investigate the hypothesis that lubricated friction in hydraulic actuators has a dependency on the acceleration. As such, the choice was dictated by which actuation system would facilitate such measurements in the low velocity regions where, as mentioned above, nonlinear friction behavior dominates. It will be shown later how the restricted stroke also limits regions in which data can be collected. A further consideration was that the double-acting and double-rod actuator had equal effective piston areas on both sides of the piston. This facilitated system control due to this symmetrical arrangement, and made measurements easier because only the differential pressure across the piston was needed to calculate friction.

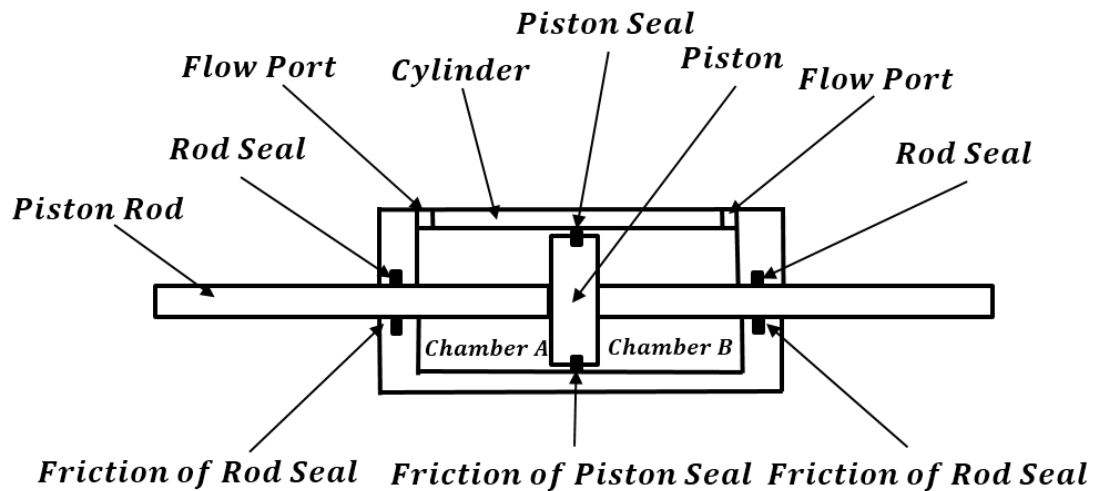


Figure 3.8 Schematic of a double-acting and double-rod end linear hydraulic actuator (The stroke is limited by the ends of the each cylinder housing)

A linear hydraulic actuator consists of a piston, piston rod, cylinder (or housing) and seals (piston seals and rod seals) and is illustrated in Figure 3.8. The limitation on this type of actuator is that the stroke (or maximum displacement) of the piston is restricted by the housing end plates.

The lubricated friction force of the linear hydraulic actuator was a consequence of the lubricated friction between the piston seal and cylinder surfaces plus the lubricated friction between the piston rod and rod seals. In both actuators, external masses could be attached to the piston rods, but made no contact with any surface [41].

As has been mentioned, two linear hydraulic actuators of different sizes and construction were selected for the experimental portion of this research and subjected to similar operating conditions. Two different cylinders were chosen to ascertain whether the trends shown by both were similar. The parameters of the two selected hydraulic actuators are provided in Table 3.1 and have been labeled as HA1 and HA2.

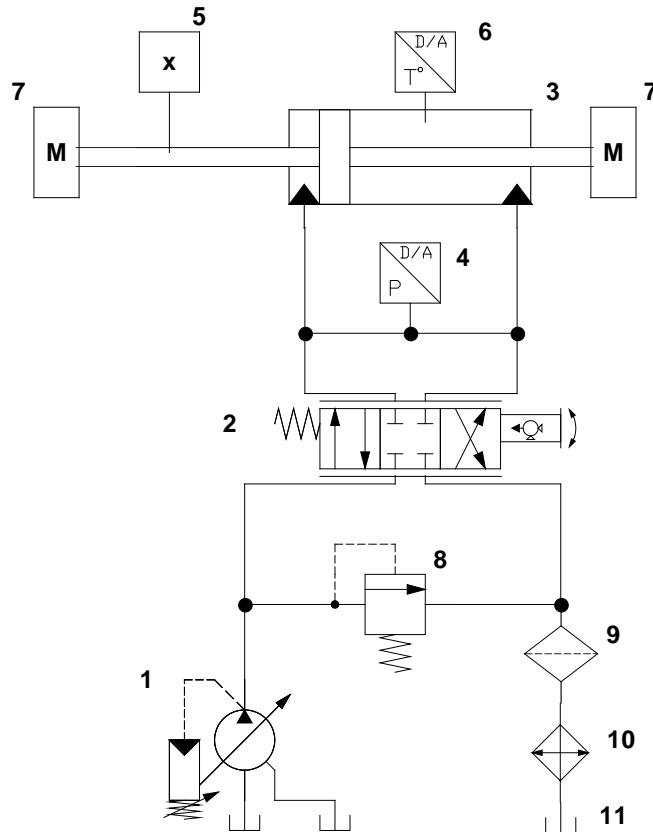
Table 3.1 Parameters of two hydraulic actuators selected

	HA1	HA2
Model	SHEFFER 1-1/8HH46L6AD	Parker ANNIPIN KC2H
Piston Mass (kg)	3.91 (including attached mass)	1.67
Piston Active Area (m ²)	4.43*10 ⁻⁴	9.42*10 ⁻⁴
Stroke (m)	0.15	0.2

These two system configurations were believed to be sufficient to establish a set of procedures which would allow confirmation of the fundamental hypothesis proposed in Chapter 1, that is, the lubricated friction versus velocity curve for hydraulic actuation systems is dependent on acceleration. Thus each system must accommodate conditions in which acceleration could be the controlled variable.

3.4.2 Hydraulic Circuit Configuration and Instrumentation

Two separate hydraulic circuits were built to accommodate the two selected hydraulic actuators for all experiments. Valve control was chosen for both hydraulic circuits. The reason for this is because it is well known that valve controlled hydraulic systems exhibit better response characteristics than pump controlled hydraulic systems [1]. In addition, several valve controlled systems were readily available in the laboratory and the author had substantial experience with these types of systems. The two valve controlled hydraulic actuation systems (VCHAS1 and VCHAS2) were set up using the same layout configurations as shown in Figure 3.9.



- (1) Pressure compensated variable displacement pump, (2) Flow control servovalve, (3) Double acting double rod end hydraulic cylinder, (4) Differential pressure transducer, (5) Position transducer, (6) Temperature sensor, (7) Attached mass, (8) Relief valve, (9) Oil filter, (10) Oil cooler, (11) Oil Tank

Figure 3.9 Schematic of the valve controlled hydraulic actuation system (VCHAS) [2]. The two experimental systems used in this study were located in the fluid power research lab in the College of Engineering at the University of Saskatchewan.

The two systems have been labelled in this thesis as VCHAS1 and VCHAS2 respectively. The reason for using the same configurations was to facilitate experimental result comparisons. The hydraulic actuator was fixed horizontally on a solid surface plate. The actuator was connected to a four-way servovalve with the flow provided by a pressure compensated pump. A differential pressure transducer was installed across the actuator ports. A position transducer was attached to one end of the rod and a mass attached to the other. The mass could be changed as needed. The total mass of the actuator consisted of the mass of piston, the mass of the rod on both sides of the piston, and the external mass attached to the rod.

VCHAS1 and VCHAS2 were carefully instrumented for accurate measurements. For position measurements, a Lucas Schaevitz 5000 DC-E DCDT was used in VCHAS1 and a laser displacement sensor (MTI Instruments type LTS-300-200) was used in VCHAS2. The differential

pressures of both hydraulic actuation systems were measured using Validyne DP15-20 differential pressure transducers. In addition, temperature information was monitored by a temperature transducer (a T type thermocouple) and recorded. Velocity and acceleration sensors were NOT used in this research. The velocity and acceleration data were derived from displacement data by using numerical differentiation methods. This is discussed in greater detail in Section 3.6.3. Table 3.2 summarizes the instrumentation used in this study.

Digital signals from the transducers were input into a Personal Computer (IBM type MT-M 2212 WDS) through a 12 bit analog-to-digital (A/D) converter (National Instruments type pci-6025e), and a signal from the computer was supplied to the servovalve through a 12-bit digital-to-analog (D/A) converter (National Instruments type pci-6025e). Piston positions and differential pressures were recorded at intervals of 1 ms (or sampling rate of 1000 Hz) for all experiments.

Table 3.2 Instrumentation of VCHAS1 and VCHAS2

	VCHAS1	VCHAS2
Position Transducer	Lucas Schaevitz 5000 DC-E DCDT	MTI Instruments type LTS-300-200
Differential Pressure Transducer	Validyne DP15-20	Validyne DP15-20
Temperature Transducer	T type Thermocouple	T type Thermocouple

Consider Figure 3.9. Piston motion control was accomplished using an electrohydraulic servovalve. Fluid was ported from the electrohydraulic servovalve to the actuator which resulted in a differential pressure drop across the actuator piston and hence a displacement of the actuator. The motion was detected by an appropriate position transducer and the corresponding electrical signal fed back to an electronic comparator (a control box). This signal was compared to the desired signal with the error signal directed to the electrohydraulic servovalve via a servo amplifier (Figure 3.10). The hydraulic actuation system was a closed-loop system. The piston motion was controlled by a Proportional (P) controller. Initial studies indicated that the P controller could achieve good control performance that was required for steady state conditions and non-steady state conditions of both VCHAS for this research.

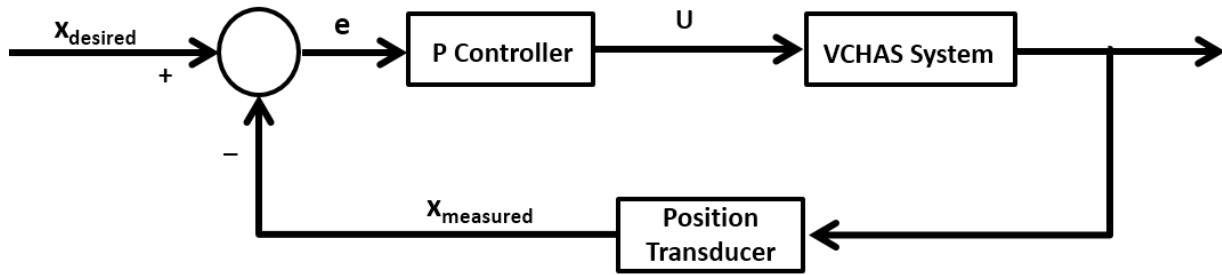


Figure 3.10 Schematic of closed loop control of the piston position (proportional controller) for VCHAS1 and VCHAS2

As mentioned, the hydraulic actuation systems consisted of linear hydraulic cylinders of various sorts in which the cylinder rods' displacement, velocity and acceleration as well as differential pressure across the cylinder piston were measured or estimated. These measurements were used to extract the dynamic properties over a range of accelerations as well as providing a basis for verification and validation of the models. The objective of the circuit was to control the motion conditions (position(x), velocity(v) or acceleration(a)) of the hydraulic actuator. The displacement was controlled to make the piston move in a triangular motion at various constant velocities in order to create steady state conditions or to make the piston move in a parabolic motion at various constant accelerations to create non-steady state conditions.

3.5 Experimental Procedures

In general, in order to develop an experimentally based model, only one parameter is usually allowed to vary whilst others are assumed (or held) approximately constant. This approach is often called the “one-factor-at-a-time” rule in scientific and engineering research [100]. This approach facilitates a more precise study and understanding of the effects of that parameter [47]. This was the approach that was used in the author's research study. Acceleration was considered to be the “family parameter” and hence was allowed to vary in a “discrete” fashion. Lubricated friction (via measurement of the pressure drop across the actuator) was measured as a function of velocity by holding acceleration constant during a test. The procedure was repeated at various accelerations until a physical limit on the test system was encountered.

Amongst all the methods of measuring dynamic lubricated friction reviewed in Chapter 2, an indirect and continuous measurement method was chosen for measuring the lubrication

friction under non-steady state conditions. An indirect and discrete measurement method was chosen for measuring the lubricated friction under steady state condition for later comparisons.

The nonlinear lubricated friction of the hydraulic actuation system was measured indirectly by measuring differential pressure across the piston and then converting it to a friction force value by Newton's second law.

The temperature in the hydraulic actuation systems was carefully held constant at $29 \pm 1^\circ\text{C}$. The temperature was monitored and the experiments spaced in time to allow the oil to cool down and reach the same temperature before the next set of experiments were performed.

The pressure transducers were initially "bled" to release any entrained air or free air inside the hydraulic actuation systems. In all cases, the supply pressures were set at 10342 kPa (1500 psi) for VCHAS1 and 6895 kPa (1000 psi) for VCHAS2 respectively.

Calibrations of pressure transducers of both VCHAS1 and VCHAS2 were made before and after all the tests. Details are provided in Appendix C. It was observed that the calibration did not vary from test to test or day to day.

3.5.1 Steady State Dynamic Friction Measurement

Lubricated friction under non-steady state conditions is the main focus of this study. However, it is important to determine lubricated friction under steady state conditions which will be used in Chapter 5 for model validation purposes.

Preliminary experimental results indicated that the lubricated friction versus velocity curve at small accelerations is similar to the Stribeck model (see Section 3.7.3). Recall from Chapter 2, that the Stribeck model implies discrete measurements. However, the Stribeck model can also be obtained by continuous motion if a very small acceleration is used. The problem is determining how small the acceleration can be. It is desirable that the maximum velocity at half the stroke for the parabolic positional input (constant acceleration) be larger than the Stribeck velocity in order to observe the Stribeck shape. Experimentally this may not be possible due to the limited stroke of the actuators. This limitation is discussed in greater detail in Section 3.6.2.

A common way to measure the steady state dynamic friction is to keep the piston moving at a constant velocity (zero acceleration) and then measuring the differential pressure (or force) across the actuator at that specific point (reference to Burton, Chinniah etc. in Chapter 2) [2, 15]. The velocity is then changed and the procedure repeated. As mentioned in Chapter 2, because the

differential pressure is obtained at a specific point when velocity is constant, this approach has been labelled as a “discrete” approach. In addition, since this is a discrete approach, the more velocity points used, the higher the resolution of the friction curve.

There are two types of signals that were used in this study to obtain steady state friction measurements. In the initial EHA system, where only Quadrant 1 was examined, a ramp input position signal was controlled to be as shown in Figure 3.11 [24]. The resulting calculated velocity and acceleration curves are also shown. It should be noted that the blue lines in this figure are “stable zones” for data collection; that is regions in which transients have died down. The red lines are zones for the transition zones in which transients may well exist.

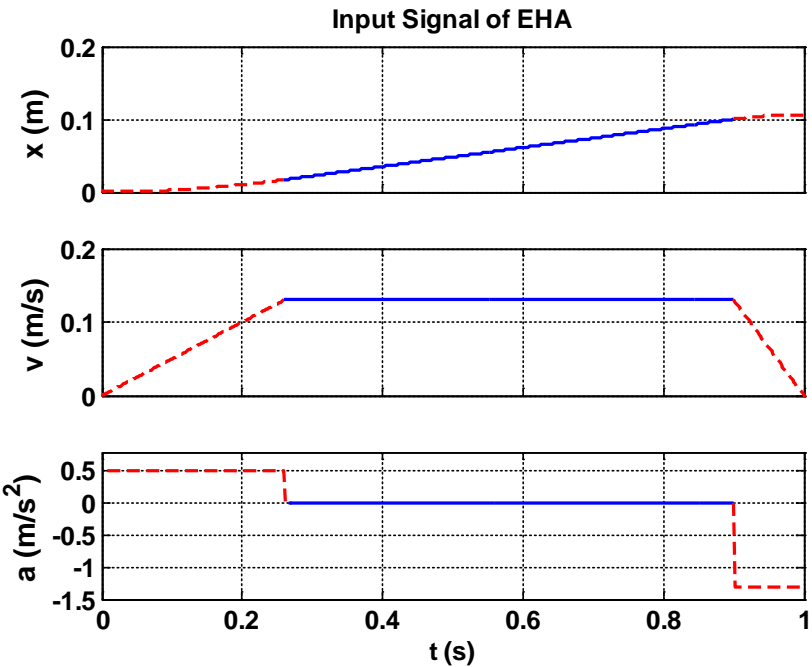


Figure 3.11 EHA input ramp displacement signal (blue line) for steady state friction measurements

In the VCHAS, a second type of input signal was used to determine the steady state friction data. A periodic triangular position translated into a square wave type signal in which velocity was constant, is shown in Figure 3.12 for one cycle.

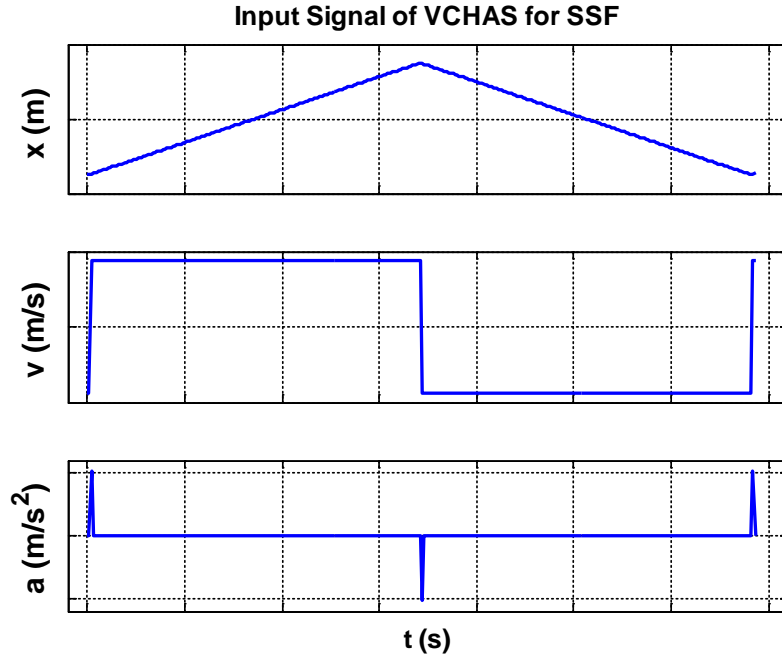


Figure 3.12 A cycle of input triangular displacement signal (x) (periodic) to the VCHAS1 and VCHAS2 for steady state friction (SSF) measurements and the expected actuator velocity (v) and acceleration (a).

It should be pointed out that at the transition points (the points where the velocity changes sign), the acceleration is not zero but can be considered zero once transients have died down. It is also important to recall that any measurement taken under constant velocity has no “official” quadrant assigned to it as discussed in Section 3.2. The velocity can be varied by changing the frequency of the triangular input signal as shown in Equation (3.1).

$$|v| = 2Lf_s \quad (3.1)$$

where L is the actuator stroke and f_s is the frequency of the input signal. It is apparent that a constant velocity of the piston has a linear relationship with the frequency of the input signal. Information regarding the derivation of this equation is given in Appendix D.

For steady state friction measurement, care was taken to prepare a “velocity list” which could be physically realizable experimentally (details provided in Appendix E). The experimental procedure to obtain the steady state friction data was as follows:

1. A list of desired discrete velocities (velocity list) at which measurements were to be made was created. From the list and using Equation (3.1), the required frequency of the triangular position input signal was established (details are

provided in Appendix D). This is now the desired position input to the closed loop system.

2. The experiment started by using the minimum desired velocity (and hence input frequency of the positional triangular waveform).
3. The differential pressure (ΔP) and displacement (x) were measured and recorded, and temperature was monitored.
4. The experiment was repeated under the same conditions three times.
5. The frequency of the input triangular displacement signal was changed to correspond to the next desired velocity.
6. Steps 3 to 5 were repeated until the velocity of the input signal reached the maximum desired velocity.

In the steady state situation, for zero acceleration (no inertial force terms), the lubricated friction force of the hydraulic actuation system was obtained from:

$$F_f = \Delta P A_p \quad (3.2)$$

where F_f is the lubricated friction force of the actuator including the friction force of the piston seal(s) and rod seals, ΔP is the differential pressure across the piston and, A_p the effective area of the piston. It needs to be emphasized that physically, the lubricated friction could not be measured directly and could only be calculated using Equation (3.2).

From Equation (3.2), the steady state friction can be calculated from the measured differential pressure (ΔP). The challenge was to obtain a steady state value of ΔP in a very short period of time because of transients that existed in the pressures signals (Figure 3.13).

As the desired velocity increased (increase in the input frequency), the point in which the transients died down approached the point in which a change in the signal waveform occurred. Under these conditions, measurement of a steady state pressure signal was compromised due to the fact that transients did not adequately settle down. Essentially this limited the maximum velocity that could be reliably used.

Direct measurement of breakaway friction was not possible using this method due to the experimental limitations (resolution and noise) encountered when the velocity approached zero (minimum velocity), and had to be estimated using numerical extrapolation methods. Some typical experimental results for this type of input are presented in Section 3.7.1.1 and Section 3.7.2.1.

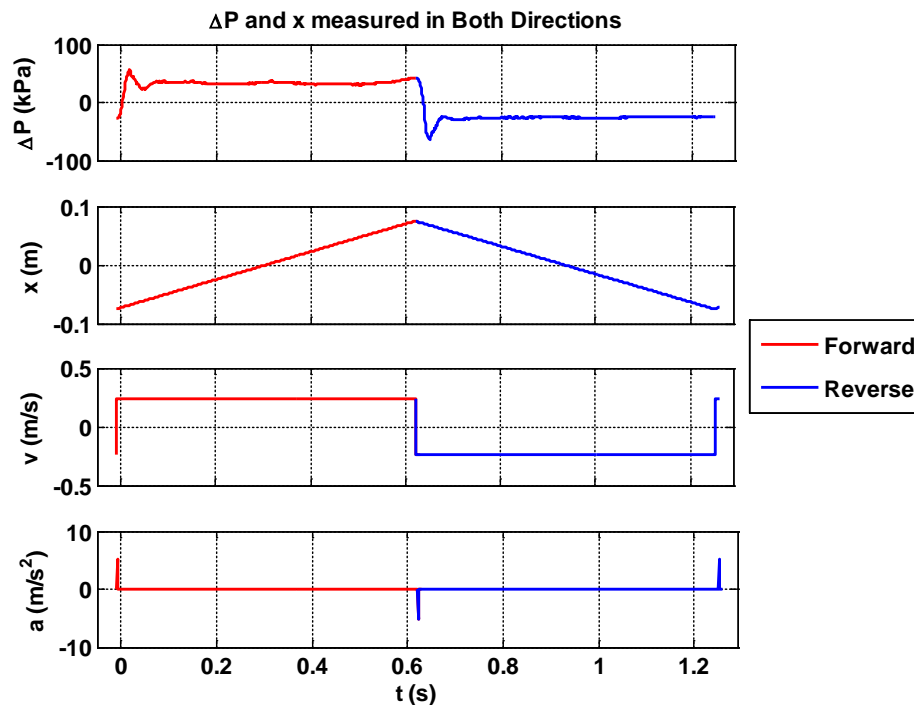


Figure 3.13 An example of a cycle of measured differential pressure (ΔP) and measured displacement (x) in both directions. Please note: Velocity and acceleration were not measured but were obtained by differentiating the position (x) once for velocity (v). No filtration of any signal was required

3.5.2 Non-Steady State Dynamic Friction Measurement

A challenge for this research was to come up with a process which would facilitate the continuous measurement of friction as a function of velocity, but with acceleration as a family parameter. In this thesis, a novel approach was proposed and implemented. To the author's knowledge, this particular approach has not been published in the literature. The objective of this approach was to create a plot of friction vs. velocity in a continuous manner, with acceleration held constant for each test.

If one works backwards, a periodic constant acceleration implies a triangular velocity waveform which further implies a parabolic position (displacement) waveform in the actuator. If this logic is reversed and if the parabolic input to the servo system is controlled, then the velocity waveform is a triangular wave and the acceleration is a square wave. This then was the approach

adopted for this study and illustrated graphically in Figure 3.14. Details of the implementation of the parabolic waveform using Matlab © and Simulink © are given in Appendix F.

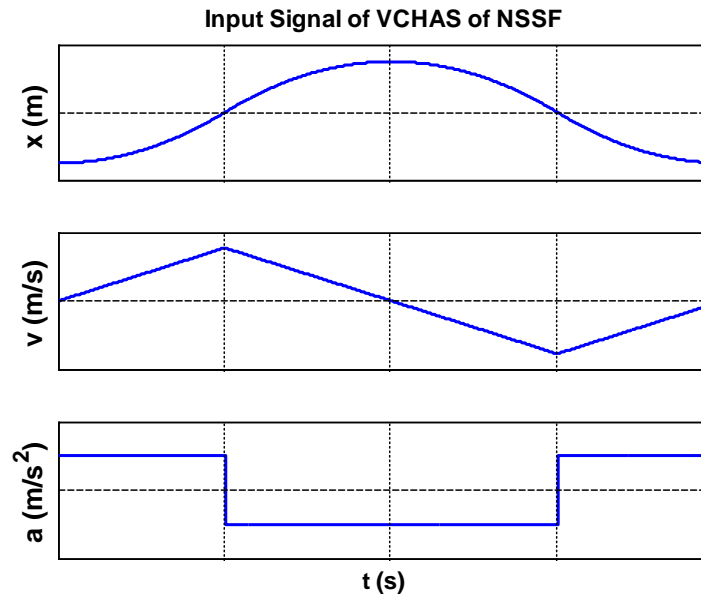


Figure 3.14 A typical one cycle of the input parabolic displacement signal (x) to the VCHAS1 and VCHAS2 and the expected actuator triangular velocity (v) and square acceleration (a). NSSF refers to non-steady state friction.

With reference to Figure 3.14, because velocity varies linearly with time in sampling intervals of the digital data acquisition system, the measurement of friction is considered continuous, as opposed to discrete in the traditional steady state friction measurement. The acceleration can be varied by changing the frequency of the parabolic input signal as illustrated by Equation (3.3).

$$|a| = 16Lf_s^2 \quad (3.3)$$

where L is the stroke and f_s is the frequency of the input parabolic displacement signal. From Equation (3.3), it is apparent that the acceleration of the piston has a quadratic relationship with the frequency of the input signal. Information regarding the derivation of this Equation is given in Appendix D.

For non-steady state friction measurement, care was taken to prepare an “acceleration list” which could be physically realizable experimentally (details provided in Appendix E). This acceleration list was determined by the author in order to create as many data points as possible for the experimental lookup table (to be defined in Chapter 4). The maximum acceleration is constrained by the system bandwidth and flow capacity. Figure 3.15 shows a typical set of

experimental results (measured differential pressure (ΔP) and measured position(x)) for VCHAS1 in all quadrants (defined in Section 3.2). Velocity and acceleration were not measured, but were obtained by differentiating the position (x) once for velocity (v) and the once again for acceleration(a). No filtration of any signal was made. The rationale for this approach will be discussed in Section 3.6.1.

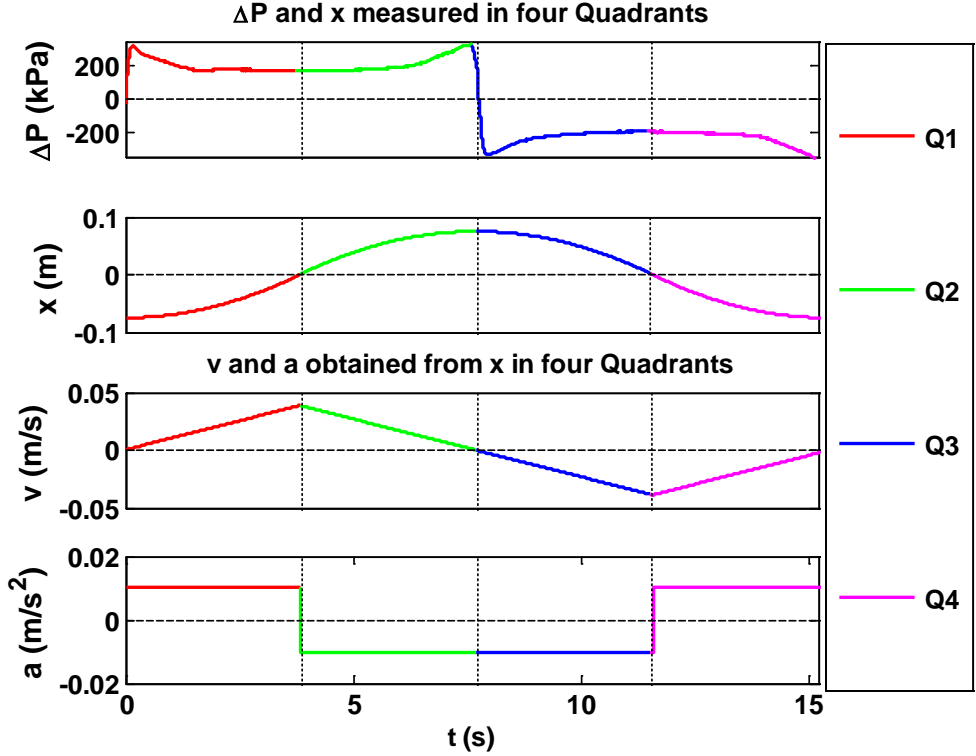


Figure 3.15 An example of measured differential pressure (ΔP) and measured displacement (x) in all four quadrants. Please note: velocity and acceleration were not measured but were obtained by differentiating the “curve fitted” position (x) once for velocity (v) and then once again for acceleration(a). No filtration of any signal was required

Consider Figure 3.15. Because this experimental approach is considered to be a continuous measurement, the velocity can pass through a zero velocity region continuously. Thus by changing the frequency of the displacement waveform, lubricated friction forces (calculated via measuring pressure differential across the actuator) could be obtained and plotted as a function of velocity at a constant acceleration. Acceleration became the family parameter in the resulting plots.

The experimental procedure to obtain the continuous non-steady state friction data is as follows:

1. A list of desired discrete accelerations (acceleration list) at which measurements were to be made was created. From the list and using Equation (3.3), the required frequency of the parabolic position input signal was established (details are provided in Appendix D). This is now the desired position input to the closed loop system.
2. The experiment started using the minimum desired acceleration (and hence input frequency of the positional parabolic waveform).
3. The differential pressure (ΔP) and displacement (x) were measured and recorded, and temperature was monitored.
4. The experiment was repeated under the same conditions three times.
5. The frequency of the input parabolic displacement signal was changed to correspond to the next desired acceleration.
6. Steps 3 to 5 were repeated until the acceleration of the input signal reached the maximum desired acceleration.

Because acceleration is a family parameter, inertial forces must be subtracted out of the overall calculated friction force (from ΔP) as shown in Equation (3.4).

$$F_f = \Delta P A_p - M a \quad (3.4)$$

where F_f is the lubricated friction force of the actuator including the friction force of the piston seal(s) and rod seals, ΔP is the differential pressure across the piston, A_p the effective area of the piston, M is the lumped mass of the actuator rod, piston and any attached mass (where appropriate) and a is the actuator acceleration. There is no external load (force) applied to either VCHAS1 or VCHAS2.

3.6 Experimental Limitations

3.6.1 Limitation of Velocity and Acceleration Sensors

Initial studies indicated a problem with some noise on all transducers. Velocity transducers and indeed, acceleration transducers were found to produce very noisy signals to the extent that it was not possible to extract reliable information. As such, an alternate approach was considered in which the position of the actuator was measured using high quality transducers and then by using numerical techniques, computing the derivatives of this signal for velocity and

taking the derivative again for acceleration. Initial studies indicated that if the position signal was essentially noiseless, this approach would be quite feasible.

Typical examples of the measured position waveforms are shown in Figure 3.15. The noise on the velocity signal after differentiation was acceptable, but the noise on the acceleration signal was very significant and essentially unusable as it was. Filters were considered, but an initial feasibility study indicated that they introduced distortion and phase shifts on the signals which produced other issues.

A second approach, one that was finally adopted, was to “curve fit” a parabolic curve to the measured position signal (an easy task since the input to the VCHAS was a parabolic curve in the first case) and then differentiate the best fit theoretical curve to get velocity and acceleration [101]. Typical results are shown in Figures 3.16 to 3.18. Additional parabolic curve fitting results are presented in Appendix G. It is quite evident that the curve fit on position was excellent (for all test conditions experienced in this study).

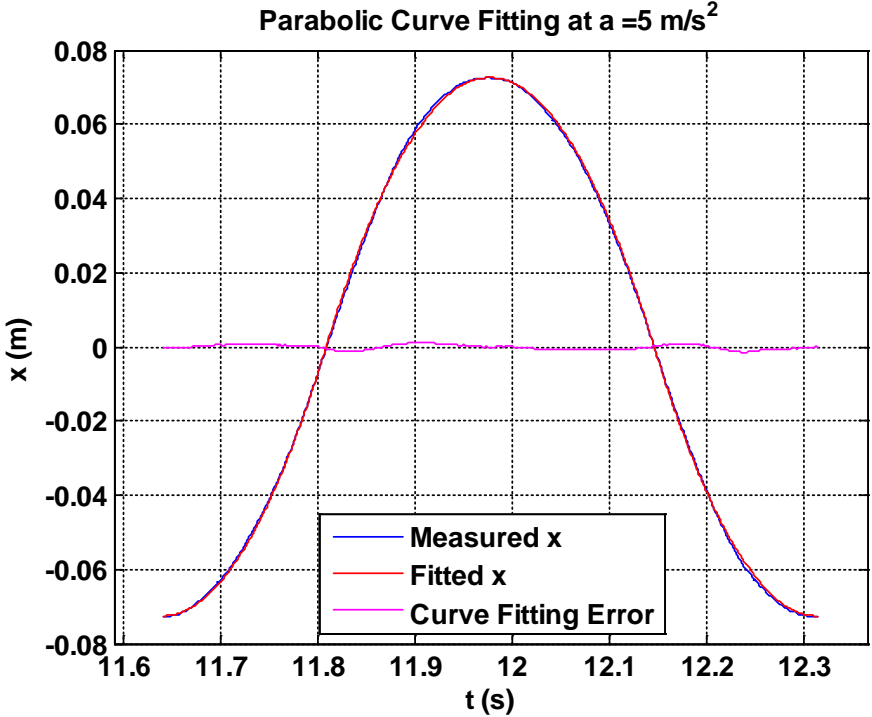


Figure 3.16 A typical parabolic curve fitting of the measured displacement at acceleration = 5 m/s²

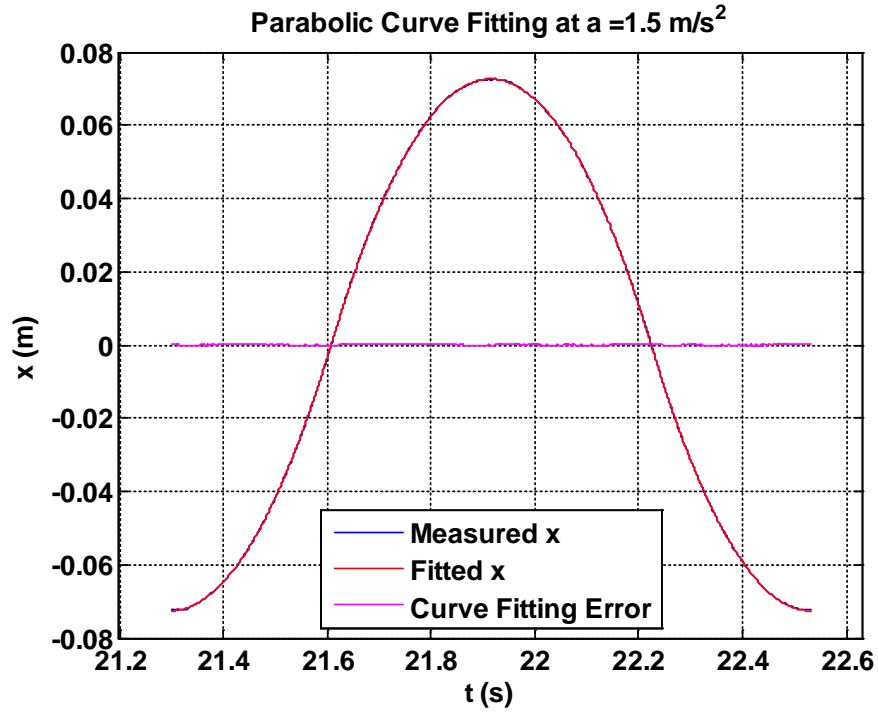


Figure 3.17 A typical parabolic curve fitting of the measured displacement at acceleration $= 1.5 \text{ m/s}^2$

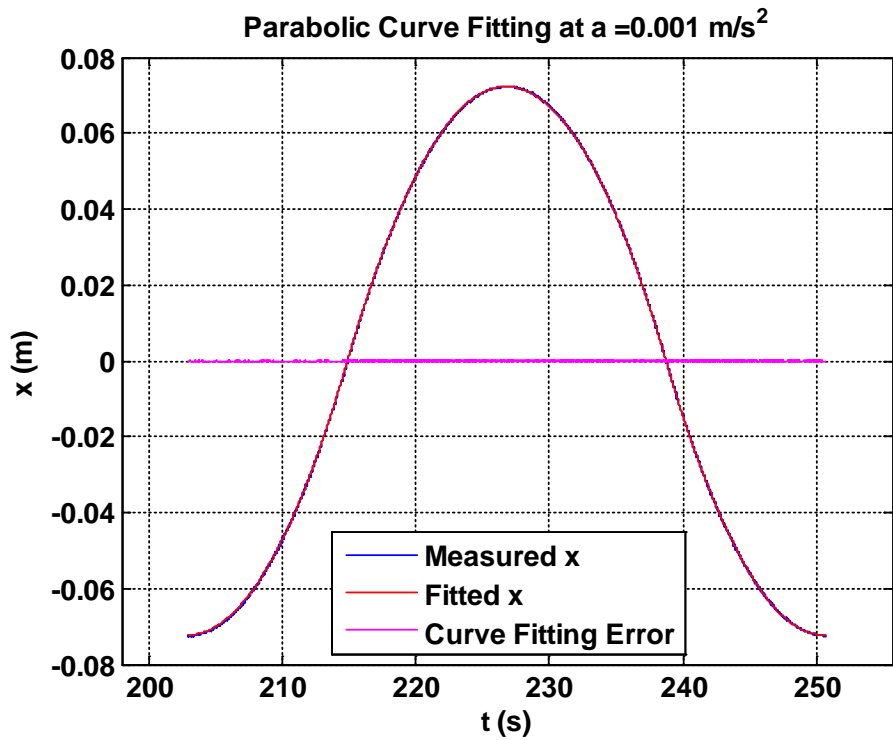


Figure 3.18 A typical parabolic curve fitting of the measured displacement at acceleration $= 0.001 \text{ m/s}^2$

Figure 3.19 illustrates the superimposition of the derivative of the fitted position, velocity and acceleration curves on the measured position, and derivative based velocity and acceleration of the measured position signal. It is observed that the extracted velocity and acceleration were “clean signals” with no phase shifts or significant distortion.

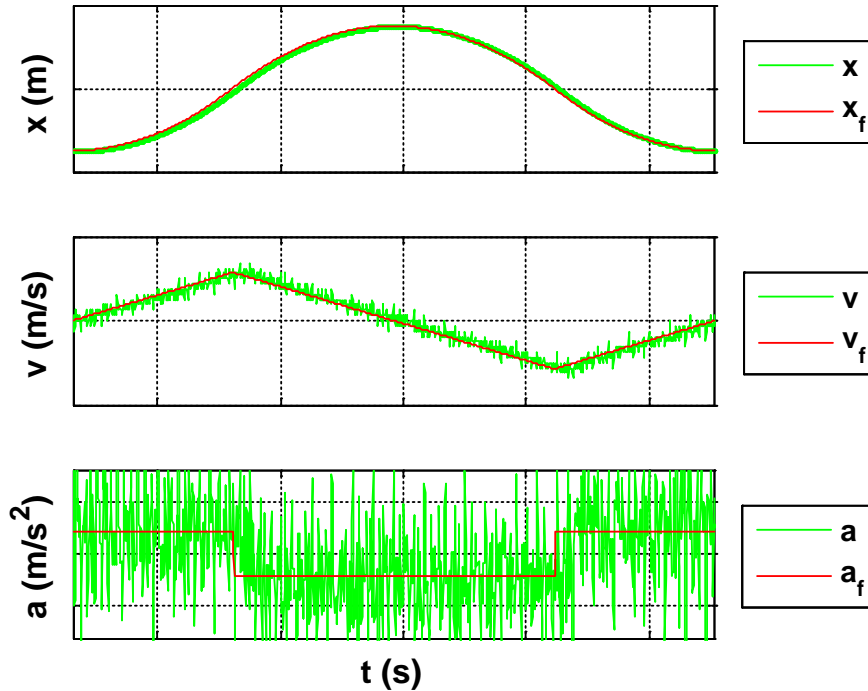


Figure 3.19 The measured position (x), the velocity (v) from the first derivative of the measured position (x), and acceleration (a) for the second devative of position are shown in green lines. The red lines are theoretical based on an optimal fit of a parabolic curve shown superimposed on the position curve (x), using experimental data and by differentiating a best fit curve (x_f) to the position signal (x) to get velocity (v_f) and acceleration (a_f). No filtration of any signal was made

It was understood that using this approach would introduce some errors if the position signal did not follow a parabolic or triangular waveform. Every test that was conducted using this waveform was checked to ensure that the fitted curve was acceptable and as such, (as discussed in Section 3.6.3) when the frequency of the input signal was changed and a distortion was observed (that is, the fit was starting to deteriorate), data was not used.

This study considered only two types of waveforms for the position signals: parabolic and sinusoidal. As such, the fitting approach was considered to be very feasible and produced very

repeatable results. This was not the case when the initial studies attempted to use non fitted data. This author believed that the fitting approach could be used with great confidence in this study.

3.6.2 Limitation of the Velocity Triangular Waveform Approach

In Section 3.5.2, a novel technique to experimentally obtain data for the friction model was introduced. A choice of input signal to the test system was very important. To enable repeatable data collection for the different friction conditions and to accommodate the effect of hysteresis, a periodic parabolic displacement waveform (for the NSSF case only) was chosen which enabled the acceleration to be a family parameter. It is, however, important to understand that this technique does have inherent restrictions and hence imposes some data limitations. Any actuator has a physical limit in terms of its stroke. This has a significant consequence in terms of regions in which friction data can be collected. This will now be considered.

Consider Figures 3.20 and 3.21. The maximum displacements of the piston are the same for all accelerations. As the acceleration increases for each test, the times at which the cylinder bottoms out reduces. At low accelerations, the velocity of the actuator is small when half stroke is achieved. At high accelerations, the velocity can be high at half stroke (recall for the last half of the stroke, the actuator is decelerating). Therefore, for each acceleration, there is a limit on the maximum velocity that the actuator piston can achieve at half stroke. Figure 3.20 illustrates the maximum velocity (and subsequently maximum acceleration) that can be reached for various position waveforms of different frequencies. Figure 3.21 shows an expanded view at higher accelerations. What this implies is that at some stated acceleration and for this particular positional waveform, the maximum velocity at the midpoint cannot be exceeded. Therefore, there will be regions in which data CANNOT be collected.

Figures 3.20 and 3.21 consider the cases where the stroke of the actuator has been reached in the time domain. As the frequency of the triangular waveform changes, it is clear that a maximum velocity and acceleration occurs at points at which the actuator reaches its midpoint of stroke ($\frac{L}{2}$). To illustrate regions where data can be collected and regions where it is not possible, a plot of the maximum velocity versus acceleration in the operating motion condition plane is useful. This is shown in Figure 3.22 where the “boundaries” are defined by the relationship given by Equation (3.5). The derivation of Equation (3.5) is given in Appendix H.

$$v_{\max_a} = \sqrt{La} \tag{3.5}$$

$$\Delta v_a = a * \Delta t \tag{3.6}$$

where v_{\max_a} is the maximum velocity for any constant acceleration (a) and L is the stroke of the actuator, Δv_a is the velocity interval for any constant acceleration (a), and Δt is the sampling time. It is important to re-emphasize that this maximum occurs at the stroke midpoint and not at full stroke for the assumed positional waveform.

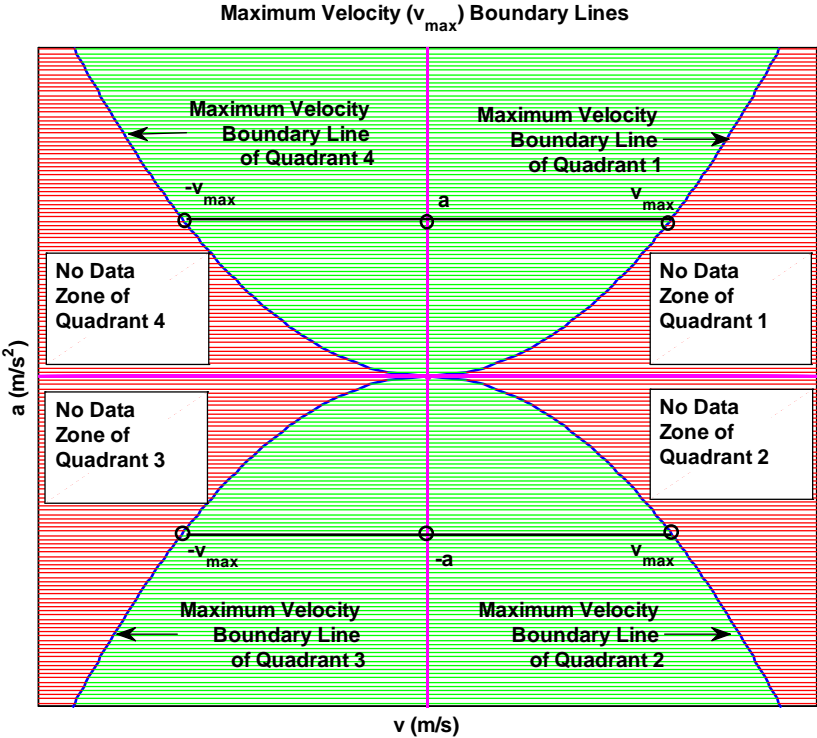


Figure 3.22 Maximum velocity boundary lines of four quadrants. Outside the boundary lines (areas in red) experimental data cannot be collected using the parabolic displacement signal waveform approach. Details are provided in Appendix H

For convenience, the data from VCHAS1 is considered in the following discussion. As will be shown later, the data from VCHAS2 show similar trends.

From Figure 3.22, for any non-steady state motion with an acceleration (a or $-a$), there is an effective velocity range (*e.g. from* $-v_{\max_a}$ *to* v_{\max_a}) where the experimental data can be collected. As the value of the acceleration (a) increases, the effective velocity range increases (if a increases n times, the effective velocity range increases $2\sqrt{Ln}$ times), which helps to generate a better “friction-velocity” curve to cover all the lubrication regimes under a higher constant acceleration (a). This factor facilitates investigation of the lubricated friction dependency on acceleration by observing more characteristics of the friction-velocity curves at higher accelerations.

In summary, for parabolic displacement signals, only the green areas are operating conditions that can be accomplished for the parabolic position input. The red areas labelled as “No Data”, are where the parabolic displacement signals cannot reach. As will be presented in Chapter 5, the consequence of this is that when the friction model is implemented, there will be regions in which the output has no data it can use. In order to compensate for this lack of data, the data is simply set to zero for all these cases.

As mentioned, this limitation in regions in which data cannot be collected is a consequence of the parabolic positional waveform assumed. Other waveforms could have been used which might have extended the green regions but the ability to maintain acceleration as the family parameter with the parabolic waveform was deemed very desirable. In Chapter 6 ways in which the limitation can be compensated will be introduced. It was believed that the objective to confirm the hypothesis of friction dependency on acceleration could be established with the data limited to the green regions.

It is evident from Figure 3.22 that the effective velocity ranges in the low acceleration regions are much smaller, which definitely will affect the friction-velocity curve and thus limit the information that can be observed. However, since the non-steady state motion at low accelerations approach steady state motion, the friction-velocity curves at low accelerations may be replaced by the Stribeck model which is measured under steady state conditions.

It must be emphasized, however, that the main objective was to demonstrate experimentally that friction is not just a function of velocity (Stribeck model), but is additionally dependent on acceleration. The periodic parabolic positional waveform facilitates continuous

measurement of friction as a function of both velocity and acceleration to prove that this dependency does exist. Since acceleration is a family parameter, it is not considered to be a continuous measurement. A sinusoidal signal would be continuous for both velocity and acceleration. More will be discussed on this in Chapters 5 and 6.

Another limitation on the experimental approach lies in the resolution of the transducers and high sampling rates at low accelerations for the continuous motion studies. Under very low acceleration conditions, using a standard sampling rate of 1000Hz, the amount of data collected was substantial and reached the limit of the data acquisition system. These limitations were essentially those associated with the equipment that was available in the laboratory. It is very difficult to quantify these limitations as was done in Figure 3.22. A discussion of the transducers resolution is presented in Appendix C.

3.6.3 Limitations of the Experimental Systems

There is also a second limitation imposed on regions within the green area of Figure 3.22. This limitation is a consequence of the dynamic frequency response of the servovalve and actuator. This limitation was determined experimentally by observing the velocity and acceleration values at which the output position waveform did not follow the desired input waveform.

As was illustrated in Figure 3.10, the hydraulic actuation systems were controlled by a proportional position controller. The output displacement followed the desired displacement very well at very low accelerations (0.001m/s^2) for both VCHAS1 and VCHAS2 (see Figure 3.23).

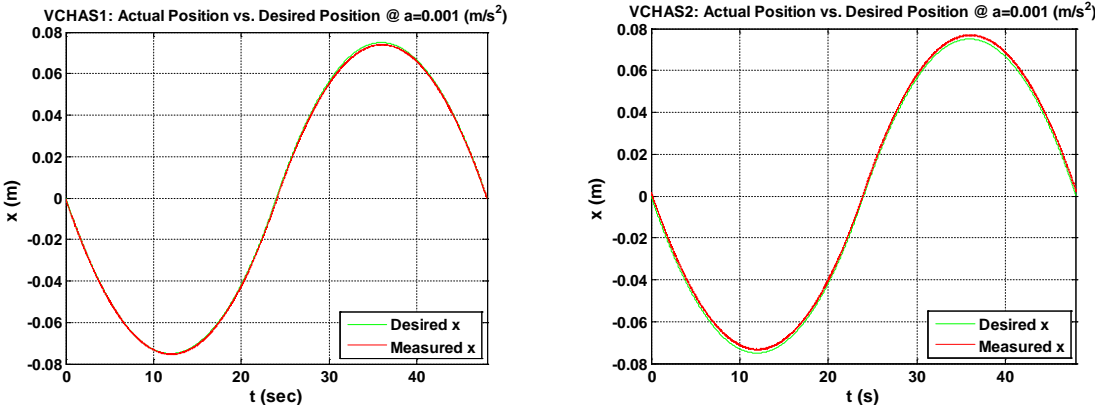


Figure 3.23 VCHAS1 & VCHAS2: the measured position follows the desired position very well when $a = 0.001 \text{ m/s}^2$

But as the acceleration increased, some distortion in the output position waveform was noticed. The upper limit on acceleration was established when the distortion became visually noticeable. The upper limits of acceleration of VCHAS1 and VCHAS2 were 5 m/s^2 and 2 m/s^2 respectively. This can be seen in Figure 3.24.

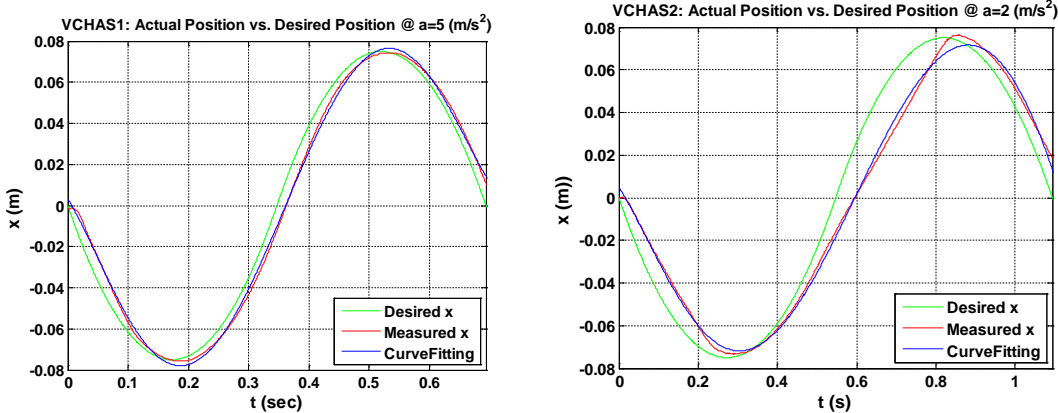


Figure 3.24 VCHAS1 & VCHAS2: the measured position follows the desired position but a small distortion is introduced, when $a = 5 \text{ m/s}^2$ for VCHAS1 and $a = 2 \text{ m/s}^2$ for VCHAS2. This established the upper limits for acceleration (a_{max})

It is interesting to note that even at this upper limit, the integrity of the parabolic curve fit was minimally compromised and hence further confidence in the curve fitting approach was established, which is limited by system bandwidth (frequency response limit) and system supply capacity (flow capacity). These upper limits on acceleration and velocity were established and are summarized in Table 3.3.

It was recognized that establishing these maximum limits was very subjective but in the author’s opinion, these limits were reasonable from a visual point of view.

Table 3.3 Maximum velocity (v_{max}) ranges and maximum acceleration (a_{max}) ranges of VCHAS1 and VCHAS2

	v_{max} (m/s)	$-v_{max}$ (m/s)	a_{max} (m/s ²)	$-a_{max}$ (m/s ²)
VCHAS1	0.8432	-0.8432	5	-5
VCHAS2	0.5	-0.5	2	-2

Minimum acceleration for non-steady state friction is established when stick-slip motion occurs or when the memory space of the data acquisition and data processing system reaches its limits (Table 3.4).

Table 3.4 Minimum velocity (v_{min}) ranges and minimum acceleration (a_{min}) ranges of VCHAS1 and VCHAS2

	v_{min} (m/s)	$-v_{min}$ (m/s)	a_{min} (m/s ²)	$-a_{min}$ (m/s ²)
VCHAS1	0.003	-0.003	0.001	-0.001
VCHAS2	0.001	-0.001	0.001	-0.001

Consider Figure 3.22. The limitations due to the actuator stroke and the limitations associated with the dynamic response of the valve and actuators are superimposed. It is quite evident that the limitations of VCHAS2 are more significant than for VCHAS1. The red rectangles (illustrated in Figures 3.25 and 3.26) represent the physical limits of VCHAS1 and VCHAS2 which imply that it is physically impossible to have any actuator motion condition outside of the “limit box” for this particular choice of positional input waveform.

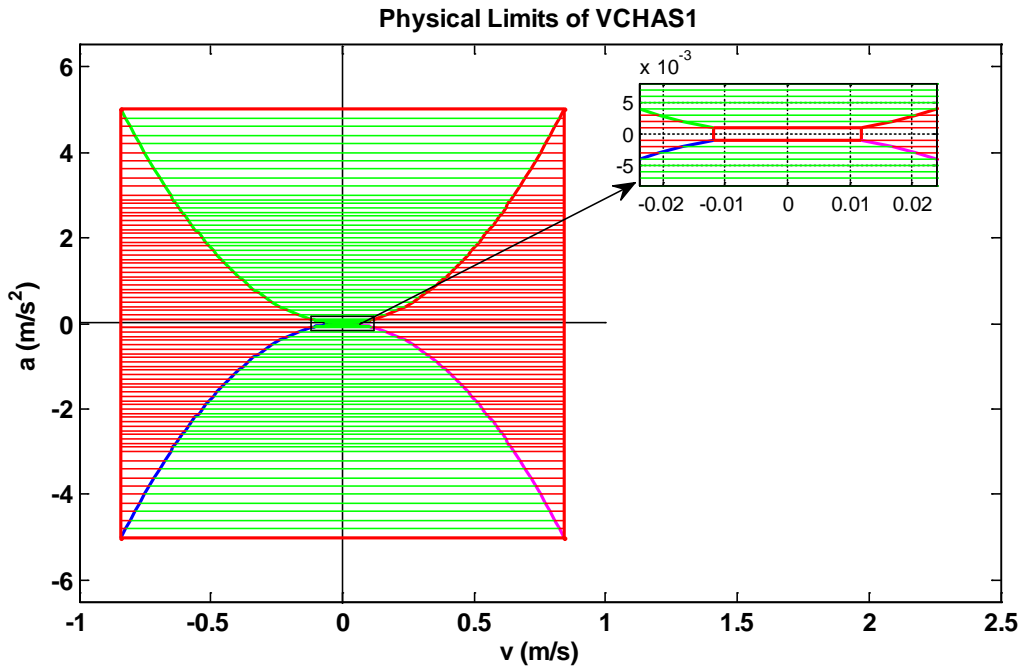


Figure 3.25 Physical limits (red boxes) of VCHAS1. Please note: the zoom view shows the minimum physical limit box

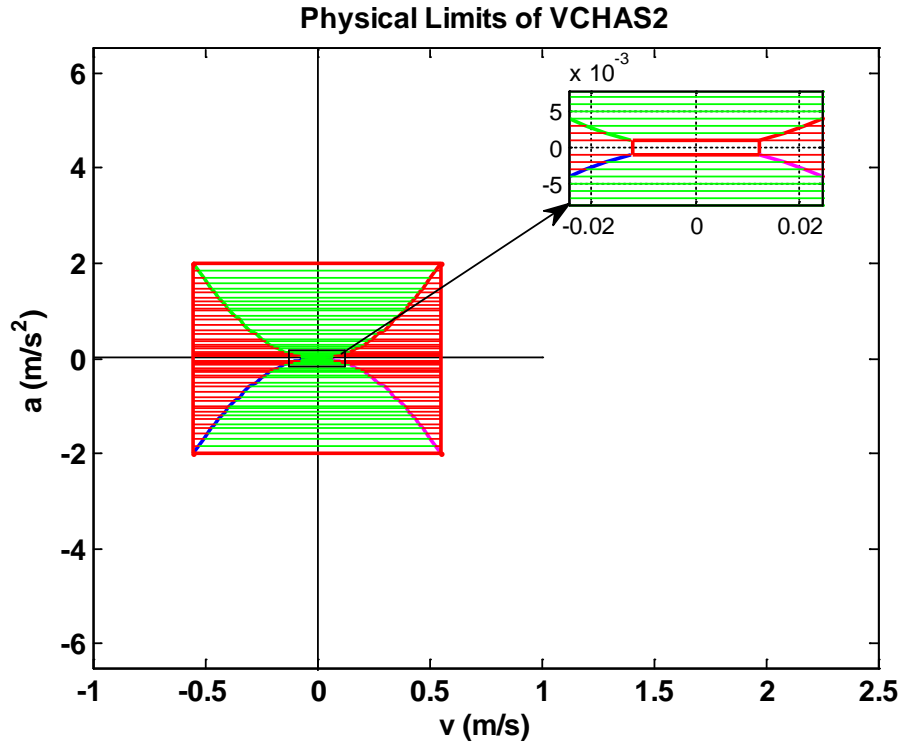


Figure 3.26 Physical limits (red boxes) of VCHAS2. Please note: the zoom view shows the minimum physical limit box

The physical limits of both VCHAS are bounded by the rectangle boxes (illustrated in Figures 3.25 and 3.26) which represent the maximum, minimum velocities and maximum, minimum accelerations respectively. These limits can be determined by the length of the stroke and the maximum acceleration that the hydraulic actuator can achieve. With reference to Figure 3.22, it is possible to extend the “green region” within the red rectangular box by using a different type of input signal such as a sinusoidal waveform. It is not possible to extend the size of the red box unless a system with a larger stroke, higher performance servovalve, and larger capacity pump is chosen. The details and the equations to determine this boundary are developed in Appendix H.

3.7 Experimental Results

This section will present some of the experimental results that were obtained for the steady state friction and non-steady state dynamic friction tests for VCHAS1 and VCHAS2. Many results were taken for repeatability, but only representative results are presented here.

As discussed, in Section 3.4, two VCHASs were used. For each system, the temperature was held constant at $29 \pm 1^\circ\text{C}$. The same hydraulic oil was used for both systems (NUTO Oil H68 Imperial Oil). Each test was repeated three times sequentially, and then repeated three times again on a different day.

3.7.1 Experimental Results of VCHAS1

3.7.1.1 Steady State Friction by Increasing Velocities Only

A typical plot of steady state dynamic friction versus velocity for VCHAS1 is shown in Figures 3.27 and 3.28. Note how the experimental data is plotted at discrete points and how well the data follows a Stribeck model. The Stribeck velocity was estimated from the experimental data to be approximately 0.06 m/s (location of lowest friction force on the curve). Since data was not available at very low velocities (the minimum velocity that could be measured was 0.003 m/s), an extrapolation procedure of the discrete data was completed (for modeling purposes) to estimate the breakaway friction (which was 202.9 N and -288.6 N as seen Figure 3.28). Further it is apparent that the friction curves of VCHAS1 are NOT symmetrical about zero velocity.

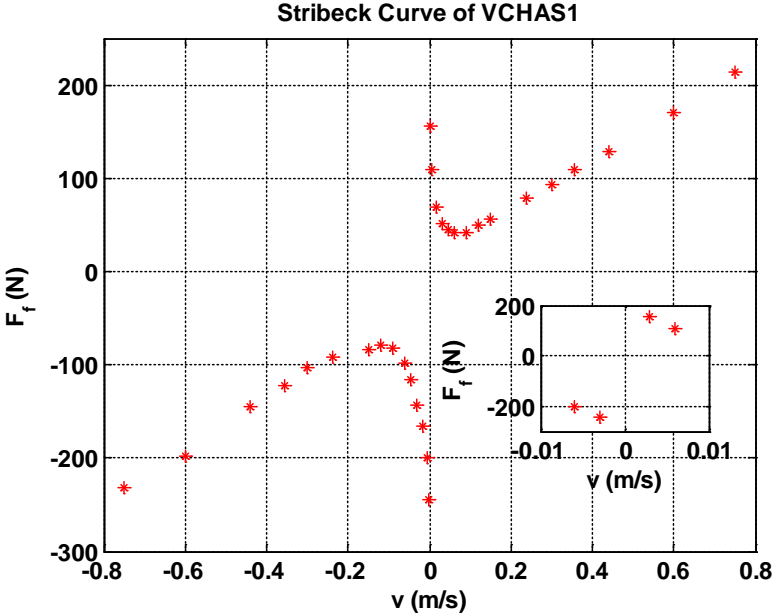


Figure 3.27 Stribeck curve of VCHAS1 – a list of discrete calculated friction points (steady state dynamic friction in both directions). There is no data near the velocity zero from -0.003 m/s to 0.003 m/s (see the zoom view for details)

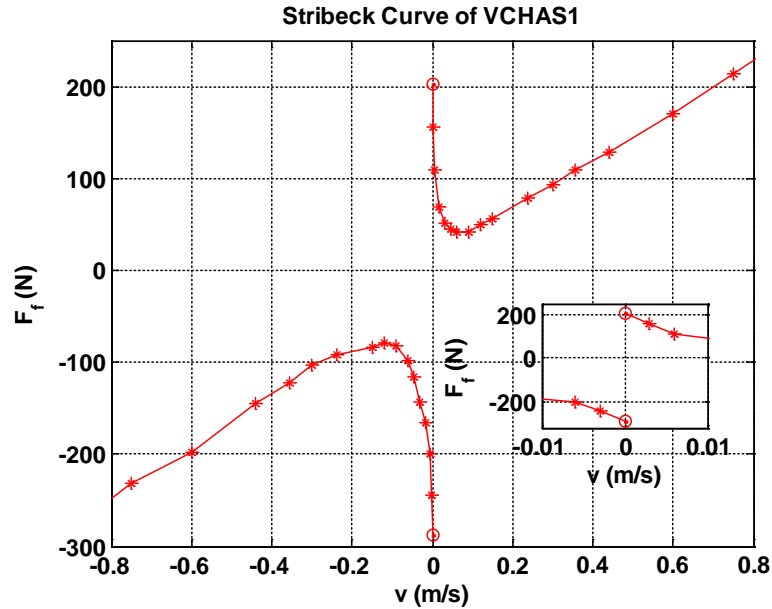


Figure 3.28 Curve fitting of Stribeck curve of VCHAS1 (steady state dynamic friction in both directions). An extrapolation technique is needed to estimate the break-away frictions. The breakaway friction of VCHAS1 in the forward direction is around 202.9 N and the breakaway friction of VCHAS1 in the reverse direction is around 288.6 N (See zoom view for details)

3.7.1.2 Steady State Friction by Increasing and Decreasing Velocities

It is known that the Stribeck model is obtained from steady state conditions, and as discussed in the literature review, should not demonstrate any hysteresis. To verify this assumption, a special experiment was carried out on the VCHAS1 system by systematically increasing and then decreasing discrete velocity points to obtain two steady state dynamic friction curves. The results were superimposed on the same plot and are shown in Figure 3.29 for both velocity directions. The red marker trace represents the case where the constant velocity increases gradually from low to high; the blue marker trace represents the case where the constant velocity decreases gradually from high to low. It is quite evident that the Stribeck model for increasing and decreasing velocities essentially overlap and display no hysteresis. Differences between the increasing and decreasing curves are minor and are associated with experimental measurement error. It was concluded that the assumption that the discrete approach for measuring friction did not, indeed, indicate hysteresis.

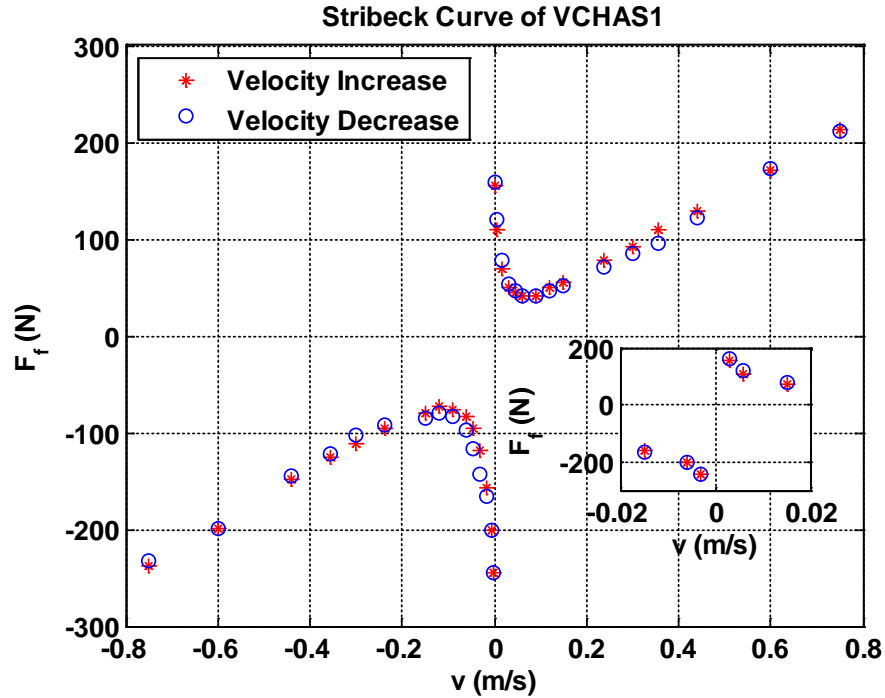


Figure 3.29 Superimposed steady state friction of VCHAS1 of increasing and decreasing velocities (see zoom view for details)

3.7.1.3 Non-Steady State Friction

Typical experimental results for the non-steady state friction using the parabolic position waveform for VCHAS1 are shown in Figure 3.30. The measurements are continuous with acceleration being the family parameter and held constant. Figure 3.30 shows the results of friction plotted for each quadrant for three representative accelerations (low, medium and high). It is quite evident that the non-steady state friction does vary substantially with acceleration. What is very evident is that at low accelerations (for example, 0.2 m/s^2), the curve shape approaches the Stribeck model as predicted, but is very difficult to observe due to the limited velocity range at low accelerations. Hysteresis is detected in all quadrants and for all accelerations (even at low accelerations where the curve converges to the Stribeck model in Quadrants 1 and 3).

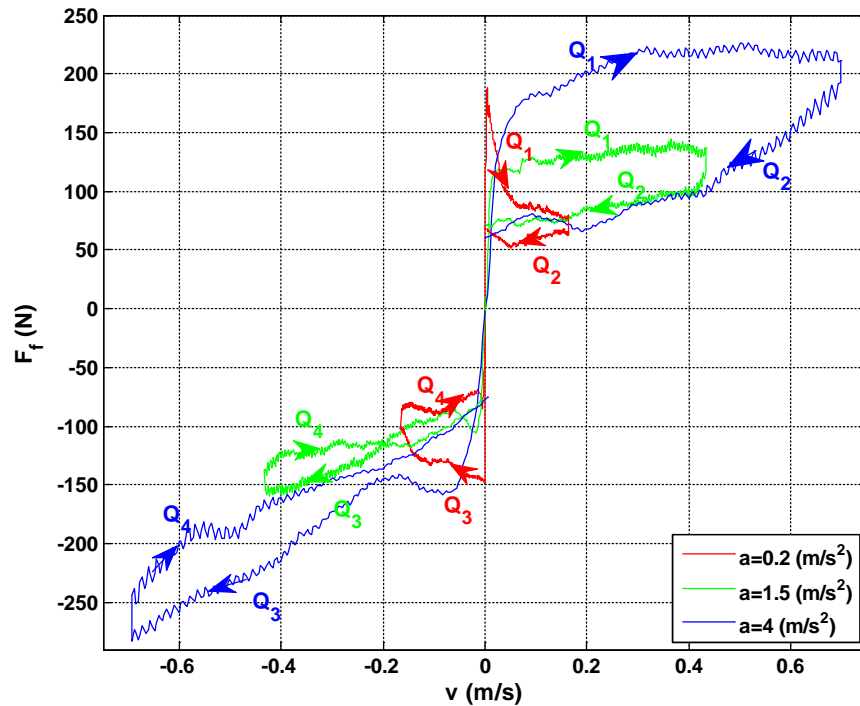


Figure 3.30 Acceleration dependent non-steady state dynamic friction curves of VCHAS1 – four quadrants at three different accelerations

3.7.2 Experimental Results of VCHAS2

3.7.2.1 Steady State Friction

The experimental procedures used for VCHAS2 were the same as for VCHAS1. The discrete results for SSF are shown in Figures 3.31 and 3.32 and follow similar trends to that of VCHAS1. The Stribeck velocity of VCHAS2 was estimated from the experimental data to be approximately 0.08 m/s (location of lowest friction force on the curve). Since data was not available at very low velocities (the minimum velocity that could be measured was 0.001 m/s), an extrapolation procedure of the discrete data was completed (for modeling purposes) to estimate the breakaway friction (which was 150 N and -150 N as seen Figure 3.32). Further it is apparent that the friction curves of VCHAS2 are symmetrical about zero velocity.

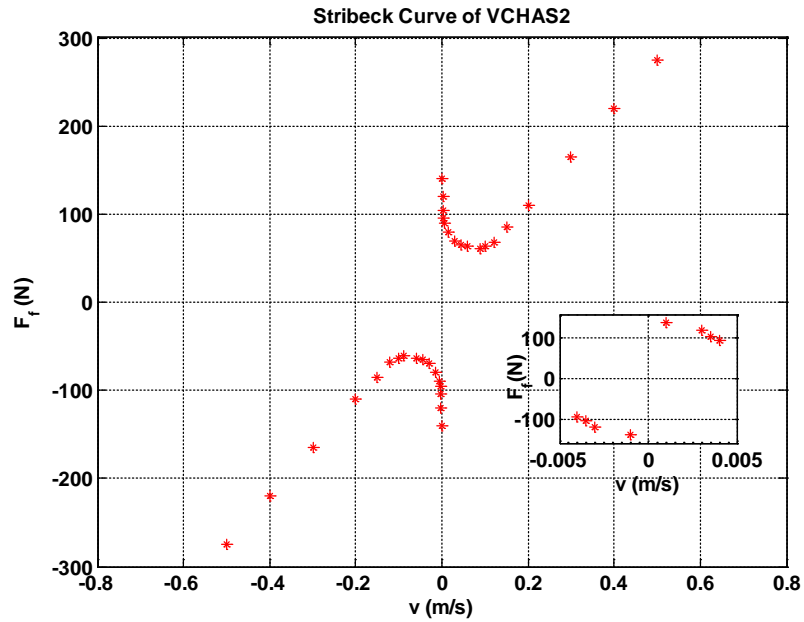


Figure 3.31 Stribeck curve of VCHAS2 – a list of discrete measured friction points (steady state dynamic friction in both directions). There is no data near the velocity zero from -0.001 m/s to 0.001 m/s (see the zoomed in view for details)

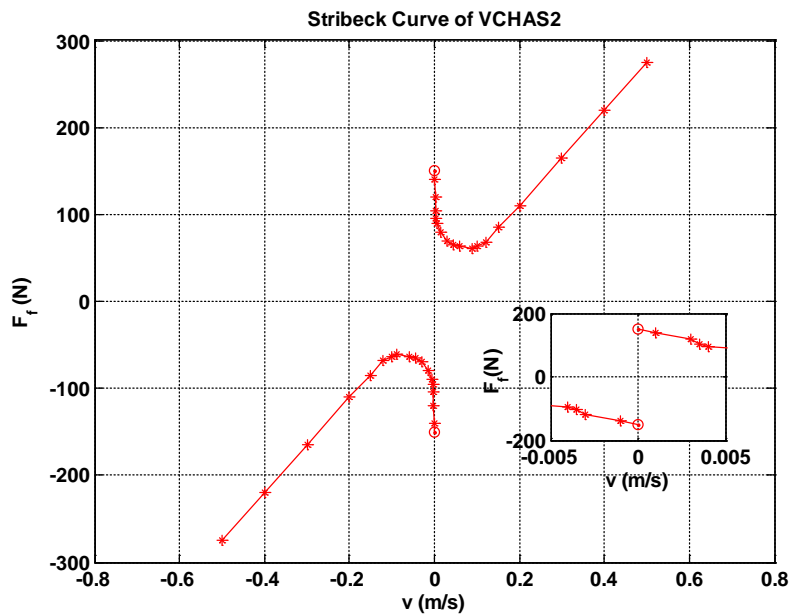


Figure 3.32 Curve fitting of Stribeck curve of VCHAS2 (steady state dynamic friction in both directions). An extrapolation technique is needed to estimate the break-away frictions. The breakaway friction of VCHAS2 is around 150 N (See the zoomed in view for details)

3.7.2.2 Non-Steady State Friction

Typical experimental results for the non-steady state friction using the parabolic position waveform for VCHAS2 for three representative accelerations (low, medium and high) are shown in Figures 3.33. The measurements are continuous with acceleration, the family parameter, being held constant. It is quite evident that the non-steady state friction does vary substantially with acceleration. As with VCHAS1, at very low accelerations (0.2 m/s^2), the curve shape approaches the Stribeck model as predicted. The hysteresis is detected in all quadrants and for all accelerations (even at low accelerations where the curve converges to the Stribeck model in Quadrants 1 and 3). It is interesting to note that the data was not as “well behaved” as for VCHAS1. However, the results were very repeatable.

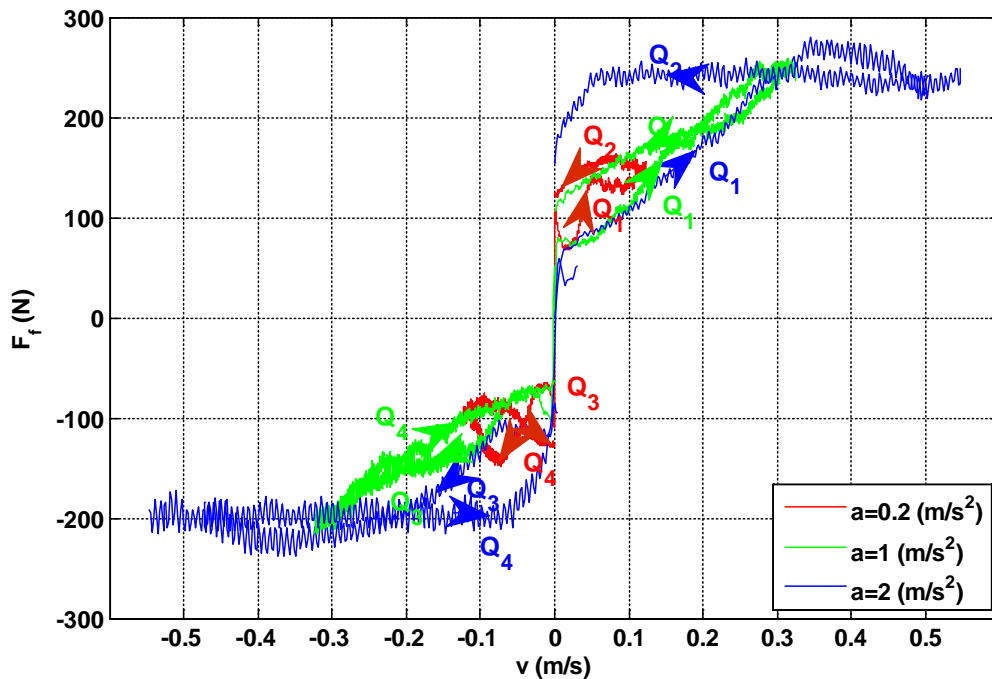


Figure 3.33 Acceleration dependent non-steady state dynamic friction curves of VCHAS2 – four quadrants at three different accelerations

3.7.3 Discussion

A review of Figures 3.30 and 3.33 shows that, as was experienced in the EHA system in Quadrant 1 (Chapter 1), the lubricated friction forces of VCHAS1 and VCHAS2 are strongly dependent on acceleration. These dependencies appear in all quadrants. Thus it is believed that the hypothesis stated in Chapter 1 is consistent with the experimental evidence shown by three

different actuators (EHA, VCHAS1 and VCHAS2). Further, it can also be observed that the traditional Stribeck form (steady state dynamic friction) does change with increasing acceleration to the point that the standard breakaway friction almost disappears. The results for VCHAS1 and VCHAS2 show hysteresis for the non-steady state friction, but not for the discrete steady state friction plots as predicted.

As was observed for both VCHAS1 and VCHAS2, at low accelerations, the non-steady state friction curves approaches the Stribeck model. The results for VCHAS1 are expanded upon in Figure 3.34 where the non-steady state friction and steady state friction (Stribeck model) are superimposed. This excellent correlation will be used in Chapter 5 to provide additional information for the so developed semi-empirical model.

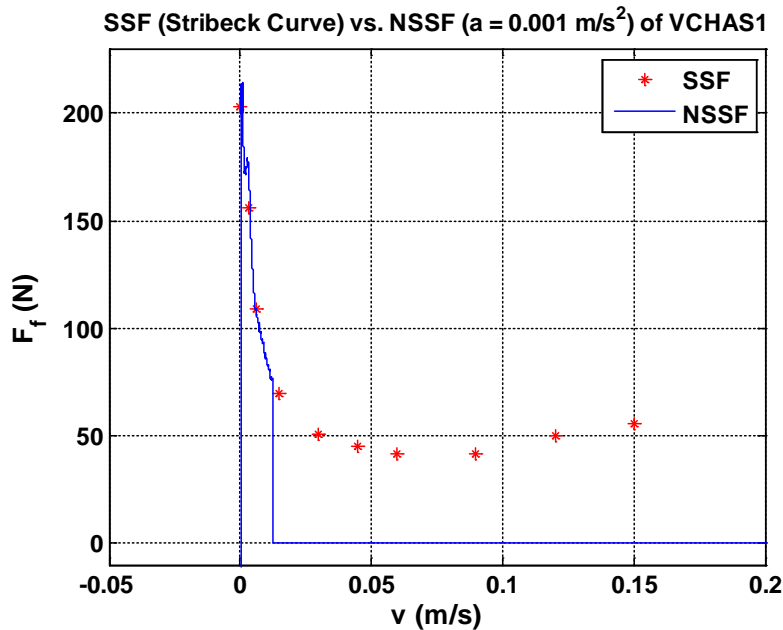


Figure 3.34 Stribeck curve (in red markers) and non-steady state friction curve at acceleration $a = 0.001 \text{ m/s}^2$ (in blue line) of VCHAS1 as an example. NSSF refers to non-steady state friction. SSF refers to steady state friction which essentially is the Stribeck curve

3.7.4 Repeatability and Stability of Experimental Results

Repeatability of the results was considered to be very important for this study. Each test was repeated at separate times at approximately the same operating conditions. In addition, it was noticed that in any test, it took some time (many cycles) to stabilize the results. Therefore repeatability was concerned with both the ability to obtain repeatable results from test to test and to obtain the results only when the tests had stabilized.

To demonstrate the repeatability of ordinate data points taken at a specified variable on the abscissa, traditionally, the difference between the maximum and minimum values is used as the indicator. Since the data represented in these figures are dynamic, representing repeatability becomes more of a challenge if this traditional method is used. The approach used here was simply to superimpose the traces on each other which create the resulting “envelope” (which essentially covers the data points) that give a visual representation of the repeatability. This is demonstrated in Figures 3.35 – 3.37. It is evident that the trends of each trace follow the same pattern and as such, the repeatability was considered acceptable.

3.7.4.1 Repeatability of VCHAS1

To show the repeatability of the VCHAS1, three representative results were selected: a low acceleration (0.001 m/s^2), a medium acceleration (2.5 m/s^2), and a high acceleration conditions (5 m/s^2). These results were obtained on three different times.

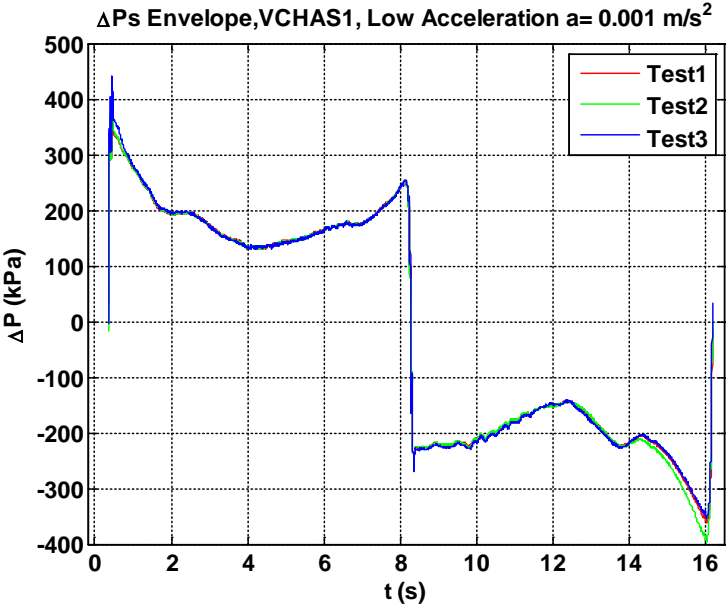


Figure 3.35 Repeatability of VCHAS1 – an envelope of three measured differential pressures (ΔP) acceleration conditions. Although small deviations are noted, the trends are maintained

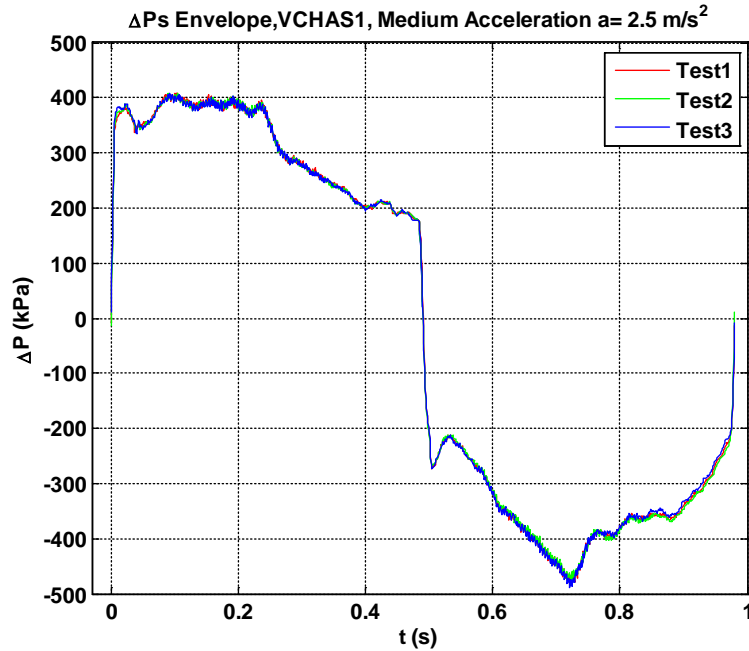


Figure 3.36 Repeatability of VCHAS1 – an envelope of three measured differential pressure (ΔP) at medium acceleration conditions. Although small deviations are noted, the trends are maintained

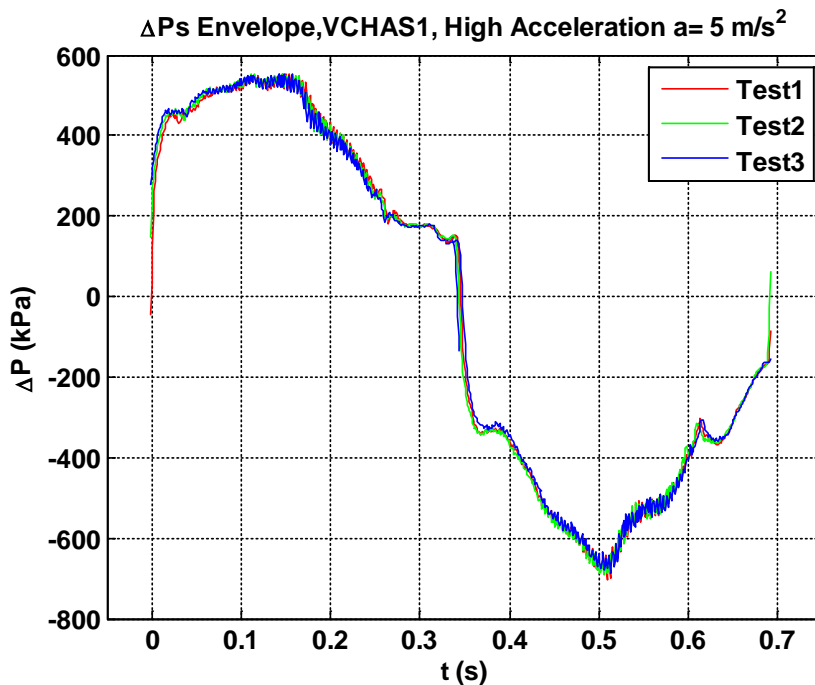


Figure 3.37 Repeatability of VCHAS1 – an envelope of three measured differential pressures (ΔP) high acceleration conditions. Although small deviations are noted, the trends are maintained

These results were repeatable under the same operating conditions and hence confidence in the procedure and experimental results was obtained. It was noted that it took some time for the results to stabilize as the test proceeded. It was desirable to collect the experimental data of a complete cycle when the waveforms were fully stabilized. The experimental data under some acceleration conditions stabilized quickly (one or two cycles, usually at lower accelerations), whereas higher accelerations took up to 15 - 20 cycles. In this study, the middle period of the last 3 complete stable periods was chosen as the experimental data. To illustrate this, consider Figure 3.38. At an acceleration $a = 1.5 \text{ m/s}^2$, the actuator was cycled 20 times and was stable.

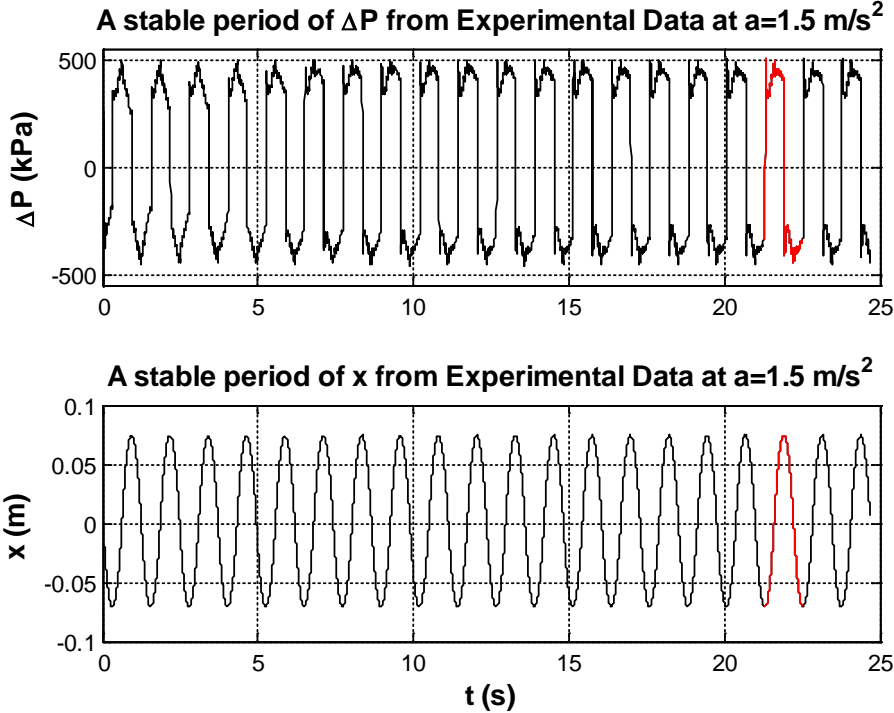


Figure 3.38 An example of measured differential pressure (ΔP) and displacement (x) at acceleration $a = 1.5 \text{ m/s}^2$. Data was collected for the lookup table (LUT) modelling at the 18th cycle (in red)

3.7.4.2 Repeatability of VCHAS2

To show the repeatability of the VCHAS2, three representative results were selected: a low acceleration (0.03 m/s^2), a medium acceleration (0.6 m/s^2) and a high acceleration condition (1.2 m/s^2). The results also stabilized in the same fashion as was observed for VCHAS1 (from Figures 3.39 to 3.41). These results were obtained on three different times.

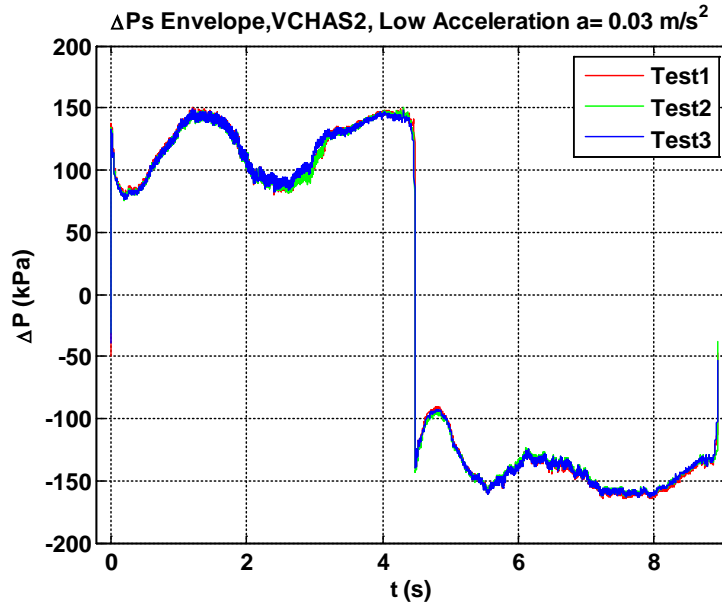


Figure 3.39 Repeatability of VCHAS2 – an envelope of three measured differential pressures (ΔP) at low acceleration conditions. Although small deviations are noted, the trends are maintained

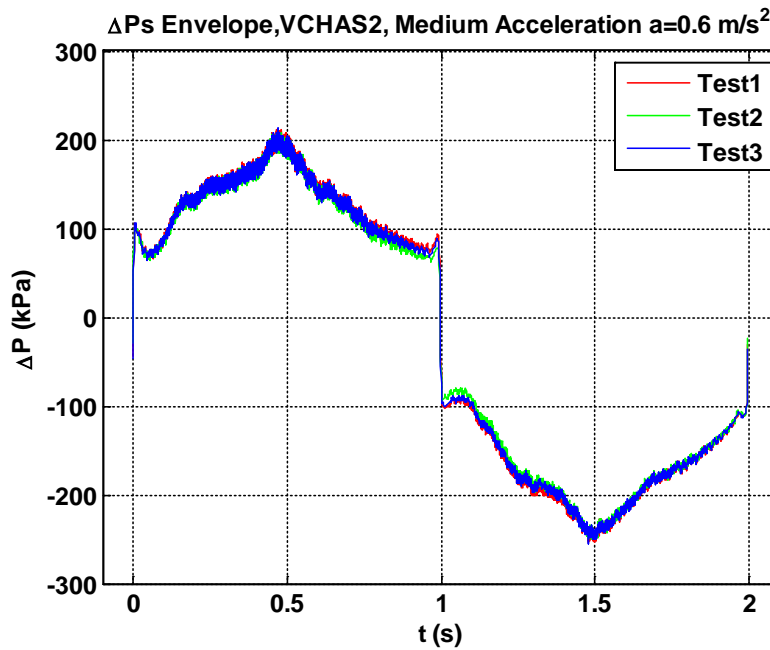


Figure 3.40 Repeatability of VCHAS2 – an envelope of three measured differential pressures (ΔP) at medium acceleration conditions. Although small deviations are noted, the trends are maintained

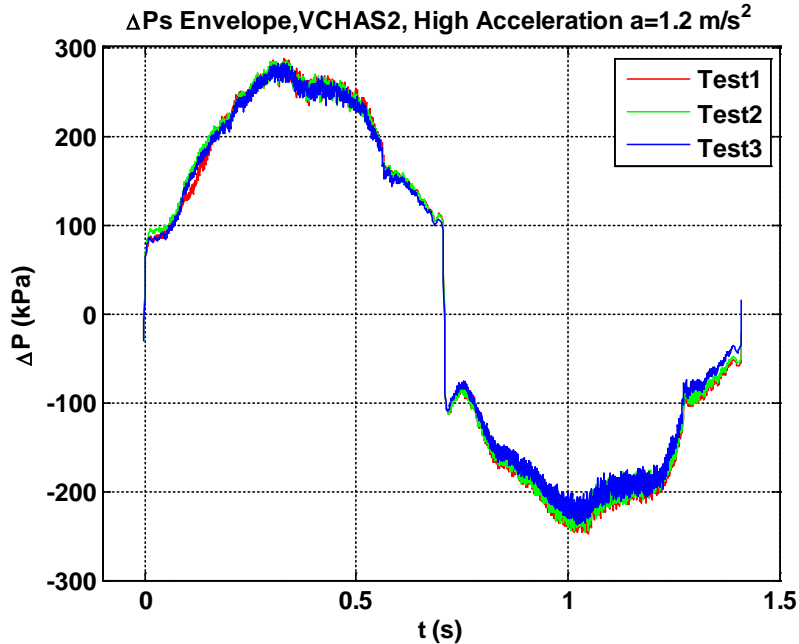


Figure 3.41 Repeatability of VCHAS2 – an envelope of three measured differential pressures (ΔP) at high acceleration conditions. Although small deviations are noted, the trends are maintained

3.7.5 Pressure Effect Consideration

Lubricated friction is known to be a function of many variables such as velocity, system pressure (absolute pressure, differential pressure), temperature, type of seal, condition of seals, viscosity etc. It was hypothesized in Chapter 1 that the lubricated friction was also a function of linear acceleration. Temperature could be controlled experimentally so this factor was not an issue. However, friction dependency on pressure posed a specific challenge since pressure was a measure of friction. This challenge was overcome by choosing the experimental systems to have small pressure differentials so as to minimize deformation of the seals due to this parameter.

To verify this, the mass on VCHAS1 was doubled in a series of constant acceleration tests and the results are shown in Figures 3.42 to 3.45. In Figures 3.42 and 3.44, the pressure differential traces are shown. When the mass inertial forces are subtracted out (see Equation (3.4)) the non-steady state friction forces are superimposed as in Figures 3.43 and 3.45. These results are shown in a format to be discussed in the next Chapter, and indicate that the effect of doubling the mass (and hence changing the pressure differential) was minimal on the results (note that there was some deviation at higher velocities, but this was considered to be within experimental repeatability of the test). Hence it was believed that the experimental approach used here could

be used to isolate the effect of acceleration on friction and that small variations of pressure on the deformation of the seals was negligible.

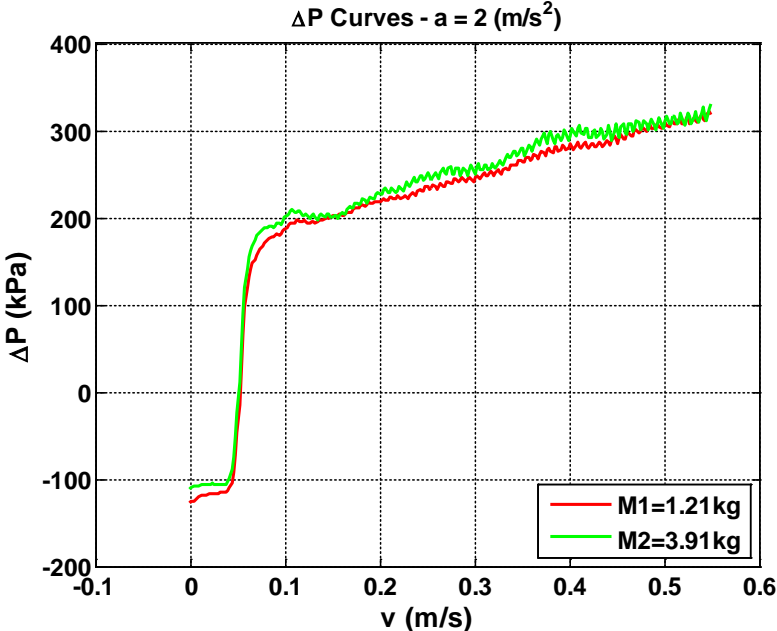


Figure 3.42 Measured pressure drop across the seals versus velocity at a constant acceleration of 2 m/s² (two masses) for VCHAS1

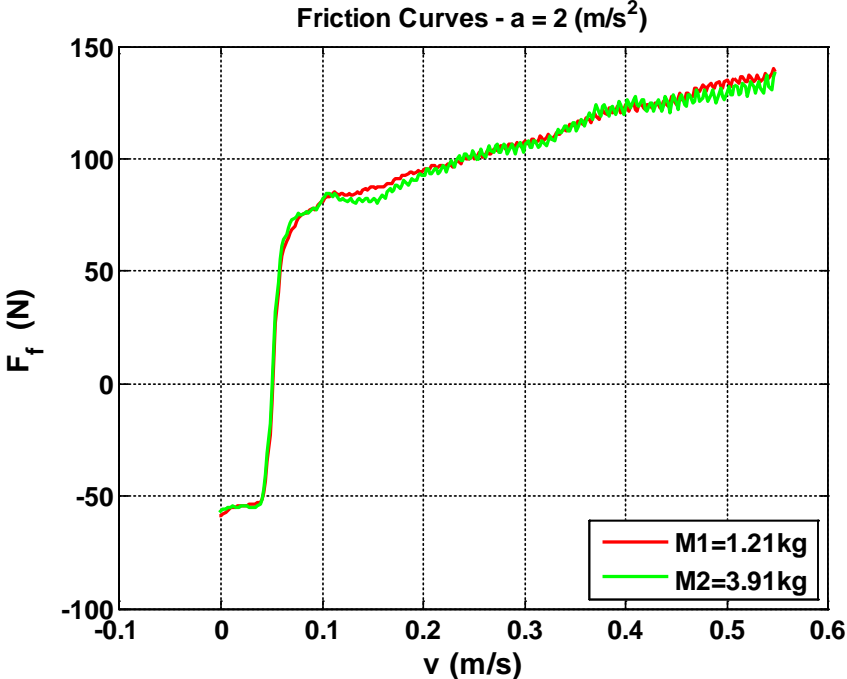


Figure 3.43 Equivalent friction versus velocity at a constant acceleration of 2 m/s² (two masses) for VCHAS1

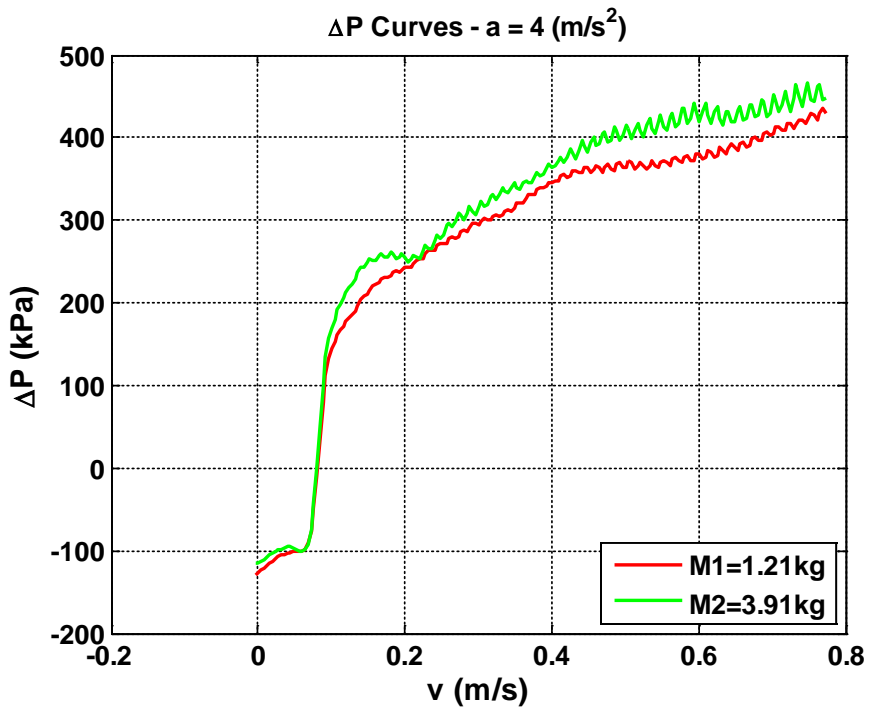


Figure 3.44 Measured pressure drop across the seals versus velocity at a constant acceleration of 4 m/s² (two masses) for VCHAS1

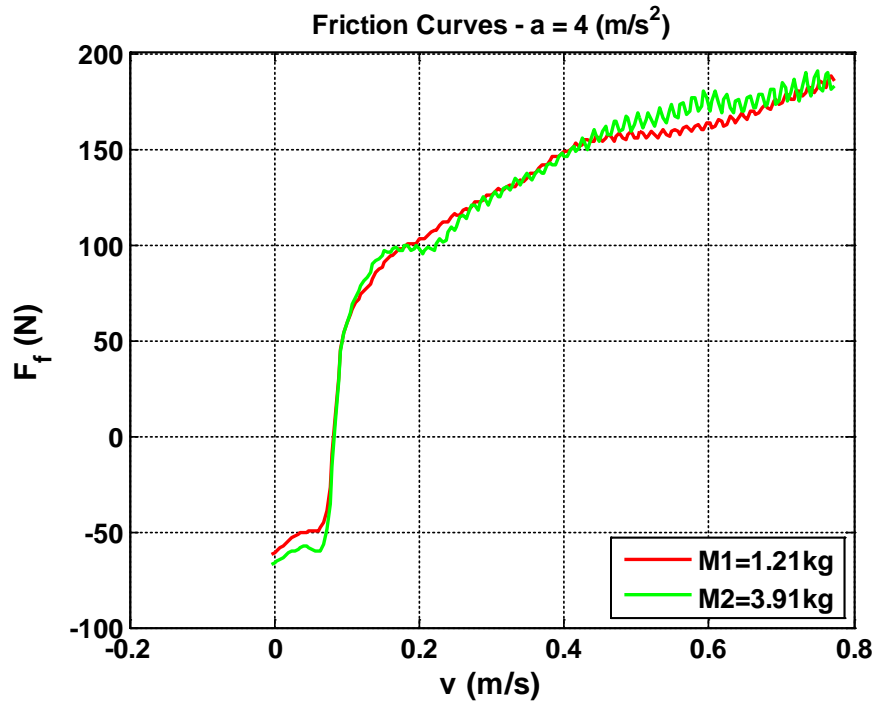


Figure 3.45 Equivalent friction versus velocity at a constant acceleration of 4 m/s² (two masses) for VCHAS1

3.8 Summary

In this Chapter, the experimental set up to measure two important parameters for the hydraulic actuation system, namely velocity and acceleration (via piston displacement) and friction force (via differential pressure) was described. The instrumentation and data acquisition system used in the measurements were briefly introduced. Two important concepts of friction - steady state dynamic friction and non-steady state dynamic friction were introduced and explained in detail. Four quadrants ($Q1$, $Q2$, $Q3$ and $Q4$) and other relevant concepts were also defined. A novel approach to continuously collect data for non-steady state friction as a function of velocity and acceleration was introduced. This approach involved the use of a periodic parabolic waveform for position control. The limitations of the approach were also defined. The “two masses experiments” were carried out to make sure the pressure effect on the lubricated friction measurement was minimal.

The experimental results (with good repeatability) indicated that non-steady state friction is a function of velocity (expected) as well as acceleration (hypothesized). In addition, strong hysteresis was experienced as the data moved from quadrant to quadrant. In the next Chapter, friction modelling will be developed from the experimental results obtained in this Chapter.

CHAPTER 4: DEVELOPMENT OF A SEMI-EMPIRICAL FRICTION MODEL WITH ACCELERATION EFFECT

4.1 Introduction

In Chapter 3, the experimental data was collected for VCHAS1 and VCHAS2 under various acceleration conditions in all quadrants. The results from the experimental investigations on two different VCHAS showed that the lubricated friction forces in the actuators are related to velocity and acceleration. This Chapter will present a friction model developed from the experimental data using a lookup table approach.

In the traditional Stribeck model of lubricated friction, a plot of friction versus velocity can readily be translated into models for practical use in simulations. In this Chapter, semi-empirical 3D friction models for predicting the non-steady state friction of VCHAS1 and VCHAS2 are presented. These models are 2D lookup table (2D LUT) based [102]. The development of these lookup table models is quite challenging due to the fact that the lookup table is based on experimental data which was obtained at different velocities (that are a function of acceleration). This created difficulties for the 3D visualization of the semi-empirical 2D LUT friction models of both VCHAS. The algorithm which involved interpolation in the formulation of the lookup table is also considered.

It should be noted that in this Chapter, the emphasis is verification of the lookup table using inputs which were used to create the original lookup table. In Chapter 5, model validation of the lookup table using inputs that were not used to create the original lookup table is considered. It should also be noted that since pressure differential across the actuator is directly related to friction, and since pressure differential was the parameter measured, all subsequent plots in this Chapter use pressure differential as the output variable rather than friction. The pressure differential is used in the model validation in Chapter 5 for the same reason. Friction will only be used in the model implementation in the model simulation process. In Appendix I, the additional 3D visualizations and alternative views of 2D LUT of Quadrants 2, 3 and 4 are provided.

4.2 Model Development

As mentioned in Section 4.1, it was an objective to create a lookup table of pressure differential across the actuator as a function of velocity and acceleration. When a second parameter such as acceleration is introduced, translation of the data to a model becomes far more

complex. Further when combined with hysteresis, (which is inherent in the lubricated friction plots), the challenges become quite substantial in establishing a model which could readily and practically be used for design and simulation purposes. There are approaches other than lookup tables which could be used to overcome this particular challenge. One method is to train a Neural Network to do the interpolation. Neural networks are very powerful in doing such tasks especially if the data is nonlinear [103-105]. However, the issue of “data spread” at higher accelerations could pose a problem as the data is “scarce” in some regions. Further, if the data “crosses over” due to experimental error, the neural network can become “confused” and produce erroneous results. Lastly, the computational cost of employing different software to process the neural network based lookup table could be expensive. This approach was therefore not pursued, but it is a possibility to be explored in the future.

Another approach would be to fit a group of nonlinear curves or a nonlinear surface to the data and then use the analytical model for implementation purposes [106]. In fact this was the first approach that the author pursued, but because of the severe nonlinearity of lubricated friction of the hydraulic actuation system over 2 critical parameters (velocity and acceleration), a suitable set of reliable equations could not be found. The author acknowledges the many hours of assistance from Professor Fangxiang Wu from the Mechanical Engineering Department at the University of Saskatchewan in this attempt to derive suitable fitting equations by a parameter estimation technique. This approach was abandoned when it became evident that an accurate set of fitting equations could not be established and that a lookup table as proposed in this work might be a more user friendly approach. But the approach of curve or surface fitting still has some potential for future research.

It is desirable to model the nonlinear lubricated friction of both VCHAS in a form which will facilitate verification and validation (verification in the sense that the lookup table is correct and validation in the sense that the lookup table can be used in a simulation format). In this Chapter, the process of developing a three dimensional (3D) semi-empirical model is introduced. This model is defined as semi-empirical because it is based on experimental data as well as data manipulation using interpolation techniques. This model appears as a 2D lookup table (2D LUT, which has 2 inputs, and 1 output) which can now be readily used in subsequent model validation studies and simulation implementations in Chapter 5.

4.2.1 Lookup Table Model Approach

The objective of using a lookup table for this application is to input any value of velocity and acceleration to predict a value of friction as shown in Figure 4.1. In this Chapter, since friction is calculated directly from the differential pressure ΔP across the actuator, the output of the differential pressure lookup table is ΔP (here within now referred to as ΔP LUT). The theory is that if the ΔP LUT is verified and validated, then the friction lookup table is also verified and validated. This equivalence is shown in Figure 4.2.

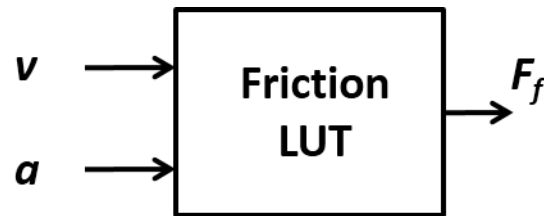


Figure 4.1 Friction lookup table (LUT) with two inputs (v, a) and its output friction (F_f)

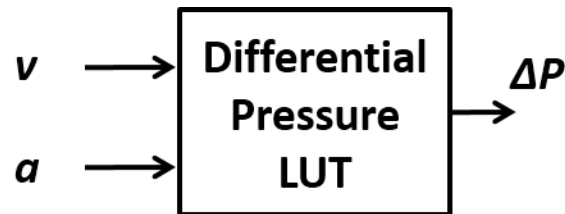


Figure 4.2 Differential pressure ΔP LUT with two inputs (v, a) and its output differential pressure (ΔP)

A lookup table consists of discrete points. Therefore, there will be differential pressure (ΔP) (friction) values of the input (v, a) that are not represented in the table. The challenge then is to create a lookup table which will allow interpolation between data points to provide an approximation of the differential pressure (ΔP) or friction value (F_f).

Lookup tables must meet strict conditions. Nakla [102] states, “The lookup table (LUT) is basically a normalized data bank of experimental data collected from different sources. The LUT approach for predicting two-phase heat transfer and fluid flow is consider one of the most accurate tools for prediction. The main benefits of using the LUT approach are summarized as follows:

- The LUT covers wide ranges of applications that supersede all the combined ranges of the individual prediction methods.
- The accuracy of the LUT is much better than other prediction methods for the ranges of conditions where experimental data exist. In other regions where there is a lack of experimental data, the prediction of the LUT is the same as other prediction methods.
- The use of LUT is simple and does not need extensive programming.
- The LUT offers correct parametric trends.
- The prediction accuracy of the LUT can be improved once new data is available.”

The issue now becomes one of how to develop this 2D LUT. Using Nakla’s approach, the requirements of a 2D LUT for this study are as follows.

1. The lookup table requires a common velocity (v) range for each set of data.
2. Two independent input variables must be used; in this study, velocity (v) and acceleration (a) (hence the name 2D).
3. The data has to be discrete and must fit into selected discrete intervals; in this study, the intervals increase along the velocity and acceleration axis as illustrated in Figure 4.3.
4. Each variable has to be monotonically increasing or decreasing.

An example of a 2D LUT that demonstrates these requirements is illustrated in Figure 4.3. The center row (abscissa) of the table contains the values of v and the center columns (ordinate) contains the values of a . Figure 4.4 indicates a 2D LUT, but from a 3D perspective. Each (v, a) point has a corresponding differential pressure (or friction) value.

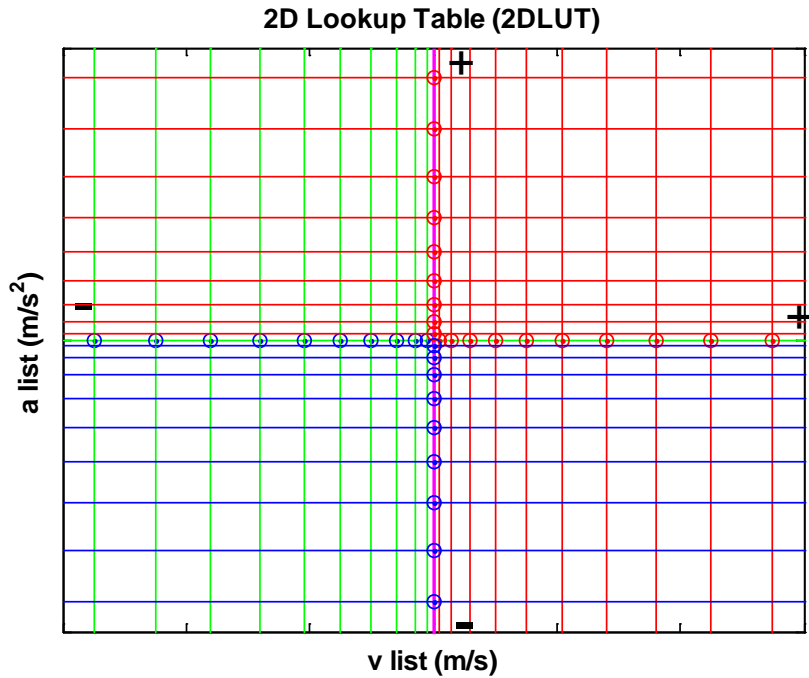


Figure 4.3 A 2D LUT layout which illustrates the requirements for such a table

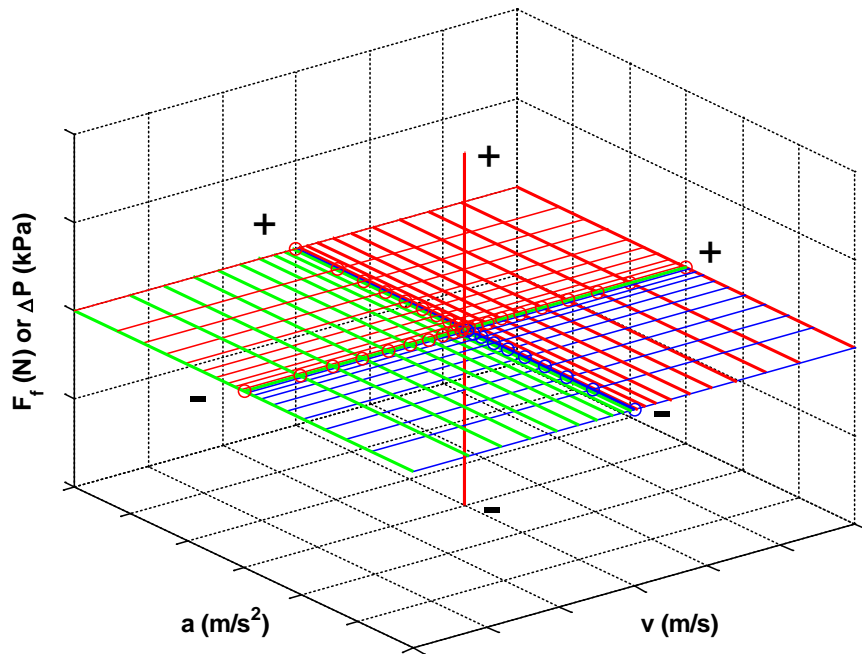


Figure 4.4 2D LUT layout in a 3D presentation

In Chapter 3, various 2D differential pressure (ΔP) (friction) curves which use a range of constant accelerations as the family parameter were generated by plotting the measured lubricated

friction versus measured velocity. However, in real applications, machines can operate under non-steady state conditions (i.e., very rapid changes in velocity and in acceleration) where the velocity and/or acceleration of the actuators or motors are not constant. An example of this is where the actuator position or velocity follows some prescribed continuous pattern (sinusoidal for example) in which velocity and acceleration change with time. Therefore, it is critical to create a “universal” friction model which can realistically be used in a computer simulation environment.

An additional issue arises out of the fact that the data so obtained is not necessarily collected at common velocity intervals or “set points”. A lookup table requires having data fall on a common set of points such as velocity and acceleration (to be expanded upon in the next Section). This means that interpolation of the data between velocity and acceleration set points must be made if the model is to be used in a practical manner. This process involves first pre-processing the raw data (using interpolation techniques) and then using interpolation again in the implementation stage. This Chapter will deal with the first pre-processing stage with the implementation stage deferred until Chapter 5.

4.2.2 Analysis of Experimental Data

Before introducing the 2D LUT “building” process, it is important to understand what challenges exist in transferring the raw data into a lookup table format.

In order to facilitate the discussion, only Quadrant 1 is considered, but the discussion applies to all quadrants. Three acceleration parameters (a_1 , a_2 and a_3) are used to represent various multiple acceleration conditions; a_1 represents a low acceleration, a_2 a median acceleration, and a_3 a high acceleration (that is, $a_1 \ll a_2 \ll a_3$). It must be pointed out that in the following figures, no units or actual values (data) are being used. These generic shapes are simply used to facilitate explanations.

Consider Figure 4.5 which represents the piston motion from one end to the middle of the cylinder (Quadrant 1). For a constant acceleration output waveform of the actuator, the corresponding velocity of the actuator would appear as in Figure 4.5.

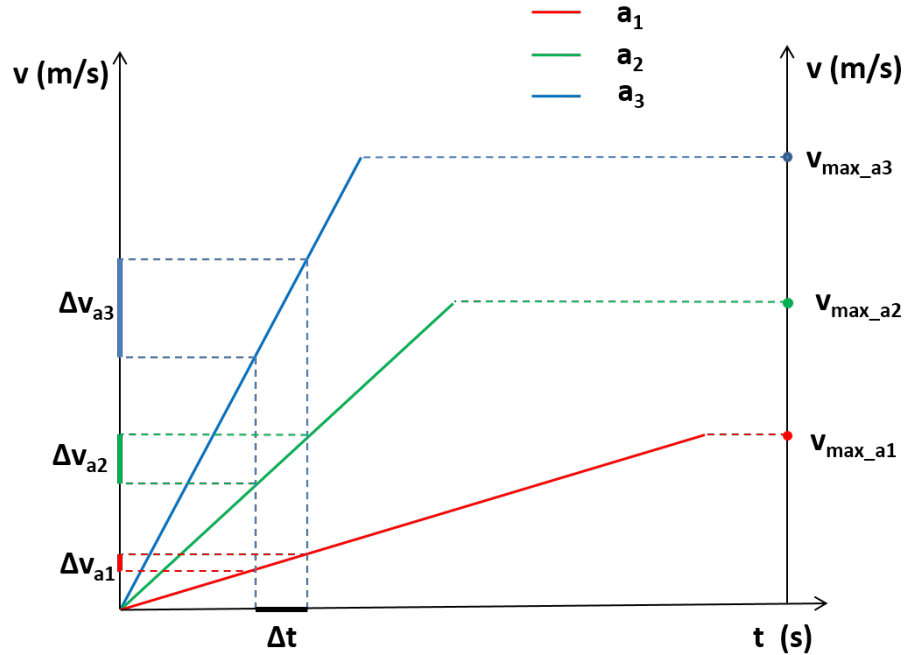


Figure 4.5 Representation of actuator velocities at three constant accelerations (a_1, a_2 and a_3). a_1 represents low acceleration, a_2 represents median acceleration and a_3 represents high acceleration ($a_1 \ll a_2 \ll a_3$). For the same sampling interval (Δt), the change in velocity over the interval is not the same ($\Delta v_{a1} \ll \Delta v_{a2} \ll \Delta v_{a3}$). v_{\max_a} is a function of acceleration (a) ($v_{\max_a1}, v_{\max_a2}, v_{\max_a3}$)

From Figure 4.5, it is quite apparent that the maximum velocity (v_{\max_a}) the piston can achieve at the cylinder midpoint for any given acceleration is quite different. For the same sampling time interval (say Δt) the change in the velocity Δv_a at various accelerations is not the same. A question of “what is the consequence of this?” arises. As mentioned in Chapter 3 (Equations (3.5) and (3.6)), the sampling time (Δt) for all experiments was the same (e.g. $\Delta t = 0.001$ s). Therefore, in the time domain, the intervals are constant, but in the velocity domain, the intervals vary with acceleration. It is also known that the velocity interval has a linear relationship with acceleration; that is, as acceleration increases, the velocity interval (and the maximum velocity) increases.

Consider Figure 4.6. The measured differential pressure (ΔP_1) with a low acceleration a_1 ends at a velocity v_{\max_a1} , ΔP_2 with a median acceleration a_2 ends at a larger velocity v_{\max_a2} , and (ΔP_3) with a high acceleration a_3 ends at the largest velocity v_{\max_a3} .

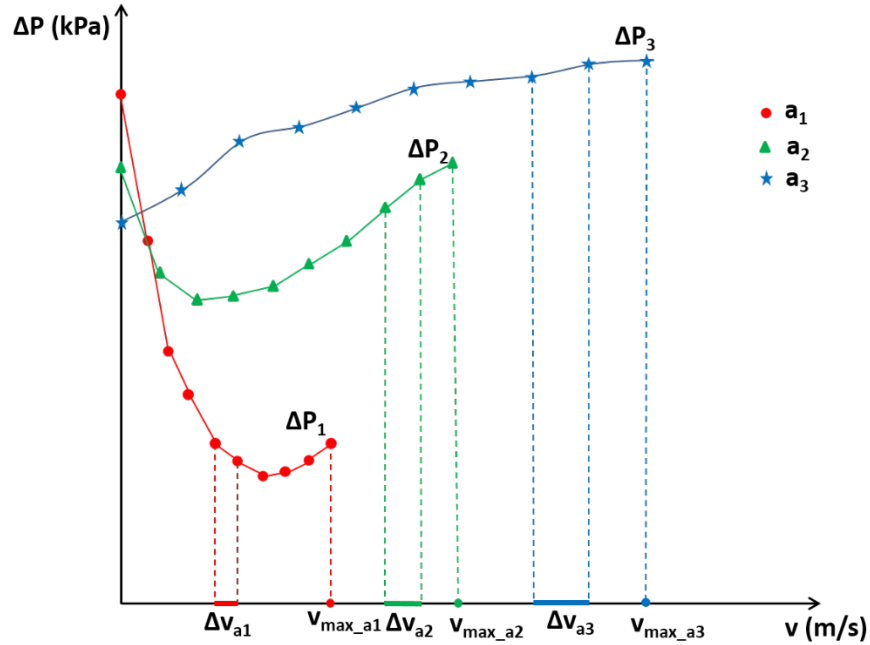


Figure 4.6 An example of superimposed measured differential pressures ($\Delta P_1, \Delta P_2, \Delta P_3$) versus velocity (v) at three accelerations (a_1, a_2, a_3). Note how the data is spread out because of different Δv_a at a constant sampling time (Δt). (Please note: the data is greatly exaggerated for clarity)

Therefore, it is quite evident that the velocity ranges at different accelerations are not the same and equally important, the changes in velocity Δv_a at a constant sampling rate are also different. It is apparent that as the acceleration increases, the range of velocity (or the maximum velocity can be achieved) and the velocity interval Δv_a increases. Further it is noted that the “density” of the data is higher at lower acceleration curves and that there is no data in the higher velocity range after the maximum velocity points.

For $a = a_1$, Δv_1 is chosen from the expression $\Delta v_1 = a_1 \Delta t$; this defines range 1 ($0 \leq v \leq v_{\max_a1}$). For $a = a_2$, Δv_2 is chosen from the expression $\Delta v_2 = a_2 \Delta t$; this defines range 2 ($v_{\max_a1} < v \leq v_{\max_a2}$). For $a = a_3$, Δv_3 is chosen from the expression $\Delta v_3 = a_3 \Delta t$; this defines range 3 ($v_{\max_a2} < v \leq v_{\max_a3}$).

The length of each range does not have to be the same. However, because the sampling time was constant, the Δv within each range was also constant, but varied from range to range. At the transition between any of the two ranges, some minor adjustment has to be made.

To facilitate the use of a lookup table within a range, it is necessary for a given v to have equivalent values of (ΔP) at each acceleration. However, because of the constant sampling time,

this was not possible. What this means is that for the smallest acceleration, and for values of v in that range, new data had to be “created” for higher accelerations in the interval $v = 0$ to $v = v_{\max_a1}$. This same issue applies for the next range of velocities and accelerations. The result of developing the velocities into a form that can be used by the lookup table is call a “Universal Velocity Set”. This means that data which does not fall on the values in the Universal Velocity Set will be “forced” to fall on these selected velocities using interpolation. This process is now described.

It must be noted that the term Universal Velocity Set (Universal Acceleration Set) is not the same as Velocity Set (Acceleration Set) in that Velocity Set refers to a set of velocities (accelerations) determined by the author in order to create as many data points as possible for the experimental lookup table in Chapter 4. See Section 4.2.5 for details.

As mentioned previously, some new data had to be created for each (Δv_a) range. This was accomplished by using interpolation approaches. The objective was to use interpolation between some of the data to place new data to “fall” on common “velocity set points”. The common velocity set points formed the Universal Velocity Set (expanded upon in Section 4.2.5). The Universal Velocity Set has to be generated in such a way so as to keep a balance between the data accuracy and memory limitation of the data processing software and hardware.

One important step in preprocessing the data must now be introduced. As mentioned in Chapter 3, at any acceleration, the maximum stroke of the actuator also defines a velocity limit. Thus beyond this maximum velocity, no ΔP information is available. In the lookup table, ΔP is set to zero beyond the maximum velocity value for each acceleration family parameter. Thus in all plots, the data shows a line from ΔP (or friction) beyond the maximum velocity of a velocity set to zero.

Because the data now all falls on common set points through the plot, a lookup table can readily be established. However, in a practical implementation of the lookup table, if the actual velocity falls within the velocity interval, or if the acceleration is not one of the family values used in the table, then a two dimensional linear interpolation technique needs to be used to approximate these friction values during the implementation stage. This would be very difficult to do if the data had not been preprocessed as proposed here. Chapter 5 considers the actual implementation of the 2D LUT model.

4.2.3 Preprocessing of Experimental Data

4.2.3.1 Development of the Sampling Point Index Number (SPIN)

The use of the sampling time (Δt) as a parameter was not conducive to modeling in a lookup table. So it was necessary to convert the time domain information into an index which in this thesis is defined as a sampling point index number (SPIN). This index number is used in appropriate figures instead of time. This process is shown in Figure 4.7 in which the correlation between the sampling points (index numbers) and the sampling times is illustrated.

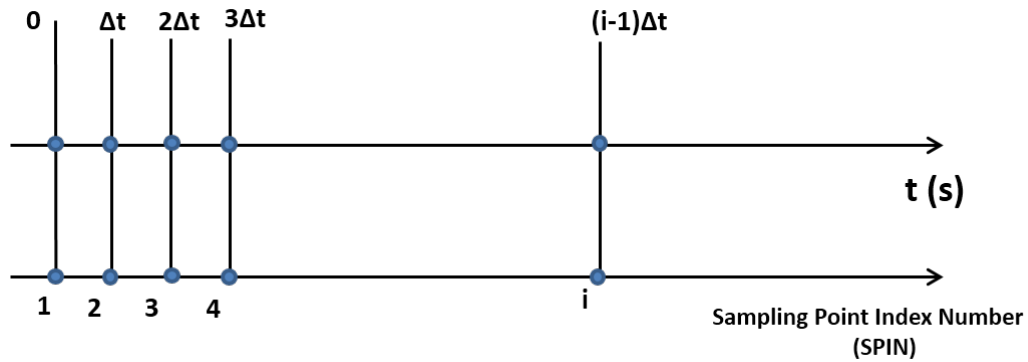


Figure 4.7 Sampling point index numbers (SPIN) vs. sampling time

4.2.3.2 Selection of Start Point (Sp) and End Point (Ep) in Each Quadrant

To facilitate the collection and organization of data into the lookup table, a starting point (Sp) on the cycled data needed to be defined. Furthermore, if (Sp) is chosen correctly, then a clear distinction between the four quadrants is possible. However, because the sampling rate was constant and as discussed above, the velocity interval was not, then choosing the (Sp) became more of a challenge.

It was decided to set the value of (Sp) to be the location on the cycle where the velocity is equal to zero for Quadrants 1 and 3, and velocity equal to maximum for Quadrants 2 and 4. In addition the endpoints (Ep) must also be defined for each quadrant. However, as mentioned previously, because the data was discrete, an exact (Sp) at a velocity of zero or maximum was only an approximation. This created a challenge to define both the (Sp) and the (Ep) of each quadrant.

The approach was to use as the (Sp), the smallest measured value of velocity that was greater than zero for the first quadrant. The (Ep) was chosen to be the maximum discrete value

in the first quadrant. The (Sp) for the next quadrant would therefore be the next value of velocity that followed the (Ep) . In implementation, if the measured value of velocity fell between the (Ep) of the last quadrant and the (Sp) of the next quadrant then the value of acceleration and pressure were chosen to be the value at the last (Ep) . A similar approach was used for all the transition points (the transition between the quadrants). Figure 4.8 illustrates a typical cycle in which the (Sp) and the (Ep) locations of each quadrant are defined. The algorithm for determining start points (Sp) and end points (Ep) is provided in Appendix J.

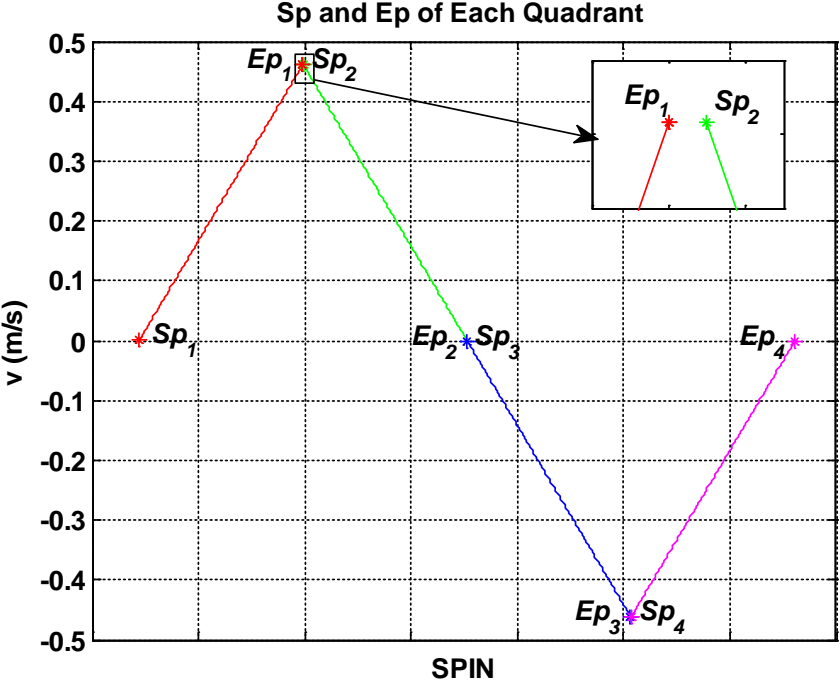


Figure 4.8 An example of start point (Sp) and end point (Ep) of each quadrant at acceleration $a = 1.5 \text{ m/s}^2$ (See zoom view for details)

4.2.3.3 Complexity Associated with the Start Point

If the measurement of differential pressure was static in nature, then one would expect that the value of ΔP would be between zero and breakaway. However the measurement in this approach is dynamic and hence it is very difficult to preconceive what the pressure would actually be at the (Sp) of each quadrant. To demonstrate this, an example of one cycle is shown in Figure 4.9. It is noticed that at (Sp) in Quadrant 1, the differential pressure is negative and not in the range of zero to breakaway as in the static case. This illustrates the complexity of dynamic friction.

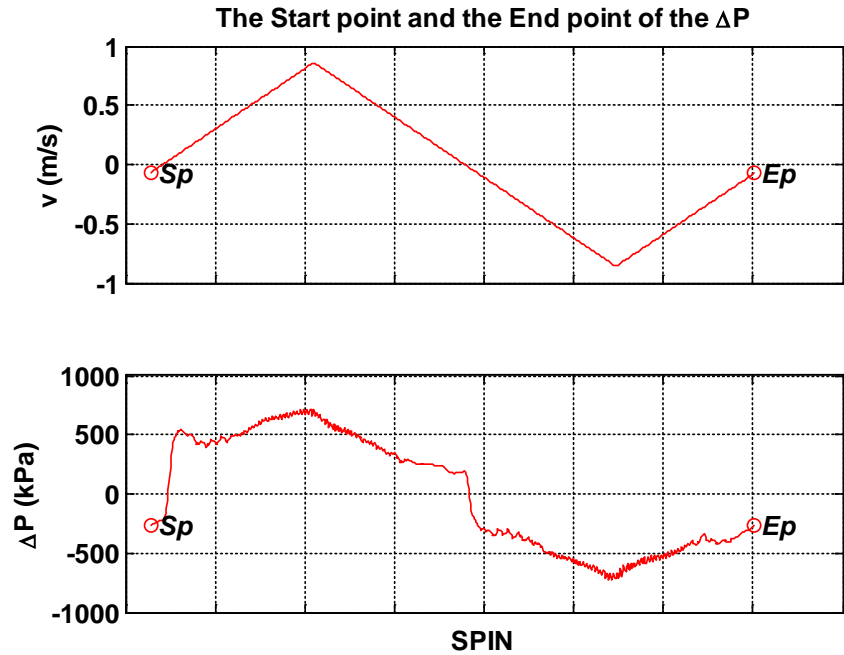


Figure 4.9 An example of the start point of the 18th cycle measured ΔP determined at acceleration = 5 m/s^2

4.2.3.4 From Time Domain to Velocity Domain

As previously mentioned, the data was collected in the time domain. In order to build a lookup table model, the experimental data had to be converted to the velocity domain. As discussed in Section 4.2.3.1 the time domain was converted to SPIN. At each index point, there corresponded a velocity, acceleration and pressure differential. Once this was accomplished, time was no longer a variable in the lookup table. The SPIN facilitated plotting acceleration or pressure differential as a function of velocity. Using this approach, a typical example of a trace using SPIN is shown in Figure 4.10 in which the (Sp) and (Ep) for each quadrant are shown.

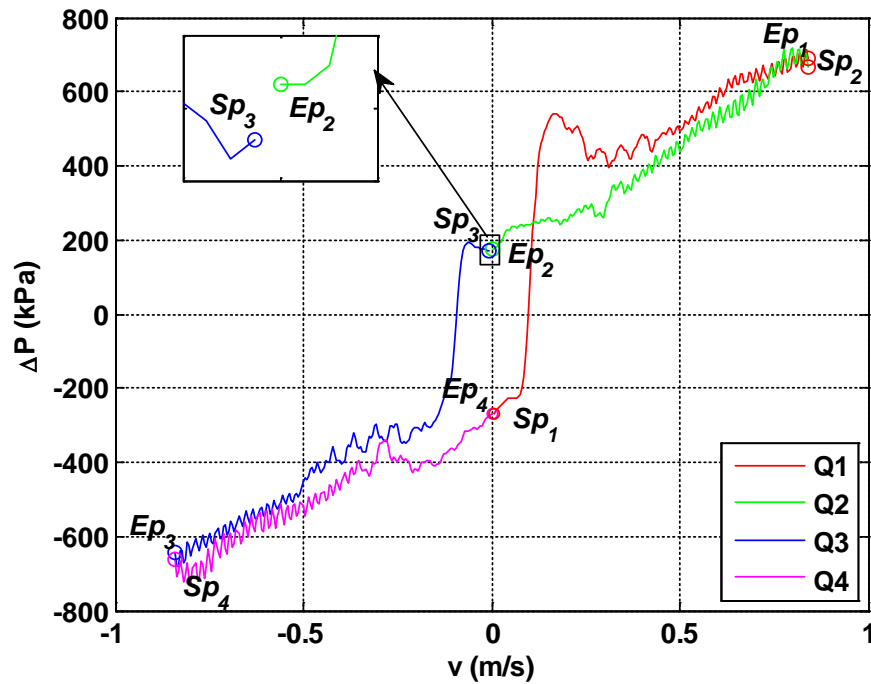


Figure 4.10 An example of four quadrants of ΔP separated by start and end points at $a = 5 \text{ m/s}^2$ (See zoom view for details). SPIN was used to develop these curves.

4.2.4 Velocity Range Specification

The maximum velocity at each acceleration varies; therefore, the velocity ranges for all the accelerations are not the same. As mentioned in Section 4.2.2, in order to make a lookup table, the overall velocity range must be the same for all accelerations. For the two VCHAS used in this study and based on the limited stroke of the two actuators, the maximum velocities were determined and were presented in Table 3.2 of Chapter 3. The maximum velocity at the highest acceleration will be used as the velocity range (v_{max}) of the 2D LUT. This means that at any constant acceleration (a), for velocities that lie between the maximum velocity (v_{a_max}) and the velocity range (v_{max}), all pressure differentials ΔP (and hence friction) are set to zero. Thus the overall range for all accelerations is the same (see Figure 4.11). As before, in order to facilitate the following section, only Quadrant 1 is considered, but the concept applies to all quadrants.

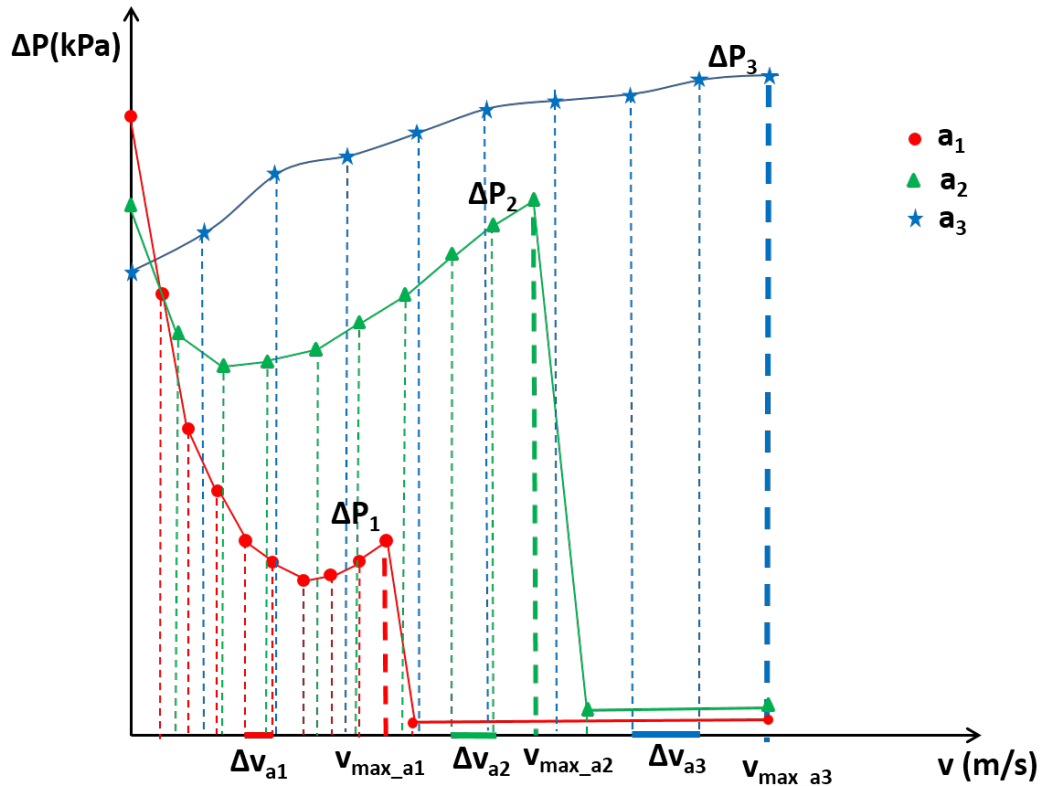


Figure 4.11 An example of velocity range specifications at three representative accelerations (a_1, a_2, a_3)

4.2.5 Universal Velocity Set and Universal Acceleration Set

In Section 4.2.2 the term Universal Velocity Set was introduced. As illustrated graphically in Figure 4.5, (which shows how the raw data could possibly appear) it is quite evident that the data does not (necessarily) fall on common velocity set points (using the velocity points established by the lowest acceleration curve and fixed sampling rate).

Ideally if (Δv_{a1}) was used for all accelerations, then the concept of a constant (Δv_a) for the full range would exist. However, if the smallest velocity set point interval (Δv_{a1}) was used (set by the sampling rate and lowest acceleration), the amount of data which would be entered into the lookup table would be very large (especially considering sample rates of 1000 Hz are not uncommon, see Figure 4.11). Thus a new approach was implemented which did not compromise accuracy, but dramatically reduced the data points in the lookup table. As introduced in Section 4.2.2, the approach was to change the velocity set point interval when reaching the maximum velocity at a fixed acceleration (Δv_{a1} changed to Δv_{a2}) in the range $v_{\max_a2} - v_{\max_a1}$ and so

on. The exact same procedure was then used to calculate the new data points via interpolation as before. The data on the abscissa (which defines the Universal Velocity Set) would now appear as in Figure 4.12.

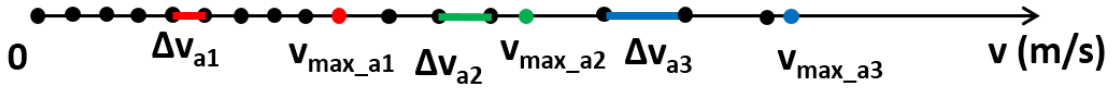


Figure 4.12 An example of Universal Velocity Set (UVS) of three representative accelerations

In the lower velocity regions, a lot of data is retained (especially important as this is where the Stribeck phenomenon is most apparent). In the higher velocity regions, the data is sparser, but this is acceptable since the friction tends to be a more viscous and demonstrates a linear dependency on friction.

The algorithm to reduce the data number, yet not losing the data accuracy, is based on the information shown in Table 4.1. It is also the foundation for generating the Universal Velocity Set.

Table 4.1 Universal Velocity Set Intervals

Velocity Ranges	Universal Velocity Set Intervals
$0 \leq v \leq v_{\max_a1}$	Δv_{a1}
$v_{\max_a1} < v \leq v_{\max_a2}$	Δv_{a2}
$v_{\max_a2} < v \leq v_{\max_a3}$	Δv_{a3}
...	...
$v_{\max_an-1} < v \leq v_{\max_an}$	Δv_{an}

The next step was to translate the information from Table 4.1 into a new table which reflected all the relevant velocity set points in each velocity range. These new velocity set points defined a velocity set which then could be used as the set points for the lookup table. That is for each v_{10} , v_{20} etc., there exists a ΔP as a function of a . This new Universal Velocity Set is shown in Table 4.2.

Table 4.2 Universal Velocity Set

Universal Velocity Ranges	Universal Velocity Intervals	Universal Velocity Sub-set
$0 \leq v \leq v_{\max_a1}$	Δv_{a1}	$v_{10}, v_{11}, v_{12}, \dots, v_{\max_a1}$
$v_{\max_a1} < v \leq v_{\max_a2}$	Δv_{a2}	$v_{20}, v_{21}, v_{22}, \dots, v_{\max_a2}$
$v_{\max_a2} < v \leq v_{\max_a3}$	Δv_{a3}	$v_{30}, v_{31}, v_{32}, \dots, v_{\max_a3}$
...
$v_{\max_an-1} < v \leq v_{\max_an}$	Δv_{an}	$v_{n0}, v_{n1}, v_{n2}, \dots, v_{\max_an}$

The Universal Velocity Set can be listed as follows (Equation (4.1)). In a likewise process, a Universal Velocity Set (*UVS*) can be generated for all quadrants.

$$(UVS) = \{v_{10}, v_{11}, v_{12}, \dots, v_{\max_a1}, v_{20}, v_{21}, v_{22}, \dots, v_{\max_a2}, v_{30}, v_{31}, v_{32}, \dots, v_{\max_a3}, \dots, v_{n0}, v_{n1}, v_{n2}, \dots, v_{\max_an}\} \quad (4.1)$$

It was necessary to initially determine the acceleration range (and subsequently, the number of curves of constant acceleration), which usually is limited by the bandwidth of the system. In order to get a smooth surface, 58 and 53 acceleration points were used for each quadrant for VCHAS1 and VCHAS2 respectively.

As discussed in Chapter 3, a “list” of desired accelerations was to be generated. Let the number of acceleration curves be designated as “*n*” (For example, *n* = 58 for VCHAS1). The total *n* accelerations is labelled as the Universal Acceleration Set and is defined as follows (Equation (4.2)). In a likewise process, a Universal Acceleration Set (*UAS*) can be generated for all quadrants.

$$UAS = \{a_1, a_2, a_3, \dots, a_n\} \quad (4.2)$$

In Section 4.2.6, the concept of interpolating the data to lie on the Universal Velocity Set points as defined by the lowest sampling rate was presented. The challenge became one of actually implementing a computer based process or algorithm to accomplish this. The following sections will now introduce this process. It was an objective here to introduce “generic” steps such that the algorithm could be universally applied in pre-processing any experimental data taken in this context.

4.2.6 Data Interpolation Process

The following step involves the process to interpolate ΔP data points to match the Universal Velocity Set. This is done by inputting a vector stream of data points into “*n*” special

interpolation algorithms. The implementation of these algorithms is illustrated graphically in Figures 4.12 and 4.13. Recall from Section 4.2.2 that velocity intervals for each acceleration were different. In addition, to reduce the amount of data, the velocity intervals changed as each maximum velocity was reached (Figure 4.15).

The new interpolated points are not exact values, but if the original locations are not that far apart (Δv_{a1} from Figure 4.5 being close to Δv_{a2}), then a reasonable approximation can be expected. However, if the change in the family parameter acceleration is too large, then this approximation would deteriorate. On the other hand, if the acceleration changes are too small (meaning too many acceleration levels are used), the amount of data could be excessive and so a compromise between memory size and accuracy always has to be given some consideration. It should be pointed out that at preprocessing, computational expensiveness and complexity is not an issue since all the calculations are done “off-line”.

In this Chapter the data interpolation process in generating the 2D LUT ΔP model is introduced. Whereas in Chapter 5, the data interpolation progress (defined as a meshing technique) in model validation and simulation implementation is considered. Mathematically, the interpolation is carried out using Equation (4.3) and the nomenclature shown in Figure 4.13.

$$\Delta P_i = \Delta P_1 + \frac{(v_i - v_1)}{(v_2 - v_1)} (\Delta P_2 - \Delta P_1) \quad (4.3)$$

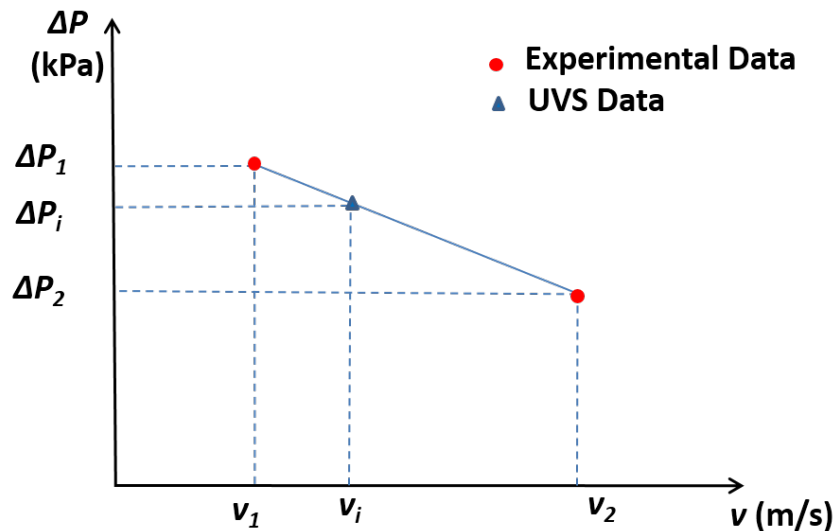


Figure 4.13 Nomenclature used for the interpolation process under a constant acceleration condition (a). v_i is an Universal Velocity Set (UVS) point

The same process is then carried out in the same fashion for higher acceleration levels at the same set point. If the two data points fall within v_1 and v_2 , the lower data point ΔP_1 is dropped for the next calculation and v_2 and ΔP_2 become the new lower points in the interpolation calculation. There will be some situations at set point v_i where the higher data point falls outside of the $v_2 - v_1$ interval. In this case, the lower data point ΔP_1 is retained to calculate a new value at v_2 . If this process is carried out for all the data points, then the new differential pressure ΔP (friction force) versus velocity would appear as in Figure 4.14. Note that now all the data lie on common Universal Velocity Set. Consider Figure 4.14. This scenario illustrates the situation where the set points V_{i1} , V_{i2} and V_{i3} (points in the Universal Velocity Set) fall within the data points ΔP_1 and ΔP_2 . Thus three new ΔP points, ΔP_{i1} , ΔP_{i2} and ΔP_{i3} must be calculated and moved to V_{i1} , V_{i2} and V_{i3} using the interpolation Equations (4.4), (4.5) and (4.6):

$$\Delta P_{i1} = \Delta P_1 + \frac{(v_{i1}-v_1)}{(v_2-v_1)}(\Delta P_2 - \Delta P_1) \quad (4.4)$$

$$\Delta P_{i2} = \Delta P_1 + \frac{(v_{i2}-v_1)}{(v_2-v_1)}(\Delta P_2 - \Delta P_1) \quad (4.5)$$

$$\Delta P_{i3} = \Delta P_1 + \frac{(v_{i3}-v_1)}{(v_2-v_1)}(\Delta P_2 - \Delta P_1) \quad (4.6)$$

where the nomenclature is defined in Figure 4.14.

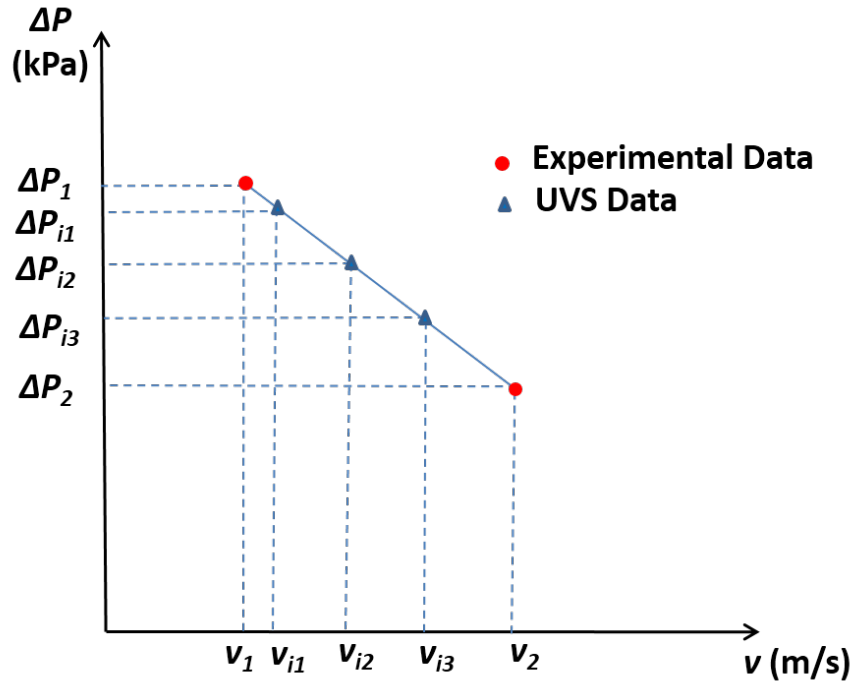


Figure 4.14 Nomenclature for when Universal Velocity set points fall within the ΔP (friction) data points. v_{i1}, v_{i2}, v_{i3} are points in the Universal Velocity Set (UVS)

Physically, a new data value is calculated at the Universal Velocity Set point via interpolation between the two closest data points on a constant acceleration curve. It was therefore decided that using a linear interpolation approach to preprocess the data would be a good choice since interpolation algorithms are standard and appear in a variety of simulation software.

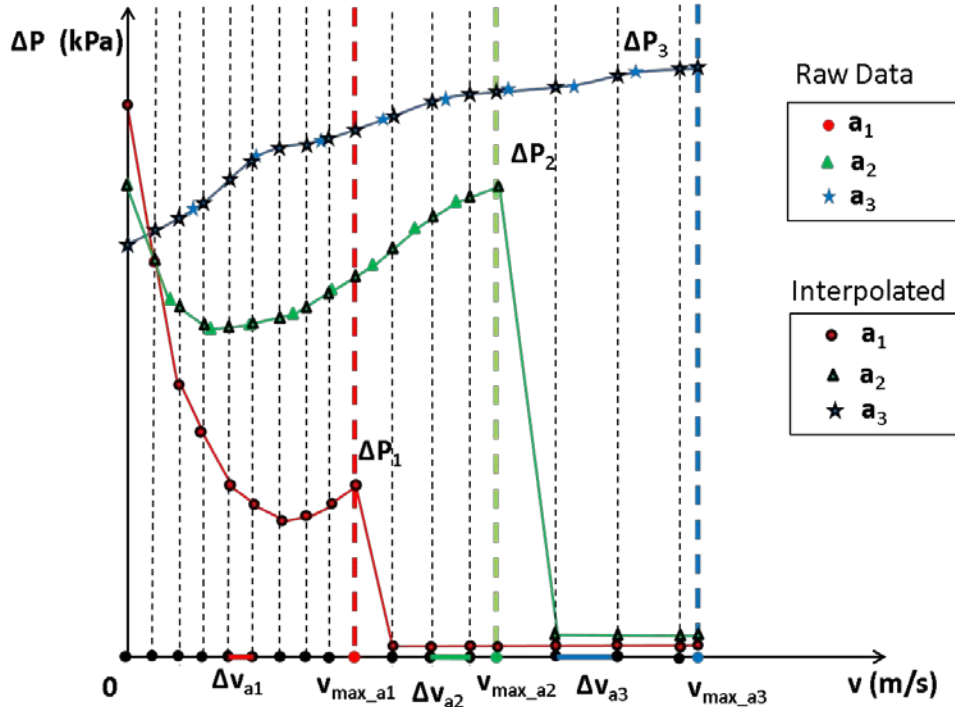


Figure 4.15 An example of interpolation in the Universal Velocity Set (UVS) which is a plot of pressure differential as a function of the Universal Velocity Set at three accelerations (a_1, a_2, a_3)

Figure 4.15 shows the curves with the interpolated data at higher acceleration levels lying on the Universal Velocity Set (Figure 4.12). In this form, a 2D lookup table (2D LUT) can now readily be established.

4.3 3D Visualization of the 2D LUT Model

In the previous sections of this Chapter, the steps required to create the 2D lookup table (semi-empirical model) has been presented. This is one of main contributions of this study as it allows the semi-empirical model to be readily integrated into simulation packages (expanded upon and applied in Chapter 5). In this section, a visual form of the 2D ΔP LUT model is presented for the two actuators used in this study. Although a visual model of the friction is not required for

simulation purposes, the 3D form does provide the user with insight into the behavior of ΔP (or dynamic friction) when acceleration is presented.

The software used to take the semi-empirical friction model and produce a 3D visual representation was achieved using the “3D Plot” from Simulink [5]. The following sections present the 3D visual plots for the two systems VCHAS1 and VCHAS2.

4.3.1 3D Plot of 2D LUT of VCHAS1

The 3D representations of the pressure differential (friction) characteristics for VCHAS1 is given in Figure 4.16. It is evident that the four quadrants are not symmetrical about zero velocity which further illustrates the nonlinear feature of friction and the difficulties this creates in modeling for simulation purposes. Since quadrant 1 contains the traditional Stribeck model, a more detailed view of Quadrant 1 is shown in Figure 4.17.

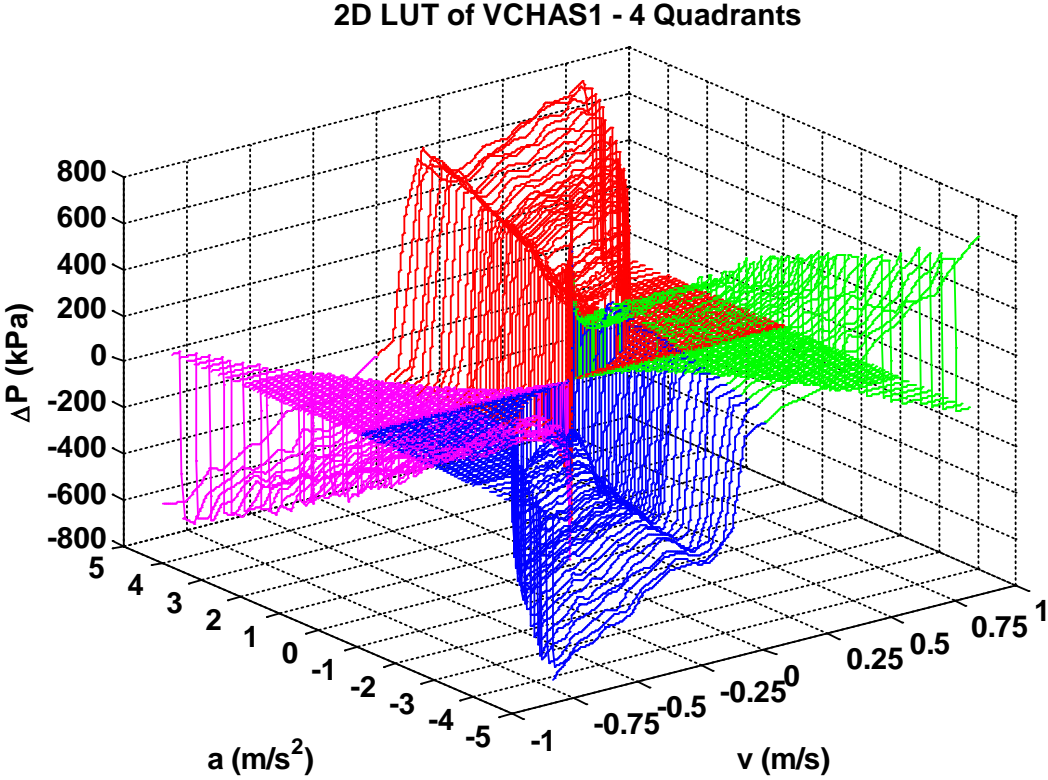


Figure 4.16 3D visual plot for all 4 quadrants of VCHAS1

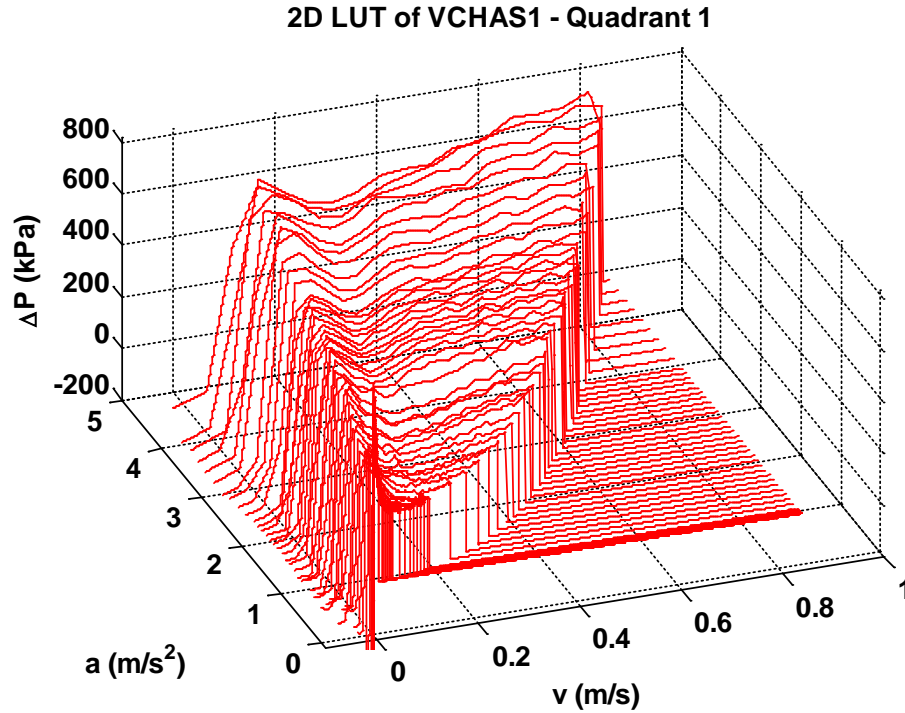


Figure 4.17 3D visual plot for Quadrant 1 of VCHAS1

Additional 3D visual plots of Quadrants 2, 3, and 4 of 2D LUT of VCHAS1 are provided in Appendix I.

4.3.2 3D Plot of 2D LUT of VCHAS2

The 3D representation of the friction characteristics for VCHAS2 is given in Figures 4.18. It is evident that the results are very similar to these shown for VCHAS1. As for VCHAS1, Quadrant 1 for VCHAS2 is shown in expanded form in Figure 4.19.

2D LUT of VCHAS2 - 4 Quadrants

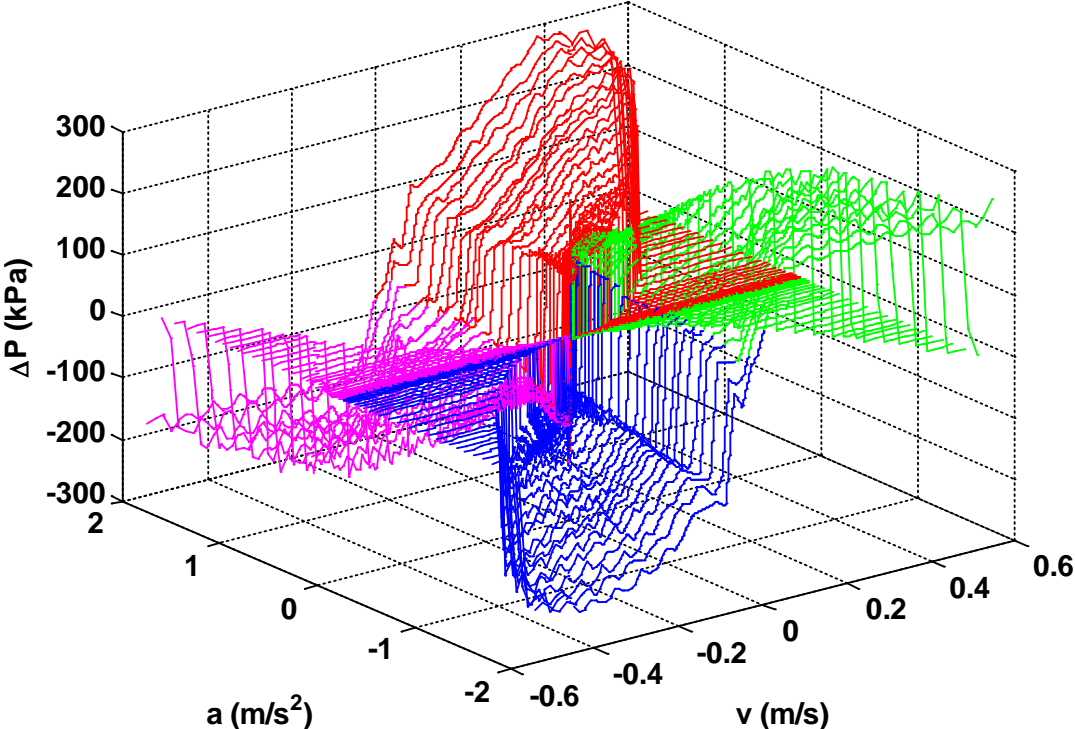


Figure 4.18 3D visual plot for all 4 quadrants of VCHAS2

2D LUT of VCHAS2 - 4 Quadrants

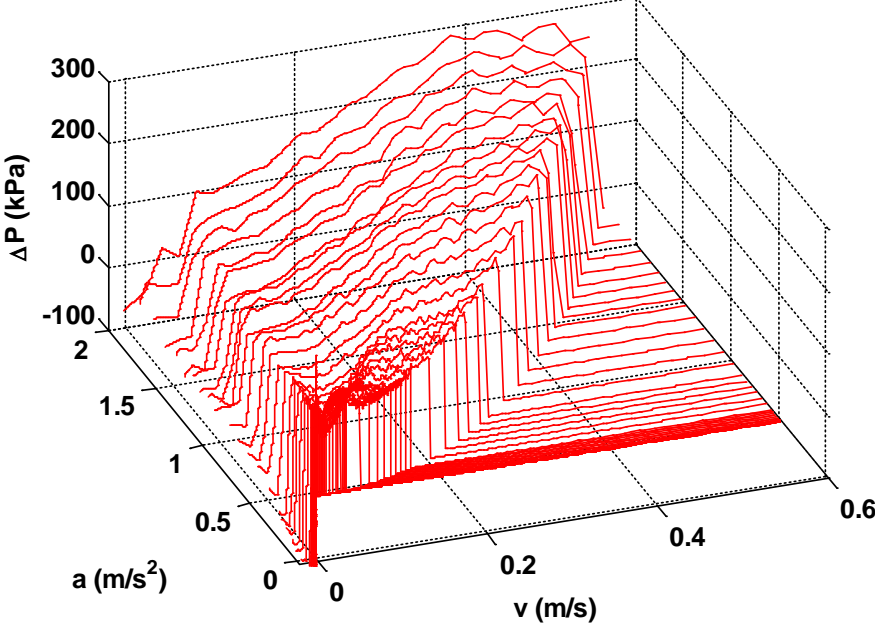


Figure 4.19 3D visual plot for Quadrant 1 of VCHAS2

Additional 3D visual plots of Quadrants 2, 3, and 4 of 2D LUT of VCHAS2 are provided in Appendix I.

4.3.3 Alternative Views of 3D Data

It is interesting to plot the data from the top view of the 3D plots of both VCHAS (Figures 4.20 and 4.21). This view is useful because it clearly shows the regions in which data could not be collected (cyan color regions). The front and side views of these 3D plots are given in Appendix I.

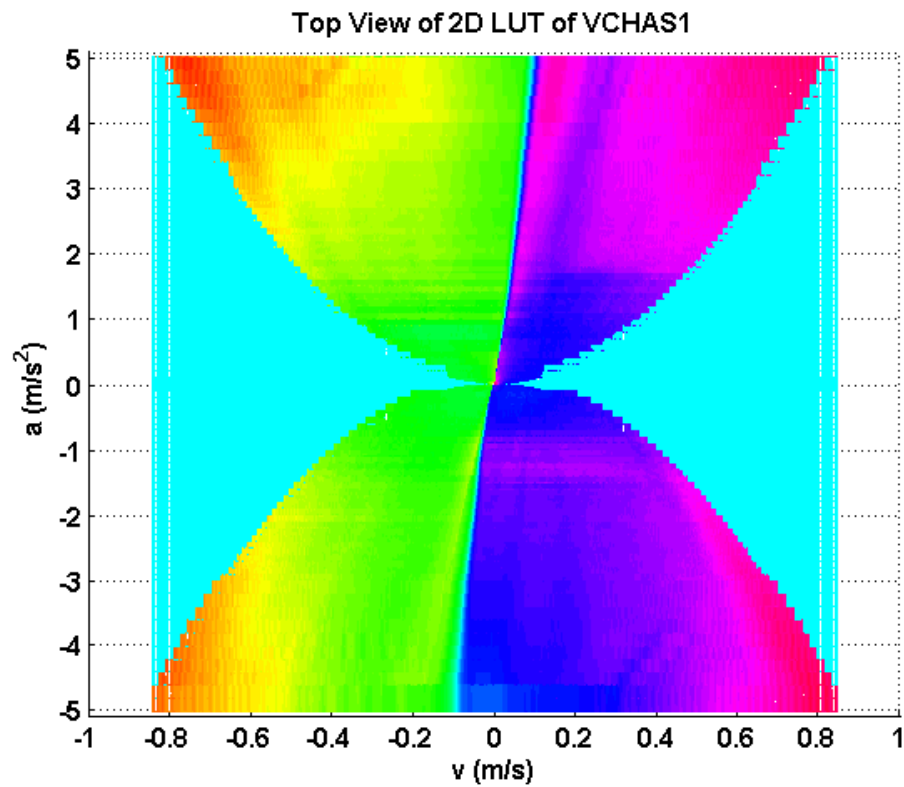


Figure 4.20 Top view of the 3D plot of ΔP 2D LUT model for VCHAS1. Note the cyan region in which no experimental data exists

Additional 3D isometric, front and side views of 2D LUT of VCHAS1 are provided in Appendix I.

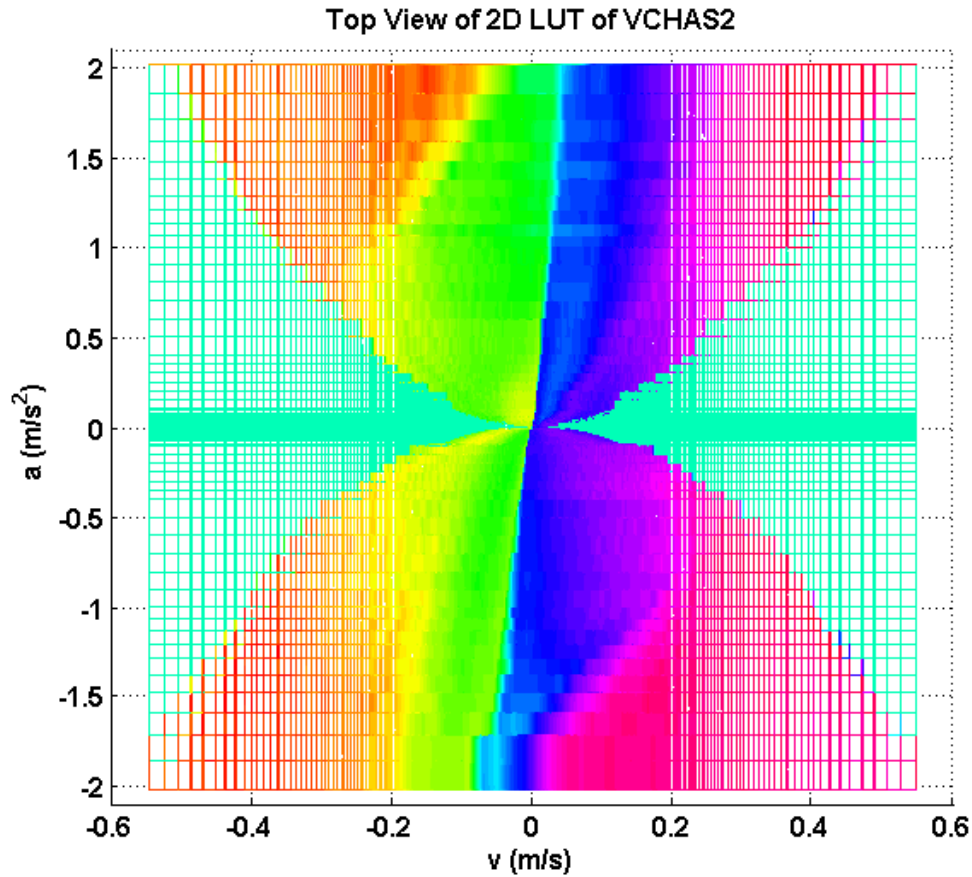


Figure 4.21 Top view of the 3D plot ΔP 2D LUT model for VCHAS2. Note the cyan region in which no experimental data exists

Additional 3D isometric, front and side views of 2D LUT of VCHAS2 are provided in Appendix I.

4.4 Model Verification

Before proceeding, the definitions of model verification and model validation from the American Institute of Aeronautics and Astronautics (AIAA G-077-1998) are provided to facilitate the discussion of model evaluation in this Chapter and Chapter 5.

Model Verification: “The process of determining that a model implementation accurately represents the developer's conceptual description of the model and the solution to the model” [45].

Model Validation: “The process of determining the degree to which a model is an accurate representation of the real world from the perspective of the intended uses of the model” [45].

Please note, the ΔP is used in the model verification and validation in this study. Verification is similar to debugging, in that it is used to ensure the model does what it is intended to do. Figure 4.22 shows the algorithm of the model verification in this study. Model validation is the work of demonstrating that the model is a reasonable representation of the actual system, which will be discussed in great detail in Chapter 5. For model verification, the lookup table and the experimental system are input with a parabolic position signal. The resulting pressure differential from the model and the lookup table were compared. This was done for representative acceleration values (low, medium and high) and the results are shown in Figures 4.23 through 4.25. Additional model verification results will be provided in Appendix G. The error in all cases is very small and hence confidence in the creation of the lookup table was established. The three results are shown for VCHAS1; the results of VCHAS2 are not shown in this thesis, but similar results were found to exist for VCHAS2.

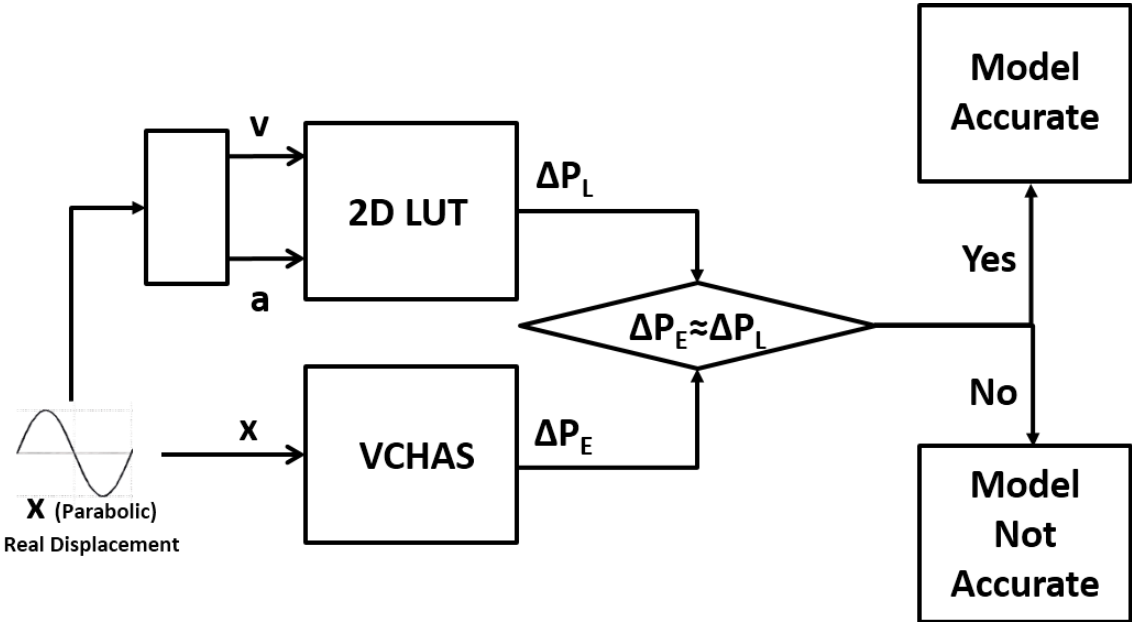


Figure 4.22 Model verification of the 2D LUT under constant acceleration levels

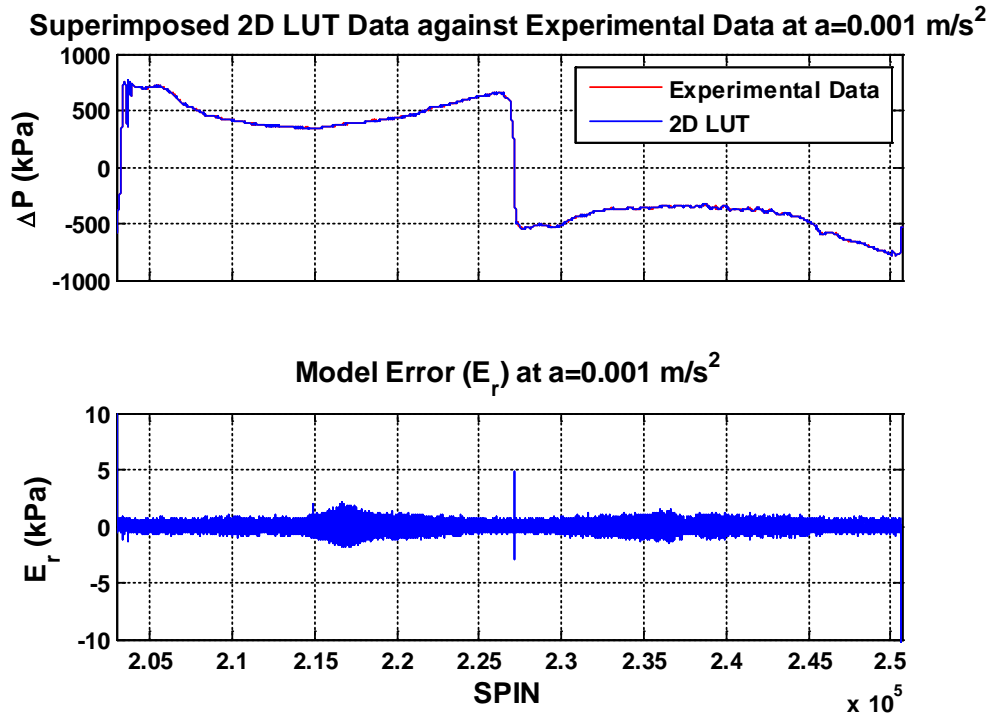


Figure 4.23 Model verification of the 2D LUT at $a = 0.001 \text{ m/s}^2$.
Please note, $E_r = \Delta P_L - \Delta P_E$

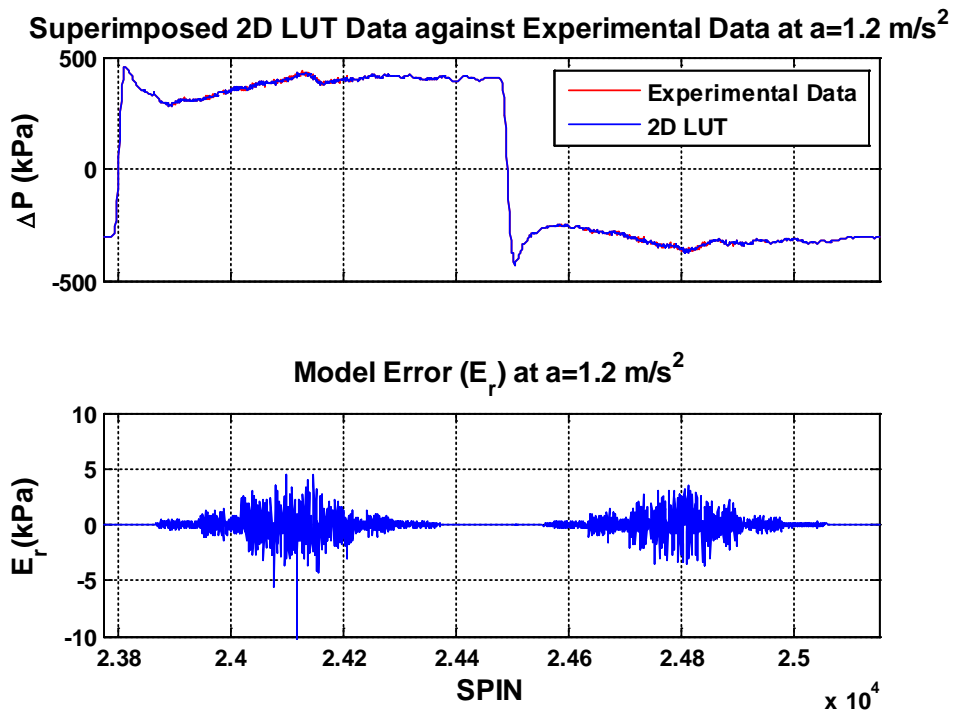


Figure 4.24 Model verification of the 2D LUT at $a = 1.2 \text{ m/s}^2$.
Please note, $E_r = \Delta P_L - \Delta P_E$

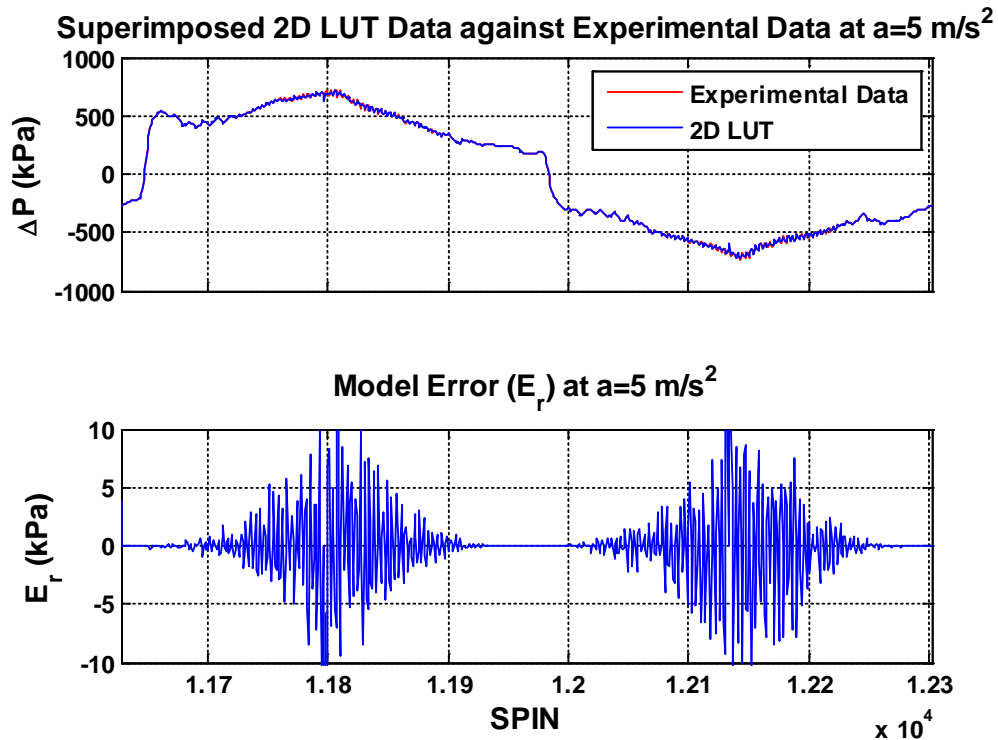


Figure 4.25 Model verification of the 2D LUT at $a = 5 \text{ m/s}^2$.

Please note, $E_r = \Delta P_L - \Delta P_E$

4.5 Summary

In this Chapter, a 3D semi-empirical model for differential pressure (ΔP) (friction) for two actuators have been presented. The steps that were required to create this model were introduced and represents one of the original contributions of this study. 2D differential pressure (ΔP) (friction) lookup tables were generated for two actuators (VCHAS1 & VCHAS2) and the results presented in 3D visual forms. The lookup table was verified under various constant acceleration conditions. It is clear that differential pressure (ΔP) (hence friction) is dependent on velocity and acceleration and that the characteristics are not symmetric about zero velocity.

This Chapter also illustrates the many challenges of setting up a lookup table when the change in velocity differs from acceleration to acceleration and data does not lie exactly on a velocity set point.

The next step, then, is to do the model validation, and integrate the model into simulation implementation. This then is considered in the next Chapter.

CHAPTER 5: MODEL VALIDATION AND IMPLEMENTATION

5.1 Introduction

In Chapter 3, experiments based on the hypothesis proposed in Chapter 1 indicated that lubricated friction-velocity curves of the hydraulic actuation system vary over different acceleration conditions (under conditions of constant temperature and small variations in pressure or differential pressure). In Chapter 4, semi-empirical friction models were created for two VCHAS in the form of a 2D lookup table (referred to 2D LUT). Developing these models required the use of interpolation to calculate new friction values to lie on a Universal Velocity Set and the acceleration points on a Universal Acceleration Set. It was considered important to be able to “practically” translate this dependency of lubricated friction on velocity and acceleration into a usable form which then could be implemented in a computer simulation package. In this Chapter, the implementation of these semi-empirical models is presented. It is most important that the implementation is readily achieved for any simulation package which requires the use of friction models. The lookup table was based on the differential pressure (ΔP) across the actuator since measuring friction directly was not possible with the experimental systems studied. However, as discussed in Chapter 4, the relationship between ΔP and lubricated friction is known. In this chapter, then, the model validation will be presented in terms of ΔP , similar to the approach used in Chapter 4.

Because of the unique approach in setting up the models, implementation of the lookup table requires only the use of a double interpolation procedure which is readily available (or programmable) in modern simulation packages. In this Chapter, the method for implementation is first presented using a “meshing technique” via double interpolation. Implementing this technique in a simulation environment is then examined by incorporating the ΔP models in a dynamic simulation of an actuator and then comparing the responses to experimental data for the same input.

A sinusoidal displacement signal was chosen as the input which was different from the signals (parabolic displacement signal) used in developing the semi-empirical models. Sinusoidal signals with different frequencies were input to the experimental VCHAS, to the Stribeck models and to the semi-empirical models. It will be shown that the predictions of ΔP from the semi-empirical models were superior to those from the Stribeck models when compared to the

experimental ΔP over all the frequencies considered. The dynamic accuracy of the models is then considered. The Chapter concludes by discussing the limitations of the models for the type of input considered.

It must be noted here that only results from VCHAS1 are considered in the validation study. It was believed that one system was sufficient to demonstrate the validity of the 2D LUT in a simulation format.

5.2 Model Validation

As discussed in Chapter 4, model validation is the “process of determining the degree to which a model is an accurate representation of the real world from the perspective of the intended uses of the model” [5]. It is very difficult to quantify the term degree of accuracy when validating any model. In the literature, a value of accuracy is seldom mentioned or discussed.

In this study, the model will be considered validated if the trends predicted by the model of the 2D LUT follow the experimental results better than that predicted by the standard Stribeck model (which is used in most simulation studies). A quantitative comparison is not presented, but as was done in the verification study of Chapter 4, the accuracy will be based on a visual comparison of the real versus simulated outputs for inputs signals NOT used in the development of the lookup table and observations of the difference between the model and experimental outputs. Indirectly, validation reinforces the hypothesis that friction is dependent on velocity and acceleration.

In this section, the model validation strategy is discussed. The rationale for the input signal choice is presented followed by the model validation process.

5.2.1 Model Validation Strategy

In Chapter 4, the 2D LUT model was verified, which indicated that the 2D LUT model was a good representation of the VCHAS at constant accelerations. However, a question arises: “Can the 2D LUT model be a good representation of the VCHAS at varying accelerations?” An objective of this Chapter was to examine the validity of the model under a simulation situation. The section then considers, a new validation strategy.

The steps to validate the model were as follows (these are illustrated in Figure 5.1):

1. Design a validation input signal which would be common for both the experimental system, the 2D LUT model and the Stribeck model.
2. Input the validation signal to the experimental system and the models and record the measured differential pressures (ΔP_E) and the predicted differential pressures of the new semi-empirical models (ΔP_L) and Stribeck models (ΔP_S).
3. Third, determine the error between the experimental and the simulation results of the semi-empirical model ($e_{EL} = \Delta P_E - \Delta P_L$),
4. Fourth, determine the error between the experimental and the simulation results of the Stribeck model ($e_{ES} = \Delta P_E - \Delta P_S$).
5. Compare the two errors ($|e_{EL}|$ & $|e_{ES}|$).

If the error of the new semi-empirical model is, in general, smaller than the error of the Stribeck model ($|e_{EL}| < |e_{ES}|$), then it can be concluded that the new semi-empirical model which included the acceleration effect is validated as defined in Section 5.1. In order to implement the model validation strategy of Figure 5.1, the type of the model validation signal, and the generation of the experimental ΔP_E , the 2D LUT ΔP_L and the Stribeck ΔP_S are discussed in the following sections.

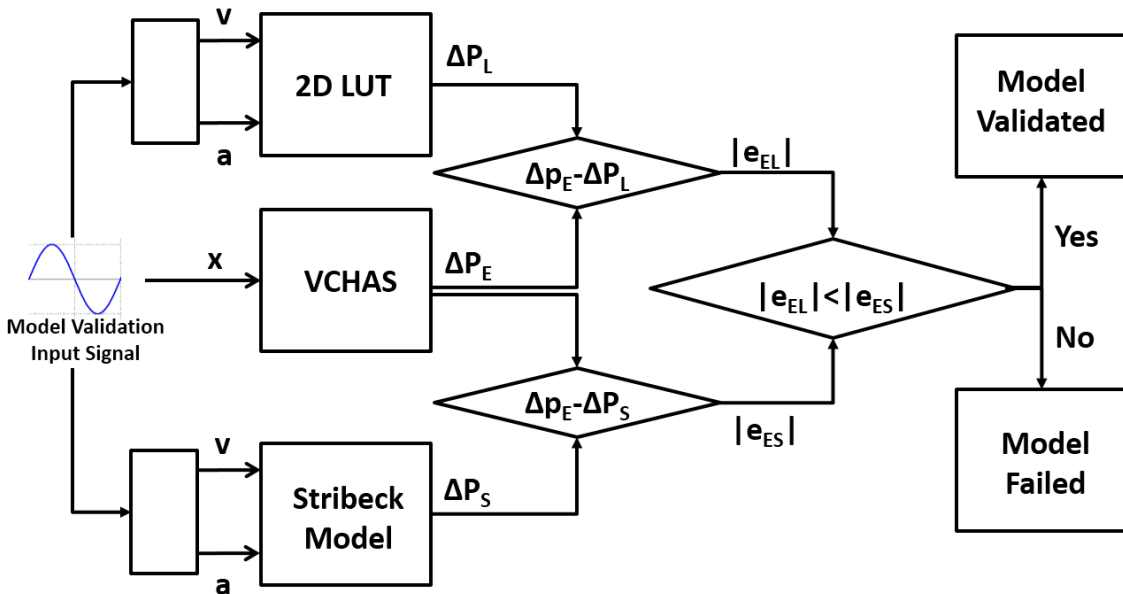


Figure 5.1 Model validation strategy - error comparisons of the 2D LUT model and Stribeck model

5.2.2 Causality Issues

The choice of what the input signal should be ($\Delta P A_p$, or v and a) and its form (step, triangular, sinusoidal etc.) required some thought. In many applications, ΔP across the actuator could be the input to the model with the corresponding position (x), velocity (v) and acceleration (a) as the outputs (Equations 5.1 and 5.2). This is demonstrated using the following causal relationships:

$$a = \frac{\Delta P A_p - F_f(v, a)}{M} \quad (5.1)$$

$$x = \iint \frac{\Delta P A_p - F_f(v, a)}{M} \quad (5.2)$$

where differential pressure, ΔP , is the input in this case, and A_p is the effective piston area. Observation of this form shows that the equations are “stiff” in that acceleration (a) exists on both sides of Equation 5.1. In Matlab, this would result in an algebraic loop. Algebraic loops are difficult to solve mathematically. Theoretically it can be implemented by incorporating a small time delay ($\frac{1}{z}$) between the outputs and input to the friction model (2D LUT) (Figure 5.2). However, in practice, it is difficult to determine the appropriate time delay which would be valid for all operating conditions. Indeed, the simulation could become unstable. Therefore, this approach was not pursued in this study.

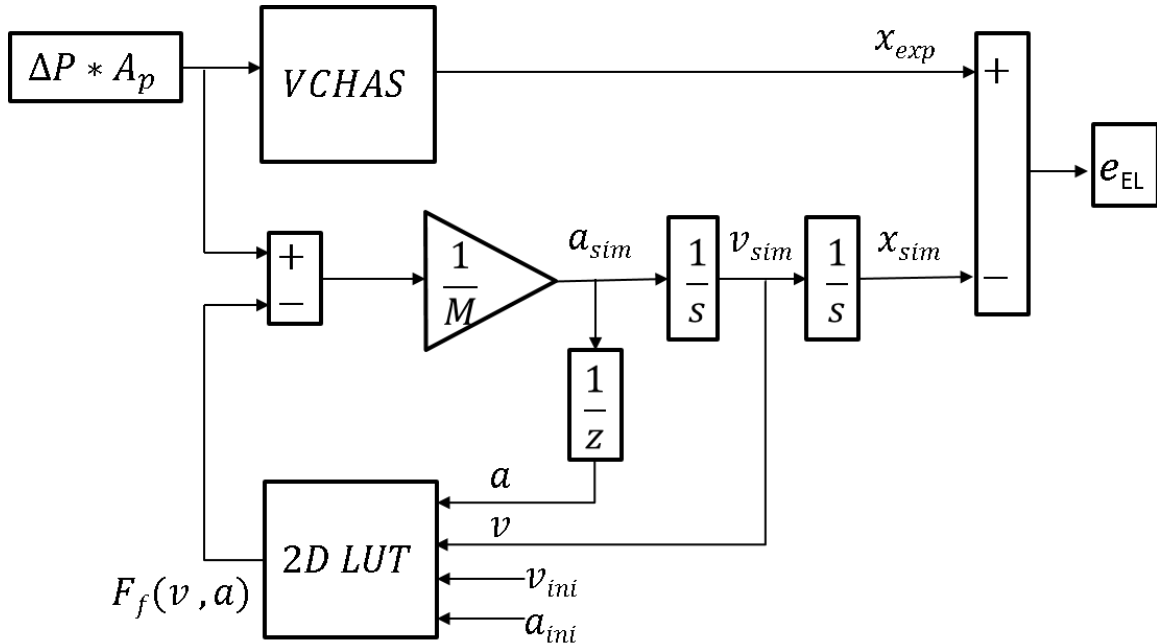


Figure 5.2 A possible Matlab formulation of the model in which $\Delta P A_p$ (hydraulic force) is the input. The term 2D LUT is already defined.

An alternate approach (and that used here) is to change the causality to be:

$$\Delta P = \frac{1}{A_p} \{F_f(v, a) + Ma\} \quad (5.3)$$

In this case, x is the input (v and a calculated) and ΔP is the output. No delay is required in this situation. The Simulink © program to implement this approach is shown in Figure 5.3. Note that the Stribeck model under conditions of zero acceleration ($a = 0$) is also included to provide a base line for comparison of the outputs.

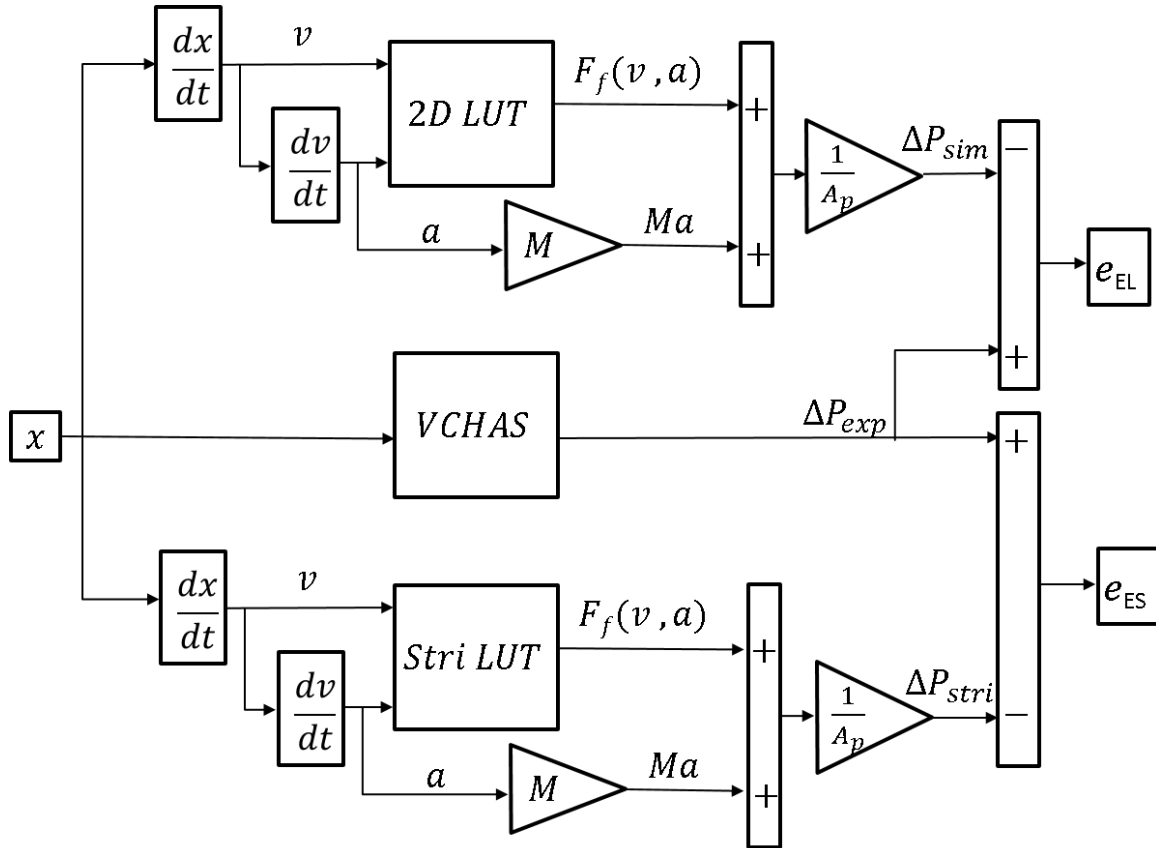


Figure 5.3 A possible Matlab formulation of the model in which x , v and a are the inputs and ΔP (hydraulic force) the output.

5.2.3 Design of Input Signal of Model Validation

A second consideration for the input form had to be made. Many input forms could be used, but a criteria that was adopted was that the input should not be the same as that used in the development of the 2D LUT. A signal that had both velocity (v) and acceleration (a) changes inherent in it was a sinusoidal signal (Figure 5.4). Such a signal was believed to be appropriate to challenge the 2D LUT model's ability to predict ΔP_L . It should be noted that the input signal is in

fact a cosine form in order to ensure the start of the experimental test occurred at one end of the actuator.

A drawback to this form of the input signal was that there were portions of the waveform in which the model (2D LUT) could not predict the ΔP_L value. Details of this limitation will be discussed in Section 5.2.4.5.

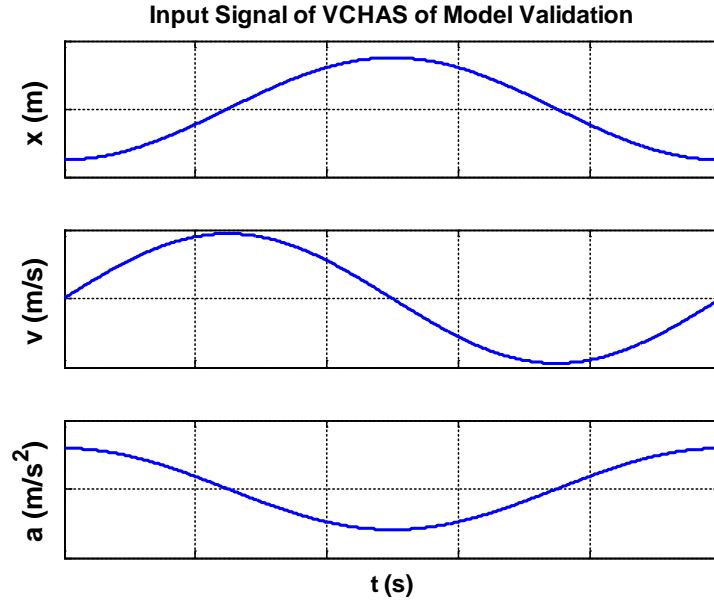


Figure 5.4 An example of an input sinusoidal displacement signal (x) to the VCHAS and the expected actuator velocity (v) and acceleration (a)

The mathematical equations for the input sinusoidal displacement signal (x) and the expected velocity (v) and acceleration (a) are given as:

$$x = -A\cos(\omega t) \quad (5.4)$$

$$v = A\omega\sin(\omega t) \quad (5.5)$$

$$a = A\omega^2\cos(\omega t) \quad (5.6)$$

$$v_{max} = A\omega \quad (5.7)$$

$$a_{max} = A\omega^2 \quad (5.8)$$

$$\omega = 2\pi f \quad (5.9)$$

where x is the sinusoidal displacement (m), A is the amplitude of x (m), v is the sinusoidal velocity (m/s), $A\omega$ is the amplitude of v (m/s) and a is the sinusoidal acceleration (m/s^2). Also, $A\omega^2$ is the amplitude of $a(m/s^2)$, ω is the angular frequency of the input sinusoidal signal (rad/s), t is the sampling time (sec) and f is the frequency of the input sinusoidal signal (Hz).

As was done in Chapter 4, to facilitate discussions, the sampling index numbers (SPIN) are used in the following sections instead of time.

Consider Figure 5.5. At any specific time, acceleration (a_1) can be plotted as a function of velocity (v_1). The “motion condition” for any point (v_1, a_1) in the v and a space versus SPIN (for a sinusoidal input) produces an ellipse as illustrated. Figure 5.5 also shows the start and end points for the full cycle. The mathematical formulation of the sinusoidal $v - a$ ellipse is given in Equation 5.10 which illustrates the dependency of the ellipse on the frequency and amplitude of the sinusoidal signal.

$$\frac{v^2}{v_{max}^2} + \frac{a^2}{a_{max}^2} = 1 \quad (5.10)$$

where v_{max} is the amplitude of the sinusoid velocity (Equation 5.7) and a_{max} is the amplitude of the sinusoid acceleration (Equation 5.8). From Equation 5.10 and Figure 5.5, it is evident that the radius of the velocity axis and acceleration axis of the sinusoidal $v - a$ ellipse are the amplitudes of velocity and acceleration respectively. When $f < \frac{1}{2\pi}$, the radius of velocity axis is larger than the radius of acceleration; hence the $v - a$ is a horizontal ellipse. When $f = \frac{1}{2\pi}$, the radius of velocity axis is equal to the radius of acceleration; hence the $v - a$ is a circle. When $f > \frac{1}{2\pi}$, the radius of the velocity axis is smaller than the radius of acceleration; hence the $v - a$ is a vertical ellipse.” Details of the derivation of Equation 5.10 is provided in Appendix H.

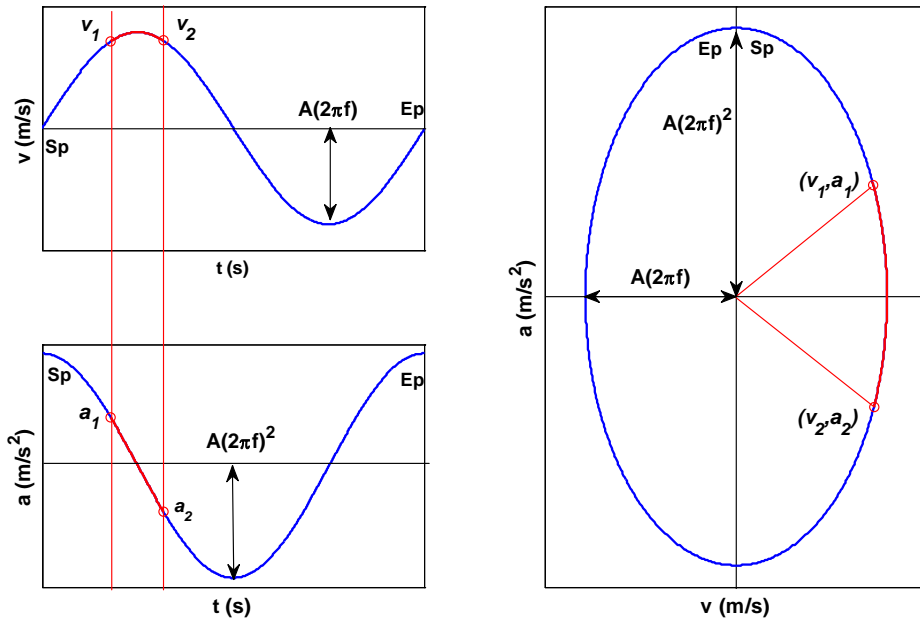


Figure 5.5 An example of motion condition (v, a) in the sinusoidal velocity (v), acceleration (a) and $v - a$ curve. The $v - a$ curve is an ellipse and is dependent on frequency (or period) of the sinusoidal signal

From Figure 5.5, during any specific period of time, the motion condition of the sinusoidal signal changes. (v_1, a_1) to (v_2, a_2) , can be correlated to a segment of the sinusoidal $v - a$ ellipse which will be used extensively in Sections 5.2.4.5 and 5.2.6.

5.2.4 Experimental Data – ΔP_E

The frequency range of the sinusoidal signal that could be used experimentally was limited by the VCHAS bandwidth (frequency response limit) and the hydraulic system supply capacity (flow capacity). The output displacement followed the desired displacement very well at low frequencies (0.02 Hz), but as the frequency increased, some distortion in the output position waveform was noticed. When the distortion became visually significant, higher frequencies were not used. (Please note, a quantitative limitation on the maximum frequency was not used. The decision was purely based on the author's visual inspection). The maximum frequency of the sinusoidal signal for VCHAS1 was set to be $f = 1.48\text{Hz}$. It should be noted that this maximum was the same maximum frequency as used in the parabolic input study.

Eight representative frequencies of sinusoidal signals were chosen for model validation studies: 0.02, 0.03, 0.07, 0.3, 0.73, 0.98, 1.22, and 1.48 Hz. In the following section only four frequencies are presented: 0.02 Hz was chosen as the low frequency, 0.73 Hz the medium frequency, 1.22 Hz the high frequency, 1.48 Hz the extreme high frequency. Other results will be provided in Appendix J.

5.2.4.1 Experiment of Sinusoidal Accelerations

The experimental procedure to validate the model was as follows (please note that these procedures were similar to those used in the verification tests):

1. A list of desired discrete frequencies of the sinusoidal position input signal at which measurements were to be made was created (details are provided in Appendix I) This is the desired sinusoidal position input to the closed loop system.

2. The experiment was started using the first input frequency of the positional sinusoidal waveform.
3. The experiment was repeated up to 20 cycles under the same conditions until the system was stable with temperature maintained at $29^\circ \pm 1^\circ$.
4. The differential pressure (ΔP_E), displacement (x) and temperature were measured and recorded.
5. The frequency of the input sinusoidal displacement signal was changed to correspond to the next selected frequency.
6. Steps 3 to 5 were repeated until the all selected frequencies of the input signals were tested.

Some typical experimental results are shown in Figure 5.6. Based on the data from Figure 5.6, a 3D view of ($\Delta P, v, a$) can be generated (Figure 5.7). Figure 5.7 also provides the top view, front view and side view of this 3D curve. It is interesting to observe how the motion condition (v, a) changes over a cycle, and how the velocity and acceleration influence the ΔP over a cycle.

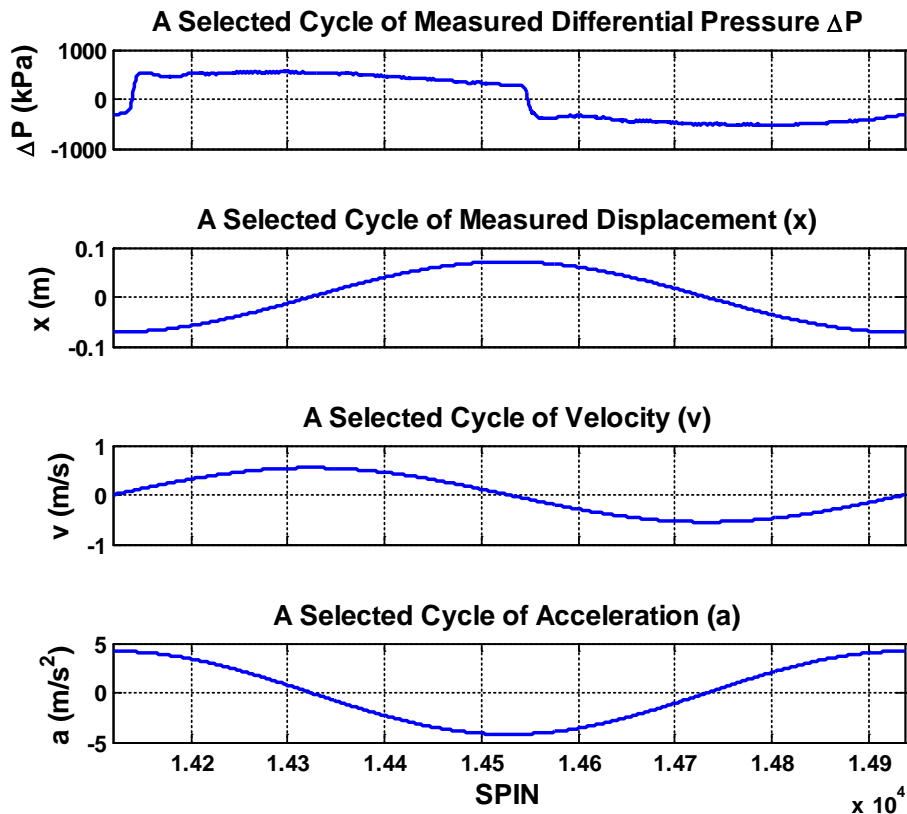


Figure 5.6 An example of a selected cycle of measured differential pressure (ΔP) and measured displacement (x) at frequency $f = 1.22$ Hz. Please note: velocity and acceleration were not measured, but were obtained by differentiating the curve fitted position (x) once for velocity (v) and once again for acceleration (a) (see Section 5.2.4.3 for details)

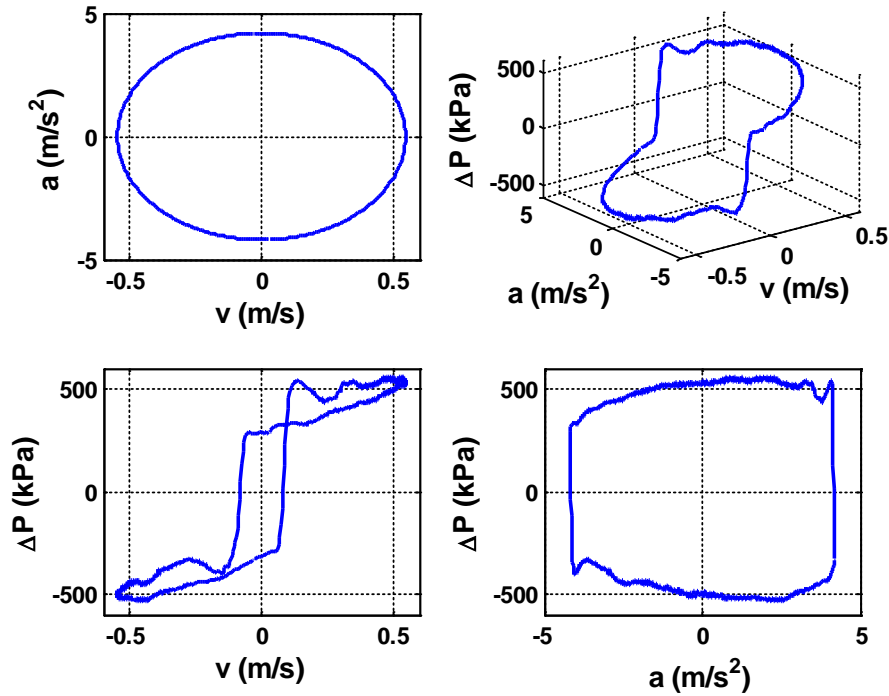


Figure 5.7 An example of a selected cycle of the measured differential pressure (ΔP) under non-steady state conditions by a sinusoidal signal at frequency $f = 1.22$ Hz in four views – front view (ΔP vs. v), top view (a vs. v), side view (ΔP vs. a) and isometric view (ΔP vs. v , a).

5.2.4.2 Selection of a Stable Period of Experimental Data

Due to the repeatability issue (discussed in Chapters 3 and 4), it was desirable to collect the experimental data of a complete cycle when the system was fully stabilized. The experimental data under some acceleration conditions stabilized quickly, (one or two cycles), whereas others took up to 15 cycles. As was done in Chapter 4 for a parabolic input, the middle cycle of the last 3 complete cycles was chosen as the experimental data to be used. To illustrate this, consider Figure 5.8, at a frequency of 0.73 Hz, where the actuator was cycled 20 times. The measured ΔP started to stabilize after 10 cycles and by the 18th cycle, the data was considered to be stable and thus was selected for model validation. In general, at higher frequencies, the 17th or 18th cycles were chosen for model validation.

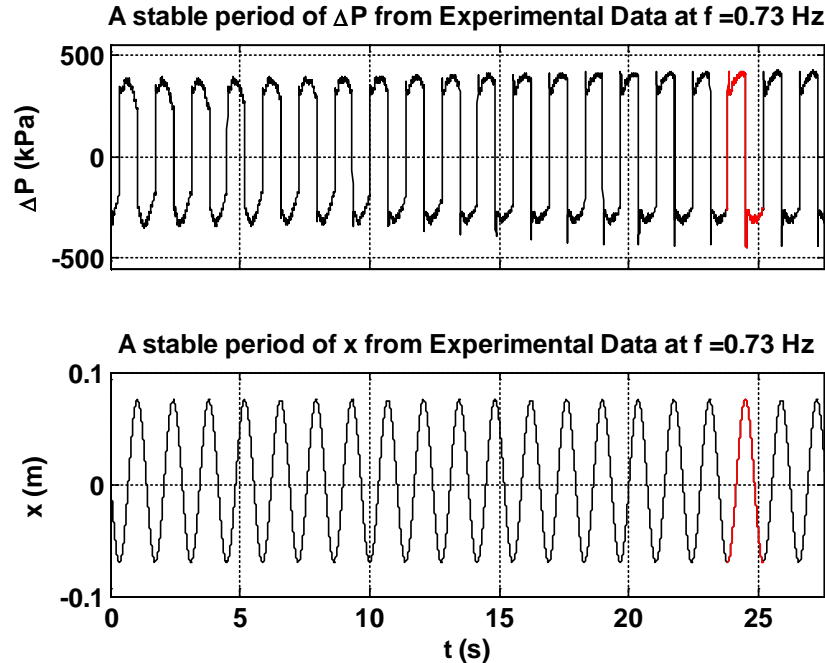


Figure 5.8 An example of measured differential pressure (ΔP) and displacement (x) at a frequency of 0.73 Hz. Data was collected for model validation at the 18th cycle (in red).

5.2.4.3 Estimation of Sinusoidal Velocity and Acceleration by Curve Fitting

As mentioned in Chapters 3 and 4, there was no sufficiently accurate velocity transducer available for the experiments of this study. The velocity data was simply derived from the measured displacement (x_m). Because the measured displacement signal displayed some noise from the system, a direct derivative of the measured displacement was too noisy to be useful. The approach used in this study was to use sinusoidal curve fitting of the measured displacement (recall in Chapter 4, fitting of a parabolic function to the input signal was implemented). Figures 5.9 – 5.12 demonstrates the accuracy of the curve fitting approach of the position at various accelerations. Additional sinusoidal curve fitting results will be presented in Appendix G. As was found in the parabolic curve fitting of Chapter 4, it is quite apparent that the error associated with this curve fitting approach is also very small. The sinusoidal velocity (v_c) and sinusoidal acceleration (a_c) can be obtained by taking the first and second derivative of the “clean” curve fitted displacement (x_c) respectively.

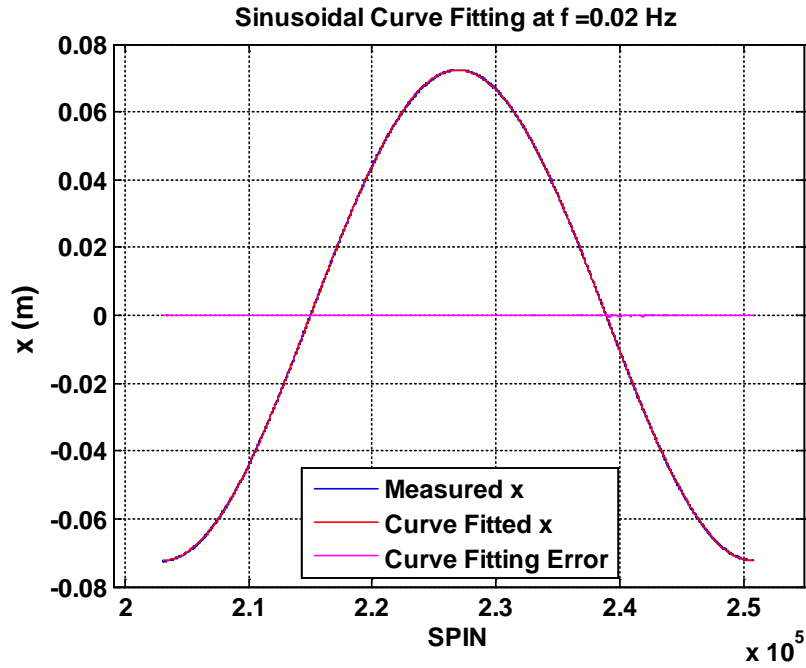


Figure 5.9 Sinusoidal curve fitting of the measured displacement at frequency $f = 0.02$ Hz

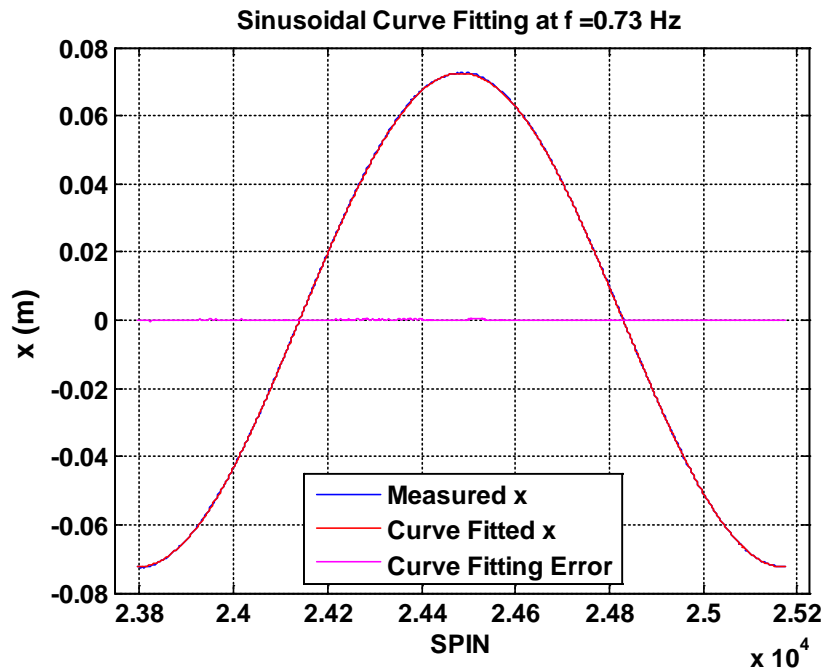


Figure 5.10 Sinusoidal curve fitting of the measured displacement at frequency $f = 0.73$ Hz

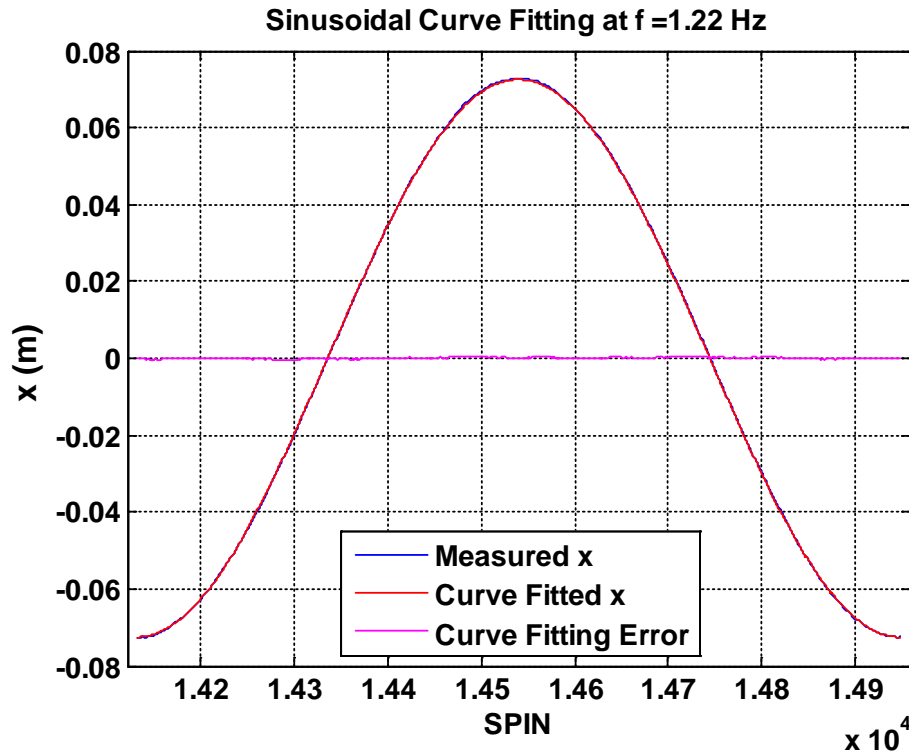


Figure 5.11 Sinusoidal curve fitting of the measured displacement at frequency $f = 1.22$ Hz

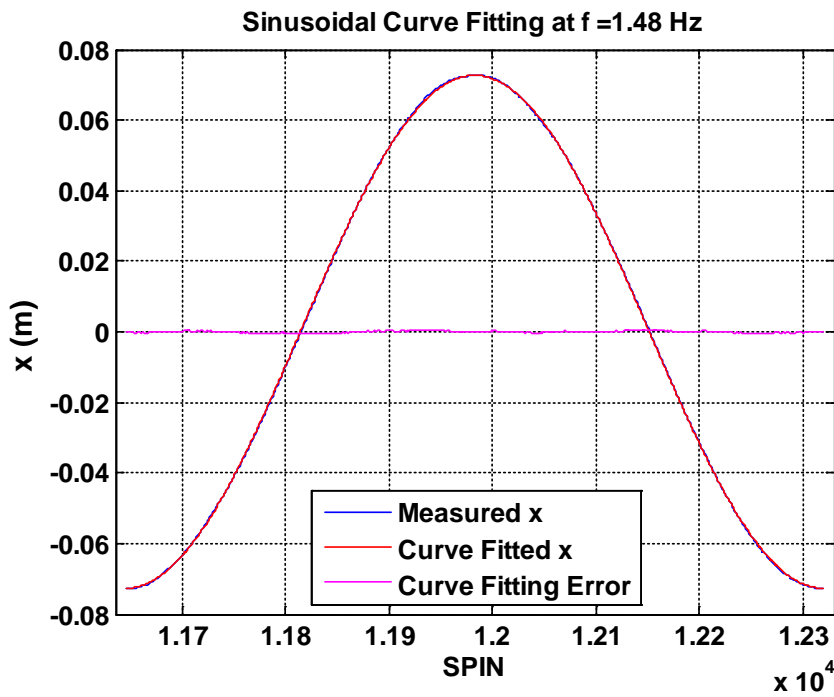


Figure 5.12 Sinusoidal curve fitting of the measured displacement at frequency $f = 1.48$ Hz

5.2.4.4 Selection of Start Point (*Sp*) and End Point (*Ep*)

To facilitate model validation, a starting point (*Sp*) and an end point (*Ep*) on the cycled sinusoidal data needed to be defined. The process of finding the *Sp* and *Ep* was determined in a similar fashion to that used in Chapter 4. *Sp* and *Ep* define the beginning and end of a stable cycle for model validation. Figures 5.13 and 5.14 illustrate a typical cycle in which the *Sp* and the *Ep* locations are defined.

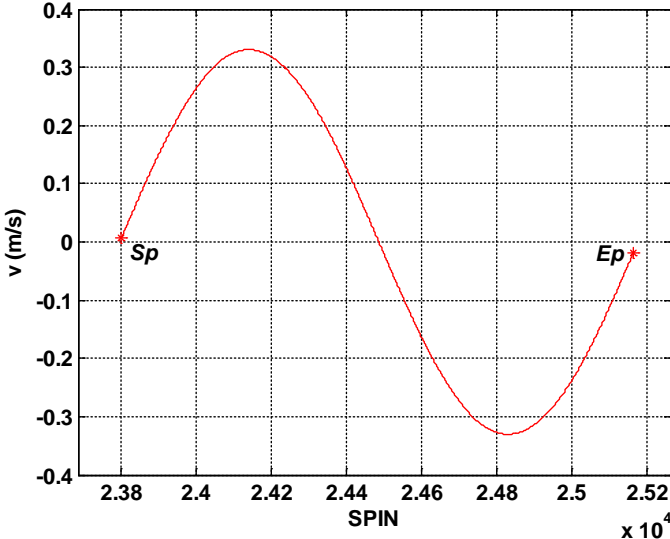


Figure 5.13 An example of start point(*Sp*) and end point (*Ep*) of a selected cycle of the sinusoidal signal at frequency $f = 0.73$ Hz

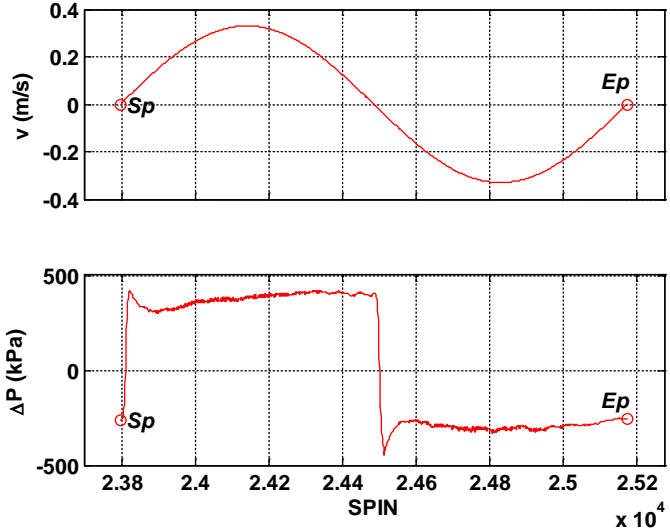


Figure 5.14 An example of the start point (*Sp*) of the 18th cycle measured ΔP determined at frequency $f = 0.73$ Hz

5.2.4.5 Determination of No Model Data Zone

In Chapter 3, Figure 3.22 showed the boundary between the regions where data could and could not be collected using the parabolic signals (hence the modeling process data limitation). There are two additional “experimental” limitations that need to be considered for the validation studies. The upper maximum acceleration and the maximum velocity constraint (maximum physical limit boundary) is a consequence of the hydraulic system not being able to provide sufficient flow to the actuator. The lower minimum acceleration and minimum velocity limit (minimum physical limit boundary) is a consequence of the excessive time to complete a full stroke of the actuator and the control problems that arose. For data less than the minimum acceleration region, the standard Stribeck approach presented in Chapter 3 was used (essentially acceleration can be considered to be zero in this region). Thus the 2D LUT model in the regions where data could be collected was a combination of the Stribeck and acceleration dependent models.

Consider Figure 5.15. The ellipse representations of the velocity-acceleration curves for four sinusoidal inputs (0.02 Hz, 0.73 Hz, 1.22 Hz and 1.48 Hz) are superimposed on the physical limitations figure (Figure 3.22) that was presented in Chapter 3. It is evident that the $v - a$ ellipses vary with frequency; the higher the frequency, the larger the ellipse (amplitude). The low frequency input (0.02 Hz) is shown in the insert of Figure 5.15, where it is evident that the curve crosses the boundary at certain locations.

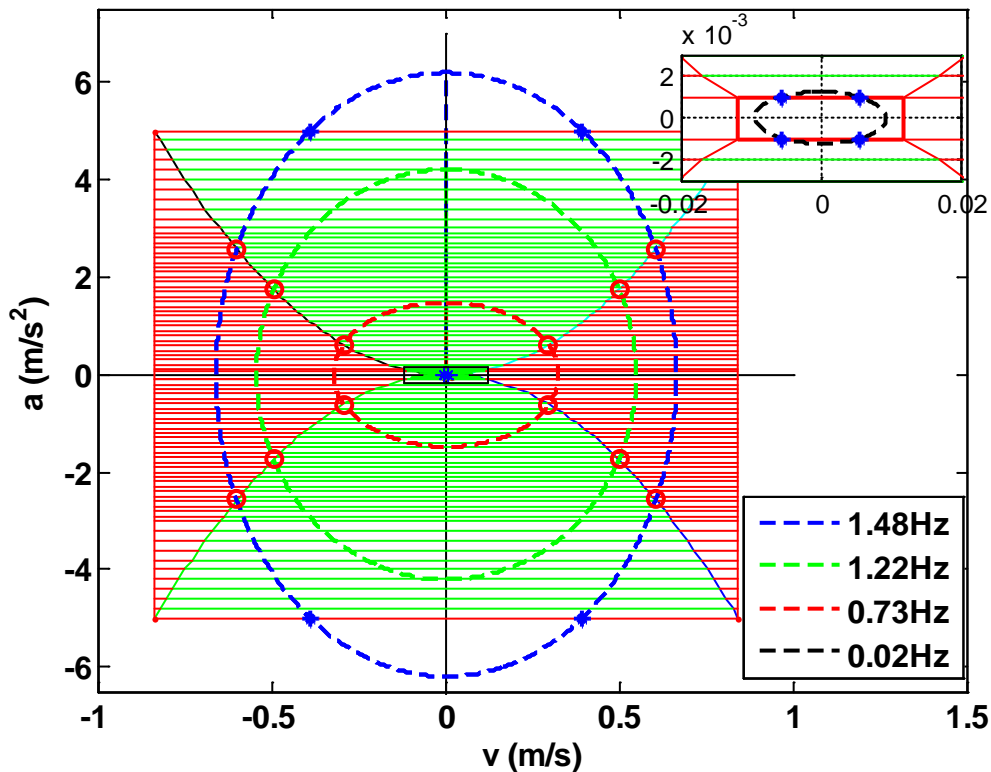


Figure 5.15 $v - a$ curves of sinusoidal signals for low, medium, high and extreme high frequencies (0.02Hz (see the zoom view for details), 0.73 Hz, 1.22 Hz and 1.48 Hz), the background (red hatched region) shows the limits of the parabolic signals

There are also limitations of data collection for the sinusoidal signals based on the constraints of the system, similar to the parabolic signal limitations discussed previously (Chapter 3). Consider Figure 5.15. When the frequency exceeds a certain value, the ellipse falls outside the rectangular box which means that no model data exists in that region because of either the physical constraints due to velocity limitations or signal distortion issues caused by high acceleration due to the system bandwidth limitation. The rectangular box is defined by two limitation boundary curves: one where acceleration is maximum and one where velocity is maximum. As the amplitude of the ellipse increases, the ellipse intersects or falls outside these boundaries. Figure 5.15 shows the situation where the acceleration boundaries are exceeded. A similar situation would occur if the maximum velocity boundaries are exceeded. Thus, two limitations on the maximum frequency of the input signal can be established beyond which no data can be secured. These maximum frequencies are given as:

$$f_{\max_v} = \frac{1}{2\pi} \frac{v_{\max}}{A} \quad (5.11)$$

$$f_{\max_a} = \frac{1}{2\pi} \sqrt{\frac{a_{\max}}{A}} \quad (5.12)$$

where A is the amplitude of the sinusoid displacement (x) and f_{\max_v} is the maximum frequency of the sinusoidal input signal when the maximum velocity of the sinusoidal signal reaches the maximum velocity of the maximum physical box. f_{\max_a} is the maximum frequency of the sinusoidal input signal when the maximum acceleration of sinusoidal signal reaches the maximum acceleration of the maximum physical box. The derivation of Equations 5.11 and 5.12 is provided in the Appendix H.

For VCHAS1, $f_{\max_v} = 1.88\text{Hz}$, and $f_{\max_a} = 1.33\text{Hz}$. To be consistent with the experiments performed using the parabolic signal, the maximum frequency of the sinusoidal signal chosen for the experiment was 1.48 Hz. For this case, there was no intersection with the maximum velocity limit; however, the ellipse did intersect the maximum acceleration limit boundary and exceeded it. Even though data could be obtained past the boundary, there was no data available from the parabolic signal experiment to compare it to. The consequence of this on the validation results will be considered later.

The value of the velocity at the intersection of the sinusoidal $v - a$ ellipse and the maximum or minimum acceleration boundaries of the limit boxes are determined to be:

$$v = \sqrt{\frac{A^2(2\pi f)^4 - a^2}{(2\pi f)^2}} \quad (5.13)$$

$$a = a_{\max} \quad \text{or} \quad a = a_{\min} \quad (5.14)$$

where A is the amplitude of the sinusoid displacement (x) and f is the frequency of the sinusoidal input. Details of derivation of Equations 5.13 is provided in Appendix H.

It must be noted that if part of the sinusoidal $v - a$ ellipse falls outside the maximum acceleration lines it is possible to extrapolate the model output using the meshing technique. If part (or all) of the sinusoidal $v - a$ ellipse falls inside the minimum acceleration lines (box) it is also possible to extrapolate the model output using the meshing technique. If part of the ellipse falls outside the maximum velocity lines, then no extrapolation is possible since the lookup table data in that region is zero (see Section 3.6.2).

Consider Figure 5.16. The elliptical $v - a$ curves show an expanded view of Figure 5.15 of the path of acceleration and velocity in Quadrant 1 when sinusoidal inputs are used.

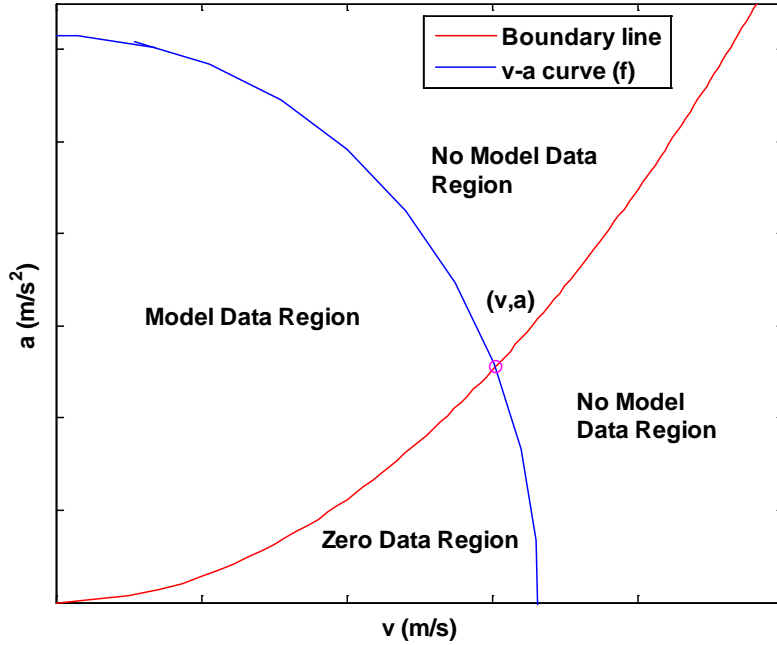


Figure 5.16 The intersection point (v, a) of the elliptical curve $(v - a)$ of sinusoidal signal and physical limit boundary line in Quadrant 1

As was pointed out in Chapter 3, it is quite evident that there are regions in which data does not exist in the models and hence the output is set to zero in these regions. Thus in subsequent figures, the output is set to zero in the waveforms because there is no data available (labelled as “Zero Data Region” in Figure 5.16). As discussed in Chapter 3, this clearly indicates a limitation of the 2D LUT model which was developed using the triangular velocity waveform approach. However, for demonstration purposes, a comparison of the 2D LUT model and Stribeck model can be illustrated in the regions where data has been obtained. Mathematically the intersection points can be found from the following equations:

$$v = A(2\pi f)\sqrt{2(\sqrt{2} - 1)} \quad (5.15)$$

$$a = A(2\pi f)^2(\sqrt{2} - 1) \quad (5.16)$$

where A is the amplitude of the sinusoid displacement (x) and f is the frequency of the sinusoidal input signal. Details of the derivation of Equations 5.15 and 5.16 are provided in Appendix H.

It should be noted that the intersection point of the $v - a$ curve of the sinusoidal signal and experimental boundary line applies to Quadrant 1 (Figure 5.16), but this same kind of intersection point occurs in all of the quadrants. The intersection points of other quadrants are provided in Appendix H.

Another limitation exists at very low frequencies in which part of the ellipse falls just outside the small rectangular box shown in Figure 5.15. Any data inside the box cannot be collected for this VCHAS and as for the case where data falls outside the larger box, in the following validation results, the data is extrapolated from the boundary data since the acceleration in these regions is very small.

The consequence of these limitations can be illustrated with four examples shown in Figures 5.17, 5.18, 5.19 and 5.20. The green lines represent real data (experimental data). The blue lines represent the small box extrapolated data. The red lines represent where data could not be collected (from the lookup table model) which are set to zero in the traces. Thus validation is only made in the regions in which the data is green and blue.

It should be noted that the green lines for the data available zone and the red lines for the no data zone will be removed for clarity in the following figures (Figures 5.17 - 19). The amplitude of the sinusoid is constant and only the frequency is changed.

Consider Figure 5.17. The 2D LUT data is available in following ranges (in green solid): Start Point (Sp) to Point 1, Point 2 to Point 3, and Point 4 to End Point (Ep). The 2D LUT data is not available in following data ranges (in red dash): Point 1 to Point 2, and Point 3 to Point 4.

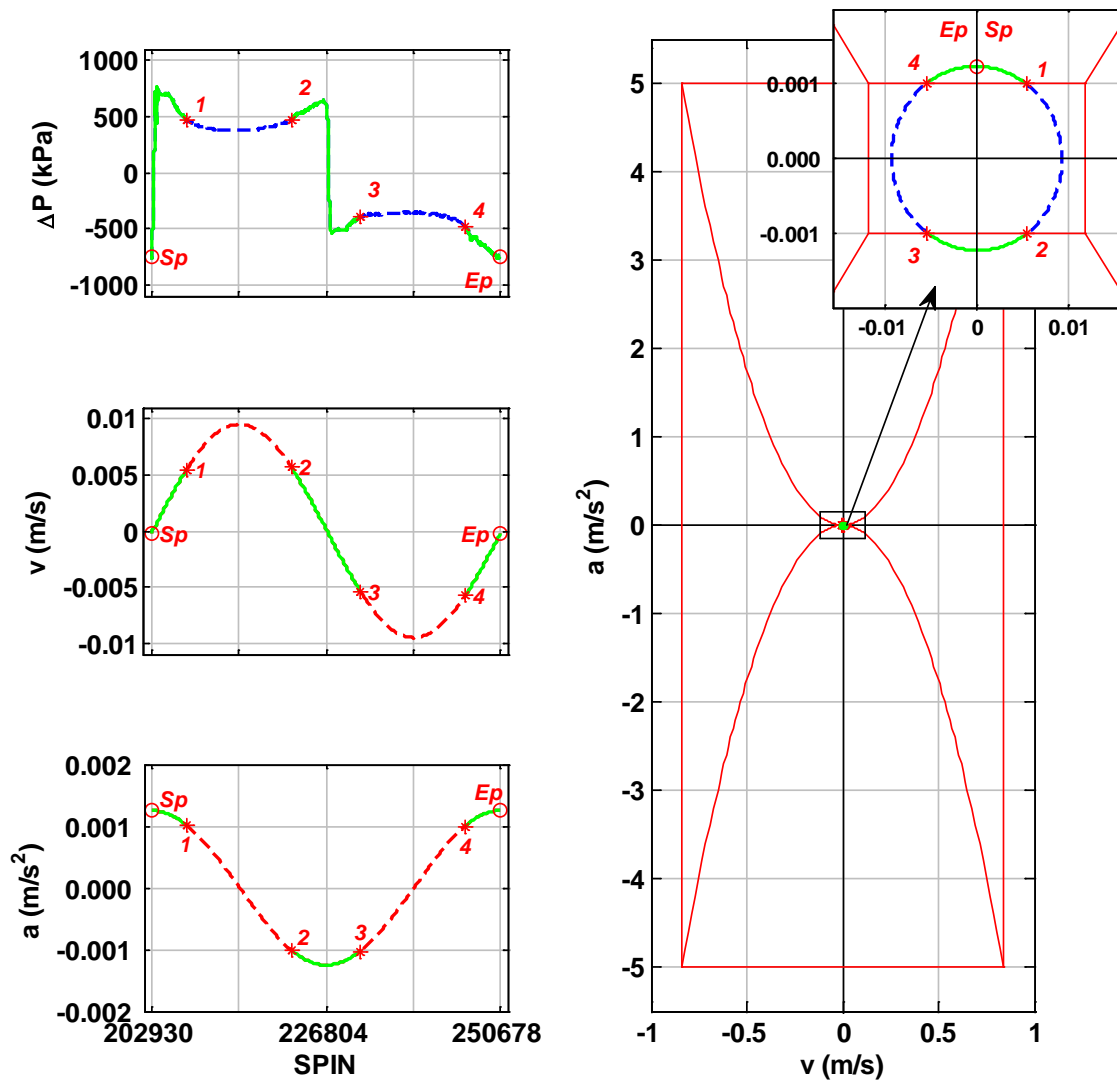


Figure 5.17 Sinusoidal signal for model validation at low frequency $f = 0.02$ Hz (see the zoom view for details). The experimental physical limitations are provided by red lines. The different colors in the elliptical paths of velocity, acceleration and ΔP curves of one cycle represent the model data availability. Derivation of the data ranges is given in Appendix H. (Red solid: Limitations of 2D LUT; Green: Model validation zone; Blue dash: Extrapolation data).

Consider Figure 5.18. The 2D LUT data is available in the following ranges (in green solid): Start Point (Sp) to Point 1, Point 2 to Point 3, and Point 4 to End Point (Ep). The 2D LUT data is not available in following data ranges (in red dash): Point 1 to Point 2, and Point 3 to Point 4.

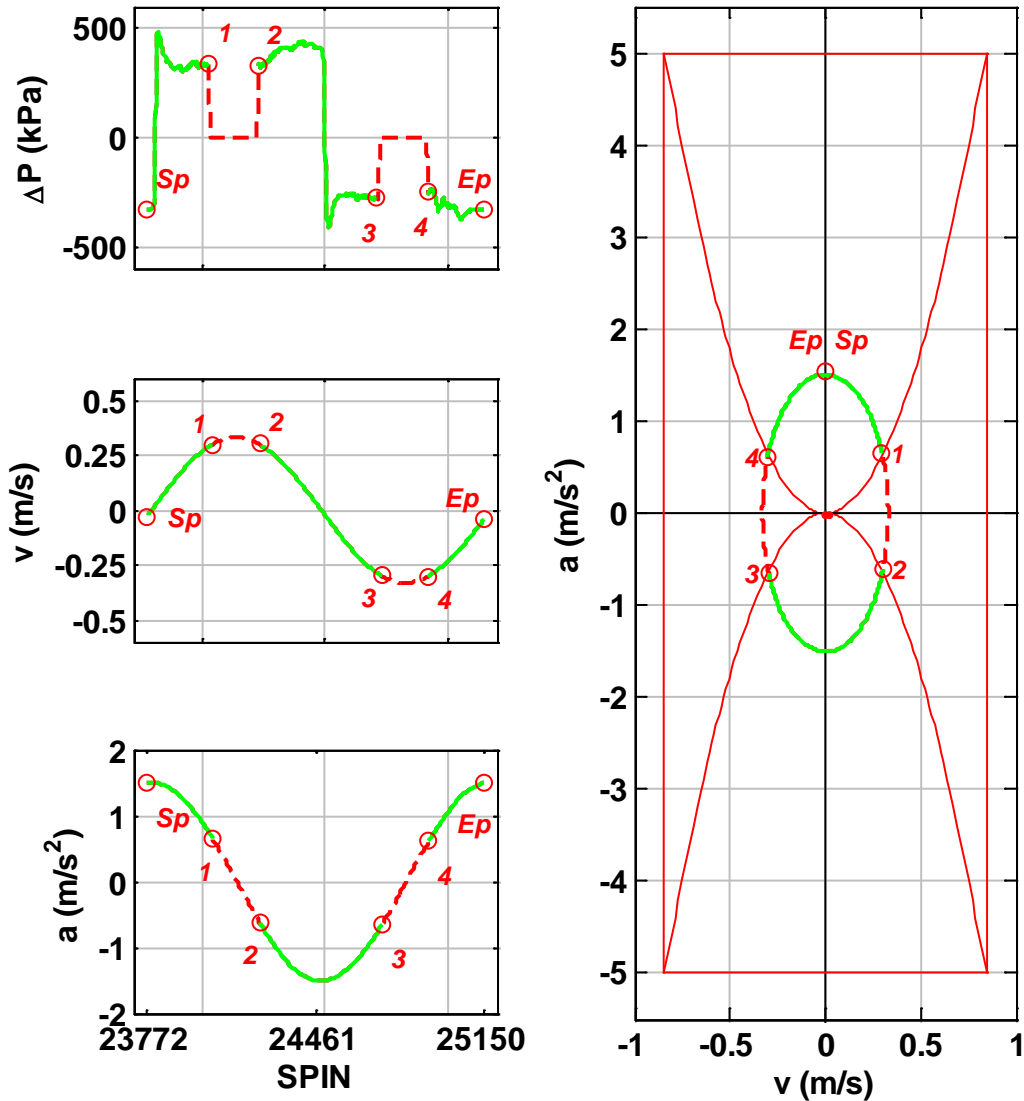


Figure 5.18 Sinusoidal signal for model validation at medium frequency $f = 0.73$ Hz. The experimental physical limitations are provided by red lines. The different colors in the elliptical paths of velocity, acceleration and ΔP curves of one cycle represent the model data availability. Derivation of the data ranges is given in Appendix H. (Red solid: Limitations of 2D LUT; Green: Model validation zone; Red dash: No model data zone).

Consider Figure 5.19. The 2D LUT data is available in following ranges (in green solid): Point 1 to Point 2, Point 3 to Point 4, Point 5 to Point 6 and Point 7 to Point 8. The 2D LUT data is not available in following data ranges (in red dash): Start Point (Sp) to Point 1, Point 2 to Point 3, Point 4 to Point 5, Point 6 to Point 7 and Point 8 to End Point (Ep).

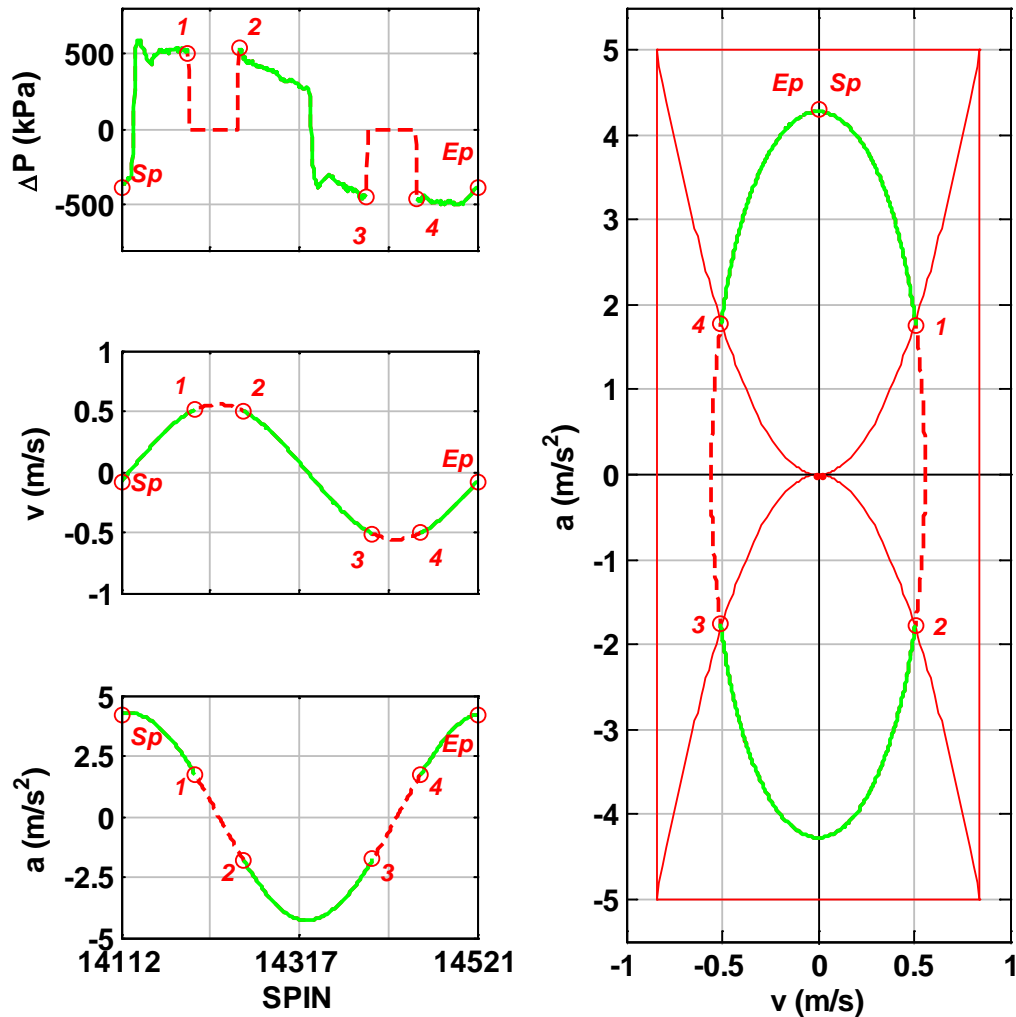


Figure 5.19 Sinusoidal signal for model validation at high frequency $f = 1.22$ Hz. The experimental physical limitations are provided by red lines. The different colors in the elliptical paths of velocity, acceleration and ΔP curves of one cycle represent the model data availability. Derivation of the data ranges is given in Appendix H. (Red solid: Limitations of 2D LUT; Green: Model validation zone; Red dash: No model data zone).

Consider Figure 5.20. The 2D LUT data is available in following ranges (in green solid): Point 1 to Point 2, Point 3 to Point 4, Point 5 to Point 6 and Point 7 to Point 8. The 2D LUT data is not available in following data ranges (in red dash): Start Point (Sp) to Point 1, Point 2 to Point 3, Point 4 to Point 5, Point 6 to Point 7 and Point 8 to End Point (Ep).

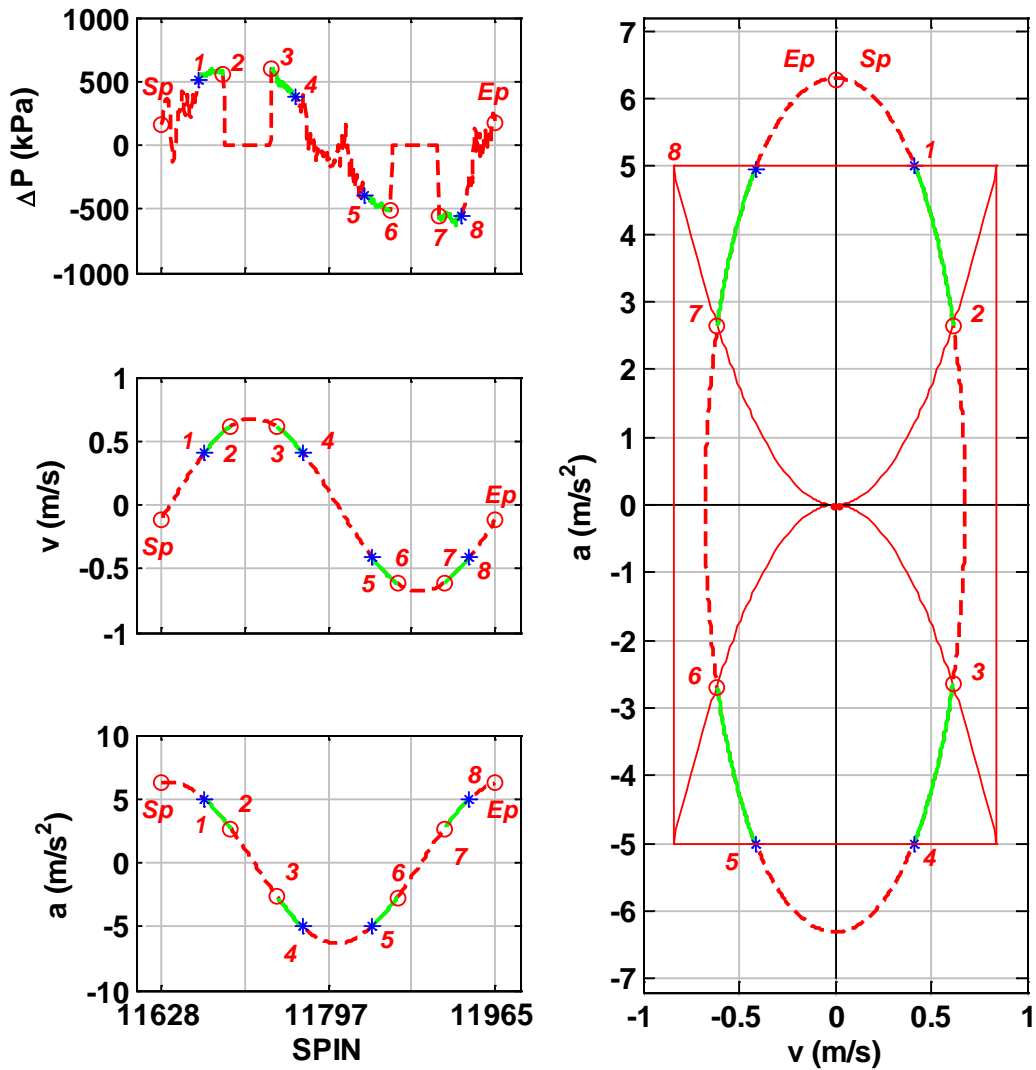


Figure 5.20 Sinusoidal signal for model validation at extreme high frequency $f = 1.48$ Hz. The experimental physical limitations are provided by red lines. The different colors in the elliptical paths of velocity, acceleration and ΔP curves of one cycle represent the model data availability. Derivation of the data ranges is given in Appendix H. (Red solid: Limitations of 2D LUT; Green: Model validation zone; Red dash: No model data zone).

5.2.5 2D LUT Data – ΔP_L – Meshing Technique

An important step in developing the semi-empirical model was the interpolation procedure to calculate new data to lie on the velocity set points. The model required two inputs: velocity and acceleration. Further, the model used velocity set points (defined as Universal Velocity Set points in Chapter 4) with acceleration as the family parameter. In using the model, however, it is highly

unlikely that the input velocity and acceleration values lie exactly on the Universal Velocity Set points velocity set point or acceleration family parameter value (defined as the Universal Acceleration Set points in Chapter 4). This is not a problem because all that is required is to use double interpolation between adjacent Universal Velocity Set points and Universal Acceleration Set points (family parameters). This is defined as a “meshing technique” and is illustrated graphically in Figure 5.21. In this Chapter, then, an interpolation meshing technique is introduced which in effect, allows any motion condition (v, a) (within the permissible data range) to be input into the model with the resulting output being an approximate ΔP (friction) value. In addition, this approach can be applied to all four quadrants which were introduced in Chapter 3.

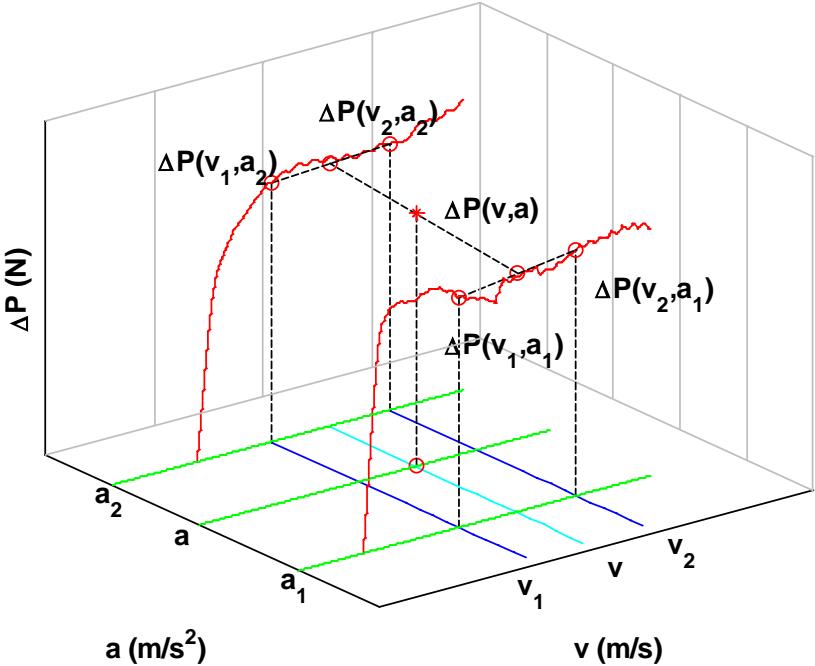


Figure 5.21 Meshing technique which employs double interpolation of an operating point (v, a)

In Figure 5.21, v and a are measured quantities. Also note that in the following discussions, v_1, v_2 and v are part of the Universal Velocity Set and a_1, a_2 and a are part of the Universal Acceleration Set. The objective then is to estimate $\Delta P(v, a)$ from the lookup table data. The simulation package used in this study was Matlab/Simulink© [107]. Matlab does not have a dedicated program to do double interpolation. The basis of the interpolation was the Newton method. This process is outlined in Figures 5.22, 5.23 and 5.24. The following steps to accomplish the meshing techniques are shown in these Figures in the form of a flow chart. Figure 5.22 shown

the general decision process and Figure 5.23 and Figure 5.24 describe the steps for single and double interpolation respectively. Figure 5.26 shows details of the interpolation.

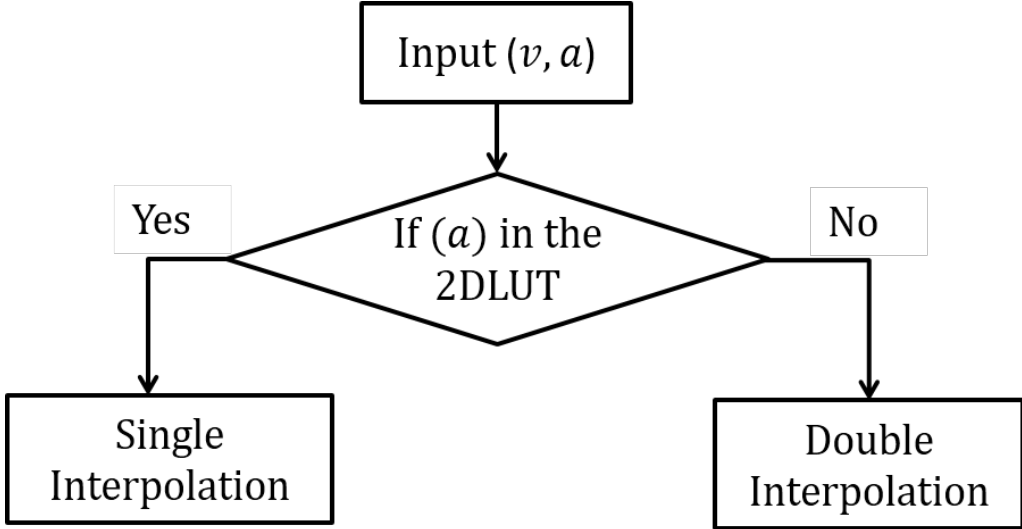


Figure 5.22 Flow chart of the meshing technique for determining single or double interpolation.

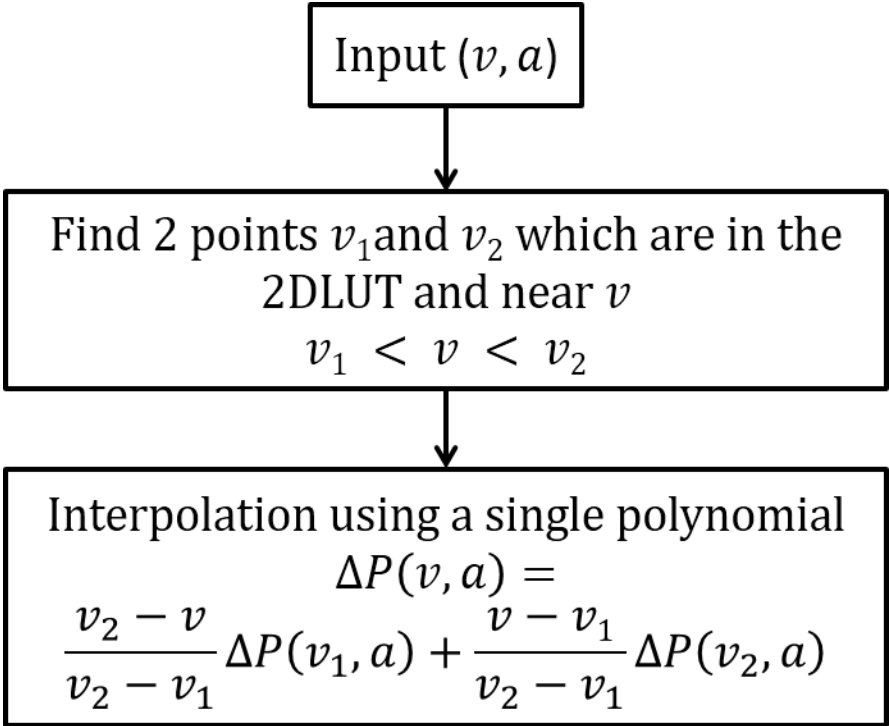


Figure 5.23 Single Interpolation algorithm. $\Delta P(v, a)$ is the calculated pressure differential (friction) value at input estimated velocity (v) and acceleration (a). All other terms are defined in Figure 5.2. Note that v_1, v_2 and v are part of the Universal Velocity Set and a_1, a_2 and a are part of the Universal Acceleration Set.

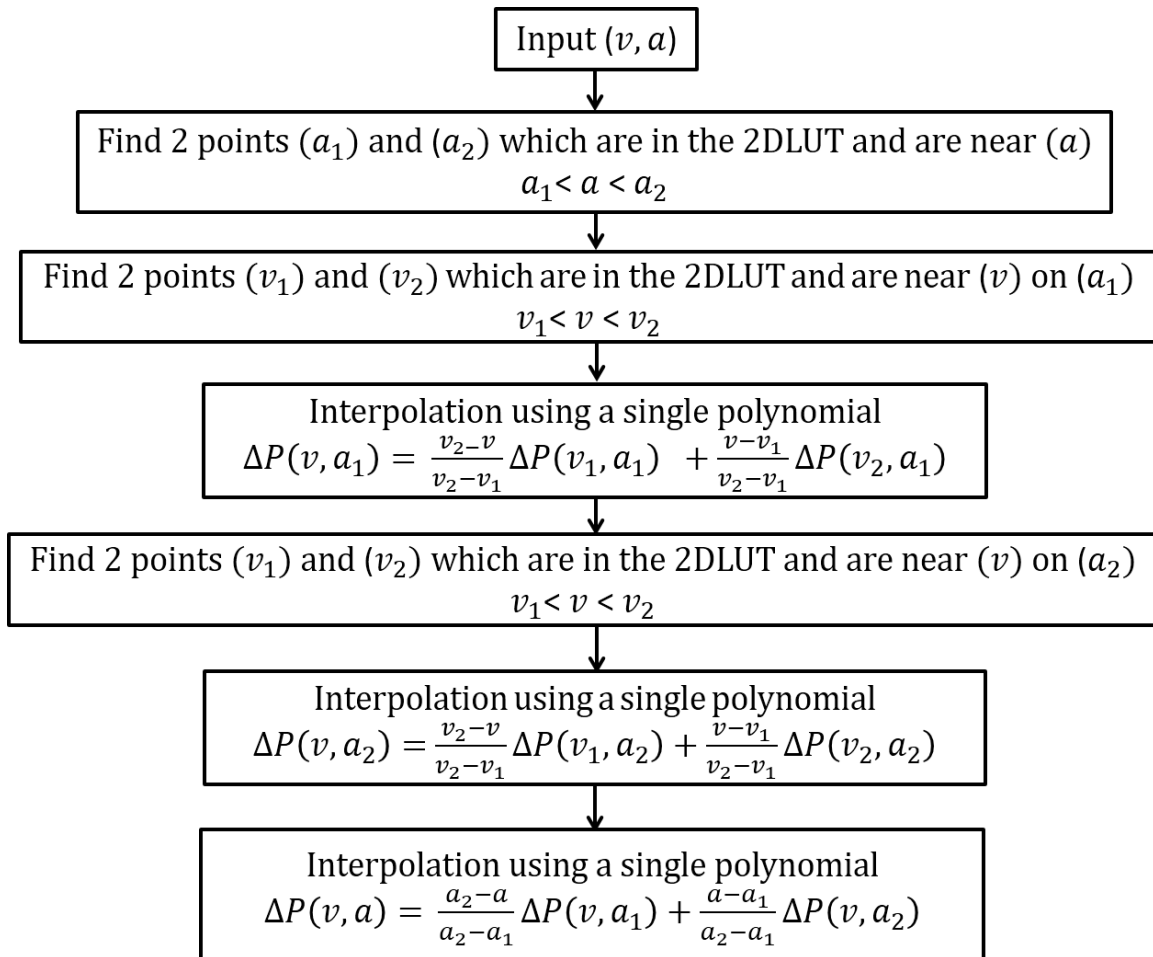


Figure 5.24 Double interpolation (or meshing) algorithm. $\Delta P(v, a)$ is the calculated pressure differential (friction) value at input estimated velocity (v) and acceleration (a). All other terms are defined in Figure 5.21. Note that v_1, v_2 and v are part of the Universal Velocity Set and a_1, a_2 and a are part of the Universal Acceleration Set

Please note, there are some locations in the 2D LUT where double interpolation does not give accurate results. This occurs near the boundary line where data and no data exist (see Figure 5.25). Since the double interpolation needs 4 points on the (v, a) plot to calculate a value (see Figure 5.21), any of the 4 interpolation points outside of the boundary (in the no data region) will lead to an underestimation of ΔP . This underestimation is a result of ΔP in the no data region being set to zero. A consequence of this is shown in Figure 5.26 where the red dash rectangles highlight the underestimated value of ΔP .

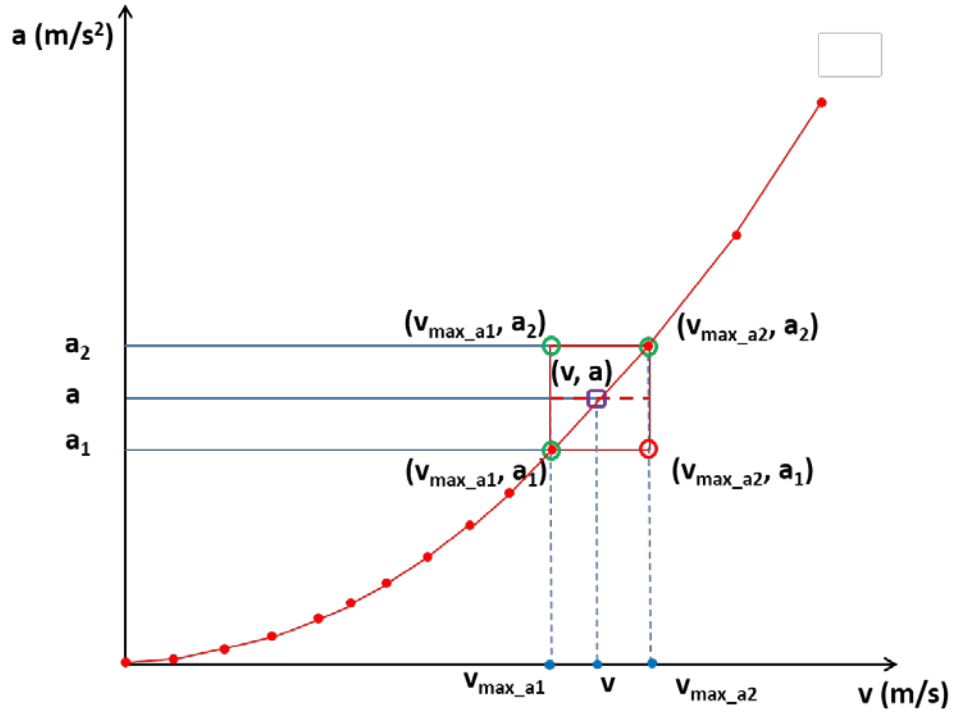


Figure 5.25 Interpolation limitation between two accelerations due to the 2D LUT model boundaries (Please note: the data in this figure is greatly exaggerated for clarity. Also Green circles can represent experimental data whereas red circles do not.)

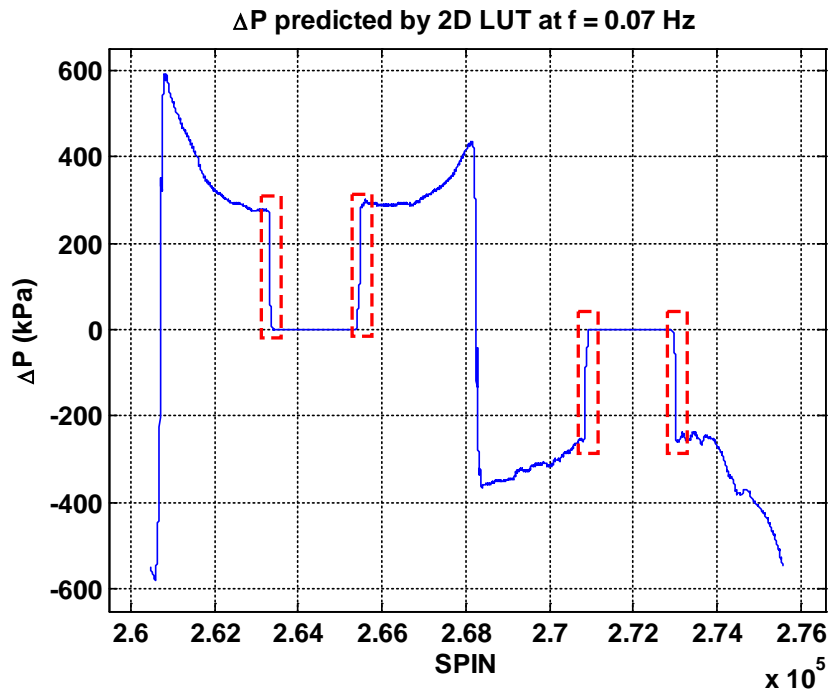


Figure 5.26 An example of the interpolated underestimation of ΔP predicted by the 2D LUT near the boundary lines at frequency $f = 0.07$ Hz

5.2.6 Stribeck Data – ΔP_s – Stribeck Lookup Table

As mentioned above, it was an objective of the thesis to be able to compare the 2D LUT model with the traditional Stribeck model for a sinusoidal input as was used for validating the 2D LUT model.

The model of a 2D Stribeck ΔP LUT is shown in Figure 5.27. It can be seen in the figure that the traces for each acceleration value are the same which indicates that the Stribeck model is acceleration independent. In contrast, the traces for the 2D LUT model shown in Figure 4.15 are all acceleration dependent.

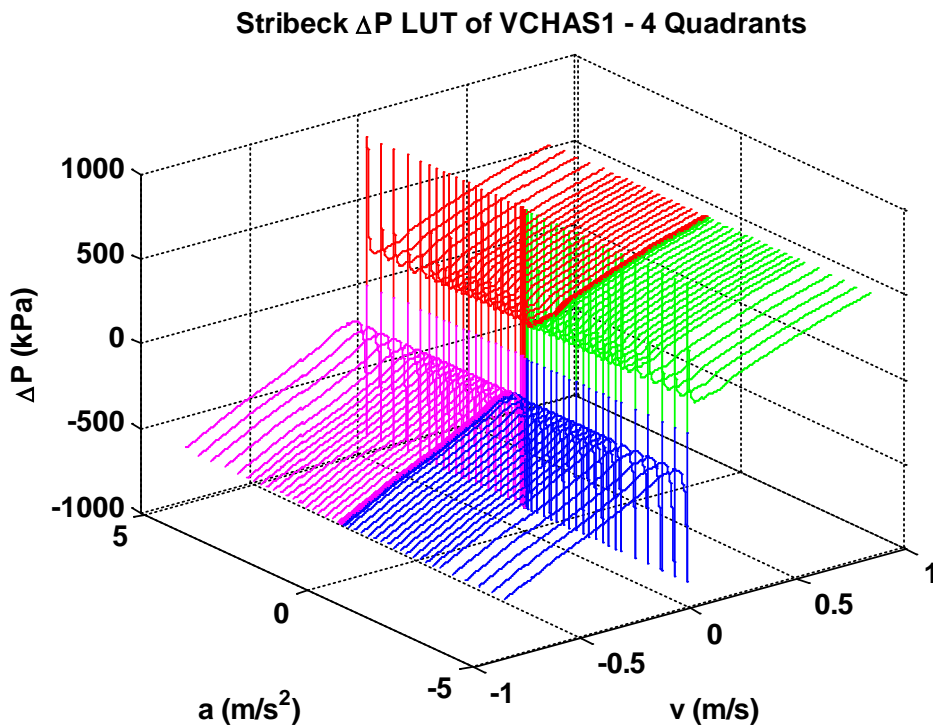


Figure 5.27 The 3D experimentally obtained Stribeck ΔP LUT for VCHAS1 which is used in the model comparison study (Red for Quadrant 1, Green for Quadrant 2, Blue for Quadrant 3, and Magenta for Quadrant 4).

5.2.7 Model Validation of 2D LUT of VCHAS1

Some typical results for a sinusoidal position input to the actuator model for VCHAS1 are shown in Figures 5.28 to 5.31. The model outputs using the Stribeck curves (shown in Figure 5.27 for VCHAS1) are also presented. In Figures 5.28 – 5.31, the regions where modeling data could not be collected is clearly labeled. It is equally apparent in the transition regions for the Stribeck model alone, that a large static friction is predicted for most frequencies which is not

consistent with the experimental results. This is not the case for the 2D LUT model except at very low frequencies (essentially low acceleration values). This again supports the hypothesis that friction is dependent on both velocity and acceleration.

Four different representative frequency sinusoidal signals have been chosen: low (0.01 Hz), medium (0.73 Hz), high (1.22 Hz) and extreme high (1.48 Hz). To facilitate further discussion, specific regions of the traces are highlighted by a “box”. The contents of each box is shown beneath each trace ((a), (b) (c)) in order to enlarge the traces and facilitate observation of the traces and the differences between the various models. In all cases, it apparent that the trend of the error is less for the 2D LUT than for the Stribeck model. It is noteworthy that regions in which the error of the two cases are similar correspond to regions of higher velocity. These are, in fact, regions of viscous friction in which the two models would tend to converge. The regions in which the trends of the error between the two models diverge are at low velocities where the 2D LUT model predicts a substantial reduction of the friction at all accelerations.

In all the plots, the measured and predicted responses (2D LUT and Stribeck only) are superimposed for visual inspection. In addition, the errors (e_{EL} and e_{ES} from Section 5.2.1) are plotted for the four selected representative frequencies. Where no data is available, the error will not be shown since it has no real meaning in these regions. Thus validation is only made in the regions in which the data is green and blue.

Consider Figures 5.28, for a sinusoidal signal at a very low frequency (0.02 Hz). The maximum acceleration is only 0.0012 (m/s^2), which is just a little over the minimum acceleration (0.001 m/s^2). From the “zoom view” of Figure 5.17, it is clear that most of the (v, a) points are inside the minimum physical limit box of the model data. However, accelerations are very low inside this box, and as such, the influence of acceleration is very limited. Extrapolation can be used to provide the model data for model validation. Comparing to the Stribeck model, the ΔP predicted by the 2D LUT matches the experimental data very well (between Start Point (Sp) to Point 1, Point 2 to Point 3 and Point 4 to End Point (Ep)). The ΔP value of 2D LUT between Point 1 to Point 2, and Point 3 to Point 4, are obtained by extrapolation of 2D LUT. It is observed that the extrapolation results match the experimental data with reasonable accuracy.

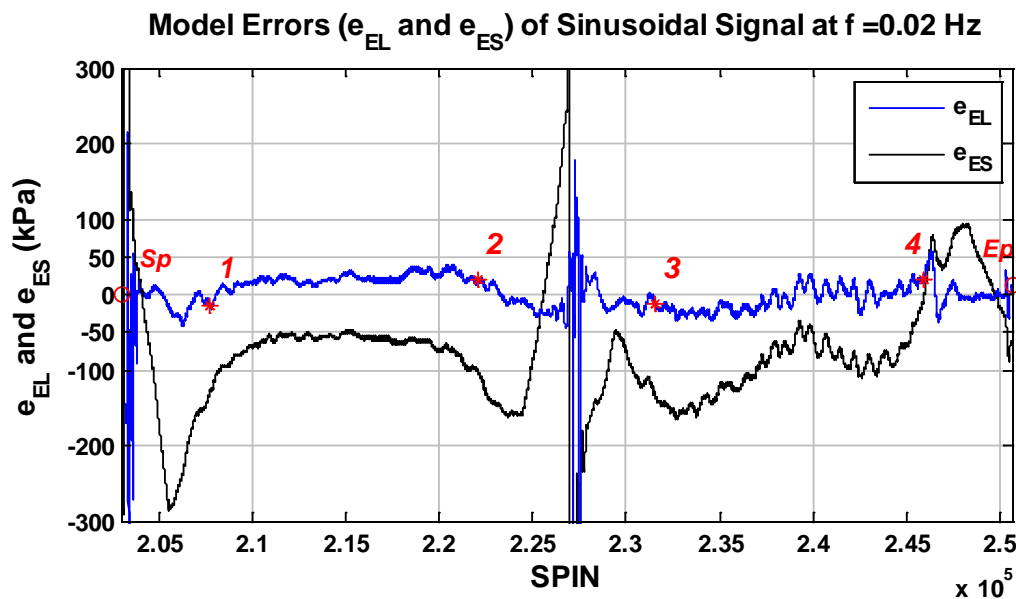
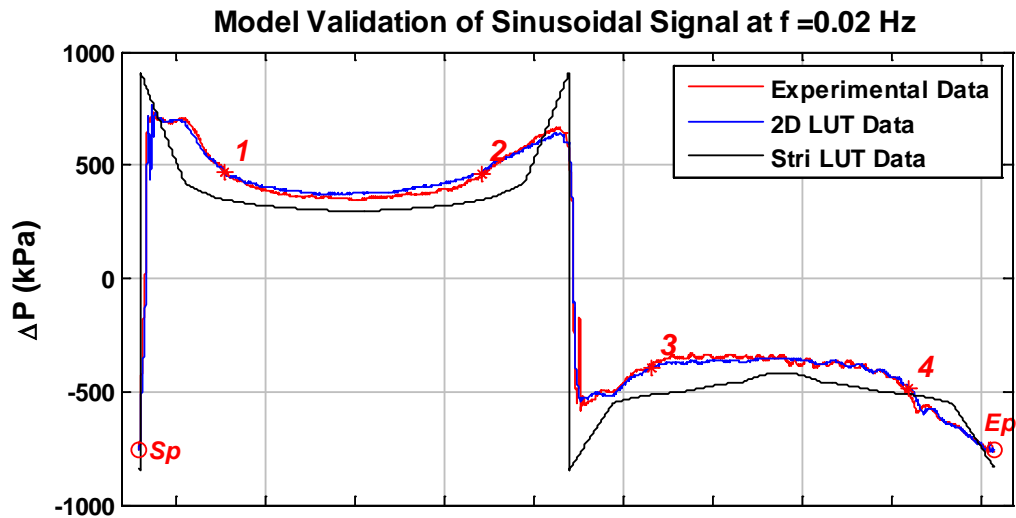


Figure 5.28 Model validation of the 2D LUT at a low sinusoidal frequency $f = 0.02$ Hz by superimposing the ΔP measured, ΔP from the 2D LUT and ΔP from the Stribeck model (Refer to Figure 5.17 for details of the regions (indicated by asterisks) with no model data of the 2D LUT at sinusoidal frequency $f = 0.02$ Hz)

In Figures 5.29 and 5.30, the model output (for model validation regions (that is from Start Point (Sp) to Point 1, Point 2 to Point 3, and Point 4 to End Point (Ep)), indicated in Figures 5.18 and 5.19) also follows the experimental results very closely compared to the Stribeck model. All the data (ellipses) fall within the rectangular boxes (Figure 5.18 and 5.19) for the two cases.

Since 2D LUT data is not available between Point 1 to Point 2, and Point 3 to Point 4. No comparison is possible. The model errors are left blank.

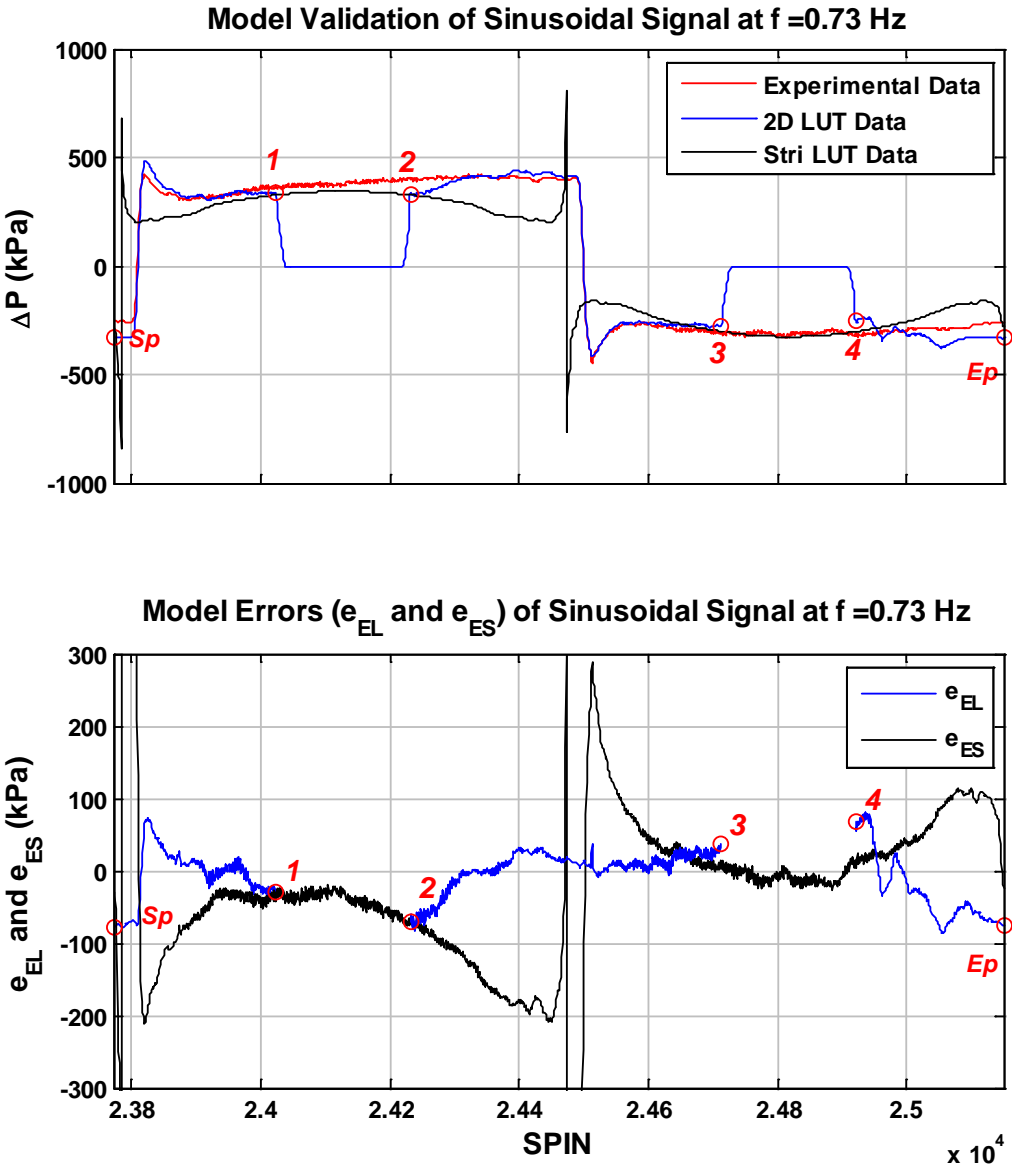


Figure 5.29 Model validation of the 2D LUT at a medium sinusoidal frequency $f = 0.73$ Hz by superimposing the ΔP measured, ΔP from the 2D LUT, and ΔP from the Stribeck model (Refer to Figure 5.18 for details of the regions (indicated by circles) with no model data of the 2D LUT at sinusoidal frequency $f = 0.73$ Hz). Stri LUT refers to the Stribeck model lookup table

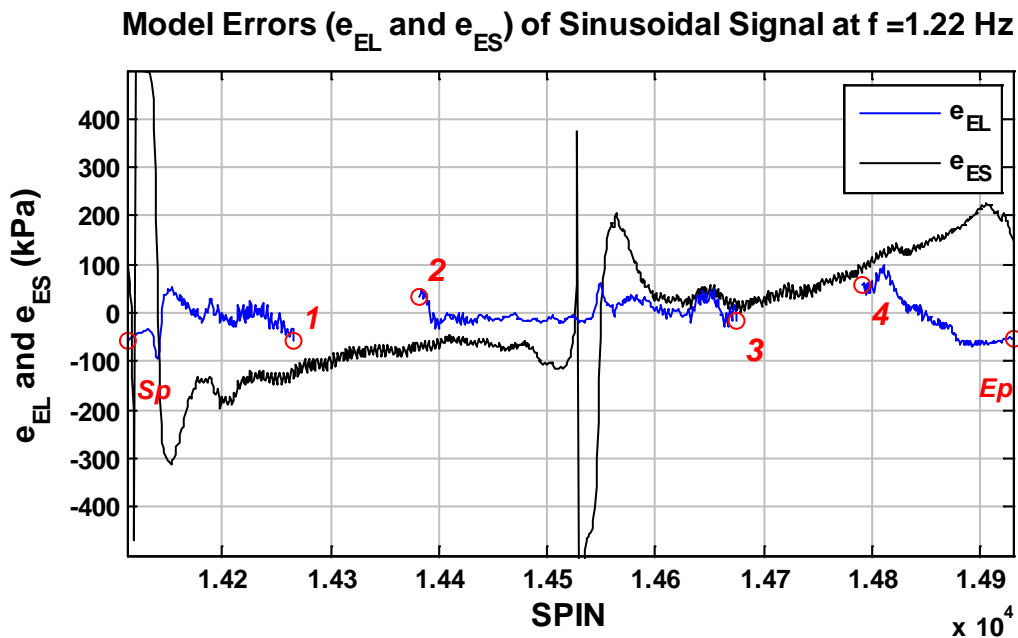
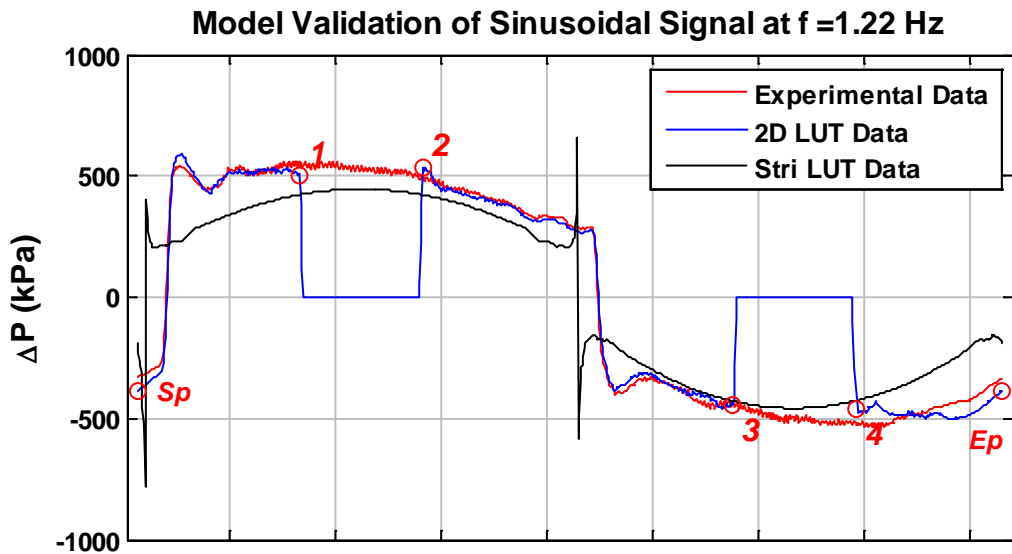


Figure 5.30 Model validation of the 2D LUT at a sinusoidal frequency $f = 1.22$ Hz by superimposing the ΔP measured, ΔP from the 2D LUT, and ΔP from the Striebeck model (Refer to Figure 5.19 for details of the regions (indicated by circles) with no model data of the 2D LUT at sinusoidal frequency $f = 1.22$ Hz). Stri LUT refers to the Striebeck model lookup table

Figure 5.31 shows the consequence of having some of the input sinusoid points fall outside the rectangular box (Figure 5.20). The portion of the curves in which validation can only be examined is indicated in following ranges: from Point 1 to Point 2, Point 3 to Point 4, Point5 to

Point 6, and Point 7 to Point 8. The ΔP predicted by 2D LUT matches the experimental data reasonably well.

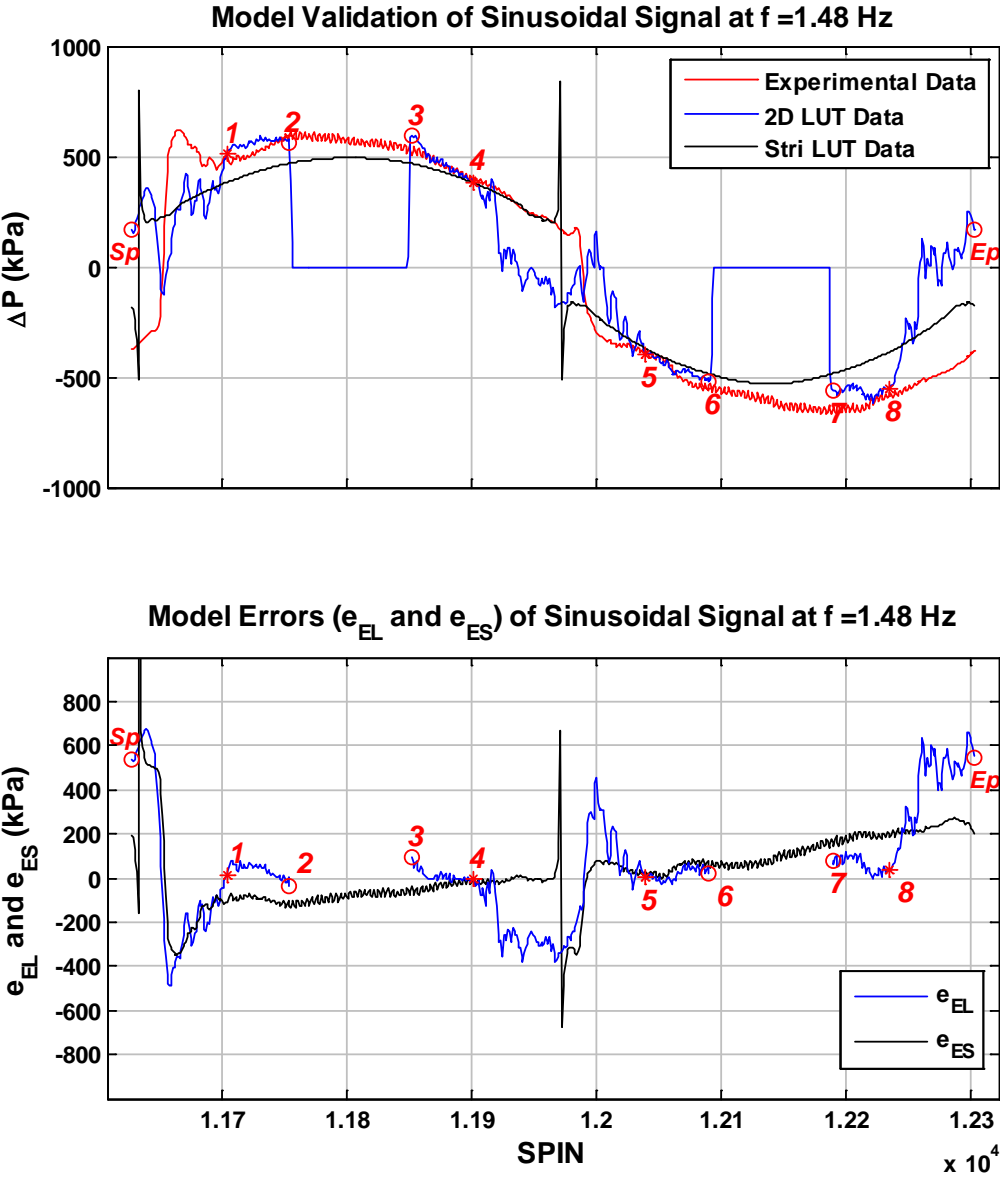


Figure 5.31 Model validation of the 2D LUT at a sinusoidal frequency $f = 1.48$ Hz by superimposing the ΔP measured, ΔP from 2D LUT, and ΔP from Stribeck model (Refer to Figure 5.20 for details of the regions (indicated by asterisks and circles) with no model data of the 2D LUT at sinusoidal frequency $f = 1.48$ Hz). Stri LUT refers to the Stribeck model lookup table

The ΔP between Start Point (Sp) to Point 1, Point 4 to Point 5, and Point 8 to End Point (Ep) are obtained by extrapolation of the 2D LUT. It is observed that the extrapolation results do not match the experimental data. It is because accelerations are very high (over 5 m/s^2) in those ranges, the influence of acceleration is significant (Figure 5.20). Extrapolation is no longer valid to provide the model data for model validation. Since 2D LUT data is not available between Point 2 to Point 3, and Point 6 to Point 7. No comparison is possible. The model errors are left blank. The blue predictions during the transition regions are invalid and cannot be used for comparison.

Representative model validation results for VCHAS1 were shown in Figures 5.28, 5.29 5.30 and 5.31 for frequencies of 0.02 Hz, 0.73 Hz, 1.22 Hz and 1.48 Hz respectively. Additional model validation results are provided in Appendix G. The model errors in model validation zones in all cases for the 2D LUT are very small and considered to be quite acceptable. Small errors do exist at various points of the traces, but this should be expected given that interpolation had to be made between known data points. Sources of error include: Error from the experimental measurement, error associated with a limited number of accelerations in the Universal Accelerating Set, error from modeling and interpolation that was used in the lookup table and simulation error in the mesh interpolation.

From Figure 5.31 it is observed that the predicted ΔP in the range where part of the input signal (ellipse) falls outside the maximum acceleration limit, is very poor suggesting that the extrapolation does not give accurate results in this region.

It was concluded that the 2D LUT model of VCHAS1 is validated for various sinusoidal signals at various frequencies for regions in which the data is considered valid or could be estimated using interpolation techniques. Further it is concluded that the 2D LUT model based on experimental data and the process outlined in Chapter 4 can be used for model implementation.

5.3 Discussion and Summary

In all cases, the 2D LUT model tends to follow the experimental results more closely than the Stribeck model. In particular, transition regions where slip-stick dominates (low velocities) do show significant errors when using the Stribeck model. It is interesting to note, however, that in quadrants 2 and 4, the error differences of the two models in some of the results tend to converge. As mentioned above, this is the region where velocity is much higher and viscous effects dominate.

Sinusoidal signals with different frequencies were input into the VCHAS1, to a Stribeck model and a semi-empirical models. It was observed that compared to the experimental results for all frequencies in all tests, the predictions (ΔP values) of the semi-empirical models (2D LUT models) were better than those of the Stribeck model.

The limitations of the 2D LUT model as developed using the triangular velocity waveform have been discussed in Chapters 3 and in Section 5.2. This does not take away the importance of the fact that friction shows a dependency on acceleration and velocity or the fact that a meshing technique can be used to extract the friction in a dynamic simulation environment. It simply means that the triangular velocity approach has its limitation in collecting a wide range of data. If that range could be expanded, then the meshing technique can readily be applied to extend the model. This will be discussed in greater detail in Chapter 6.

CHAPTER 6: CONCLUSIONS AND FUTURE WORKS

6.1 Summary

Lubricated friction plays a very important role in the response and accuracy of hydraulic servosystems. The model which is employed the most to represent the characteristics of friction is that of Stribeck in which the dependency of the friction force is based on velocity alone. In a simulation of step response of an Electrohydraulic Actuation System (EHA) using this Stribeck model (steady state friction model), the output response was predicted to be oscillatory (in form of limit cycles). Experimentally, no limits cycles were experienced which tended to show that perhaps the friction model was not complete and thus prompted the further investigation into the mechanism of lubricated friction. In this study, it was proposed that lubricated friction for this type of system could be classified as non-steady state friction as there appeared to be a dependency of the lubricated friction force on velocity and acceleration.

This thesis then has proposed a method to obtain a semi-empirical non-steady state friction model which relates the lubricated friction force to both velocity and acceleration. Limitations of the experimental approach were identified, but the dependency was clearly established. The relationship of lubricated friction (in this work, pressure differential, ΔP , across the actuator) as a function of velocity and acceleration was presented in a unique 2D lookup table (2D LUT).

The ΔP lookup table model was then integrated into a simulation of VCHAS1 and the output response compared to its experimental counterpart under sinusoidal input signals with various frequencies. In addition, a model employing only the Stribeck friction model was also considered and the results compared to the non-steady state friction model.

This Chapter will consider the objectives of the thesis and demonstrate how the objectives were met and present conclusions that can be drawn for each objective. In addition the major contributions will be summarized and a discussion on future work will also be presented.

It must be reiterated in this research that the lubricated friction could not be measured directly. However, because pressure drop (or pressure differential ΔP) across the actuator can be directly related to the lubricated friction, all data and results are presented in terms of ΔP . In these discussions, the terms friction and ΔP are used interchangeably.

6.2 Outcomes

The fundamental hypothesis for this work was as follows (Section 1.4): *Lubricated friction in hydraulic actuation systems is not only a function of velocity, but is also a function of both velocity and acceleration.* This hypothesis was addressed by considering the following objectives and conclusions.

Objective 1: To conduct a literature review on nonlinear friction modeling in hydraulic actuation systems;

This was accomplished in Chapters 1 and 2 in which the major publications that directly related to lubricated friction were presented. It was concluded that the primary model for lubricated friction in hydraulic actuators was based on the Stribeck model in which lubricated friction is modelled as a force which is a function of velocity only. However, other studies did identify that friction was a function of other parameters, but the relationship was not explicitly presented. The literature has shown that very little has been published on acceleration dependence of lubricated friction.

Objective 2: To experimentally investigate acceleration dependent nonlinear friction in hydraulic actuation systems;

This part of the study is directly related to the original hypothesis. The standard model of friction using “discrete” measurements was introduced which formed the basis of the classical Stribeck model in which friction was considered to be a function of velocity only (defined essentially as a static model). The concept of non-steady state friction (defined essentially as a dynamic model) was introduced in which it was postulated that the lubricated friction is in fact, a function of a second parameter, acceleration. A novel experimental technique for measuring this non-steady state friction was introduced in which a triangular velocity waveform was created in a valve controlled hydraulic actuation system (VCHAS) with closed loop control. This allowed the lubricated friction forces to be measured as a function of velocity in a continuous manner, but now with acceleration being held constant as a family parameter. It was also ascertained that the experimental approach did have limitations in that there were operating regions in which data could not be collected. This limitation did not interfere with the verification and validation of the hypothesis.

The data that could be collected was plotted as a function of velocity with acceleration as the family parameter and it was very evident that acceleration did influence the non-steady state friction characteristic. Two different actuators (VCHAS1 and VCHAS2) were tested and the results were consistent from actuator to actuator.

The conclusion was that the primary hypothesis “Lubricated friction in hydraulic actuation systems is not only a function of velocity but is also a function of both velocity and acceleration” was established.

Objective 3: To develop a semi-empirical data based model (2D LUT) of velocity and acceleration dependent nonlinear friction (in terms of ΔP);

With the hypothesis established, it was necessary to develop a methodology to implement the model in a simulation environment. A method of taking the experimental data and presenting the results in a 3D model was introduced. This involved preprocessing the data to fall on Universal Velocity Set points via interpolation with acceleration being used as a family parameter (Universal Acceleration Set). In addition, a technique to reduce the number of data points in the lookup table was forwarded. The model could be preprocessed offline and as such, the time to preprocess is not an issue. As a last point, the proposed approach was able to capture true friction characteristics (and hence model non-steady state friction) in all four quadrants. The lubricated friction lookup table was verified and validated by verifying and validating ΔP LUT. It was concluded that a data based 2D LUT (semi-empirical model) could be created using this approach.

Objective 4: To experimentally implement the new semi-empirical data based model in a simulation environment and to compare the outputs to a model in which the Stribeck model of friction was used.

In order to implement the model, a double interpolation was necessary because the data was expressed at Universal Velocity Set points with acceleration as a family parameter and the actual input velocity and acceleration would not necessarily lie on these points. A sinusoidal actuator displacement input was chosen to test the simulations as it was not used in the collection of the original data. The output of the simulation was compared to the experimental results and it was evident that for the range in which data could be collected in developing the model, the proposed 2D LUT model predicted an output that was superior to a model which used a standard Stribeck model. It was concluded that the semi-empirical model could be integrated into a

simulation environment and predict outputs in a superior fashion when compared to the Stribeck friction model.

6.3 Discussion on the Limitations of the Triangular Velocity Waveform

As mentioned several times through this discourse, one disappointing outcome in this research was the limitation of the triangular velocity approach in collecting data for the semi-empirical 2D LUT model. This did not in any fashion interfere with verification and validation of the main hypothesis. Indeed, it was the fact that a method in which acceleration could be made a family parameter brought to light the conclusion that non-steady state friction was a function of both velocity and acceleration. Further, the approach made it possible to observe lubricated friction behavior in all quadrants illustrating the presence of hysteresis.

The limitations of the triangular velocity approach essentially defined regions in which data could not be collected. Where this created an issue was in the implementation of the model into a simulation environment. To compensate, the output of the simulation was set to zero in these regions.

6.4 Important Contributions

- A comprehensive review of nonlinear friction modeling methods has been conducted.
- Concepts of steady state friction and non-steady state friction have been introduced which clearly define operating conditions.
- It has been established that non-steady state friction is a function of velocity and acceleration and that the Stribeck model is a subset of this dynamic friction model in which acceleration is zero.
- A novel technique of measuring non-steady state friction using a triangular velocity waveform was introduced. Limitations in the approach were established.
- A novel 3D nonlinear friction model (semi-empirical) with acceleration effects incorporated has been developed and verified in the form of a 2D lookup table (2D LUT). Several unique steps were introduced to place data on Universal Velocity Set points and to reduce the number of data points in the lookup table.

- The 3D novel nonlinear friction model could readily be integrated into a simulation environment and validated by sinusoidal signals with various frequencies.
- The semi-empirical 2D LUT model so developed is a more global representation of hydraulic actuator lubricated friction.

6.5 Conclusions

From the outcomes of this research, it was concluded that the lubricated friction of hydraulic actuation systems is very complicated. The Stribeck model was measured and obtained under steady state conditions which cannot describe the hysteresis of the system, as was observed for both VCHAS1 and VCHAS2. It was also observed that at low accelerations, the non-steady state friction curves approach the Stribeck model.

Experimental results in this study reveal that non-steady state friction is a more general form of the dynamic friction. In addition steady state friction is just a special case of the non-steady state friction, which is highly acceleration dependent. When the acceleration increases, the Stribeck effect decreases, and indeed, can reach conditions where it no longer exists within the operating velocity range. The results of this study imply that one must use traditional friction models (velocity dependent only) with care when the system experiences non-steady state motion conditions. This result can be applied to any actuator (linear and rotary) and provides a new way in which the dynamic friction can be viewed and modeled.

It was also concluded that the lubricated friction forces of VCHAS1 and VCHAS2 are strongly dependent on acceleration. These dependencies appear in all quadrants. Thus it is believed that the hypothesis stated in Chapter 1 is consistent with the experimental evidence shown by three different actuators (EHA, VCHAS1 and VCHAS2).

It was also concluded that parabolic curve fitting for model verification and sinusoidal curve fitting for model validation are very effective. The velocity and acceleration extracted from curve fitted displacements were “clean signals” with no phase shift or significant distortion.

Finally, it was concluded that the 2D LUT is a viable tool for modeling the non-steady state friction of hydraulic actuation systems. However, in those regions in which the data could be integrated into the 2D LUT model, the output from the simulations were in much better agreement with the experimental results than if the traditional Stribeck model was used. This further enforces the conclusion that the model which incorporated non-steady dynamic friction as

a function of acceleration reflected the true physical situation more closely, which in turn further substantiated the prime hypothesis.

The 2D LUT non-steady state friction models based on the experiments of this study appeared to represent the actual friction in the system more accurately than the traditional Stribeck model. A further point needs to be raised. The basic concept in the development of the 2D LUT model was **not** influenced by the limitation of the triangular velocity waveform issue. The concept of creating a Universal Velocity Set with acceleration as the family parameter (Universal Acceleration Set) was enhanced by the approach. Indeed, implementing a 2D LUT required that data fall on set points of the Universal Velocity Set. All the limitation did was to restrict the simulation (the application) to be used in regions in which data was able to be collected. This then was considered to be the weakness in the triangular velocity waveform approach.

6.6 Future Research Recommendations

Recommendation for future works of this study include:

6.6.1 Increase the Cylinder Stroke

Increasing the stroke of the cylinder will help to increase the data collection area, which would make the model verification and validation more accurate. However, increasing the stroke will not fully remove the “no data” area, unless it is accompanied with a higher flow capacity pumping systems. Use of a rotary system would remove the stroke limitation. The rotary systems will be the better option to completely overcome this limitation. With much larger maximum acceleration and maximum velocity possibilities, they are still limited by the pressure and flow capacity of the hydraulic power supply.

6.6.2 Use Other Types of Input Signals

It should be recalled that the 2D LUT was accomplished using a triangular position signal which facilitated acceleration being used as the family parameter. It is suggested that the 2D LUT model be enhanced by using other types of input signals (sinusoidal, random for example). The author of this thesis has spent some time examining methods in which the model data collection limitation could be overcome. It is suggested that a grid of velocity and acceleration set points (Universal Velocity Set and Universal Acceleration Set) required for a 2D LUT could be

expanded into these regions of no data. Then using some other type of input (including sinusoids for example), numerous data points could be collected and filled into the no data regions in-between the set points as illustrated in Figure 3.18. Then a variety of off line techniques could be used to calculate a representative value of all the points in that “box” (centroid, statistical average, etc.) and then assigned the value to one of the set points in the 2D LUT. Such an approach could overcome the issue of missing data regions. This then would be a hybrid 2D LUT of data obtained from the triangular velocity approach (continuous), the Stribeck friction approach (discrete) for zero acceleration and the representative value from the “box”.

6.6.3 Use Adaptive Sampling Rates

It is suggested that adaptive sampling rates for the input signals be used in data collection. The objective would be to make the Δv constant over different input signals at different accelerations/frequencies. Thus, in the process of modeling the 2D LUT, no interpolation is needed to generate friction on the Universal Velocity Set, which will remove the modeling error caused by the interpolating process.

6.6.4 Use Parameter Estimation for Curve Fitting for Analytical Modeling

It is suggested that parameter estimation / identification and curve fitting techniques be considered to fit a group of nonlinear curves or a nonlinear surface to the data and then use the analytical model for implementation and control purposes, and to better understand the physical principles behind the non-steady state friction. Mathematically, curve fitting (including surface fitting) assumes equations (such as Chi-square distribution functions) are based on the characteristics of the data set to fit the data set. The parameters of the equation are determined such that the equation best fits the data points by using the least square method etc. When a small number of the data points are involved, then a single polynomial might be sufficient for the curve fitting; when a large number data points are involved, then the curve fitting could become very complicated (too complex for any practical usage in model simulation etc.).

6.6.5 Use Neural Networks to Replace the Lookup Table (LUT)

It is suggested that Neural Networks or Expert Systems be examined to do the interpolation. Neural networks are very powerful in doing such tasks especially if the data is nonlinear [103-105]. However, the issue of the data spread at higher accelerations could pose a problem as the data is “scarce” in some regions. Scarce data can be relieved by using higher sampling rates to increase the number of data points at high acceleration conditions; the limitation is the data memory limit of the data acquisition equipment. Further, if the data “crosses over” due to experimental error, the neural network can become confused and produce erroneous results.

6.6.6 Extend to Rate-Dependent Model of Static and Dynamic Friction

It would be very interesting to extend this research to a more general case, which covers the static friction range. There is a need to develop a universal rate dependent friction model to simulate the static and dynamic behavior in various motion conditions (including the presliding condition). In the presliding stage, the static friction has dependency on the applied force, but also on the applied force rate. In the sliding stage, the dynamic friction has a dependency on the velocity, but also on the velocity change rate (acceleration).

In addition since friction is dependent on the seal conditions, and since seal conditions are pressure dependent, then another future study should examine this dependency in greater detail.

LIST OF REFERENCES

- [1] Manring, N., 2005, "Hydraulic Control Systems," John Wiley & Sons, Hoboken, N.J, pp.1-446.
- [2] Chinniah, Y., 2004, "Fault Detection in the Electrohydraulic Actuator using Extended Kalman Filter," PhD Thesis, University of Saskatchewan, pp. 1-272.
- [3] Habibi, S., Burton, R., and Sampson, E., 2006, "High Precision Hydrostatic Actuation Systems for Micro-and Nanomanipulation of Heavy Loads," *Journal of Dynamic Systems, Measurement and Control, Transactions of the ASME*, 128(4) pp.778-787.
- [4] Habibi, S., and Goldenberg, A., 2000, "Design of a New High-Performance ElectroHydraulic Actuator," *IEEE/ASME Transactions on Mechatronics*, 5(2) pp.158-164.
- [5] Sampson, E., Habibi, S., Burton, R., Chinniah, Y., 2005, "Model Identification of the Electrohydraulic Actuator for Small Signal Inputs," *Bath Conference on Power Transmission and Motion Control, PTMC 2005*, pp.163-177.
- [6] Li, W., Burton, R., and Habibi, S., 2007, "Investigation of a High Precision Hydrostatic Actuation System - How Nonlinearities Affect its Performance," *ASME International Mechanical Engineering Congress and Exposition, IMECE 2007*.
- [7] Jacobson, B., 2003, "The Stribeck Memorial Lecture," *Tribology International*, 36(11) pp.781-789.
- [8] Chinniah, Y., Burton, R., Habibi, S., 2008, "Identification of the Nonlinear Friction Characteristics in a Hydraulic Actuator using the Extended Kalman Filter," *Transactions of the Canadian Society for Mechanical Engineering*, 32(2) pp.121-136.
- [9] Blau, P., 2009, "Friction Science and Technology: From Concepts to Applications," *CRC Press, Boca Raton, FL*, pp.1-420.
- [10] Pytel, A., Kiusalaas, J., 1999, "Engineering Mechanics Statics," *Pacific Grove: Brooks/Cole*, pp.1-526.
- [11] Szeri, A., 2011, "Fluid film lubrication," *Cambridge University Press, Cambridge; New York*, pp.1-547.
- [12] Yanada, H., Sekikawa, Y., 2008, "Modeling of Dynamic Behaviors of Friction," *Mechatronics*, 18(7) pp.330-339.
- [13] Olsson, H., Astrom, K., Canudas de Wit, C., Gafvert, M., Lischinsky, P., 1998, "Friction Models and Friction Compensation," *European Journal of Control*, 4(3) pp.176-195.

- [14] Akers, A., Gassman, M., and Smith, R.J., 2006, "Hydraulic power system analysis," CRC/Taylor & Francis, Boca Raton, FL, pp. 365.
- [15] Burton, R., 1975, "Analytic and Experimental Prediction of Limit Cycle Oscillations in an Inertially Loaded Hydraulic Control Valve," PhD Thesis, University of Saskatchewan, pp.1-164.
- [16] Armstrong-Helouvry, B., 1991, "Control of Machines with Friction," Kluwer Academic Publishers, Boston, pp.1-173.
- [17] Sekhavat, P., 2006, "Impact Stabilizing Controller for Hydraulic Actuators with Friction: Theory and Experiments," *Control Engineering Practice*, 14(12) pp.1423-1433.
- [18] Goerres, M., and Murrenhoff, H., 2004, "Investigation of Friction of Piston Rod Sealing Systems," Bath Conference on Power Transmission and Motion Control, PTMC 2004, pp.37-50.
- [19] Drincic, B., 2012, "Mechanical Models of Friction that Exhibit Hysteresis, Stick-Slip, and the Stribeck Effect," PhD Thesis, The University of Michigan, pp.1-162.
- [20] Sugimura, J., Jones, W., Spikes, H., 1998, "EHD Film Thickness in Non-Steady State Contacts," *Transactions of the ASME. Journal of Tribology*, 120(3) pp.442-452.
- [21] Hori, Y., 2006, "Hydrodynamic Lubrication," Springer, Tokyo, pp.1-231.
- [22] Owen, W., and Croft, E., 2003, "The Reduction of Stick-Slip Friction in Hydraulic Actuators," *IEEE/ASME Transactions on Mechatronics*, 8(3), pp. 362-371.
- [23] Harnoy, A., 2008, "Modeling and Measuring Friction Effects," *IEEE Control Systems Magazine*, 28(6) pp.82-92.
- [24] Li, W., Burton, R., Habibi, S., Schoenau G., Wu, F., 2010, "Novel Dynamic Friction Modeling of a High Precision Electro-Hydrostatic Actuator (EHA) System," Bath/ASME Symposium on Fluid Power and Motion Control, FPMC 2010, pp.120-128.
- [25] Li, S., Bitner D., Burton, R., Schoenau G., 2013, "Experimental Investigation of Acceleration Dependent Nonlinear Friction in Hydraulic Actuation Systems," 24th Canadian Congress of Applied Mechanics (CANCAM) 2013, CS-9.
- [26] Armstrong-Helouvry, B., Dupont, P., and Canudas De Wit, C., 1994, "A Survey of Models, Analysis Tools and Compensation Methods for the Control of Machines with Friction," *Automatica*, 30(7) pp.1083-1138.
- [27] Feeny, B., Guran, A., Hinrichs, N., Popp, K., 1998, "A Historical Review on Dry Friction and Stick-Slip Phenomena," *Applied Mechanics Reviews*, 51(5) pp.321-341.

- [28] Shih, Y., Lee, A., 2003, "Survey on Modeling and Control for Motion Systems with Friction," *Journal of the Chinese Society of Mechanical Engineers*, 24(4) pp.337-352.
- [29] Oden, J., Martins, J., 1985, "Models and Computational Methods for Dynamic Friction Phenomena," *Computer Methods in Applied Mechanics and Engineering*, 52(1-3), pp.527-634.
- [30] Lischinsky, P., Canudas-de-Wit, C., Morel, G., 1999, "Friction Compensation for an Industrial Hydraulic Robot," *IEEE Control Systems Magazine*, 19(1) pp.25-32.
- [31] Armstrong-Helouvry, B., 1990, "Stick-slip arising from Stribeck friction, Robotics and Automation," *Proceedings 1990 IEEE International Conference on Robotics and Automation*, (2), pp.1377-1382.
- [32] Wensrich, C., 2006, "Slip-Stick Motion in Harmonic Oscillator Chains Subject to Coulomb Friction," *Tribology International*, 39(6) pp.490-495.
- [33] Choux, M., Tyapin, I., Hovland, G., 2012, "Extended friction model of a hydraulic actuated system," *Annual Proceeding of Reliability and Maintainability Symposium, RAMS2012*, pp.1-6.
- [34] Parr, E., 2011, "Hydraulics and Pneumatics: a Technician's and Engineer's Guide," Butterworth-Heinemann, Amsterdam, pp.1-238.
- [35] Nikas, G., 2010, "Eighty Years of Research on Hydraulic Reciprocating Seals: Review of Tribological Studies and Related Topics since the 1930s," *Proceedings of the Institution of Mechanical Engineers, Part J: Journal of Engineering Tribology*, 224(1) pp. 1-23.
- [36] Sullivan, J., 1975, "Fluid power: Theory and Applications," Reston Pub. Co., Reston, Va., pp.1-460.
- [37] Salant, R., Maser, N., Yang, B., 2007, "Numerical Model of a Reciprocating Hydraulic Rod Seal," *Transactions of the ASME Journal of Tribology*, 129(1) pp.91-97.
- [38] Wassink, D., 1996, "Friction Dynamics in Low Speed, Lubricated Sliding of Rubber: A Case Study of Lip Seals," PhD Thesis, The University of Michigan, pp.1-223.
- [39] Nikas, G., 2003, "Elastohydrodynamics and Mechanics of Rectangular Elastomeric Seals for Reciprocating Piston Rods," *Journal of Tribology*, 125(1) pp.60-69.
- [40] Meikandan, N., Raman, R., Singaperumal, M., 1994, "Experimental Study of Friction in Hydraulic Actuators with Sealless Pistons," *Wear*, 176(1) pp.131-135.
- [41] Tran, X., Hafizah, N., Yanada, H., 2012, "Modeling of Dynamic Friction Behaviors of Hydraulic Cylinders," *Mechatronics*, 22(1) pp.65-75.

- [42] Blackburn, J., Reethof, G., Shearer, J., 1960, "Fluid Power Control," Technology Press of M.I.T., Cambridge, Mass., pp.1-710.
- [43] Tran, X., Matsui, A., Yanada, H., 2010, "Effects of Viscosity of Type of Oil on Dynamic Behaviors of Friction of Hydraulic Cylinder," *JFPS International Journal of Fluid Power System*, 3(2) pp.16-23.
- [44] Merritt, H., 1967, "Hydraulic Control Systems," Wiley, New York, pp.1-358.
- [45] American Institute of Aeronautics and Astronautics (AIAA), 2002, "Guide for the Verification and Validation of Computational Fluid Dynamics Simulations (AIAA G-077-1998(2002))," AIAA Standards, pp.1-20.
- [46] Hess, D.P., and Soom, A., 1990, "Friction at a Lubricated Line Contact Operating at Oscillating Sliding Velocities," *Journal of Tribology*, 112(1) pp.147-152.
- [47] Kwak, B., 2000, "Nonlinear System Identification with an Application to Hydraulic Actuator Friction Dynamics," PhD Thesis, The University of Michigan, pp.1-165.
- [48] Stribeck, R., 1902, "Die Wesentlichen Eigenschaften der Gleit- und Rollenlager," *Zeitschrift des Vereines deutscher Ingenieure*, 46(37) pp.1341-1470.
- [49] Jelaili, M., Kroll, A., 2003, "Hydraulic Servo-systems: Modeling, Identification and Control," Springer, London, New York, pp.1-355.
- [50] Lee C., Polycarpou, A., 2007, "Static Friction Experiments and Verification of an Improved Elastic-Plastic Model Including Roughness Effects," *Transactions of the ASME Journal of Tribology*, 129(4) pp.754-760.
- [51] Bhojkar, A., 2004, "Fault simulator for proportional solenoid valves," M.Sc. thesis, University of Saskatchewan, pp.1-101.
- [52] Garacia, E., Gonzalez de Santos, P., Canudas de Wit, C., 2002, "Velocity Dependence in the Cyclic Friction Arising with Gears," *International Journal of Robotics Research*, 21(9) pp.761-771.
- [53] Ferreira, J. A., 2007, "A Review of Mathematical Models of Non-Linear Mechanical Systems that Involve Friction," *WSEAS Transactions on Systems*, 6(12) pp.1337-1346.
- [54] Hamrock, B.J., Schmid, S.R., Jacobson, B.O., 2004, "Fundamentals of fluid film lubrication," Marcel Dekker, New York, pp.1-699.
- [55] Lu, X., Khonsari, M., Gelinck, E., 2006, "The Stribeck Curve: Experimental Results and Theoretical Prediction," *Journal of Tribology*, 128(4) pp.789-794.

- [56] Marks, L. S., 1978, "Marks' Standard Handbook for Mechanical Engineers," McGraw-Hill Education, New York, pp.1-1936.
- [57] Smith, E.H., 1998, "Mechanical Engineer's Reference Book," Butterworth Heinemann, Oxford, England, pp.1-832.
- [58] ASTM, 2011, "Standard Test Method for Conducting Friction Tests of Piston Ring and Cylinder Liner Materials Under Lubricated Conditions," ASME Standards, pp.1-35.
- [59] Budinski, K., 2007, "Guide to Friction, Wear and Erosion Testing," ASTM International, West Conshohocken, pp.1-132.
- [60] Harnoy, A., Friedland, B., Semenov, R., Rachoer, H., Aly, A., 1994, "Apparatus for Empirical Determination of Dynamic Friction," Proceedings of American Automatic Control Conference, 1, pp.546-550.
- [61] Richard, C., Cutkosky, M. R., MacLean, K., 1999, "Friction Identification for Haptic Display," Proceeding of ASME Dynamic Systems and Control Division (DSC), pp.327-334.
- [62] Gandhi, P. S., Ghorbel, F.H., Dabney, J., 2002, "Modeling, Identification, and Compensation of Friction in Harmonic Drives," 41st IEEE Conference on Decision & Control (CDC), 1, pp.160-166.
- [63] Yang, C., Chiou, Y., Lee, R., 1999, "Tribological Behavior of Reciprocating Friction Drive System under Lubricated Contact," Tribology International, 32(8) pp.443-453.
- [64] Tafazoli, S., de Silva, C. W., Lawrence, P. D., 1998, "Tracking Control of an Electrohydraulic Manipulator in the Presence of Friction," IEEE Transactions on Control Systems Technology, 6(3) pp.401-411.
- [65] Kim, S.J., Kim, S.Y., Ha, I.J., 2004, "An Efficient Identification Method for Friction in Single-DOF Motion Control Systems," IEEE Transactions on Control Systems Technology, 12(4) pp.555-563.
- [66] Gomes, S., Santos da Rosa, V., 2003, "A New Approach to Compensate Friction in Robotic Actuators," IEEE International Conference on Robotics and Automation, 1, pp.622-627.
- [67] Sampson, E. B., 2005, "Fuzzy Control of the ElectroHydraulic Actuator," Master Thesis, University of Saskatchewan, pp.1-151.
- [68] Armstrong, B., 1988, "Friction: Experimental Determination, Modeling and Compensation," Robotics and Automation, Proceedings of 1988 IEEE International Conference on Robotics and Automation, 3, pp.1422-1427.

- [69] Tustin, A., 1947, "The Effects of Backlash and of Speed-Dependent Friction on the Stability of Closed-Cycle Control Systems," *Journal of the Institution of Electrical Engineers*, IIA, Automatic Regulators and Servo Mechanisms, 94(1) pp.143-151.
- [70] Li, C., and Pavelescu, D., 1982, "The Friction-Speed Relation and its Influence on the Critical Velocity of Stick-Slip Motion," *Wear*, 82(3) pp.277-289.
- [71] Al-Bender, F., Swevers, J., 2008, "Characterization of Friction Force Dynamics," *IEEE Control Systems Magazine*, 28(6) pp.64-81.
- [72] Rabinowicz, E., 1951, "The Nature of the Static and Kinetic Coefficients of Friction," *Journal of Applied Physics*, 22(11) pp.1373-1379.
- [73] Dahl, P.R., 1968, "A Solid Friction Model," Aerospace Report No. TOR-0158(3107-18)-1, The Aerospace Corporation, El Segundo, CA, pp.1-33.
- [74] Johansson, K., Canudas de Wit, C., 2008, "Revisiting the LuGre Friction Model," *IEEE Control Systems Magazine*, 28(6) pp.101-114.
- [75] Canudas de Wit, C., Olsson, H., Astrom, K. J., Lischinsky, P., 1995, "A New Model for Control of Systems with Friction," *IEEE Transactions on Automatic Control*, 40(3) pp.419-425.
- [76] Khayati, K., Bigras, P., Dessaint, L., 2009, "LuGre Model-Based Friction Compensation and Positioning Control for a Pneumatic Actuator using Multi-Objective Output-Feedback Control Via LMI Optimization," *Mechatronics*, 19(4) pp.535-547.
- [77] Tran, X., Khaing, W., Endo, H., Yanada, H., 2014, "Effect of Friction Model on Simulation of Hydraulic Actuator," *Proceedings of the Institution of Mechanical Engineers, Part I: Journal of Systems and Control Engineering*, 228(9) pp.690-698.
- [78] Aho, L., Moreno, J., Guerra, R., 2005, "Second-order LuGre Friction Model," *Proceedings of the 24th IASTED International Conference on Modeling, Identification, and Control, MIC 2005*, pp.86-90.
- [79] Boresi, A.P., Richard, J., 2001, "Engineering Mechanics: Statics," Brooks/Cole, Pacific Grove, CA, pp.1-683.
- [80] McLain, T. W., Iversen, E.K., Davis, C.C., Jacobsen, S.C., 1989, "Development, Simulation, and Validation of a Highly Nonlinear Hydraulic Servosystem Model," *Proceedings of the 1989 American Control Conference*, pp.385-391.
- [81] Karnopp, D., 1985, "Computer Simulation of Stick-Slip Friction in Mechanical Dynamic Systems," *Journal of Dynamic Systems, Measurement and Control, Transactions of the ASME*, 107(1) pp.100-103.

- [82] Gurfil, P., Friedland, B., "New Simple Model of Dynamic Hysteresis," Transactions of the Institute of Measurement and Control, 25(3) pp.202-216.
- [83] Tan, X.B., Iyer, R. V., 2009, "Modeling and Control of Hysteresis," IEEE Control Systems, 29(1) pp.26-28.
- [84] Alexander, M., Tomas, R., "A Rate-Independent Model for Inelastic Behavior of Shape-Memory Alloys," Multiscale Modeling & Simulation, 1(4) pp.571-597.
- [85] Berger, E. J., 2002, "Friction Modeling for Dynamic System Simulation," Applied Mechanics Reviews, 55(6) pp.535-577.
- [86] Wojewoda, J., Stefanski, A., Wiercigroch, M., Kapitaniak, T., 2007, "Hysteretic Effects of Dry Friction: Modelling and Experimental Studies," Philosophical Transactions of the Royal Society of London A: Mathematical, Physical and Engineering Sciences, 366(1866) pp.747-765.
- [87] Hensen, R. H. A., van de Molengraft, M. J. G., Steinbuch, M., 2003, "Friction Induced Hunting Limit Cycles: A Comparison between the LuGre and Switch Friction Model," Automatica, 39(12) pp.2131-2137.
- [88] Radcliffe, C., Southward, S.C., 1990, "A Property of Stick-Slip Friction Models which Promotes Limit Cycle Generation," Proceedings of the American Control Conference, pp.1198-1203.
- [89] Haessig Jr., D. A., Friedland, B., 1991, "On the Modeling and Simulation of Friction," Journal of Dynamic Systems, Measurement and Control, Transactions of the ASME, 113(3) pp.354-362.
- [90] Marton, L., 2008, "On Analysis of Limit Cycles in Positioning Systems Near Stribeck Velocities," Mechatronics, 18(1) pp.46-52.
- [91] Pervozvanski, A. A., 2002, "Asymptotic Analysis of the Dither Effect in Systems with Friction," Automatica, 38(1) pp.105-113.
- [92] Chatterjee, S., Singha, T.K., Karmakar, S.K., 2004, "Effect of High-Frequency Excitation on a Class of Mechanical Systems with Dynamic Friction," Journal of Sound and Vibration, 269(1) pp.61-89.
- [93] Dupont, P. E., Dunlap, E. P., 1993, "Friction Modeling and Control in Boundary Lubrication," Proceedings of the 1993 American Control Conference, pp.1910-1914.
- [94] Sampson, J. B., Morgan, F., Reed, D. W., 1943, "Friction Behavior during the Slip Portion of the Stick-Slip Process," Journal of Applied Physics, 14(1) pp.689-700.

- [95] Harnoy, A., 1997, "Simulation of Stick-Slip Friction in Control Systems," *Tribology Transactions*, 40(2) pp.360-366.
- [96] Rachoor, H., Harnoy, A., 1996, "Modeling of Dynamic Friction in Lubricated Line Contacts for Precise Motion Control," *Tribology Transactions*, 39(2) pp.476-482.
- [97] Harnoy, A., Friedland, B., 1994, "Dynamic Friction Model of Lubricated Surfaces for Precise Motion Control," *S T L E Tribology Transactions*, 37(3) pp.608-614.
- [98] Harnoy, A., Friedland, B., Rachoor, H., 1994, "Modeling and Simulation of Elastic and Friction Forces in Lubricated Bearings for Precise Motion Control," *Wear*, 172(2) pp. 155-164.
- [99] Courant, R., Robbins, H., 1941, "What is Mathematics? An Elementary Approach to Ideas and Methods," Oxford University Press, London, pp.1-592.
- [100] Srinagesh, K., 2006, "The Principles of Experimental Research," Elsevier, Butterworth-Heinemann, Amsterdam, pp.1-410.
- [101] Gholizadeh, H., 2013, "Modeling and Experimental Evaluation of the Effective Bulk Modulus for a Mixture of Hydraulic Oil and Air," PhD Thesis, University of Saskatchewan, pp. 1-151.
- [102] El Nakla, M., Al-Sarkhi, A., Alsurakji, I., 2013, "A Look-Up Table for Two-Phase Frictional Pressure Drop Multiplier," *Nuclear Engineering and Design*, 265(0) pp.450-468.
- [103] Nelles, O., 2001, "Nonlinear System Identification: From Classical Approaches to Neural Networks and Fuzzy Models," Springer, Berlin & New York, pp.1-785.
- [104] Xu, X. P., Burton R. T., Sargent, C. M., 1996, "Experimental Identification of a Flow Orifice using a Neural Network and the Conjugate Gradient Method," *Transactions of the ASME, Journal of Dynamic Systems, Measurement, and Control*, 118(2) pp.272-277.
- [105] Qian, W., Burton, R., and Schoenau, G., 2001, "Measured Performance of PID and Neural Net Control of a Hydraulically Driven Inertia Load with Nonlinear Friction," *International Journal of Flower Power*, FPN 2(1), pp.31-37.
- [106] Van Der Linden, G.W., 1994, "Parameter Estimation by Data Reconstruction," *Proceedings of the 1994 American Control Conference*, pp.525-529.
- [107] Duffy, D.G., 2011, "Advanced Engineering Mathematics with MATLAB," CRC Press, Boca Raton, pp.1-1079.

APPENDIX A: ASME 2007 INTERNATIONAL MECHANICAL ENGINEERING
CONGRESS AND EXPOSITION (IMECE) PAPER

This section includes the paper which was presented at ASME 2007 International Mechanical Engineering Congress and Exposition (IMECE), Seattle, USA in November, 2007.

Permission for the paper published in IMECE 2007 was asked from the copyright holder to attach this paper as an appendix. The permission is documented as follows:

Dear ASME Copyright Dept.:

I would really appreciate if you give me a permission for my paper (which was published in ASME International Mechanical Engineering Congress and Exposition, Seattle, USA, 2007) to include in my PhD thesis in University of Saskatchewan. The paper is: Wei (Scott) Li , Richard Burton, Saeid Habibi, 2007, Investigation of a High Precision Hydrostatic Actuation System - How Non-linearities Affect its Performance, ASME International Mechanical Engineering Congress and Exposition, Seattle, USA, 2007.

I am looking forward to hearing from you at your earliest convenience. Thanks.

Best Regards,
Scott Li

Dear Mr. Li:

It is our pleasure to grant you permission **to use all or any part of** the following ASME paper "Investigation of a High Precision Hydrostatic Actuation System: How Nonlinearities Affect Its Performance," by Wei Li; Richard Burton; Saeid Habibi, Paper Number IMECE2007-41650, cited in your letter for inclusion in a PhD Thesis entitled Investigation of Acceleration Dependent Nonlinear Lubricated Friction in Hydraulic Actuation Systems to be published by University of Saskatchewan. Permission is granted for the specific use as stated herein and does not permit further use of the materials without proper authorization. Proper attribution must be made to the author(s) of the materials. **Please note:** if any or all of the figures and/or Tables are of another source, permission should be granted from that outside source or include the reference of the original source. ASME does not grant permission for outside source material that may be referenced in the ASME works.

As is customary, we request that you ensure full acknowledgment of this material, the author(s), source and ASME as original publisher. Acknowledgment must be retained on all pages printed and distributed.

Many thanks for your interest in ASME publications.

Sincerely,



Beth Darchi

Publishing Administrator
ASME
2 Park Avenue, 6th Floor
New York, NY 10016-5990
Tel [1.212.591.7700](tel:1.212.591.7700)
darchib@asme.org

IMECE-2007-41650

INVESTIGATION OF A HIGH PRECISION HYDROSTATIC ACTUATION SYSTEM –
 HOW NONLINEARITIES AFFECT ITS PERFORMANCE

Wei (Scott) Li^{1*}, Richard Burton^{1**}, Saeid Habibi²

¹Department of Mechanical Engineering, University of Saskatchewan, 57 Campus Drive, Saskatoon, SK, Canada S7N 5A9

* Email: wei418@mail.usask.ca

Phone** (306)966-5373

²Department of Mechanical Engineering, McMaster University, Hamilton, ON, Canada L8S 4L7

ABSTRACT

A prototype Electro-Hydraulic Actuator (EHA) system has demonstrated a positional accuracy in the order of 100 nanometer. Linearized models of the EHA have been formulated and have shown reasonable correlation to the performance of the physical EHA. However, these models predict zero steady state error (an impossible situation given the physical limitations of seals, friction etc.). Further, the prototype EHA indicates that the cut-off frequency decreases as the amplitude of the input signal decreases. This is not predicted by the linear models. In this paper the Bond-graph large scale modeling technique was used as the basis to formulate the describing equations of the EHA. The model was made increasing more complex by introducing observable nonlinearities into the model. It was found that the introduction of nonlinear friction did show results whose trends were consistent with those observed experimentally. Assumed nonlinearities in the bulk modulus could not be substantiated. In addition, some of the observed experimental trends could not be predicted (such as order change) and pose additional challenges to be solved before a complete understanding of the true physics if the EHA can be realized.

NOMENCLATURE

Symbol	Definitions	Units
D_p	Pump volumetric displacement	m ³ /rad
P_a	Pump outlet port pressure	pa
P_b	Pump inlet port pressure	pa
Q_a	Pump outlet port flow	m ³ /s
Q_b	Pump inlet port flow	m ³ /s

P_1	Actuator chamber 1 pressure	pa
P_2	Actuator chamber 2 pressure	pa
Q_1	Actuator chamber 1 flow	m ³ /s
Q_2	Actuator chamber 2 flow	m ³ /s
Q_m	Pump internal leakage	m ³ /s
Q_{ema}	Pump outlet port external leakage	m ³ /s
Q_{emb}	Pump inlet port external leakage	m ³ /s
Q_{em1}	Actuator chamber 1 external leakage	m ³ /s
Q_{em2}	Actuator chamber 2 external leakage	m ³ /s
T_m	Motor torque	Nm
T_u	Pump upstream torque	Nm
T_d	Pump downstream torque	Nm
ω_m	Motor/Pump angular velocity	rad/s
P_{acc}	Accumulator pressure	pa

1. INTRODUCTION

A closed hydrostatic system is one in which the actuator output flow is ported back into the inlet of the pump (as opposed as the fluid passing through a reservoir first). Movement of the actuator is controlled by varying the amount of flow that comes from the pump which in turn is controlled by changing the pump swash plate angle or the angular speed of the pump driving motor. Because the system is closed, the actuator must be symmetric and thus for linear actuation special actuators have to be designed. Closed systems of this form are highly desirable because they do not require valves to modulate the flow which increases the system efficiency.

The electro-hydraulic actuation system (herein referred to as the EHA system) considered in this study is shown Figure 1. This positioning accuracy of this EHA design is in the order of $50 \pm 25 \text{ nm}$ which is quite unprecedented for such systems [1, 2]. This feat is all the more remarkable considering that most of the components (other than the actuator) were off the shelf components. The high gain feedback in the inner closed loop around the electric motor was found to compensate for dead-zone in the motor/pump operation [1]. The load was inertial (20 kg) and a linear incremental optical encode transducer (resolution of 50 nm and a guaranteed accuracy of $\pm 3 \text{ }\mu\text{m/m}$) was used to measure the actuator displacement [3].

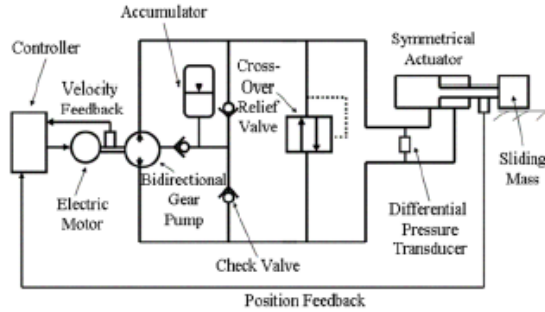


Figure 1 Schematic Diagram of the Electro-hydraulic Actuation System (EHA). The pump flow rate is varied by a variable speed motor. [9]

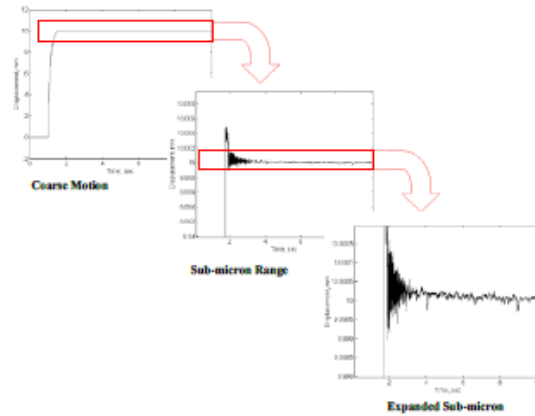


Figure 2 Step response of EHA illustrating submicron accuracy [8]

Figure 2 demonstrates the positional accuracy of the EHA prototype investigated in this study. It was very evident that the accuracy of the measurement of the position was at this point limited by the resolution of the transducer [3]. Figure 3 shows the frequency response of the open loop EHA at a large and small amplitudes and it is clear that the damping, the cutoff frequency and indeed, the order change significantly implying a very strong nonlinear behavior [3]. Figure 4 shows the friction characteristics of the actuator and gives evidence of the traditional slip-stick behaviour [6, 7]. It was also established that as the load pressure differential across the actuator increased, the positional accuracy started to decrease.

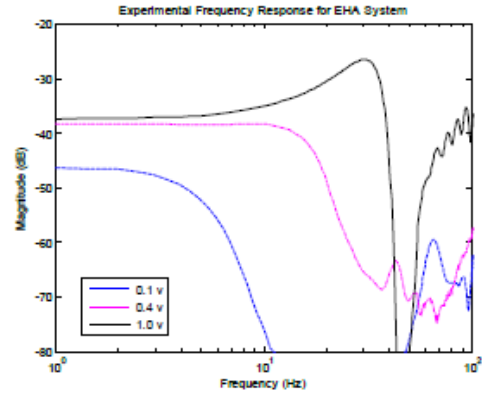


Figure 3. Frequency response of the prototype EHA as a function of input amplitude for the prototype EHA system. It is apparent that the order, the natural frequency and the damping appear to change with input voltage. Data beyond first break point (higher frequencies) is not reliable and should be ignored.

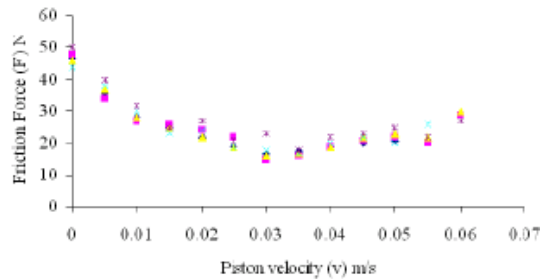


Figure 4. Nonlinear damping in the actuator [4]; the friction characteristics in the negative velocity direction are similar.

These preliminary studies on the EHA demonstrated that the system could achieve high positional accuracy in the presence

of what appears to be severe nonlinearities. An overall objective of this research was to redesign a new EHA which could handle resistive and gravity loads while maintaining the high accuracy shown by the existing EHA. However, it was realized that a true understanding of the “physics” of how this system could achieve this positional accuracy given these observed nonlinearities and their influence on the system performance was necessary before redesign could be attempted. The objective of this paper is to illustrate from a modeling point of view how various factors would affect the behaviour of the EHA to provide a better understanding. Linearized models of the EHA are presented and are used to illustrate how certain parameters can affect the overall performance. A large signal model using the Power Bond Graph is presented and nonlinear properties are incorporated into the model. The results of the linear and nonlinear model are compared and conclusion/observations forwarded.

2. LINEAR MODELS AND ANALYSIS

In [1] and [2], several linear models were developed which reflected the relationship between the input voltage to the motor controller and the output actuator position. The transfer function between the input voltage and the shaft speed on the pump was determined to be

$$\frac{\omega_p(s)}{U(s)} = \frac{2.779 * 10^{-1} s + 40.55}{5.780 * 10^{-5} s^2 + 1.061 * 10^{-2} s + 1} \quad (1)$$

This transfer function includes a high gain inner loop velocity feedback around the electric motor which minimized the effects of dead-zone in the motor. The transfer function between the pump and the symmetric actuator was found to be:

$$\frac{X(s)}{\omega_p(s)} = \frac{29.42}{s^3 + 39.04s^2 + 8.783 * 10^4 s} \quad (2)$$

The overall transfer function was hence,

$$\frac{X(s)}{U(s)} = \frac{1.41 * 10^5 (s + 145.9)}{s(s^2 + 183.6s + 1.73 * 10^4)(s^2 + 39.04s + 8.78 * 10^4)} \quad (3)$$

It is clear that the presence of the pole at $s = 0$ means that theoretically, zero steady state error in the closed loop exists. This has implications on the observed behaviour of the prototype EHA. The fact that the actual steady state error for the prototype is extremely small (at least 100 nm) implies that the inner loop velocity feedback around the motor is extremely effective in reducing nonlinearities associated with motor dead-zone. An analysis of the gear pump shows that in order to produce a displacement of 100 nm in the prototype actuator, the

gear shaft would only have to move about 0.017 degrees. This further enforces that the choice of an electric motor with appropriate feedback is critical to the success of the operation of the EHA.

In [3], an identification process was used to approximate the experimental transfer function of the EHA using a swept frequency input approach and the Empirical Transfer Function Estimation – ETFE [4] technique. For larger input amplitudes, the open loop transfer was approximated to be:

$$\frac{X(s)}{U(s)} = \frac{187200(s + 262.3)}{s(s^2 + 70.04s + 9.532 * 10^4)(s^2 + 192.2s + 3.815 * 10^4)} \quad (4)$$

By comparing the dominant poles and zeros of the transfer function in equation (4) to that of equation (3), it can be shown that the approximate experimental transfer functions for the electric motor (with feedback) and the hydraulic part of the EHA are:

$$\frac{\omega_p(s)}{U(s)} = \frac{s + 262.3}{s^2 + 192.2s + 3.815 * 10^4} \quad (\text{Motor}) \quad (5)$$

and

$$\frac{X(s)}{\omega_p(s)} = \frac{1.872e5}{s^2 + 70.04s + 9.532 * 10^4} \quad (\text{Hydraulic}) \quad (6)$$

For convenience and for the remaining analysis and figures, the transfer function between velocity and the input is used to avoid the integration term in equation (6). As mentioned in the introduction, the existence of nonlinear friction in the actuator combined with the apparent change in the frequency response characteristics at small amplitudes “flagged” some issues pertaining to the performance of the system and to what effect nonlinear friction would have on the performance of future designs of the EHA. Two hypotheses were forwarded:

1. The nonlinear friction would tend to have a more pronounced effect on the system performance at small velocities. This would tend to increase the effective damping in the system
2. A decrease in the bulk modulus of the fluid at small pressure differentials or low velocities could occur due to the presence of entrained air [9] and or initial compression of seals. This would tend to decrease the natural frequency of the system.

To establish that these hypotheses would produce trends that were consistent with the experimental evidence, the transfer function in equation (4) was used and the damping coefficient (associated with friction) and natural frequency terms (associated with bulk modulus) of the hydraulic part were

adjusted as presented above. The resulting frequency response (magnitude) is shown in Figure 5. In the figure the response with the highest natural frequency is based on equation (4). As would be expected, as damping is increased and the natural frequency decreases, the trends are very consistent with those observed in Figure 3.

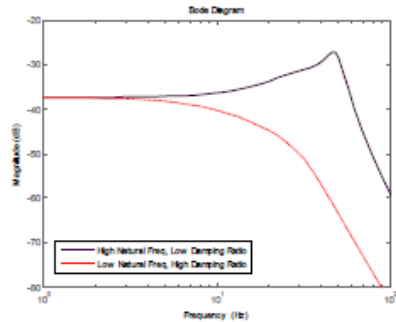


Figure 5. Theoretical Frequency response of the EHA as a function of changes in damping and natural frequency. Note that velocity is used as the output rather than displacement.

3. LARGE SIGNAL ANALYSIS

The models presented in the last section have been a very valuable tool for designing control algorithms for improving the closed loop transient response of the EHA [10]. But observation of Figures 3 and 4 clearly indicate that the system is nonlinear and as such, the trends discussed (Figure 5) can only indicate that the hypotheses “could be” correct. It was decided that a large signal model of the hydraulic part of the EHA should be used to analyze the effects that nonlinear friction and indeed, nonlinear bulk modulus would have on the performance. It must be clarified that because the system is nonlinear, a true “transfer function” in the traditional sense does not exist. The transfer function that is considered here (both in the experimental results of Figure 3 and in the model results that will be presented) is more in the line of the describing function approach in which the fundamental signal is extracted. Since the same type of input signal is (was) applied to both the experimental EHA and the large signal model, and the same method is (was) used to analyze the results, it was felt that this was a reasonable method for comparison of trends.

The Power Bond Graph (PBG) approach was used to model the hydraulic portion of the EHA [11]. The input to the PBG was preprocessed using the transfer function of the electric motor and inner loop feedback system shown in equation (5). The PBG is presented in Figure 6 and the describing equations are given in Appendix A. The equations were implemented using Matlab/Simulink®. Integration used was ode3 (Bogacki-Shampine). Simulation sampling time: 0.00001 sec.

Open loop EHA Transfer function:
Electronics motor:

$$\frac{2.779 * 10^{-1} s + 40.55}{5.780 * 10^{-5} s^2 + 1.061 * 10^{-2} s + 1}$$
Hydraulic part:

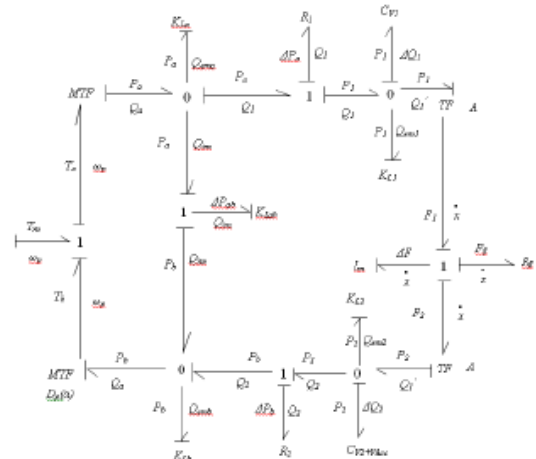


Figure 6. Preprocessor and Power Bond Graph of the EHA system

3.1 Nonlinear Friction

In the first study, the frequency response of the PBG model assuming all linear relationships was examined using parameter values obtained from the experimental system in past studies [2,3,4]. The results predicted by the PBG and those of the linearized model were in agreement within acceptable limits. This step provided confidence in the large scale equations and modeling procedures. These frequency response results provided a bench mark for which other frequency responses could be compared to.

The second step involved developing a series of nonlinear models of the friction characteristic. The first model (shown in Figure 7) assumed only linear viscous friction and was used as a benchmark in for this study. The second model (denoted as “C+V” in Figure 7) consisted of Coulomb friction and viscous friction. The third approximated the experimental friction characteristics observed by Chinniah (Figure 4) denoted as “C+NLV” where NLV is defined as nonlinear viscous friction. Symmetrical friction characteristics about zero velocity were assumed although in reality, there were some differences. To simulate a true coulomb friction performance at very small velocities, the time step was adjusted to be very small (.00001). This increased the simulation time dramatically but did produce results that were considered reliable in this region.

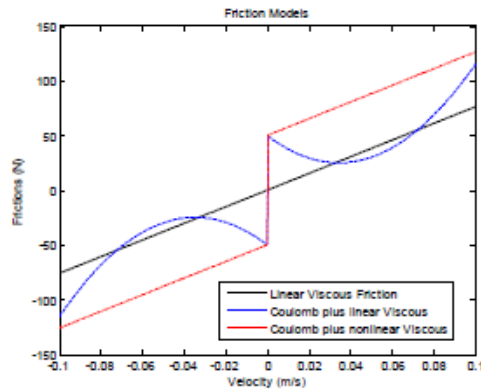


Figure 7 Assumed Nonlinear Friction forms. (NLV is defined as nonlinear viscous friction)

Two swept sinusoidal input signals were input into the model, one at 1.0 v and one at small amplitudes, 0.1v (consistent with the input signals used to generate Figure 3). The frequency responses for the Coulomb-viscous friction (C+V) model are shown in Figure 8. It is evident that the large signal input results approached the linear viscous friction model results but as the amplitude decreased, the effective damping increased which was consistent with hypothesis number 1. A somewhat surprising observation was that the natural frequency of the system appeared to be modified to a much larger extent that would be expected if only the damped natural frequency was involved; that is at higher frequencies, the linear and coulomb friction models should converge if the natural frequency was the same. It is also noteworthy that at low frequencies the C + V model showed the same trends which was further evidence of the validity of the C+V model. However, it was found that the resonant peak observed in the pure viscous friction model was always greater than that predicted by the C+V model even at large input amplitudes (10v for example).

The aforementioned procedure was then applied to the measured nonlinear actuator friction model (C+NLV) [4]. Frequency responses for large and small amplitude inputs are shown in Figure 9. As above the Coulomb friction characteristic was modified to expedite simulation times. It was evident that the large signal input results approached the linear viscous friction model results at resonance and as with the C+V model, as the amplitude decreased, the effective damping increased which is consistent with hypothesis number 1.

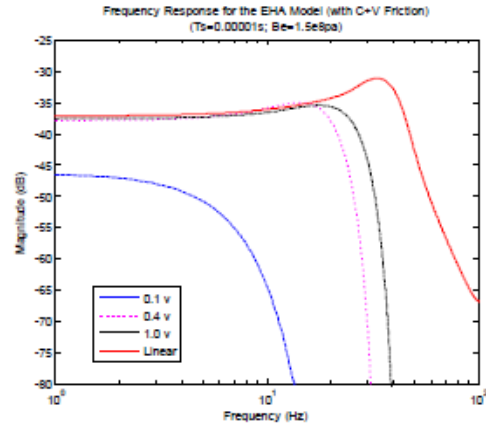


Figure 8 Frequency response for Coulomb -Viscous Friction model: large amplitude and small amplitude input signals. The frequency response for the pure viscous friction model is included as a benchmark for comparison.

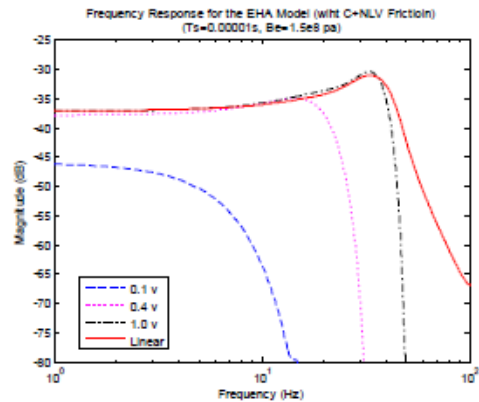


Figure 9 Frequency response of simulated model with a measured nonlinear friction characteristics (Chinniah [4]), large amplitude and small amplitude input signals. The frequency response for the pure viscous friction model is included as a benchmark for comparison.

The increase in the effective damping as the input voltage increases can be attributed to the “negative slope” in the transition regions from coulomb to viscous friction. The velocity at 0.1 and 1v (taken at 1hz) is shown on the C+NLV plot of Figure 10. It is clear that as the velocity approaches maximum velocity (1v), the slope makes a transition from negative to zero and then goes slightly positive. It would be expected then that an unstable limit cycle (one which would damp out) could be excited in this region.

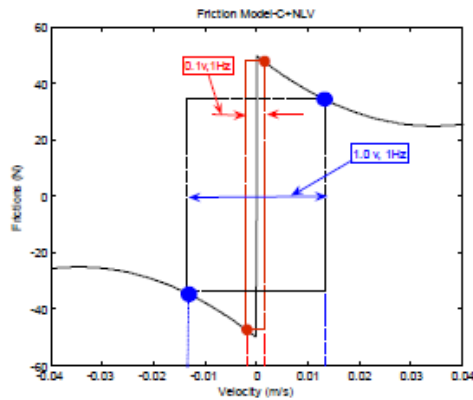


Figure 10. Location of the experimental and simulation velocities on the C + NLV models for 0.1v and 1.0v

To verify this, the simulation and the experimental system were subjected to a 1 Hz sinusoidal input of 0.1 and 1v. In this set of results, the pressure differential across the actuator was of interest because it was the parameter most likely to show this limit cycle. It was observed that indeed, a limit cycle had been excited and that the frequency of the limit cycle for both the experimental (45Hz) and simulation (50 Hz) were close.

3.2 Nonlinear Bulk Modulus

In this part of the study integration of a nonlinear bulk modulus term was pursued whose characteristics are shown in Figure 12. The assumption behind this curve is based on the assumption that a three stage process could occur during compression of the fluid. The first is that the seals are compressed until they form a solid seal after which they can be considered as a rigid shape. The second is that the entrained air is being compressed which has a significant effect at low pressures. The third is that at large compression pressures, entrained air becomes dissolved air and the bulk modulus approached that of a pure fluid. The second assumption was in part substantiated in [5] in which an effective bulk modulus was estimated using an Extended Kalman Filtering approach. This study indicated that the bulk modulus was indeed smaller than that of a pure fluid ($1.5 \times 10^9 \text{ Pa}$ vs. $1 - 2 \times 10^9 \text{ Pa}$). The nonlinear behavior of bulk modulus as a function of pressure has been identified in [9] in which the presence of entrained air has been accounted for. It is this relationship that has been assumed in this part of the study. This assumed form is illustrated in Figure 10. It must be stressed that unlike the friction behavior which was determined experimentally, the bulk modulus form was "assumed" for purpose of trend demonstration only.

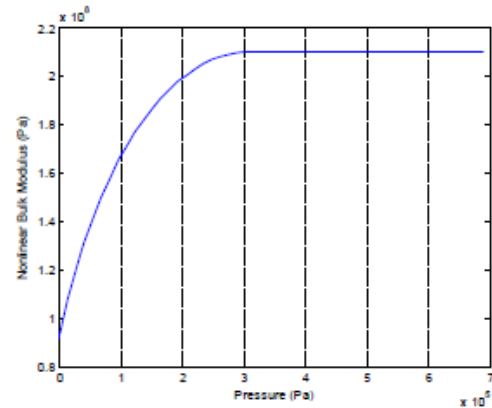


Figure 11 Assumed form of the effective bulk modulus as a function of pressure

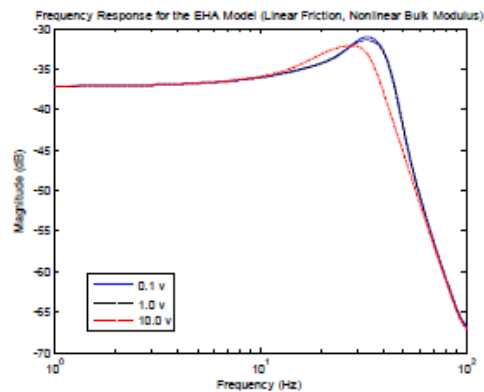


Figure 12. Frequency response assuming nonlinear bulk modulus behavior for large and small amplitude inputs. The frequency response assuming linear viscous friction and linear bulk modulus is presented to provide a benchmark for comparison.

Assuming a linear viscous friction and integrating the nonlinear bulk modulus into the PBG model, two swept sinusoidal signals were input into the model, one at large and one at small amplitudes (consistent with the input signals used to generate Figure 3). The results are shown in Figure 12. It is evident that as the input voltage increases, the natural frequency marginally decreases which was not expected since as the velocity increased, the pressure increase which should according to Figure 11, increase the bulk modulus and hence increase the natural frequency. Upon closer examination, it is not the pressure but the pressure swing about the operating point that is

critical here. As the swing increases, the average bulk modulus actually would decrease as illustrated in Figure 13. To demonstrate this effect, a very large input amplitude was used and the frequency response determined. It is evident from Figure 12 that indeed, the bulk modulus does decrease. Thus, the hypothesis that a decrease in bulk modulus would occur due to entrained air was not established.

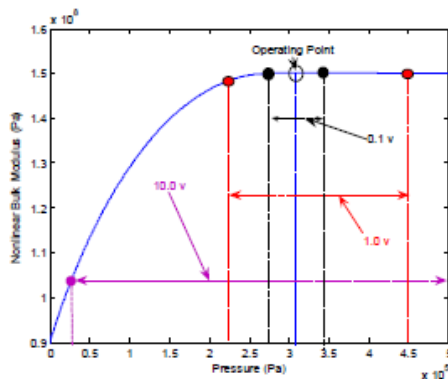


Figure 13 Operating point for bulk modulus model

4. DISCUSSION

The trends shown in this study do support the first hypotheses. Nonlinear friction does affect the apparent damping, the low frequency amplitude ratio, and the apparent natural frequency but not the order of the system. Experimentally, the slopes at higher frequencies do not converge as they do in the simulations. However, this may have more to do with the fact that at higher frequencies and larger amplitudes, higher order terms can come into play which cannot be observed at lower amplitudes. Thus no conclusive statement can be made in this regard. It is to be noted that the presence of a negative slope in the transition region decreases the effective damping.

Hypothesis 2 could not be verified using frequency response approaches since if nonlinear bulk modulus was a factor, its effects would be partially masked by friction. One of the overall aims for the EHA is to use the third chamber to compensate for gravity or external resistive type loads. This would mean that the EHA would operate at low pressures similar to those experienced in this study. Thus a means of isolating the friction effect from the bulk modulus effect needs to be pursued.

This is truly research in progress in that other forms of nonlinearities could have similar effects on the nonlinear frequency response behavior of the prototype EHA. At the writing of this manuscript, other possibilities are being pursued

and it is anticipated that results will be reported accordingly in the future.

As a last comment, the C+NLV friction is a form of dead-zone. It is evident that accurate positioning of the actuator is possible if dead-zone can be minimized or compensated as was done in the electric motor of the prototype. Indeed, it is hypothesized that dead-zone is the main restriction on improving positioning capabilities to beyond that demonstrated by the EHA prototype. Nonlinear friction and bulk modulus do have an affect on both the dynamic performance of the EHA (and hence the stability of the system - for example hunting around the steady state position) and on the steady state position error.

5. PARAMETER VALUES

Parameters	Values	Definitions
A	$5.051e^{-4}$	Pressure area in symmetrical actuators (m^2)
M	20	Load mass (Kg)
P_0	310260	Initial Pressure (Pa)
V_0	$6.1e^{-5}$	Pipe plus mean actuator chamber volumes (m^3)
V_{Acc}	$2.458e^{-5}$	Volume of the Accumulator (m^3)
D_p	$1.68e^{-7}$	Pump volumetric displacement (m^3/rad)
B_e	$1.5e^8$	Effective bulk modulus of hydraulic oil (Pa)
K_L	$1.5e^{-13}$	Leakage coefficient
K_{Lab}	$2.0e^{-15}$	Pump cross-port leakage coefficient
K_{Pipe}	$2.5e^{12}$	Pipe coefficient relating pressure drop to flow (turbulent hydraulic resistance)
F_w	50	Coulomb Friction(N)
B	760	Coefficient of friction (N/(m/s))
a_1	$2.1e^4$	Coefficients of the quadratic function of nonlinear function
a_2	-1450	Coefficients of the quadratic function of nonlinear function
a_3	50	Coefficients of the quadratic function of nonlinear function

ACKNOWLEDGMENTS

The authors would like to acknowledge the financial contribution in the form of stipends and scholarships from the Canadian Water Network and the University of Saskatchewan

REFERENCES

- [1] Habibi S.R. and Goldenberg A.A., Design of a New High Performance ElectroHydraulic Actuator, IEEE/ASME Transactions on Mechatronics, Vol. 5, No 2, pp 158-164, 2000
- [2] Habibi S.R., Pastrakuljic V. and Goldenberg A.A., Experimental Analysis of a High Performance Hydrostatic Actuation System, SAE Transactions, Journal of Commercial Vehicles, 109, pp 367-377, 2001
- [3] Samson, E., Habibi, S., Chinniah, Y. and Burton, R. Model Identification of the Electrohydraulic Actuator for small signal inputs, Bath Workshop on Power Transmission and Motion Control PTMC 2005, Bath, UK, pp 163 -178, Sept, 2005
- [4] Ljung, L. 1999. System Identification – Theory for the User, 2nd Ed. Prentice Hall, PTR
- [5] Matlab© Simulation Package, Mathworks Inc. EFTE Tool Box
- [6] Chinniah Y., Burton R. and Habibi S., “Parameter Estimation in a Hydrostatic System Using Extended Kalman Filter”, Proceedings of ASME International Mechanical Engineering Congress, FPST-Vol., New York, Nov. 10-15, pp125-136, 2001.
- [7] Chinniah, Y., Burton, R. and Habibi, S., Viscous Damping Coefficient and Effective Bulk Modulus Estimation in a High Performance Hydrostatic Actuation System using Extended Kalman Filter, International Journal of Fluid Power, FPN, Volume 4, No 3., pp. 27-34, 2003
- [8] Sampson, E., Habibi S., Burton R., High Precision Hydrostatic Actuation Systems for Micro and Nano Manipulation of Heavy Loads, ASME, Journal of Dynamic Systems, Measurement and Control, In Press, 2006
- [9] Ruan, J. and Burton, R., Bulk Modulus of Air Content Oil in a Hydraulic Cylinder, Proceedings of ASME International Mechanical Engineering Congress, Chicago, Nov. 2006.
- [10] E. Sampson, S. Habibi, R. Burton & Y. Chinniah (2004). Effect of controller in reducing steady-state error due to flow and force disturbances in the ElectroHydraulic Actuator system. International Journal of Fluid Power Vol. 5 No. 2.
- [11] P. Dransfield, Hydraulic Control Systems – Design and Analysis of Their Dynamics, Lecture Notes in Control and Information Sciences, Vol 33, Springer-Verlag, Berlin Heidelberg, New York, 1981.

APPENDIX A DESCRIBING EQUATIONS FOR THE HYDRAULIC PORTION OF THE EHA

Linear Model (TF Model)
$Q_{ema} = 0$
$Q_1 = A\dot{x} + \frac{(V_{Oacc} + Ax)}{\beta_e} \frac{dP_1}{dt} + Q_{em1}$
$Q_2 = A\dot{x} - \frac{(V_{Oacc} - Ax)}{\beta_e} \frac{dP_2}{dt} - Q_{em2}$
$Q_1 = Q_a, Q_2 = Q_b$
$Q_L = \frac{Q_a + Q_b}{2} = \frac{Q_1 + Q_2}{2}$
$Q_a = D_p \omega_p - K_{Lab} \Delta P_{ab} - \frac{V_a}{\beta_e} \frac{dP_a}{dt}$
$Q_b = D_p \omega_p - K_{Lab} \Delta P_{ab} + \frac{V_b}{\beta_e} \frac{dP_b}{dt}$
$P_{pipe} = K_{pipe} Q_L^2 \approx K_{pipe} D_p^2 \omega_p^2$
$\Delta P_{pipe} = 2K_{pipe} D_p^2 \Delta \omega_p$
$P_1(0) = 0$
$V_0 = V_{Oacc} + V_p$
$Q_{em1} = K_{l1} P_1$
$\Delta F = M \ddot{x}$
$\dot{x}(0) = 0$
$\Delta F = F_1 - F_2 - F_B$
$F_1 = P_1 A$
$F_2 = P_2 A$
$F_B = B \dot{x}$
$P_2(0) = 0$
$Q_{em2} = K_{l2} P_2$
$Q_{emb} = 0$

Nonlinear Model (PBG Model)
$Q_{ema} = K_{La} P_a$
$Q_1 = Q_a - Q_{ema} - Q_{im}$

$Q_a = D_p \omega_p$
$\Delta P_a = K_{pipe} Q_1^2$
$P_a = P_1 + \Delta P_a$
$Q_{im} = K_{lab} \Delta P_{ab}$
$\Delta P_{ab} = P_a - P_b$
$P_1 = \frac{1}{C_{v1}} \int \Delta Q_1 dt + P_1(0) = \frac{\beta_c}{V_1} \int \Delta Q_1 dt + P_1(0);$
$P_1(0) = 310264$
$V_1 = V_0 + Ax$
$\Delta Q_1 = Q_1 - Q_1' - Q_{cm1}$
$Q_{cm1} = K_{l1} P_1$
$Q_1' = A \dot{x}$
$\dot{x} = \frac{1}{M} \int \Delta F dt + \dot{x}(0); \dot{x}(0) = 0$
$\Delta F = F_1 - F_2 - F_B$
$F_1 = P_1 A; F_2 = P_2 A; F_B = B \dot{x}$
$P_2 = \frac{\beta_c}{V_2 + V_{Acc}} \int \Delta Q_2 dt + P_2(0);$
$P_2(0) = 310264$
$V_2 = V_0 - Ax$
$\Delta Q_2 = Q_1' - Q_2 - Q_{cm2}$
$P_b = P_2 - \Delta P_b$
$Q_{cm2} = K_{l2} P_2$
$Q_2 = Q_a - Q_{im} + Q_{cmb}$
$\Delta P_b = K_{pipe} Q_2^2$
$Q_{cmb} = K_{lb} P_b$

APPENDIX B1: ASME/BATH 2010 POWER TRANSMISSION AND MOTION
CONTROL (PTMC) CONFERENCE PAPER

This section includes the paper which was presented at 2010 ASME/Bath Power Transmission and Motion Control (PTMC) conference in Bath, England in September, 2010.

Permission for the paper published in ASME/BATH 2010 was asked from the copyright holder to attach this paper as an appendix. The permission is documented as follows:

Dear Dr. Johnston:

I would really appreciate if you give me a permission for the following paper (which was published in Bath/ASME Symposium on Power Transmission and Motion Control, Bath, England, 2010) to include in my PhD thesis in University of Saskatchewan. The paper is: Wei Li (Scott Li), Richard Burton, Saeid Habibi, Greg Schoenau and FangXiang Wu, 2010. Investigation of the Acceleration Effect on Dynamic Friction of EHA System, Bath/ASME Symposium on Power Transmission and Motion Control, Bath, England, 2010. I am looking forward to hearing from you at your earliest convenience. Thanks.

Best Regards,

Scott Li

Dear Scott

Yes, that is fine.

Best wishes with your PhD.

Nigel

| Dr Nigel Johnston
| Director of Studies (Research)
| Department of Mechanical Engineering
| University of Bath
| Bath BA2 7AY
| United Kingdom
| Tel: +44 (0)1225 383026
| Fax: +44 (0)1225 386928
| ensdnj@bath.ac.uk
| <http://www.bath.ac.uk/mech-eng/people/johnston>

Investigation of the Acceleration Effect on Dynamic Friction of EHA System

Wei Li †, Richard Burton †, Saeid Habibi ‡, Greg Schoenau † and FangXiang Wu †

† Department of Mechanical Engineering, University of Saskatchewan

‡ Department of Mechanical Engineering, McMaster University

ABSTRACT

In some early modeling studies on a high precision Electro-Hydrostatic Actuator (EHA) by the authors, it was observed that under certain conditions, limit cycles were predicted in the output actuator displacement but were not observed physically even though the parameters used in the modeling were based on experimental measurements. It was suspected that the measured (and subsequently modeled) friction characteristics of the actuator were part of the reason for this discrepancy.

In this paper, dynamic friction modeling of the EHA is experimentally investigated. It was found that the traditional steady-state friction characteristic – the so-called Stribeck effect obtained by measuring the friction forces at different constant velocities - is a poor representation of the true dynamic friction when the EHA experiences various accelerations during the control process, such as the step response.

In this paper, a new term “unsteady state friction” is defined and subsequently measured, examined, and analyzed. Experimental results reveal that this unsteady state friction is a more general form of the dynamic friction. In addition steady state friction is just a special case of the unsteady state friction, which is highly acceleration dependent. When the acceleration increases, the Stribeck effect decreases, indeed, can reach conditions where it no longer exists within the operating velocity range. A novel experiment to measure the friction of the EHA system is presented. A new nonlinear friction model (a 3D surface model) including the acceleration factor is proposed, which indicates that the Stribeck curve is just a special case of the dynamic friction model when the system acceleration is approaching zero. This result can be applied to any actuator (linear and rotary) and provides a new way in which the dynamic friction can be viewed and modeled.

**NOMENCLATURE AND
PARAMETER VALUES**

Variables	Definitions	Values
$A_1 = A_2 = A$	Actuator pressure area	$5.05 \times 10^{-4} \text{ m}^2$ *
D_p	Pump volumetric displacement	$1.6925 \times 10^{-7} \text{ m}^3/\text{rad}$ *
M	The mass of load	20 kg
$F_f(t)$	The friction force	N
P_1, P_2	The chamber pressures of two ends of the actuator	Pa
ΔP	The differential pressure	Pa
Q_{pMax}	Max flow rate of the pump	m^3/s
X	Displacement of actuator	m
L_{Max}	Max travel range	$\sim 0.12 \text{ m}$ *
β_e	Effective bulk modulus of hydraulic oil	$2.1 \times 10^8 \text{ Pa}$ *
ω_p	Pump angular velocity	rad/s
$\text{Acc} = \ddot{X}$	Acceleration of piston	m/s^2
X_{Max}	Max displacement	m
ω_{pMax}	Max pump angular velocity	rad/s
$v = \dot{X}$	The velocity of piston	m/s

V_{Max}	Max velocity of the piston	$\sim 0.13 \text{ m/s}$
f	The frequency of velocity	Hz
t	Time	sec
F_C	Coulomb friction	N
F_b	Breakaway friction	N
v_s	Pseudo-Stribeck velocity	m/s
B	Viscous friction coefficient	N/m/s
$F_C(a)$	Unsteady Coulomb friction	N
$F_b(a)$	Unsteady breakaway friction	N
$k_v(a)$	Velocity coefficient	No Dimension
$k_a(a)$	Acceleration coefficient	No Dimension
$v_b(a)$	Breakaway offset velocity	m/s
$v_s(a)$	Unsteady pseudo-Stribeck velocity	m/s
$B(a)$	Unsteady viscous friction coefficient	N/m/s
n	Exponent number for Stribeck curve	1 or 2

* Values obtained from [1]

1. INTRODUCTION

An Electro-hydraulic actuator (herein referred to as the EHA system) [2] as a hydraulic system can exhibit many nonlinear behaviors, the source of which can be attributed to such things as nonlinear bulk modulus, nonlinear viscosity, and nonlinear friction, amongst others [3, 4]. Of these properties, nonlinear friction is perhaps the most dominant and is a primary source of disturbance for motion control systems and may largely contribute to steady state errors, limit cycles, and poor performance. Many controller designs are highly dependent on the accuracy of the friction model used in the friction compensation loop. For this reason, friction identification and modeling has been one of the most important issues in the design of high-performance motion control systems [5].

Even though the topic of friction is a relatively old one, and has played an important role in many practical and engineering applications, surprisingly it is not as well understood as one might expect it to be [6, 7]. "Dynamic" friction has been traditionally referred to as the friction force which results once motion occurs between sliding surfaces. Literature pertaining to dynamic friction identification, measurement and modeling is vast [8, 9]. Due to its highly non-linear nature, friction is very difficult to model. Most available friction models are, in essence, empirical, that is, they are based on limited observations and interpretations. In this sense, the resulting models are valid only for the specific scope of test conditions, such as the level and type of excitation used to obtain the data [10]. Indeed, the list of frictional effects one may wish to describe varies widely from application to application. In most cases, the selection of a particular friction law is made heuristically without any explanation [11]. In some cases, the friction is simplified by a linearized model; as a result, application of this linearized model can often lead to erroneous results [12].

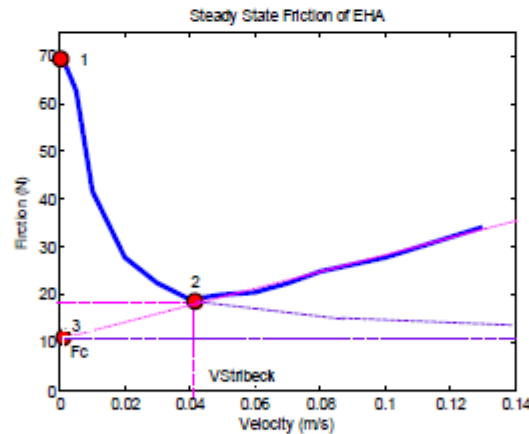


Figure 1 Typical Stribeck curve for the EHA system

Stribeck published his work on the dynamic friction between lubricated surfaces over 100 years ago, which resulted in the well-known Stribeck curve showing the correlation between friction force and velocity [13, 14]. Such a curve measured in the EHA system is illustrated in Figure 1. It is a friction phenomenon which gives rise to decreasing friction with increasing velocity at low velocity (essentially a negative viscous friction slope). In other

words, it was indicated that friction decreases after “breakaway” by overcoming the “breakaway friction” and increases after the velocity passes the Stribeck velocity. This increase was attributed to fact that the thickness of the lubricant film presented between the sliding surfaces increases with the sliding velocity [15]. It has been shown that the Stribeck effect is valid from application to application as long as lubrication between surfaces exists in the “steady state” velocity (with no acceleration) condition. It is necessary to clearly define friction terms since a new definition will be introduced. “Breakaway friction” is the friction which is generated before movement of the sliding surfaces. The static friction force will always be equal to the force applied until it reaches the “breakaway” point. With reference to Figure 1, the “peak friction” (F_b indicated by point 1 in Figure 1) value is defined as the breakaway friction (commonly labeled as the static friction). As discussed earlier, the dynamic friction is the friction under motion conditions. At this point it is necessary to clarify that usually the curve shown in Figure 1 is obtained by measuring the friction at discrete velocity points; that is, the curve is not measured in a continuous fashion. This is a very important consideration because it is not known what the acceleration is at each point; indeed, in most cases, the acceleration is zero. This will be discussed at great length in a later section. If the dynamic friction has been obtained where the acceleration at the discrete measurement velocity points is zero, the dynamic friction curve is defined as being a “steady state” friction characteristic. If acceleration at each point is not zero, this dynamic friction is defined as the “unsteady state” friction. The region where the friction decreases is called the Stribeck region and the point where the velocity again increases is the Stribeck velocity ($V_{Stribeck}$ indicated by point 2 in Figure 1).

The form of the curve in Figure 1 is the Stribeck characteristic and is defined mathematically by equation (1) as follows:

$$F_{Steadystate_friction}(v) = F_c + (F_b - F_c)e^{-\left(\frac{v}{v_s}\right)^n} + Bv \quad (1)$$

where the parameters F_c , F_b , v_s and B are constant and defined graphically in Figure 1. The Coulomb friction (F_c) can be obtained by extending the viscous friction line (indicated by point 3 in Figure 1). Coulomb friction can be defined as a dynamic friction that would exist if the system is in motion and no or little lubrication between two sliding surfaces exists, which is almost independent from the motion velocity [12].

Chinniah [1] used an experimental procedure to measure friction in the particular EHA system of interest in this study. His approach was to keep the piston moving at various constant (discrete) velocities (at zero acceleration) within the velocity range and then measure the differential pressures across the actuator to obtain the steady state nonlinear friction model. A typical result was shown in Figure 1 which displays a form consistent with the classical Stribeck curve. Because this is a discrete approach, the more velocity points used, the more continuous the friction curve becomes. However, accurate measurement of the breakaway friction could not be achieved but had to be estimated using numerical extrapolation methods. This is a problem with using discrete experimental measurement approaches. If a technique which uses a continuous measurement of force with velocity can be implemented, this problem does not exist.

From the literature, the Stribeck friction model has been verified experimentally and is quite widely used in the simulation and control of the practical systems [16]. It is apparent that most dynamic friction models reflect the Stribeck effect illustrated in Figure 1, but with some modifications such as those found in the Bristle model, the Karnopp model, the Reset Integrator model, and the LuGre model amongst others [5, 6, 16-18]. (Out of interest the name LuGre is not based on a person but a combination of a model produced at Lund and Grenoble laboratories. [19]). These models basically reflect a combination or transition between Coulomb friction, viscous friction, and the Stribeck effect. However, the Stribeck friction model has a major limitation in that it is only applicable to what the authors have labeled steady state conditions at the measurement points (i.e., constant or very slow changing sliding velocity under constant normal force). In other words, the Stribeck friction model, as one of classical friction models, does not reflect the rate of change of the velocity at the measured points.

In many applications, machines can operate under what the authors have defined as “unsteady” state conditions (i.e., very rapid changes in slip velocity) where the velocities of the actuators or motors are not constant over time. It is extremely important from a modeling and control point of view to study unsteady state friction and to develop accurate nonlinear models which reflect these specific operating conditions. Furthermore, from an experimental point of view, friction is quite difficult to measure reliably even under steady state conditions, let alone unsteady state conditions. This could account for the fact that very few publications exist which consider the Stribeck characteristic under unsteady or non zero acceleration conditions.

In 1943, Sampson et al. [20] first started to question the Stribeck friction model based on his limited experimental observations in that the friction may not be solely be a function of the velocity, but rather a function of the “past history” of the motion; however, since the “past history” of the motion was not well defined in this paper, improvement to the Stribeck model was not made. In 1990, Hess et al [21] first introduced a novel approach to explore the dynamic friction in the lubricated contact surfaces by measuring the friction under the oscillating sliding velocities at various frequencies. It was observed that the frequency of velocity variation had a significant effect on the shape and size of the friction vs. velocity curve. This study put dynamic friction in a new light by recognizing that there was a frequency effect which needed to be accounted for. This frequency effect could be considered as the history of the velocity measurement. Hamoy et al [22-27] continued this approach by developing an unique apparatus to measure friction in the presence of sinusoidally-varying velocity at various frequencies. The preliminary finding of Hamoy et al. was the effect of the reduction in the magnitude of the friction near zero velocity as the frequency of oscillation increased [27]. This echoed Sampson et al’s observation that the friction was not only a function of the instantaneous velocity, but was also a function of previous velocities. Hamoy et. al also attempted to explain the dynamic friction under unsteady state conditions by the physical principles of hydrodynamic lubrication.

On the other hand, the research of Owen et al. [28] showed that the Stribeck effect can be reduced or eliminated by rotating the piston, which clearly indicated that the Stribeck effect might not apply in some motion conditions. Further, Chatterjee et al [29] found that the breakaway friction force uniformly decreases with the increasing frequency of velocity variation which matched the conclusion from Canudas de Wit. [5], that is, the varying break-away force depends on the rate of change of the applied force. Most recently, Yanada et al. [30] modeled the unsteady state friction by a modified LuGre model which took the

lubrication film thickness into account as an extra parameter. Unfortunately, any extra parameter added to the LuGre model makes the model parameters' identification too difficult to accomplish, because the parameter-estimating task of LuGre model itself was already very tough due to the some unmeasurable states in the model .

A commonality (and perhaps a limitation) in the experimental procedures used by above researchers was that the friction force – velocity relationships were established by changing the frequencies of the velocity waveforms. It is proposed in the authors' (this) paper that the history of the velocity is more appropriately represented by the acceleration as opposed to the frequency of the velocity. In the aforementioned studies, assuming that the frequency is constant, the acceleration of the system could vary from $-X_{max}(2\pi f)^2$ to $X_{max}(2\pi f)^2$ over just one cycle, as is illustrated in equation (2). Thus acceleration is not constant during the measurement process; Changing the frequency of velocity only changes the amplitude of the acceleration.

$$Acc = -X_{max}(2\pi f)^2 \sin(2\pi ft) \quad (2)$$

It was believed that the experimental approach could be improved upon significantly by keeping the acceleration constant over the measurement of friction force. This paper presents a probing study of friction behavior in unsteady state conditions where velocity varies with time by changing acceleration from low to high. Consequently, the main focus of this paper is to introduce a new way to measure and model the unsteady state friction at the actuator. The system studied was of a particular type of high precision hydrostatic system (EHA) in which an understanding of the nature of friction was critical for precision control. It must be noted that although this paper refers to this particular system, the concept is believed to be valid for all actuators which display the Stribeck effect. A particular aspect of friction, which explores the relationship between acceleration and friction forces, is examined and a novel 3D friction model is proposed. The potential for capturing friction forces in a predictive model is also explored .

This paper initially introduces research that has been conducted in the area of friction modeling and has introduced the definitions of steady and unsteady state friction. Section 2 briefly outlines the motivation for the work. Section 3 presents the experimental setup. Sections 4 and 5 will consider the dynamic friction measurement and the experimental results and section 6 will discuss the results and provide conclusions and future works. It must be made clear that the results shown are applicable to the particular EHA systems studied. At the time of paper preparation, extension to a more generalized actuator – friction model has not been completed.

2. RESEARCH MOTIVATION

Although not central to the overall friction study, it is interesting to understand the motivation for this work. In early studies of step responses of a model of the EHA which employed the traditional Stribeck curve, it was found that in the open-loop mode, a highly under-damped response was observed (indeed, under certain conditions, severe limit cycles were exhibited). The problem was that this was not observed experimentally even though the friction model was experimentally obtained from the same system. It was therefore postulated that either the model was wrong or the parameters (noticeably the nonlinear friction) was not correct. This prompted an intense examination of the literature and

subsequent preliminary experiment tests which then led to the conclusion that acceleration effect played an important role in the behavior of unsteady state dynamic friction.

3. EXPERIMENT SETUP

In this section, the experimental setup used for friction measurement is described. The Electro-Hydraulic Actuation system (EHA) considered in this study is shown Figure 2 [31].

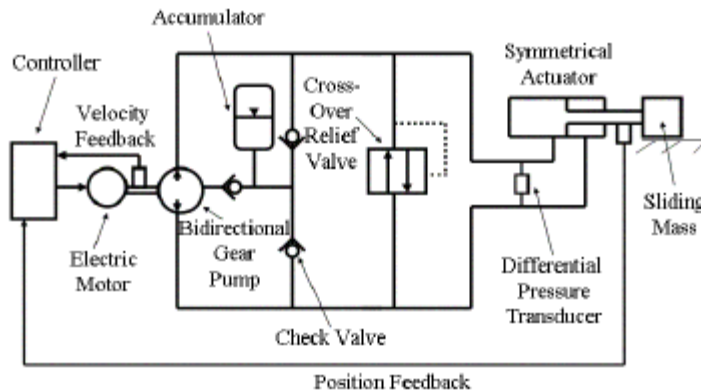


Figure 2 Schematic of Electro-Hydraulic Actuator (EHA) system [31]

The EHA is a closed hydrostatic system in which the actuator output flow is ported back into the inlet of the pump (as opposed to the fluid passing through a reservoir first in the open-circuit systems). Movement of the actuator is controlled by varying the amount of flow that comes from the pump which in turn is controlled by changing the direction and the angular speed of the pump driving motor. Because the system is closed, the actuator must be symmetric and thus for linear actuation special actuators have to be designed. A closed system of this form is highly desirable because it does not require any valve to modulate the flow which increases the system efficiency.

Studying time-varying systems requires fast and accurate measurement techniques with both storage and analyzing systems that can handle large data. An encoder with 50 nm resolution was used to measure the displacement of the mass, while a differential pressure transducer - Validyne DP15 was used to measure the differential pressure between the two ends of the actuator. The calibrations of the encoder and pressure transducer were performed before all experiments. Data acquisition was done by using a multifunction analog & digital I/O board PCI-DAS1602/16. This card with a sampling frequency of 500 Hz digitizes the analog input signals fed into the computer, and also converts the computer's digital output signal into analog form to drive the AC motor. The card features a 16-bit analog input and output resolution. It is designed to operate in computers with PCI bus accessory slots. Each test was repeated three times and the average of these tests are shown. The experimental scatter was found to be very small. Details of the EHA system used in the study can be found in [2].

4. FRICTION MEASUREMENTS

As mentioned in the introduction, earlier work on the EHA system produced a friction velocity relationship which followed the Stribeck curve [1]. Acceleration was kept zero and

as such the friction was considered to be a steady state friction. In this paper, it was proposed to create constant acceleration conditions and as such, a novel method for the friction measurement was developed. The following assumptions were made during the friction measurement experiment, for system modeling and finally for simulation:

- The relative sliding velocities and the operation time was small enough such that thermal effects could be neglected;
- The dynamics effect of the pressure transducer could be neglected due to the fast response feature of the model Validyne DP15.

The EHA friction is the sum of the mass sliding friction and piston cylinder friction. A mass in sliding contact with a surface is a common situation and can represent a highly nonlinear system due to the slip-stick friction at the contact surface. Since hydraulic actuators operate under certain supply pressures, tight sealing is required to prevent them from any leakage [32, 33]. As a result, it has been shown that the piston friction can be substantial. Let the overall friction of the EHA be represented by $F_f(t)$. Because of the inertial term, friction cannot be directly measured because the inertial force must be subtracted. This can be observed from equation (3) :

$$F_f(t) = (P_1 - P_2)A - M \ddot{X} = \Delta PA - M \ddot{X} \quad (3)$$

In order to measure the friction , it is necessary to measure the differential pressure of the actuator and the acceleration of the EHA system. However, measuring differential pressure and acceleration posed substantial challenges in constructing the experimental setup.

The first challenge was getting an accurate differential pressure between the two ends of the actuator. Because the available pressure transducer was very susceptible to outside noise associated with the AC motor driving the EHA, a low pass third order Butterworth filter with a cut off frequency of 20 Hz was used to “clean up” the differential pressure signal. The second challenge was to measure the velocity. Several methods of measuring or estimating velocity were examined. It was decided that the “cleanest” signals could be obtained by differentiating the position signal from the high precision encoder and then filtering the signal using digital filters. The acceleration was estimated from the desired position data differentiated twice with filtering being done only on the velocity signal.

By controlling the position of the actuator to follow a desired parabolic waveform, the velocity increased in a linear fashion and the acceleration became constant for the desired velocity range. Thus by changing the magnitude of the position waveform, friction forces (via pressure differential across the actuator) could be measured (and plotted) as a function of velocity at a constant acceleration. Acceleration became the family parameter in the resulting plots. It is important to note that the resulting friction curves are continuous with velocity. The EHA system has a limitation both in position (due to the stroke limitation) and in the maximum actuator velocity (due to the maximum speed of the electric motor and the pump displacement). Therefore, for the particular EHA application chosen, the limit on stroke was 0.12 (m) and velocity range was constrained to be between 0 – 0.13 (m/s) .

5. EXPERIMENTAL RESULTS

As was previously stated, under conditions of low acceleration, friction could only be estimated at discrete points by inputting the EHA with triangular positional (step velocity)

when the motion of the EHA system changes from unsteady state to steady state, $F_c(a)$ will approach F_c . $F_s(a) - F_c(a)$ will approach $(F_s - F_c)$; and unsteady item $(k_v(a)v + v_b(a))^{k_a(a)a}$ will disappear by approaching 1. Further, $v_s(a)$ will approach v_s and $B(a)$ will approach B . Therefore, the unsteady state friction will transform to the Stribeck friction. In other words, the equation (1) is just a special form of equation (4).

Based on the physical meaning of the general friction model – unsteady-state dynamic friction (see equation (4)), the Coulomb friction stays constant as F_c which can be viewed from two different perspectives. From Figure 1, the extension of the linear segment will have an intersection with the friction axis at Coulomb friction. From Figure 4, it is observed that the breakaway friction decreases but tends to converges to a constant value - Coulomb friction when the acceleration increases.

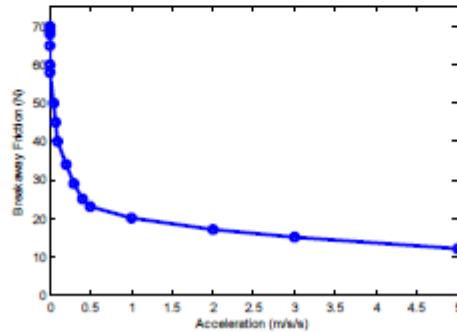


Figure 4 Breakaway Friction Curve of the EHA System

The breakaway frictions for the results of Figure 3, are shown in Figure 4. These results can be compared to the results from Olsson, H. et al. [8, 9], in which their experimental trends paralleled those shown in Figure 4., that is, the breakaway forces did depend on the accelerations. With reference to equation (4), $F_b(a)$ and $v_b(a)$ are the breakaway friction and the breakaway offset velocity respectively, which are functions of accelerations. And, which help to build the curve of breakaway frictions over accelerations (Figure 4). At low accelerations, $F_b(a)$ and $v_b(a)$ are larger, the breakaway frictions have larger values. At high accelerations, $F_b(a)$ and $v_b(a)$ are smaller, the breakaway frictions have smaller values and approaches the Coulomb friction F_c .

$k_v(a)$ and $k_a(a)$ are the velocity coefficient and the acceleration coefficient of the unsteady state friction respectively, which can significantly affect the positive slopes of the friction – velocity curves. At low accelerations, $k_v(a)$ is small, $k_a(a)$ is large, the friction – velocity curves (shown in Figure 3) have little negative or little positive slope after breakaway. At high accelerations, $k_v(a)$ is large, $k_a(a)$ is small, the friction - velocity curves will have a strong positive slope after breakaway occurs.

$k_s(a) = \frac{1}{v_s(a)}$ is defined as the Stribeck effect coefficient which can determine the negative

slope of the unsteady state friction – velocity curves after the peak frictions. A smaller $k_s(a)$ translates to a smaller negative slope of the unsteady state friction. Vice-versa. Based on the hydrodynamic lubrication theory, the viscous friction coefficient $B(a)$ stays nearly constant, and will be very close to the value of B . The last parameter is the exponent number of the Stribeck curve n , the default value being 1. In some cases, it can be 2 or greater; however, it could make the friction model too complex for practical applications.

Similar plots could be developed for peak frictions (blue line with circle markers) and Stribeck velocities (green line with cross markers); however, a more meaningful representation can be developed using a 3-D plot of the results as shown in Figure 5. In this plot, acceleration is the third parameter and hence the data shown in Figure 3 appears as the 3-D plot of Figure 5. A map such as this can be very important in simulations since the map can be represented as a 2D lookup table. If the velocity and acceleration are known, then the friction force can readily be estimated. Furthermore, for constant acceleration, the coefficients of the Stribeck equation can be estimated. In Figure 5, when the velocity = 0, the intersection curve (red dot line with star markers) represents the breakaway friction curve (shown in Figure 4), whereas, when the acceleration = 0, the intersection curve (black line with triangle markers) is the steady state friction curve or Stribeck curve (shown in Figure 1).

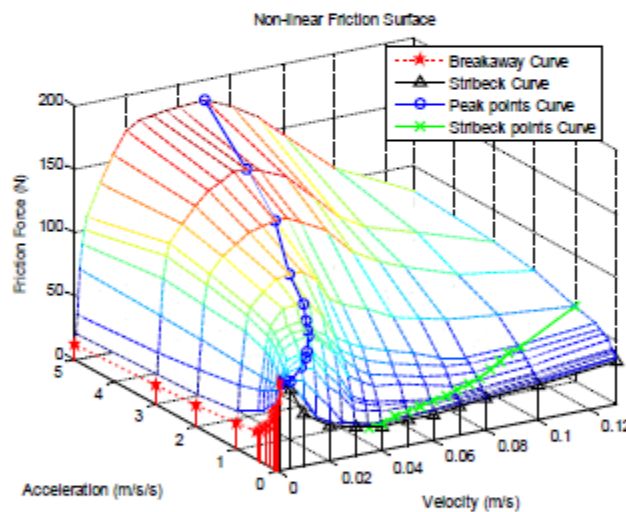


Figure 5 3D nonlinear friction surface (2D lookup table)

One observation that is worth noting is the change in the slope of the friction velocity curve at low velocities as the acceleration is increased. At low acceleration, the slope is negative

and could be destabilizing. However for the same velocity range at high accelerations, the slope is positive and hence can stabilize the system.

6. DISCUSSION AND CONCLUSIONS

For most mechanical systems, the friction in motion condition is usually defined as a dynamic friction. However, the definitions of the dynamic friction in most literature are either vague or inadequate. As previously stated, two types of dynamic friction conditions were defined: unsteady state friction and steady state friction. Steady state dynamic friction is defined as the dynamic friction under steady velocity conditions, (i.e., zero or very small acceleration condition). On the other hand, unsteady state dynamic friction is defined as the dynamic friction under unsteady velocities, where the actuator motion occurs under significant acceleration conditions.

In this paper, unsteady state friction behavior in EHA system was experimentally examined by varying velocities under various constant acceleration conditions. A 3D friction model (Figure 5) reflecting this acceleration factor has been developed. In the steady state, the peak friction point overlaps the maximum breakaway point, and the system displays negative damping during the low velocities range. As the acceleration of the system increases, the breakaway point magnitude decreases, the magnitude of the peak friction increases, and the velocity at which the peak friction increases (introducing a positive friction velocity curves at low velocities). Physical explanation of this novel 3D friction model is not immediately clear, but it is believed that this is closely associated with film thickness during the accelerating period [34].

In conclusion, just like the steady state friction is a special case of the unsteady state friction, the Stribeck effect is a special case of the more general unsteady state friction model (Figure 5 and equation (4)). This paper provides an insight on how to model the dynamic friction, particularly for the unsteady state motion. Based on this work, the authors are working toward an united friction model which can cover all the static and dynamic friction situations into a so-called rate dependent friction model (including hysteresis). In addition, the authors are working to determine the functional forms of equation (4) by system identification and parameter estimation techniques, which would then replace the 2D lookup table in simulations and controller designs. As stated in the introduction, the authors are examining other applications to establish that the friction characteristics observed in this study can be universally applied to more generalized applications.

ACKNOWLEDGMENTS

The authors acknowledge the financial support of the National Science and Engineering Research Council of Canada (NSERC) and the Department of Mechanical Engineering, University of Saskatchewan during this study. The technical assistance of Mr. D.V. Bitner is gratefully acknowledged.

REFERENCES

- [1] Chinniah, Y. A., 2004, "Fault Detection in the Electrohydraulic Actuator using Extended Kalman Filter," pp. 1- 272, PhD Thesis, University of Saskatchewan.

- [2] Habibi, S., Burton, R., and Sampson, E., 2006, "High Precision Hydrostatic Actuation Systems for Micro-and Nanomanipulation of Heavy Loads," *Journal of Dynamic Systems, Measurement and Control, Transactions of the ASME*, **128**(4) pp. 778.
- [3] Li, W., Burton, R., and Habibi, S., 2007, "Investigation of a High Precision Hydrostatic Actuation System - How Nonlinearities Affect its Performance," 2007 ASME International Mechanical Engineering Congress and Exposition, Anonymous ASME, .
- [4] Merritt, H.E., 1967, "Hydraulic control systems," Wiley, New York, pp. 358.
- [5] Canudas de Wit, C., Olsson, H., Astrom, K. J., 1995, "A New Model for Control of Systems with Friction," *Automatic Control, IEEE Transactions On*, **40**(3) pp. 419.
- [6] Feeny, B. e. a., 1998, "A Historical Review on Dry Friction and Stick-Slip Phenomena," *Applied Mechanics Reviews*, **51**(5) pp. 321.
- [7] Wikiel, B., 2000, "Stick-Slip Motion for Two Coupled Masses with Side Friction," *International Journal of Non-Linear Mechanics*, **35**(6) pp. 953.
- [8] Olsson, H., Astrom, K. J., Canudas de Wit, C., 1998, "Friction Models and Friction Compensation," *European Journal of Control*, **4**(3) pp. 176.
- [9] Armstrong-Helouvry, B., Dupont, P., and Canudas De Wit, C., 1994, "A Survey of Models, Analysis Tools and Compensation Methods for the Control of Machines with Friction," *Automatica*, **30**(7) pp. 1083.
- [10] Al-Bender, F., 2008, "Characterization of Friction Force Dynamics," *IEEE Control Systems Magazine*, **28**(6) pp. 64.
- [11] Vielsack, P., 2001, "Stick-Slip Instability of Decelerative Sliding," *International Journal of Non-Linear Mechanics*, **36**(2) pp. 237.
- [12] Berger, E. J., 2002, "Friction Modeling for Dynamic System Simulation," *Applied Mechanics Reviews*, **55**(6) pp. 535.
- [13] Stribeck, R., 1902, "Die Wesentlichen Eigenschaften Der Gleit- Und Rollenlager the Key Qualities of Sliding and Roller Bearings," *VDI-Zeitschrift = Zeitschrift Des Vereines Deutscher Ingenieure*, **46**pp. 1342-48,1432-37.
- [14] Jacobson, B., 2003, "The Stribeck Memorial Lecture," *Tribology International*, **36**(11) pp. 781.
- [15] Popovic, M. R., 1996, "Friction Modeling and Control," pp. 1-180, PhD Thesis, University of Toronto.
- [16] Armstrong-Helouvry, B., 1991, "Control of machines with friction," Kluwer Academic Publishers, Boston :, pp. xi, 173 p. .
- [17] Karnopp, D., 1985, "Computer Simulation of Stick-Slip Friction in Mechanical Dynamic Systems," *Journal of Dynamic Systems, Measurement and Control, Transactions of the ASME*, **107**(1) pp. 100.

- [18] Haessig Jr, D. A., and Friedland, B., 1991, "On the Modeling and Simulation of Friction," *Journal of Dynamic Systems, Measurement and Control, Transactions of the ASME*, 113(3) pp. 354.
- [19] Johansson, K., 2008, "Revisiting the LuGre Friction Model," *IEEE Control Systems Magazine*, 28(6) pp. 101.
- [20] Sampson, J. B., Morgan, F., Reed, D. W., 1943, "Friction Behavior during the Slip Portion of the Stick-Slip Process," *J. Appl. Phys.*, Vol.14 pp. pp.689-700.
- [21] Hess, D. P., and Soom, A., 1990, "Friction at a Lubricated Line Contact Operating at Oscillating Sliding Velocities," *Journal of Tribology*, 112(1) pp. 147.
- [22] Harnoy, A., 2008, "Modeling and Measuring Friction Effects," *IEEE Control Systems Magazine*, 28(6) pp. 82.
- [23] Harnoy, A., 1997, "Simulation of Stick-Slip Friction in Control Systems," *ASLE Transactions*, 40(2) pp. 360.
- [24] Rachoor, H., and Harnoy, A., 1996, "Modeling of Dynamic Friction in Lubricated Line Contacts for Precise Motion Control," *Tribology Transactions*, 39(2) pp. 476.
- [25] Harnoy, A., and Friedland, B., 1994, "Dynamic Friction Model of Lubricated Surfaces for Precise Motion Control," *S T L E Tribology Transactions*, 37(3) pp. 608.
- [26] Harnoy, A., Friedland, B., and Rachoor, H., 1994, "Modeling and Simulation of Elastic and Friction Forces in Lubricated Bearings for Precise Motion Control," *Wear*, 172(2) pp. 155.
- [27] Harnoy, A., Friedland, B., Semenov, R., 1994, "Apparatus for empirical determination of dynamic friction," *Anonymous American Automatic Control Council*, 1, pp. 546.
- [28] Owen, W. S., and Croft, E. A., 2003, "The Reduction of Stick-Slip Friction in Hydraulic Actuators," *Mechatronics, IEEE/ASME Transactions On*, 8(3) pp. 362.
- [29] Chatterjee, S., 2004, "Effect of High-Frequency Excitation on a Class of Mechanical Systems with Dynamic Friction," *Journal of Sound and Vibration*, 269(1) pp. 61.
- [30] Yanada, H., 2008, "Modeling of Dynamic Behaviors of Friction," *Mechatronics*, 18(7) pp. 330.
- [31] Sampson, E. B., 2005, "Fuzzy Control of the ElectroHydraulic Actuator," pp. 1- 151, Master Thesis, University of Saskatchewan.
- [32] Sekhvat, P., 2006, "Impact Stabilizing Controller for Hydraulic Actuators with Friction: Theory and Experiments," *Control Engineering Practice*, 14(12) pp. 1423.
- [33] Amin, J., 1996, "Implementation of a friction estimation and compensation technique Control Applications, 1996., Proceedings of the 1996 IEEE International Conference on," pp. 804.

[34] Sugimura, J., 1998, "EHD Film Thickness in Non-Steady State Contacts," *Journal of Tribology*, **120**(3) pp. 442.

APPENDIX B2: CANCEM 2013 CANADIAN CONGRESS OF APPLIED
MECHANICS CONFERENCE PAPER

This section includes the paper which was presented at 24th Canadian Congress of Applied Mechanics (CANCEM), conference in Saskatoon, Canada in June, 2013.

Permission for the paper published in CANCEM 2013 was asked from the copyright holder to attach this paper as an appendix. The permission is documented as follows:

Dear Professor Sumner:

I would really appreciate if you give me a permission to include my paper which was published in CANCEM 2013, Saskatoon, Canada in my PhD thesis in University of Saskatchewan. The paper is CS-9: Scott Li, Doug Bitner, Richard Burton, and Greg Schoenau, Experimental Investigation of Acceleration Dependent Nonlinear Friction in Hydraulic Actuation Systems, CANCEM 2013.

I am looking forward to hearing from you at your earliest convenience. Thanks.

Best Regards,

Scott Li

Scott,

All authors retain copyright of their CANCEM papers - therefore, you are free to use it as you wish.

Prof. Sumner

EXPERIMENTAL INVESTIGATION OF ACCELERATION DEPENDENT NONLINEAR FRICTION IN HYDRAULIC ACTUATION SYSTEMS

Scott Li
Dept. of Mechanical Engineering
University of Saskatchewan
Saskatoon, Saskatchewan, Canada
Email: we418@gmail.com

Richard Burton
Dept. of Mechanical Engineering
University of Saskatchewan
Saskatoon, Saskatchewan, Canada
Email: Richard.burton@usask.ca

Doug Bitner
Dept. of Mechanical Engineering
University of Saskatchewan
Saskatoon, Saskatchewan, Canada
Email: Doug.Bitner@usask.ca

Greg Schoenau
Dept. of Mechanical Engineering
University of Saskatchewan
Saskatoon, Saskatchewan, Canada
Email: Greg.Schoenau@usask.ca

ABSTRACT

In an initial friction study conducted by the authors, it was observed that in a pump controlled hydraulic actuation system - a high precision closed circuit Electro-Hydrostatic Actuator system (EHA), when the acceleration increased, the well-known friction characteristic called the Stribeck effect changed, and indeed, reached conditions where the slip stick behavior no longer existed within the operating velocity range. The initial results were presented at Bath/ASME Symposium on Fluid Power and Motion Control in 2010 (FPMC 2010) [1] and a challenge was forwarded to the authors to extend their work to other hydraulic actuation systems to determine if the trends so observed could be applied more universally. This paper considers the results of this extended study on a valve controlled hydraulic actuation system (VCHAS). The unsteady-state friction behavior in a VCHAS was experimentally examined by varying velocity under various constant acceleration conditions. The experimental results reveal a similar friction model to that obtained in the EHA study, which also had a strong dependency on acceleration. The results of this study imply that one must use traditional friction models (velocity dependent only) with care when the system experiences unsteady state motion conditions.

Keywords: Stribeck effect, Unsteady State Friction, Acceleration Dependent, Hydraulic Actuation System (HAS),

Electro-Hydrostatic Actuator (EHA), Valve Control Hydraulic Actuation System (VCHAS).

INTRODUCTION

In an earlier modeling study on an EHA system by the authors, it was observed that under certain conditions, such as in a step response test, limit cycles were predicted to exist in the actuator displacement, but were not observed physically even though the parameters used in the modeling were based on experimental measurements [2]. It was suspected that the measured (and subsequently modeled) friction characteristics of the actuator were part of the reason for this discrepancy. In a follow up study, the authors investigated some of the fundamental behavioral characteristics of the EHA such as nonlinear friction and found that friction forces depended not only on velocity, but also on acceleration. These initial results were presented at FPMC 2010 and a challenge was forwarded to the authors to extend their work to other hydraulic actuation systems to determine if the trends so observed could be applied more universally [1]. The objective of this paper is to consider the results of this extended study on a VCHAS and discuss the experimental results and the experimental procedures used to obtain the experimental data. Also in this paper, some of the new definitions that arose from the initial research are briefly introduced. Conclusions and discussions on the results are then presented with some recommendations for future work.

PREVIOUS WORK

A great deal of research on friction has been done over the past decades [3, 4]. For designers of hydraulic control systems, friction is perhaps one of the most important parameters which needs to be accurately modeled. As mentioned above, using a traditional approach to measuring and then modeling friction in a model of the EHA system produced erroneous results [1]. Subsequent studies indicated that friction was dependent on both velocity and acceleration. A typical result is shown in Figure 1.

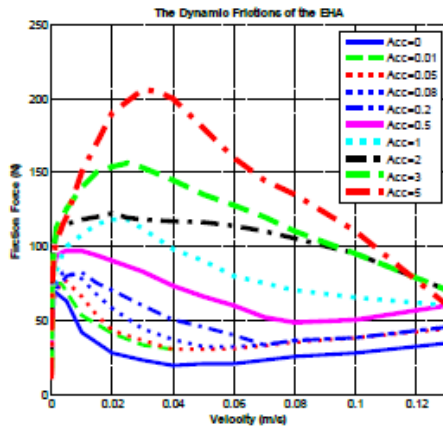


Figure 1 Acceleration Dependent Friction Curves of EHA [1]

The choice of input to the test system was very important. To enable repeatable data collection for the different friction conditions and to accommodate the effect of hysteresis, a step/ramp signal for the actuator motion was chosen (Figure 2). This choice of input waveform enabled acceleration to be the family parameter.

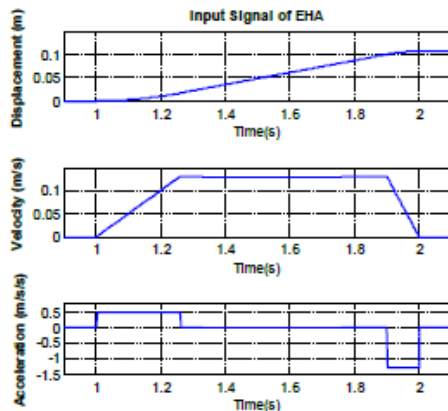


Figure 2 Input Signal of EHA

It is necessary to clearly define some important friction terms since a new definition will be introduced. “Static friction” is the friction that is generated before movement of the sliding surfaces. The static friction force will always be equal to the force applied until it reaches the “breakaway” point. “Dynamic friction” is usually defined as the friction under motion conditions. However, the definitions of dynamic friction in most literature are either vague or inadequate. In this study, two types of dynamic friction conditions are defined: unsteady state dynamic friction and steady state dynamic friction. Steady state dynamic friction is defined as the dynamic friction under steady velocity conditions, (i.e., zero or very small acceleration conditions). On the other hand, unsteady state dynamic friction is defined as the dynamic friction under unsteady velocities, where the actuator motion occurs under significant acceleration conditions.

EXPERIMENT SETUP

Several test systems and several input signal waveforms were examined (one example is shown in Figure 2 for the EHA system), but the one adopted for the particular system in this follow up study produced more consistent results than the other test setups. It should be noted that the trends were consistent, but repeatability was an issue in some of these other test facilities. The experimental test system that was ultimately used is shown in Figure 3. It is essentially a valve controlled hydraulic actuation system (here within referred to as the VCHAS).

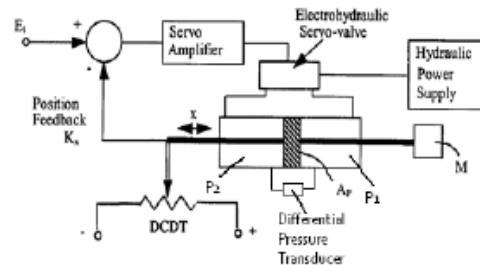


Figure 3 Experimental set-up of VCHAS system

The VCHAS consists of a hydraulic pump, an electrohydraulic servo-valve, a rectilinear hydraulic actuator to move a load, a displacement transducer to provide position feedback, a differential pressure transducer and an amplifier to obtain an error signal, provide gain and drive the valve.

The temperature in the VCHAS was held constant at $30 \pm 2^\circ\text{C}$. A specified waveform position signal was input to the VCHAS which resulted in the desired position, and hence velocity and acceleration waveforms. The objective was to create a periodic waveform in which the output acceleration was constant and various velocities could be specified. The resulting acceleration waveform when integrated resulted in a ramp velocity waveform and when integrated again, in a

parabolic waveform of position which then became the desired input signal. These input signals are illustrated in Figure 4. To achieve different steady state acceleration values, a new level of acceleration is chosen which increases or decreases the slope of the velocity curve which in turn changes the shape of the displacement curve. To enable repeatable data collection for the different friction conditions and to accommodate the effect of hysteresis, a cyclic signal for the actuator motion was chosen (Figure 4). Note the difference in the waveform shown in Figure 2.

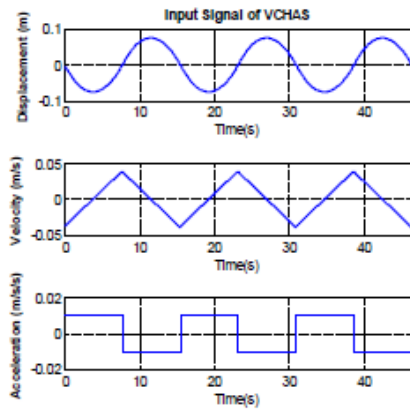


Figure 4 an Input Signal of VCHAS

EXPERIMENTAL RESULTS

As mentioned in the introduction, an earlier work on the EHA system produced a friction velocity relationship which followed the Stribeck curve where acceleration was kept small enough so that the friction could be considered to have steady state characteristics. The overall friction of the VCHAS can be represented as $F_f(t)$ which can be defined as (see Figure 3 for nomenclature).

$$F_f(t) = (P_1 - P_2)A_p - M\ddot{X} = \Delta PA_p - M\ddot{X} \quad (1)$$

In this equation, the friction cannot be determined directly from the pressure differential across the actuator ($P_1 - P_2$) because the inertial force term $M\ddot{X}$ must be determined first. By keeping acceleration (\ddot{X}) constant, the velocity can increase continuously from zero to the maximum velocity; as a result, friction can be calculated continuously from the pressure differential across the actuator at a particular level of acceleration. In order to achieve a constant level of acceleration, the position signal waveform shown in Figure 4 was applied to the input of the VCHAS system shown in Figure 3. Since there is position feedback, the output attempts to follow the input so that constant acceleration can be approximated at the actuator.

As a consequence of hysteresis, the behavior of friction is dependent on the starting and reversing point of motion, which Equation (1) does not take into account. If the cyclic signal is divided into 4 quadrants, each quadrant can be described by a unique model and then Equation (1) can be applied. Figure 5 shows typical signals and the different quadrants that are considered.

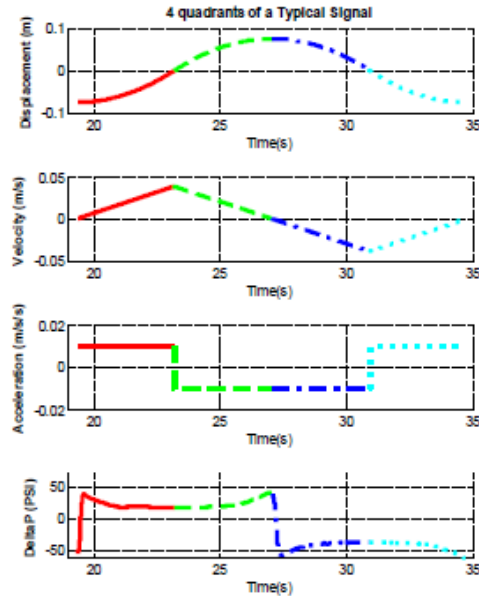


Figure 5 A Typical signal (4 quadrants, with each one highlighted in a different colour/line type)

The 1st quadrant (the red portion in Figure 5) is the most popular one for friction analysis, which is usually used as the benchmark for friction modeling. Figure 6 shows the friction versus velocity results of the VCHAS actuator in the 1st quadrant. The experimental results indicate that the unsteady state dynamic friction of the VCHAS has a strong dependency on the velocity of the moving surfaces, but also a strong dependency on acceleration. It can be seen that the friction approaches the Stribeck curve when acceleration approaches zero, but at higher acceleration values, the friction exhibits a completely different characteristic. All the experiments were performed at 10 different constant accelerations (0.01 m/s/s to 5 m/s/s). The experimental results had good repeatability and good "structure" and demonstrated reasonable accuracy when using a well-designed noise filter. The range of acceleration and velocity was limited by the dimensions of the actuator and the capacity of the VCHAS. Thus the friction curves for low acceleration values were limited at low velocities because of the waveform adopted (Figure 5); however, the main

objective was to demonstrate how the Stribeck form of friction breaks down as acceleration increases.

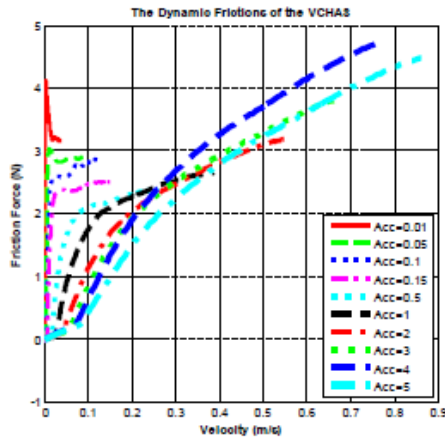


Figure 6 Acceleration Dependent Friction Curves of the VCHAS

CONCLUSIONS

Based on the experimental results above, it can be observed from Figures 1 and 6 that (1) the EHA system has more dominant coulomb friction effects, and (2) the VCHAS system has more vicious friction effects; however, both nonlinear friction versus velocity patterns of the VCHAS and the EHA system are both dependent on acceleration, which indicates that an acceleration dependent acceleration friction model can be used more universally. As is commonly experienced, the nature of this research is very data-intensive. It is understandable that in this paper just some preliminary data could be presented, which will require additional studies. The signal to noise ratio is still an issue in securing accurate experimental data – such as in the velocities and acceleration data. Other factors such as the possible expansion of the hydraulic cylinder and possible seal deformation due to the pressures in the cylinder chambers also need to be investigated to make sure that acceleration is the major factor influencing the friction in unsteady state conditions. For future work, a 3D friction model verification of the 1st quadrant will be completed by using various periodic input signals in the experiment. A challenge remains to be able to take this 3D model and to discretize the data so it can be practically integrated into a dynamic model of the EHA and VCHAS systems. This is now being pursued.

ACKNOWLEDGMENTS

The authors acknowledge the financial support from a NSERC Discovery Grant.

REFERENCES

- [1] Li, W., Burton, R., Habibi, S., Schoenau G., W, FX., 2010, "Novel Dynamic Friction Modeling of a High Precision Electro-Hydrostatic Actuator (EHA) System," Bath/ASME Symposium on Fluid Power and Motion Control FPMC 2010, ed.
- [2] Li, W., Burton, R., and Habibi, S., 2007, "Investigation of a High Precision Hydrostatic Actuation System - How Nonlinearities Affect its Performance," 2007 ASME International Mechanical Engineering Congress and Exposition, Anonymous ASME, .
- [3] Yanada, H., 2008, "Modeling of Dynamic Behaviors of Friction," *Mechatronics*, 18(7) pp. 330.
- [4] Hamoy, A., 2008, "Modeling and Measuring Friction Effects," *IEEE Control Systems Magazine*, 28(6) pp. 82.

APPENDIX C: CALIBRATION INFORMATION

In this appendix, the calibrations of the transducers and sensors used in this study are introduced. The calibration equations for the pressure transducer used are presented. The resolution of the data acquisition system is also discussed.

C.1 Calibration of Differential Pressure Transducer – Dead Weight Method

The pressure transducers used in the experimental studies on VCHAS1 and VCHAS2 are Validyne DP15-20 differential pressure transducers. These transducers were calibrated in the lab using a “dead weight tester” (Type 5525, Mansfield and Green Inc.). Differential pressure systems are calibrated with the one port open to atmosphere. The dead weight tester consisted of a “static” hand pump pressure generator and a piston of a precisely known area loaded by accurately calibrated weights. The differential pressure transducer was connected to the pressure generator outlet by attaching one side of the transducer to the pressure port of the dead weight tester with the other side of the transducer connected to atmosphere. The gauge was calibrated by systematically placing known weights on the piston, pumping the hand pump (pressurizing the dead weight tester) until the weights on the piston moved a small amount, and then recording the output voltage from the transducer. The weights on the piston translated directly to pressure.

In the calibration, the zero point of the amplifier of the pressure transducer needed to be adjusted to make the output voltage zero when the pressure was zero. The maximum range of the input analog voltage of the data acquisition systems used in this study was -10 to $+10$ v. The maximum differential pressure (peak value) in VCHAS1 was estimated to be 200 psi (1379 kPa). The span of the amplifier of the pressure transducer was adjusted to be 10 v, when the pressure was equal to be 200 psi (1379 kPa). The pressure-voltage linear relationship for the VCHAS1 system is shown in Figure C.1.

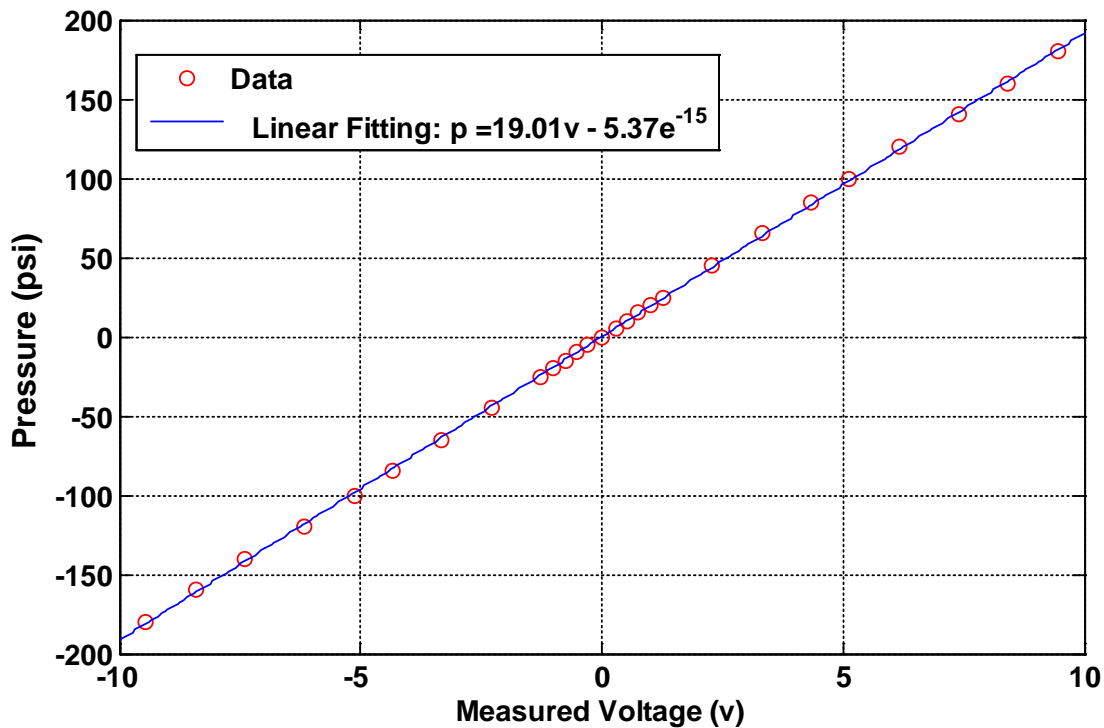


Figure C.1 The pressure-voltage relationship of the pressure transducer of VCHAS1. The data was measured in psi and hence the graph is presented in this form. The sensitivities and calibration data can be converted to metric using the usual conversion equations.

Consider Figure C.1. The linear fitting equation of calibrated data is: $p = 19.01v - 5.37e^{-15} \approx 19.01v$. The sensitivity of the transducer of VCHAS1 was determined to be 19.01 psi/v (131 kPa/v). The maximum pressure the data acquisition can accept was about 190 psi (1310 kPa).

The maximum differential pressure (peak value) in VCHAS2 was estimated to be 80 psi (552 kPa). The pressure-voltage linear relationship for the transducer used in VCHAS2 is shown in Figure C.2.

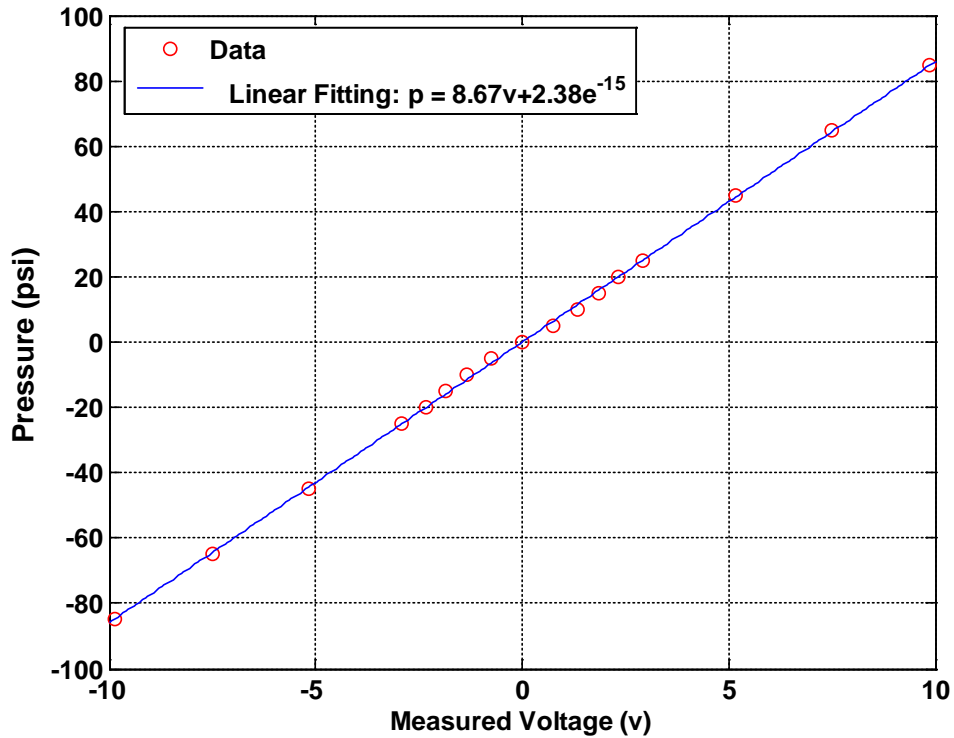


Figure C.2 The pressure-voltage relationship of the pressure transducer of VCHAS2. The data was measured in psi and hence the graph is presented in this form. The sensitivities and calibration data can be converted to metric using the usual conversion equations.

Consider Figure C.2. The linear fitting equation of the calibrated data is: $p = 8.67v - 2.38e^{-15} \approx 8.67v$. The sensitivity of the transducer of VCHAS2 was calculated to be 8.67 psi/v (60 kPa/v). The maximum pressure the data acquisition can accept was about 86 psi (592 kPa).

C.2 Calibration of Position Transducers

C.2.1 Lucas Schaevitz

The displacement sensor for the VCHAS1 study was a linear variable differential transformer (LVDT) sensor model 5000 DC-E DCDT, with a measurement range of ± 120 mm. This transducer was calibrated by Lucas Schaevitz Inc. The sensitivity of the transducer was reported as 12.8 mm/V.

C.2.2 Microtrak II

The displacement sensor for the VCHAS2 study was a Microtrak II stand-alone laser type sensor, model LTC-300-200-SA and a measurement range of ± 100 mm. This transducer was calibrated by the manufacturer, MTI Instruments Inc. The sensitivity of the transducer was reported as 25 mm/V.

C.3 Calibration of Temperature Sensor

The temperature of VCHAS1 and VCHAS2 was monitored using a T type thermocouple sensor, model 692-8000 and a measurement range of -250 to 400 °C. This transducer was calibrated by the manufacturer, Barnant Co. The temperature accuracy of the transducer was reported as ± 0.4 °C.

C.4 Data Acquisition Resolution

Digital signals from the transducers were input into a Personal Computer (IBM type MT-M 2212 WDS) through a 12 bit analog-to-digital (A/D) converter (National Instruments type pci-6025e), and a signal from the computer was supplied to the servo-valves through a 12-bit digital-to-analog (D/A) converter (National Instruments type PCI-6025e). “Real Time Windows Target” was used in the data acquisition system which is a toolbox provided in the Matlab/Simulink® environment for collecting real time data.

Piston positions and differential pressures were recorded at intervals of 1 ms (or sampling rate is 1000 Hz) for all experiments.

APPENDIX D: FREQUENCY CONTROL FOR DESIRED CONSTANT VELOCITIES AND DESIRED CONSTANT ACCELERATIONS

As mentioned in Chapter 3, for the Stribeck model of steady state friction, lubricated friction has to be measured under steady state conditions. For the 2D LUT model of non-steady state friction, lubricated friction has to be measured under non-steady state conditions. In the experimental portion of the study, periodic displacement (or position) of the piston is controlled to follow a triangular waveform signal to produce a constant velocity (specified from a selected list) in order to create steady state conditions. In addition, the piston is controlled to move in a parabolic motion to produce constant accelerations (specified from a selected list) to create non-steady state conditions. The frequency of the displacement signal can be used to achieve the desired constant velocity and desired constant acceleration. In this appendix, the relationships between the frequencies of the input displacement signal, constant velocity and constant acceleration are presented.

D.1 Frequency Control for Desired Constant Velocities

In this section, the derivation of Equation (3.1): $|v| = 2Lf$ (and hence $f = \frac{1}{2L}|v|$) is presented, where L is the actuator stroke and f is the frequency of the input signal. For steady state motion, the displacement assumes a triangular waveform shape with period P or frequency ($f = 1/P$) and amplitude A where $A = L/2$ (Figure D.1).

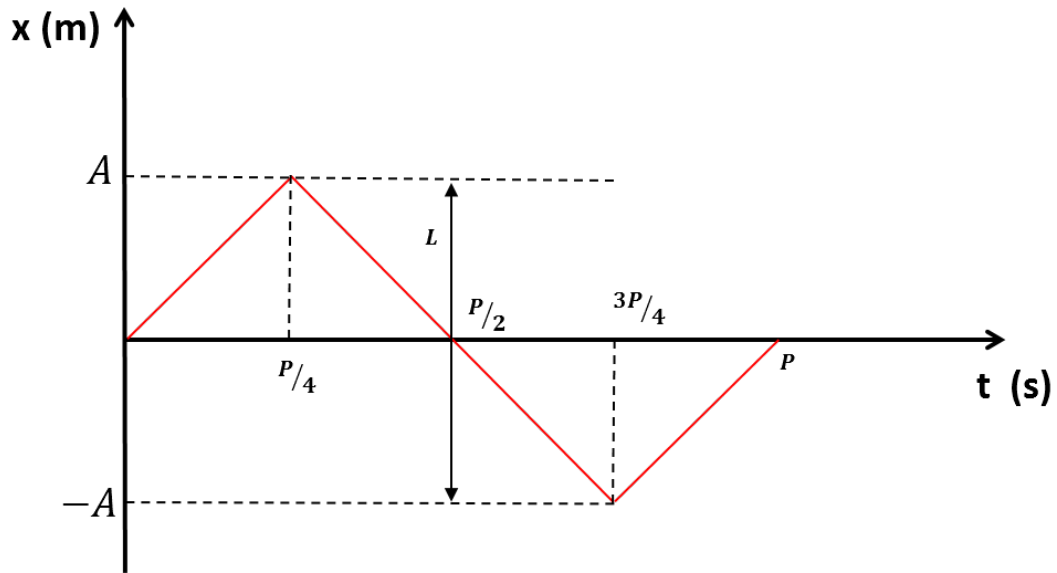


Figure D.1 A cycle of the displacement curve with constant velocity for each direction; the period of the signal is P , the amplitude of the signal is A . Please note, L is the stroke of the piston. The amplitude A is half of the actuator stroke $A = L/2$

If the displacement of the piston can be controlled to follow the desired displacement curve illustrated in Figure D.1, then, the velocity of the piston is constant in each direction as illustrated in Figure D.2.

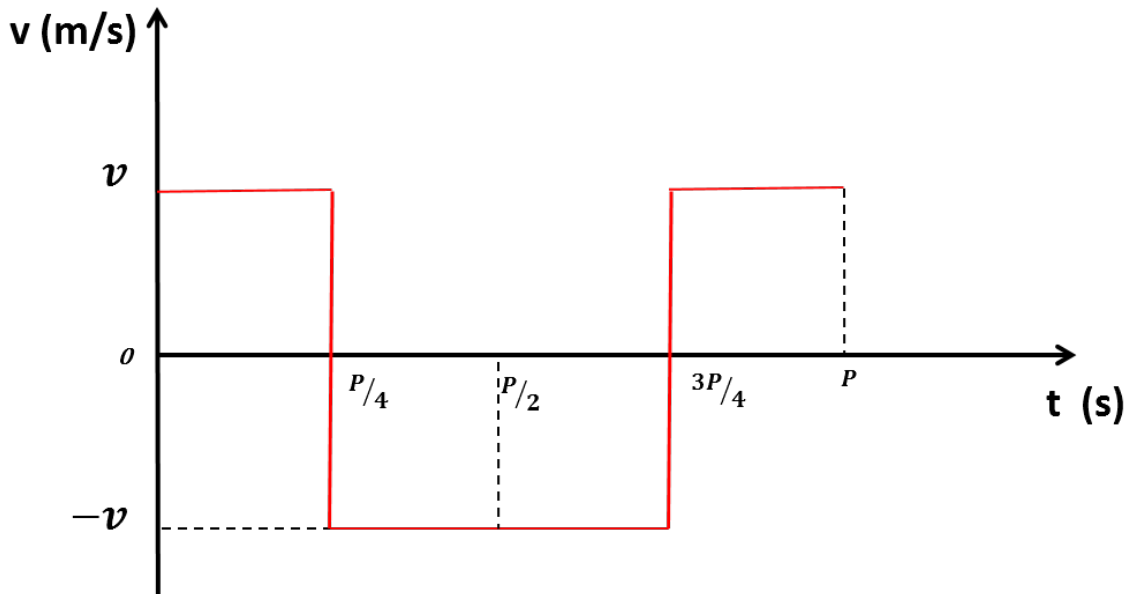


Figure D.2 A cycle of the velocity curve with constant velocity for each direction; the period of the signal is P , and the amplitude of the signal is the desired constant velocity v .

To find the relationship between the desired velocity and input signal frequency, consider Figure D.1. The constant velocity can be obtained from the slope of the displacement as:

$$v = \frac{\Delta x}{\Delta t} \quad (\text{D. 1})$$

where x is the displacement, t is the time.

$$v = \frac{\Delta x}{\Delta t} = \frac{A}{P/4} = \frac{4A}{P} = 4Af \quad (\text{D. 2})$$

where A is the amplitude of piston displacement ($A = L/2$), P is the period, and f is the frequency of the input displacement signal respectively.

It is evident that velocity is positive in one direction and negative in the other direction (Figure D.2); therefore, the relationship between the desired velocity and input displacement signal is as follows:

$$|v| = 2Lf \quad (\text{D. 3})$$

From Equation (D.3), it is observed that the piston velocity (v) has a linear relationship with the frequency of the input displacement signal. For any desired velocity (v), the frequency (f) can be obtained as follows:

$$f = \frac{1}{2L}|v| \quad (\text{D. 4})$$

Theoretically, any desired velocity can be achieved by adjusting the frequency of the input displacement signal. In addition, the longer the actuator stroke (L), the higher the velocity for the same frequency (f).

D.2 Frequency Control for Desired Constant Accelerations

In this section, the derivation of Equation (3.3): $|a| = 16Lf_s^2$ (and hence $f = \sqrt{\frac{1}{16L}|a|}$) is given. For non-steady state motion with constant acceleration (a), the velocity (v) increases linearly. The resulting displacement assumes a parabolic waveform with period P or frequency ($f = 1/P$) and amplitude A where $A = L/2$ (Figure D.3).

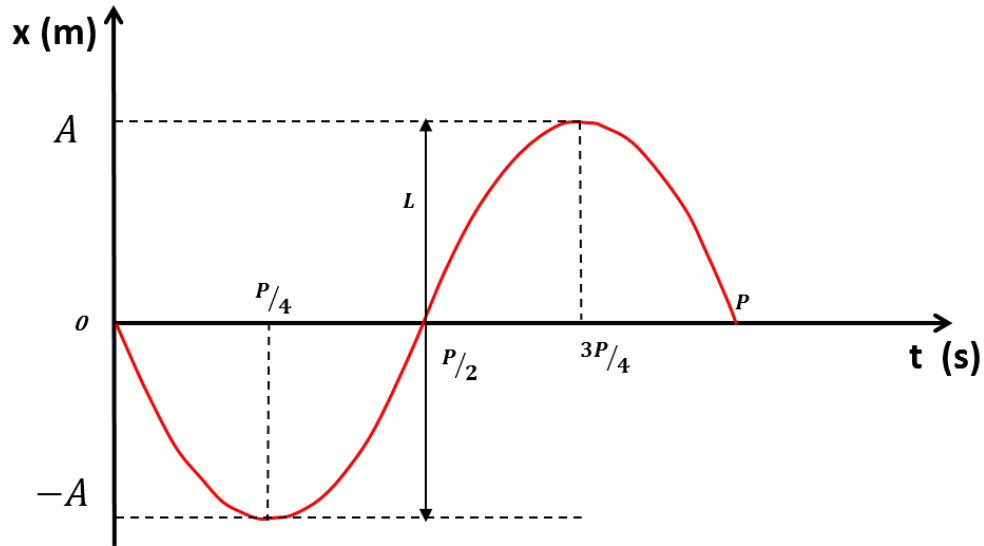


Figure D.3 A cycle of the displacement curve to produce constant acceleration for each quadrant: the period of the signal is P , the amplitude of the signal is A where $A = L/2$. Please note, L is the stroke of the piston.

Since the displacement is a parabolic waveform (Figure D.3), the velocity waveform is triangular (Figure D.4). If the displacement of the piston can be controlled to follow the desired displacement as shown in Figure D.3, then, the acceleration of the piston will be constant in each quadrant as illustrated in Figure D.5. At one frequency, constant accelerations can be obtained in 4 different quadrants.

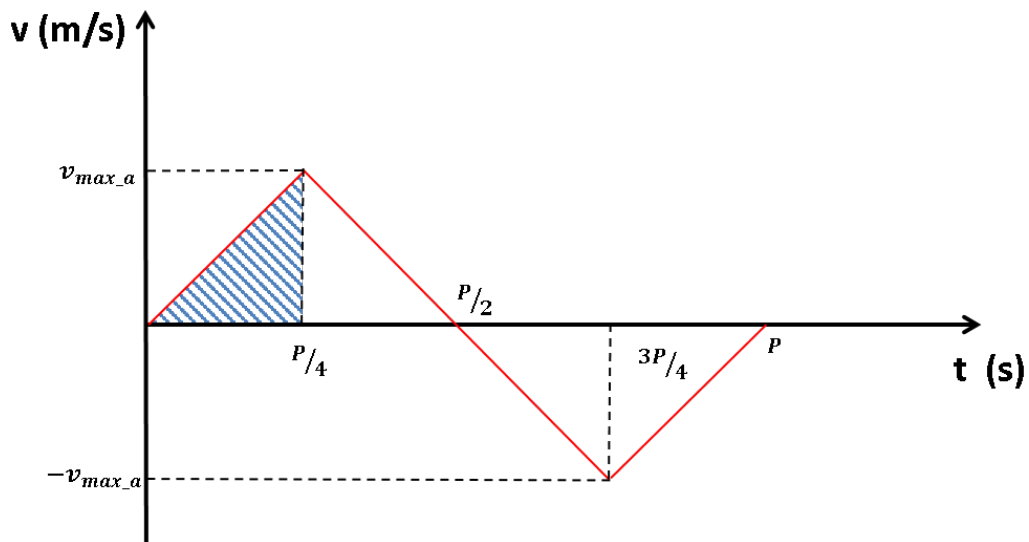


Figure D.4 A cycle of the resulting velocity curve; the period of the signal is P , the amplitude of the triangular waveform is the maximum velocity ($v_{a,max}$) the piston can achieve under constant acceleration (a) within the stroke of system.

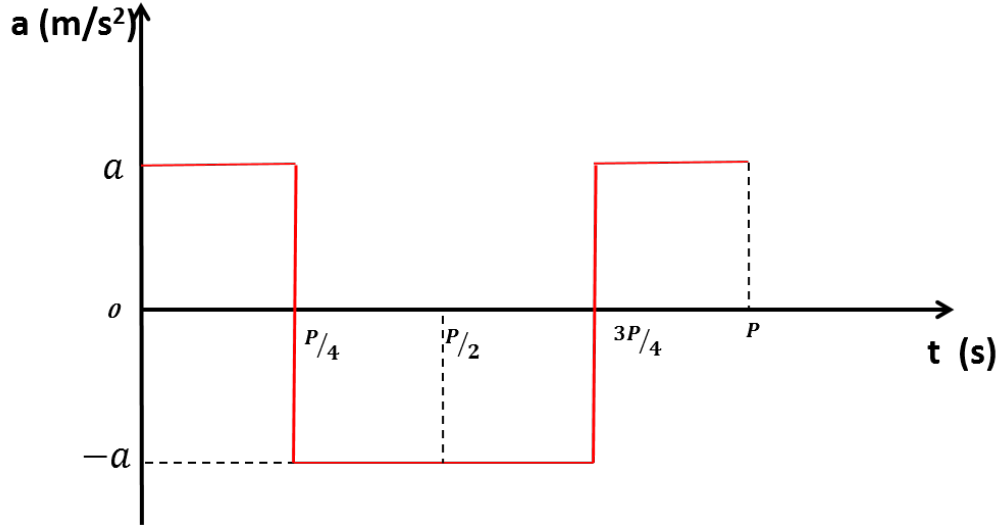


Figure D.5 A cycle of the acceleration curve with constant acceleration for each quadrant; the period of the signal is P , and a is the amplitude of the signal which is the desired constant acceleration.

To find the relationship between the desired acceleration and input displacement signal frequency, consider Figure D.4. Constant acceleration can be obtained from the slope of the velocity as:

$$a = \frac{\Delta v}{\Delta t} \quad (\text{D. 5})$$

where v is the velocity, and t is the time.

Therefore,

$$a = \frac{\Delta v}{\Delta t} = \frac{v_{a_max}}{P/4} = \frac{4v_{a_max}}{P} = 4v_{a_max}f \quad (\text{D. 6})$$

where v_{a_max} is the maximum velocity when the piston reaches the midpoint of the actuator, a is the acceleration at the midpoint, P is the period, and f is the frequency of the input displacement signal respectively.

The area of the hatched triangle in Figure D.4 is the displacement that the piston travels from the start point to the midpoint of the actuator, and A is the amplitude of the position waveform (numerically equal to $L/2$). Therefore:

$$\frac{1}{2} v_{a_max} \frac{P}{4} = A \quad (\text{D. 7})$$

Then,

$$v_{a_max} = \frac{8A}{p} = 8Af \quad (\text{D. 8})$$

Substituting Equation (D.8) into Equation (D.6) yields:

$$a = 4(8Af)f = 16Lf^2 \quad (\text{D. 9})$$

It is evident that velocity is positive in one direction and negative in the other direction (Figure D.2); therefore, the relationship between the desired velocity and input displacement signal can be written as follows:

$$|a| = 16Lf^2 \quad (\text{D. 10})$$

From Equation (D.10), it is observed that the piston acceleration (a) has a quadratic relation with the frequency of the input signal. For any desired acceleration (a), the frequency (f) can be obtained as follows:

$$f = \sqrt{\frac{1}{16L}|a|} \quad (\text{D. 11})$$

Theoretically, any desired acceleration can be achieved by adjusting the frequency of the input signal. In addition, the longer the actuator stroke, the larger the acceleration for the same frequency. However, the actuator stroke is limited by the system used. Further, the frequency of input signal is limited by the bandwidth of the selected actuation system.

APPENDIX E: DEVELOPMENT OF VELOCITY AND ACCELERATION LISTS

As mentioned in Appendix D, theoretically, any desired constant velocity motion can be achieved by adjusting the frequency of the input triangular displacement signal and any desired constant acceleration motion can be achieved by adjusting the frequency of the input parabolic displacement signal. In this Appendix, a list of desired discrete velocities and acceleration (defined in Chapter 3 as Velocity List and Acceleration List) is presented as a function of frequency. The Velocity list is developed for steady state friction measurements and the Acceleration List for non-steady state friction measurements.

For clarification, the Velocity List (and Acceleration List) is not the same as the Universal Velocity Set (Universal Acceleration List) discussed in Chapters 3 and 4.

The Velocity and Acceleration lists were determined by the author in order to create as many data points as possible for the experimental lookup table. Ideally the more data points (velocity and acceleration), the better; however, too many data points would “overwhelm” both the experimental procedures and the actual itself. The choice of points was based on the requirement to make the resulting velocity and acceleration curves “reasonably” smooth.

E.1 Velocity List

As mentioned in Chapter 3, the VCHAS1 has a large system bandwidth and therefore a wide velocity range. As per Tables 3.3 and 3.4 in Chapter 3, the minimum velocity and maximum velocity of VCHAS1 was 0.003 m/s and 0.8432 m/s respectively. For steady state friction measurements, care was taken to prepare a “list” of velocities between the maximum and minimum velocity which could be physically realizable experimentally.

In order to facilitate the measurement and calculation of steady state friction, a range of velocities at different intervals was chosen. To facilitate data organization, each velocity value was assigned a “velocity point” and as such velocity is plotted as a function of these points. The Velocity list (16 absolute values) of steady state friction measurement of VCHAS1 was selected to be (all units in m/s): 0.003 (point 1), 0.006 (point 2), 0.009, 0.015, 0.03, 0.045, 0.06, 0.09, 0.12, 0.15, 0.2, 0.4, 0.5, 0.6, 0.7 and 0.8432 (point 16) (Figure E.1). 16 points were selected between the minimum velocity and maximum velocity. It is observed from Figure E.1, that the velocity intervals for the points at low velocities (low velocity points) were much smaller than at higher

velocities (higher velocity points) because of the need to obtain friction values in regions in which the steady state friction dominated.

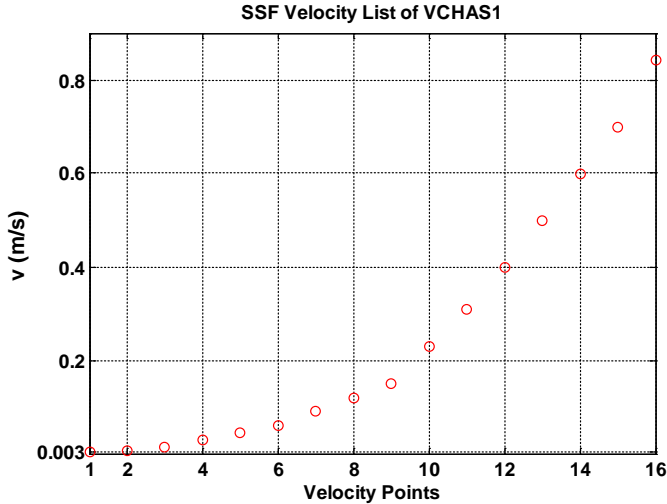


Figure E.1 16 positive velocity points were chosen for the Velocity list for VCHAS1. Note that the velocity intervals at lower velocity points are very small to accommodate measurements in which steady state friction (SSF) dominated.

To be symmetrical, same number of negative velocities were added to the list. The full Velocity list (total of 32 values) was chosen as follows (velocity in m/s): -0.8432 (point 1), -0.7 (point 2), -0.6, -0.5, -0.4, -0.2, -0.15, -0.12, -0.09, -0.06, -0.045, -0.03, -0.015, -0.009, -0.006, -0.045, -0.003, 0.003, 0.006, 0.009, 0.015, 0.03, 0.045, 0.06, 0.09, 0.12, 0.15, 0.2, 0.4, 0.5, 0.6, 0.7 and 0.8432 (point 32). This data is illustrated in Figure E.2.

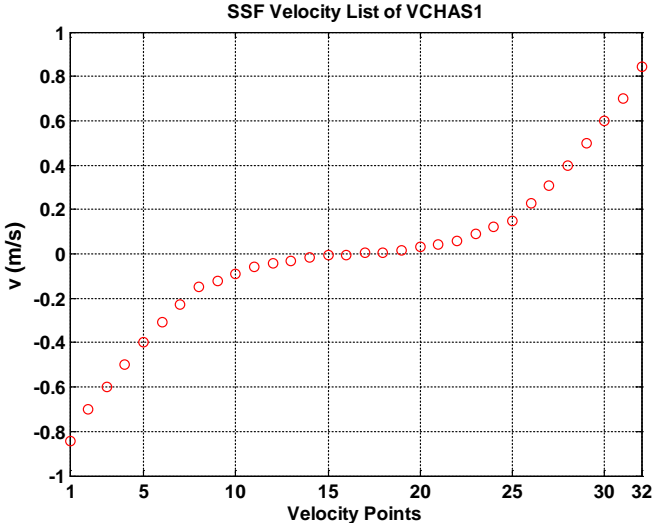


Figure E.2 A total 32 velocity points (including the negative side) was chosen for the Velocity list for VCHAS1. SSF refers to steady state friction.

Subsequently, a frequency list needed to produce the absolute value of these velocities was calculated using Equation (D.4) for the experimental study. The frequency list for absolute velocities was determined to be as follows (all units in Hz): 0.01, 0.02, 0.05, 0.11, 0.16, 0.21, 0.32, 0.42, 0.53, 0.81, 1.09, 1.40, 1.76, 2.11, 2.46 and 2.96 and is illustrated in Figure E.3. With reference to this Figure, a frequency of .01 Hz was required to create a velocity of 0.003 m/s and -0.003 m/s for example. It is observed that the range of frequencies is from 0.01 Hz to 3 Hz.

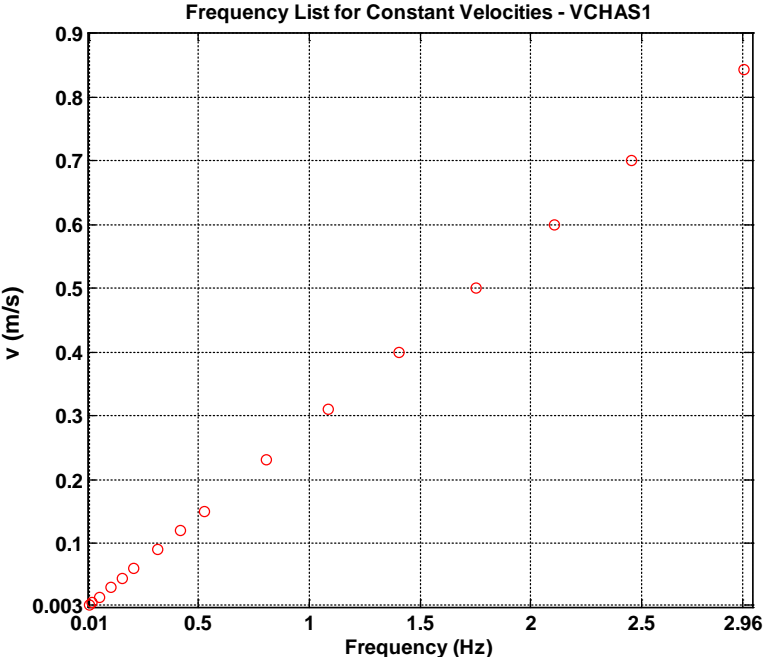


Figure E.3 Velocity vs Frequency of steady state friction measurement of VCHAS1

The VCHAS2 has a smaller system bandwidth. Therefore, as per Tables 3.3 and 3.4 in Chapter 3, the minimum velocity and maximum velocity of VCHAS2 was 0.001 m/s and 0.5 m/s respectively. As with VCHAS1, the Velocity list as a function of velocity points (15 absolute values since the list is symmetrical about 0) of SSF measurement of VCHAS2 was selected to be (all units in m/s): 0.001 (point 1), 0.003 (point 2), 0.006, 0.015, 0.03, 0.045, 0.06, 0.08, 0.1, 0.12, 0.15, 0.2, 0.3, 0.4, and 0.5 (point 15) (Figure E.4).

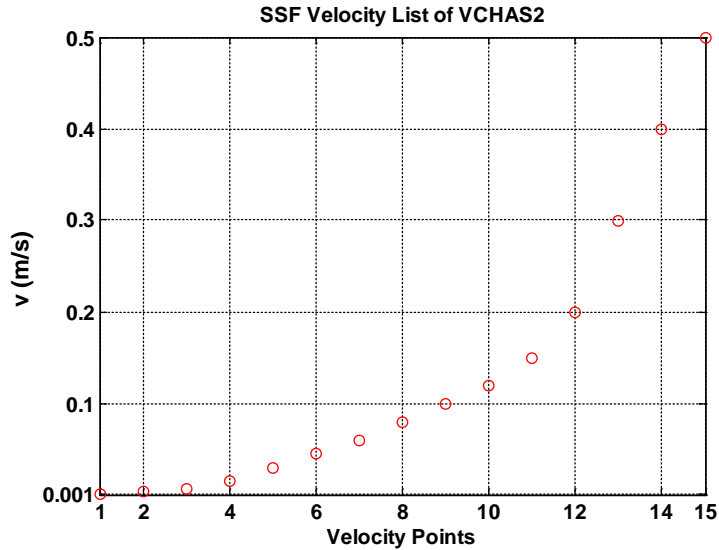


Figure E.4 15 positive velocity points were chosen for the Velocity list for VCHAS2. SSF refers to steady state friction.

To be symmetrical, the same number of negative velocities are added to the list. The full Velocity list chosen is as follows (all units in m/s): -0.5 (point 1), -0.4 (point 2), -0.3, -0.2, -0.15, -0.12, -0.1, -0.08, -0.06, -0.045, -0.03, -0.015, -0.006, -0.003, -0.001, 0.001, 0.003, 0.006, 0.015, 0.03, 0.045, 0.06, 0.08, 0.1, 0.12, 0.15, 0.2, 0.3, 0.4, and 0.5 (point 30). A total of 30 velocity “points” chosen for VCHAS2 are illustrated in Figure E.5. It is observed that all the velocity “points” form a “smooth” shape.

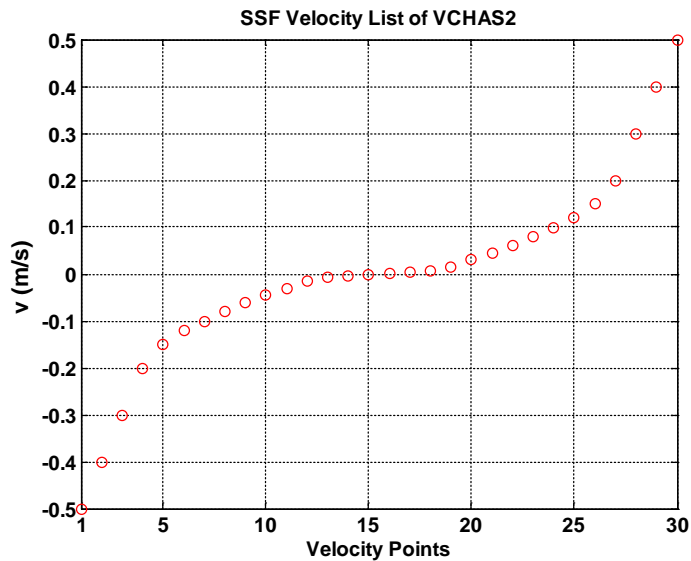


Figure E.5 A total of 30 velocity points (including the negative side) were chosen for the Velocity list for VCHAS2. SSF refers to the steady state friction.

Subsequently, the frequencies that were needed to produce this Velocity list could be calculated using Equation (D.4) for the experimental study. As with VCHAS1, the curve of absolute velocity (because the curve is symmetrical) vs frequency is illustrated in Figure E.6.

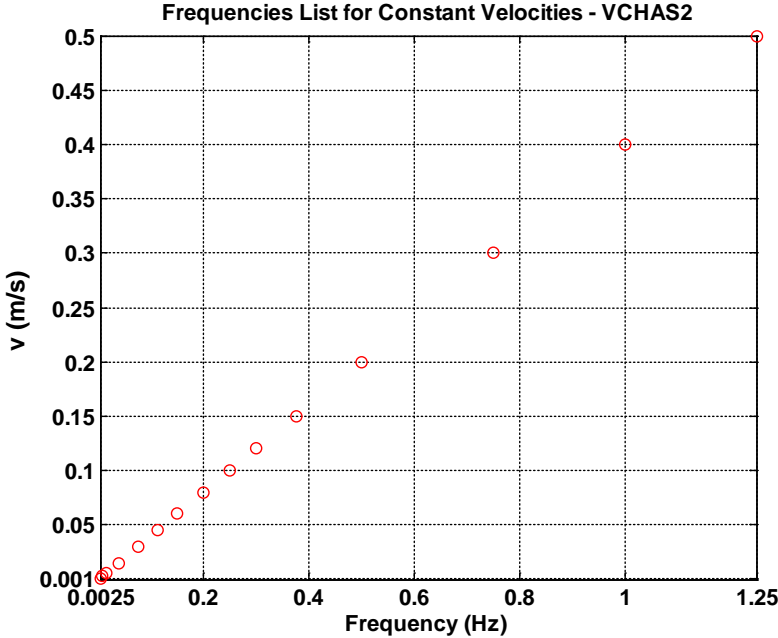


Figure E.6 Velocity vs Frequency of VCHAS2

E.2 Acceleration List

In the 2D LUT modeling process, the acceleration was considered to be a “family parameter” and hence, was allowed to vary in a “discrete” fashion. Lubricated friction was measured continuously as a function of velocity by holding acceleration constant during a test.

For non-steady state friction measurements, care was taken to prepare an “Acceleration list” which could be physically realizable experimentally.

As with the Velocity list of Section E.1, as per Tables 3.3 and 3.4 in Chapter 3, the minimum acceleration and maximum acceleration of VCHAS1 are 0.001 m/s² and 5 m/s² respectively. A list of desirable accelerations (between the minimum and maximum accelerations of VCHAS1) at different intervals was created from which the appropriate frequencies could be calculated to generate the Acceleration list. As with the Velocity list, the Acceleration list was assigned an acceleration point which facilitated the application of the information.

The Acceleration list (58 absolute values) of NSSF measurement of VCHAS1 was selected to be (all units in m/s²): 0.001 (point 1), 0.002 (point 2), 0.003, 0.004, 0.005, 0.006,

0.007, 0.008, 0.009, 0.01, 0.02, 0.03, 0.04, 0.05, 0.06, 0.07, 0.08, 0.09, 0.1, 0.2, 0.3, 0.4, 0.5, 0.6, 0.7, 0.8, 0.9, 1.0, 1.1, 1.2, 1.3, 1.4, 1.5, 1.6, 1.7, 1.8, 1.9, 2.0, 2.1, 2.2, 2.3, 2.4, 2.5, 2.6, 2.7, 2.8, 2.9, 3.0, 3.2, 3.4, 3.6, 3.8, 4.0, 4.2, 4.4, 4.6, 4.8, and 5.0 (point 58) as illustrated in Figure E.7.

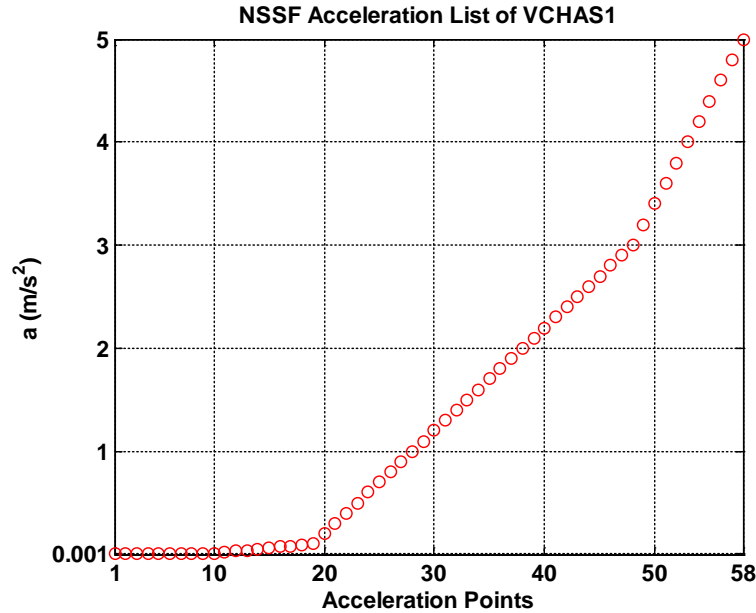


Figure E.7 58 positive acceleration points were chosen for the Acceleration list for VCHAS1. NSSF refers to the non-steady state friction.

To be symmetrical, the Acceleration list was modified to include negative accelerations. The full Acceleration list is as follows (all units in m/s^2): -5.0 (point 1), -4.8 (point 2), -4.6, -4.4, -4.2, -4.0, -3.8, -3.6, -3.4, -3.2, -3.0, -2.9, -2.8, -2.7, -2.6, -2.5, -2.4, -2.3, -2.2, -2.1, -2.0, -1.9, -1.8, -1.7, -1.6, -1.5, -1.4, -1.3, -1.2, -1.1, -1.0, -0.9, -0.8, -0.7, -0.6, -0.5, -0.4, -0.3, -0.2, -0.1, -0.09, -0.08, -0.07, -0.06, -0.05, -0.04, -0.03, -0.02, -0.01, -0.009, -0.008, -0.007, -0.006, -0.005, -0.004, -0.003, -0.002, -0.001, 0.001, 0.002, 0.003, 0.004, 0.005, 0.006, 0.007, 0.008, 0.009, 0.01, 0.02, 0.03, 0.04, 0.05, 0.06, 0.07, 0.08, 0.09, 0.1, 0.2, 0.3, 0.4, 0.5, 0.6, 0.7, 0.8, 0.9, 1.0, 1.1, 1.2, 1.3, 1.4, 1.5, 1.6, 1.7, 1.8, 1.9, 2.0, 2.1, 2.2, 2.3, 2.4, 2.5, 2.6, 2.7, 2.8, 2.9, 3.0, 3.2, 3.4, 3.6, 3.8, 4.0, 4.2, 4.4, 4.6, 4.8, and 5.0 (point 116). A total of 116 acceleration “points” were chosen for VCHAS1 and are illustrated in Figure E.8.

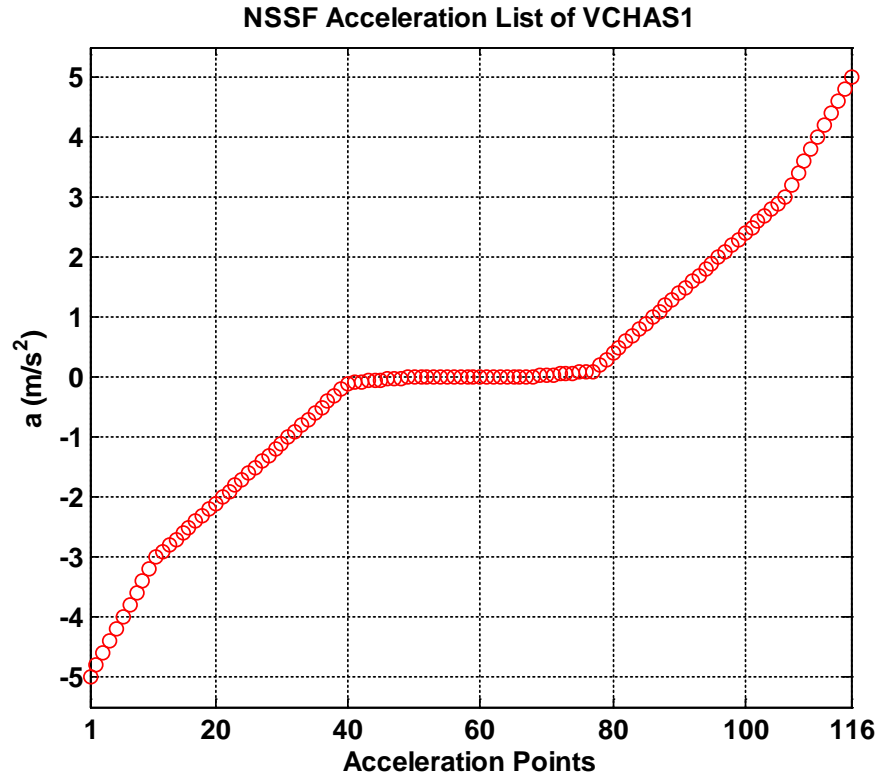


Figure E.8 A total of 116 acceleration points (including the negative side) of VCHAS1 for non-steady state friction (NSSF).

As mentioned above, any desired acceleration can be achieved by adjusting the frequency of the input signal. However, the acceleration was limited by the system bandwidth. In order to better capture the nonlinear behavior of the non-steady state friction, a range of accelerations at different intervals was chosen. As with the Velocity list, each acceleration was assigned an acceleration point. The frequencies for the non-steady state friction measurements of VCHAS1 were then calculated (using Equation (D.11)) from the Acceleration list that was pre-determined above. A graph of acceleration versus frequency is shown in Figure E.9.

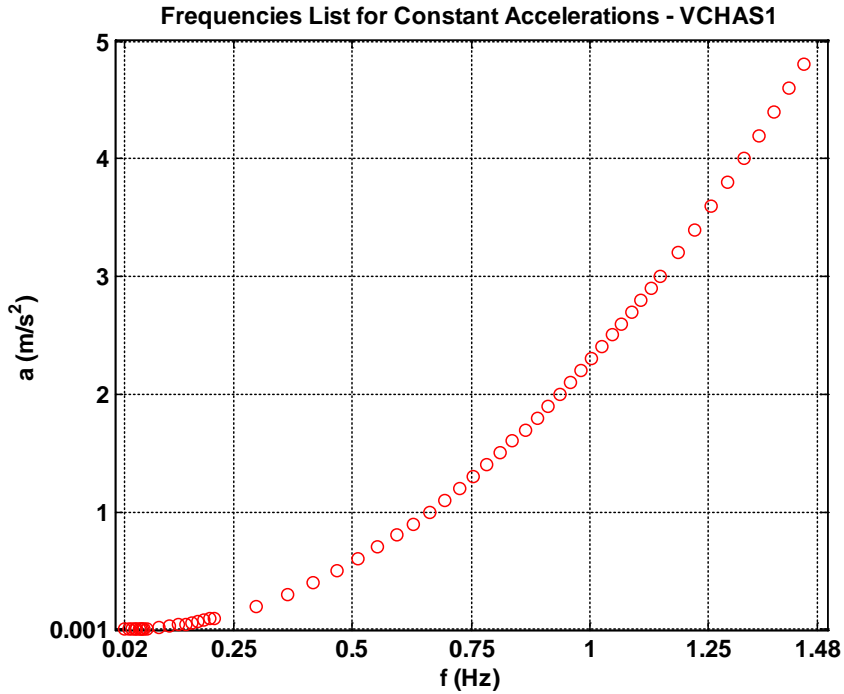


Figure E.9 Acceleration vs Frequency of VCHAS1

The VCHAS2 has a smaller system bandwidth. Therefore, as per Tables 3.3 and 3.4 in Chapter 3, the minimum acceleration and maximum acceleration of VCHAS1 was 0.001 m/s² and 2 m/s² respectively. A list of desirable accelerations (between the minimum and maximum accelerations of VCHAS1) at different intervals was created from which the appropriate frequencies could be calculated to generate the Acceleration list. As with the Velocity list, the Acceleration list was assigned an acceleration point which facilitated the application of the information.

The Acceleration list (41 absolute values) of non-steady state friction measurement of VCHAS2 was selected to be (all units in m/s²): 0.001 (point 1), 0.002 (point 2), 0.003, 0.004, 0.005, 0.006, 0.007, 0.008, 0.009, 0.01, 0.02, 0.03, 0.04, 0.05, 0.06, 0.07, 0.08, 0.09, 0.1, 0.15, 0.2, 0.25, 0.3, 0.35, 0.4, 0.5, 0.6, 0.7, 0.8, 0.9, 1.0, 1.1, 1.2, 1.3, 1.4, 1.5, 1.6, 1.7, 1.8, 1.9, and 2.0 (point 41) (Figure E.10).

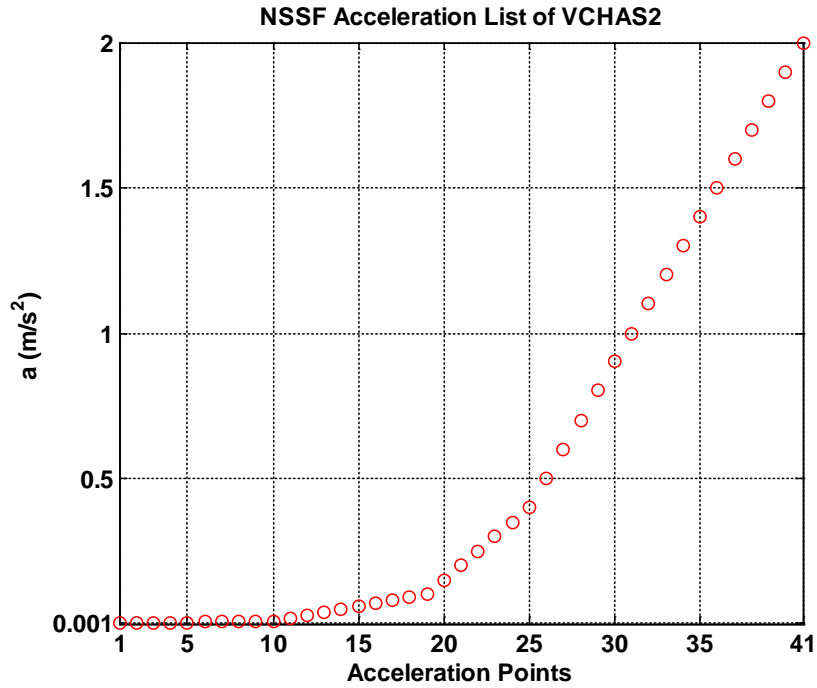


Figure E.10 41 positive acceleration points for VCHAS2 were chosen for the Acceleration list. NSSF refers to non-steady state friction

To be symmetrical, the Acceleration list was modified to include negative accelerations. The full Acceleration list is as follows (all units in m/s²): -2.0 (point 1), -1.9 (point 2), -1.8, -1.7, -1.6, -1.5, -1.4, -1.3, -1.2, -1.1, -1.0, -0.9, -0.8, -0.7, -0.6, -0.5, -0.4, -0.3, -0.2, -0.1, -0.09, -0.08, -0.07, -0.06, -0.05, -0.04, -0.03, -0.02, -0.01, -0.009, -0.008, -0.007, -0.006, -0.005, -0.004, -0.003, -0.002, -0.001, 0.001, 0.002, 0.003, 0.004, 0.005, 0.006, 0.007, 0.008, 0.009, 0.01, 0.02, 0.03, 0.04, 0.05, 0.06, 0.07, 0.08, 0.09, 0.1, 0.15, 0.2, 0.25, 0.3, 0.35, 0.4, 0.5, 0.6, 0.7, 0.8, 0.9, 1.0, 1.1, 1.2, 1.3, 1.4, 1.5, 1.6, 1.7, 1.8, 1.9, and 2.0 (point 82). A total of 82 acceleration “points” were chosen for VCHAS2 and are illustrated in Figure E.11.

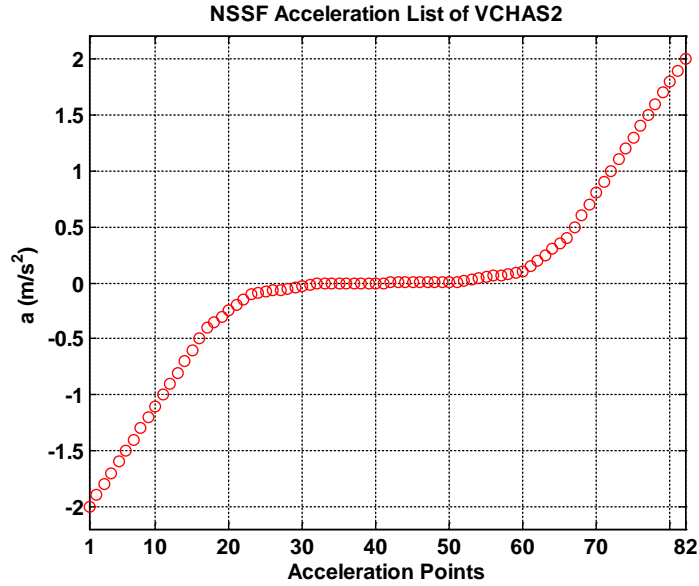


Figure E.11 A total 82 acceleration points (including the negative side) of VCHAS2 for non-steady state friction (NSSF)

As mentioned above, any desired acceleration can be achieved by adjusting the frequency of the input signal. However, the acceleration was limited by the system bandwidth. In order to better capture the nonlinear behavior of the non-steady state friction, a range of accelerations at different intervals was chosen. The frequencies for the non-steady state friction measurements of VCHAS2 were calculated (using Equation (D.11)) from the acceleration list that was pre-determined above. A graph of acceleration versus frequency is shown in Figure E.12.

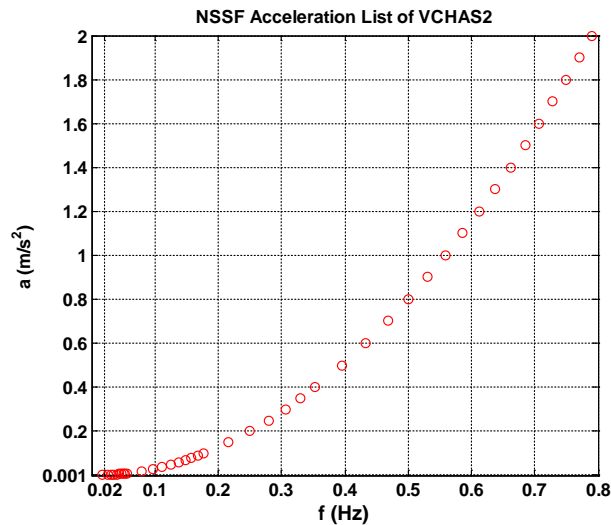


Figure E.12 Acceleration vs Frequency of VCHAS2. NSSF refers to non-steady state friction

APPENDIX F: DESIGN OF AN INNOVATIVE PERIODIC PARABOLIC INPUT SIGNAL WHICH RESULTS IN A CONSTANT ACCELERATION

In this appendix, the innovative parabolic input signal design which was used as an input to the VCHAS's is introduced. In the experiment to determine the acceleration influence on the lubricated friction of actuators, a parabolic displacement input signal was used. The question of how to mathematically and subsequently, physically (via Matlab) create a parabolic waveform is addressed in this appendix.

The equation ($x = f(t)$) of a typical parabolic displacement (which results in a constant acceleration) can be represented as follows:

$$x = \left(\frac{a}{2}\right) t^2 \quad (\text{F. 1})$$

Therefore the velocity of a parabolic displacement is:

$$v = \frac{dx}{dt} = at \quad (\text{F. 2})$$

and the acceleration of a parabolic displacement is:

$$a = \frac{dv}{dt} (\text{constant}) \quad (\text{F. 3})$$

It is evident that the parabolic signal x (Equation (F.1)) cannot be used to generate a periodic signal. However, a periodic signal is required in the experiment to both investigate the acceleration effects on all the quadrants and to obtain repeatability. A novel method was developed to generate a periodic parabolic signal by the use of a periodic square signal in the function library of Simulink ©. The procedure to do this is now considered.

The first step is to generate a periodic square wave (S) with period P , amplitude A and pulse width 50% (Figure F.1). It should be noted that in this case, A is the amplitude of the square wave and is numerically equal to half of the actuator stroke. The reason for this will be evident in the following development.

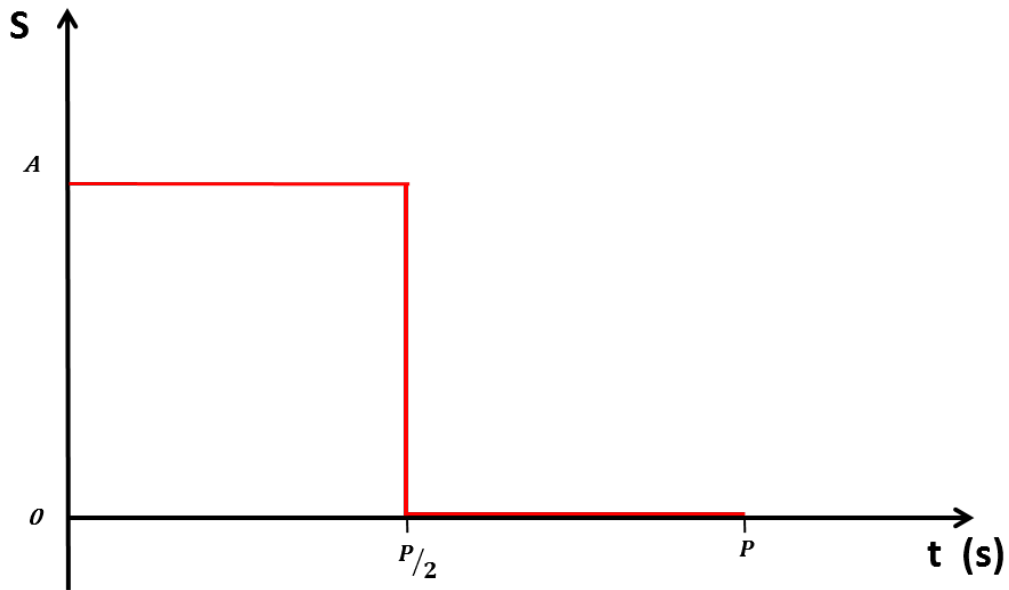


Figure F.1 A cycle of a periodic square wave S with amplitude (A), and period P

The second step is to make the square wave symmetrical over zero, with amplitude ($A/2$) (Figure F.2). This is accomplished by biasing the curve by $-A/2$.

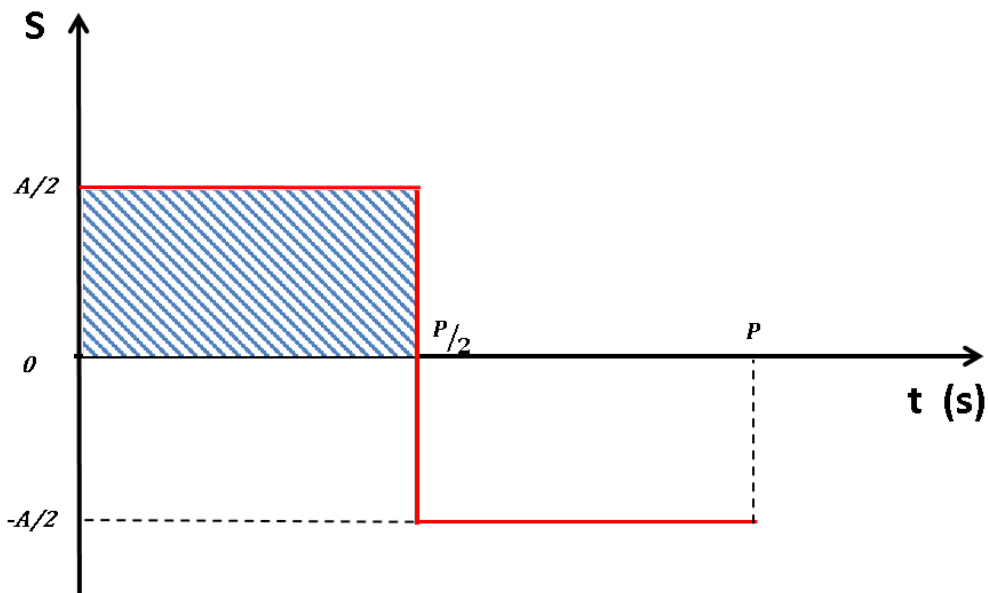


Figure F.2 A cycle of the adjusted square wave S with amplitude ($A/2$), and period P

The third step is to integrate the square wave of Figure F.2. The area of the hatched rectangle in Figure F.2 is the amplitude of the triangular wave (M) shown in Figure F.3. The amplitude of triangular wave (M) = $\left(\frac{A}{2}\right) * \left(\frac{P}{2}\right) = \frac{AP}{4}$.

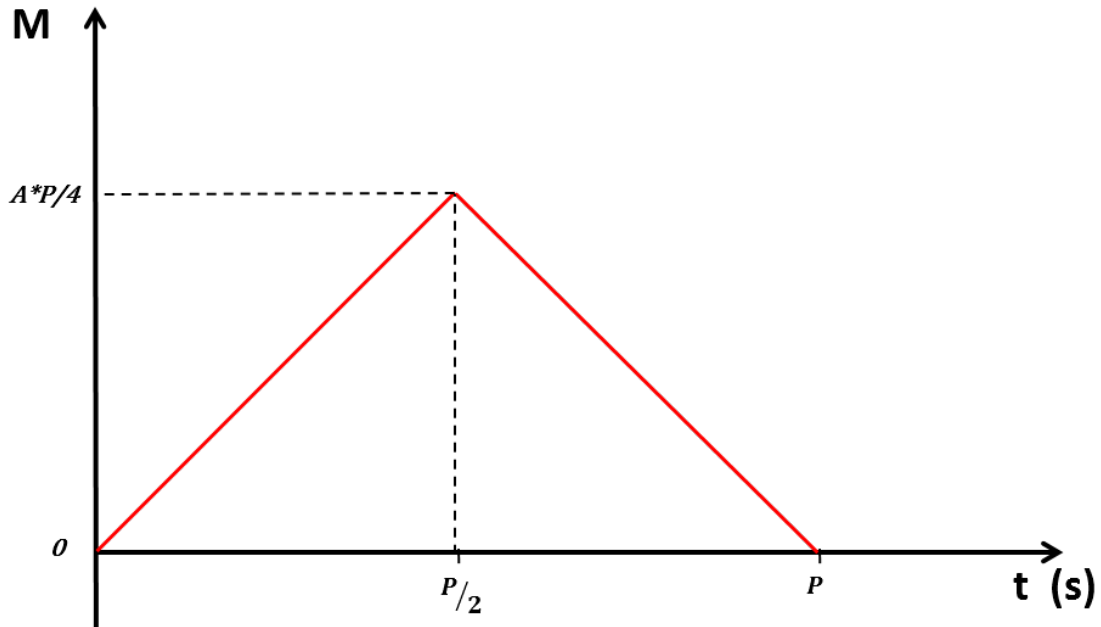


Figure F.3 A cycle of a triangular wave obtained by integrating the square wave of Figure F.2

The fourth step is to make the triangular wave M symmetrical over zero (remove the bias), with amplitude of $\left(\left(\frac{A}{2}\right) * \left(\frac{P}{2}\right) * \frac{1}{2} = \frac{A*P}{8}\right)$ (see Figure F.4):

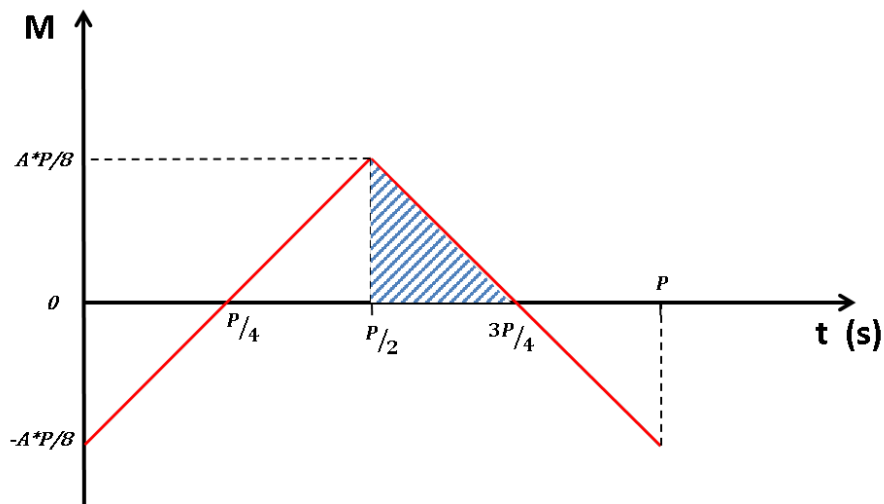


Figure F.4 A cycle of the adjusted triangular wave (M) of Figure F.3 with no bias

The fifth step is to integrate the triangular wave M of Figure F.4. The area of the hatched triangle in Figure F.4 is the amplitude of the parabolic wave (T) shown in Figure F.5. The amplitude of a parabolic wave $T = \left(\frac{AP}{8}\right) * \left(\frac{P}{4}\right) * \left(\frac{1}{2}\right) = \left(A * \frac{P^2}{64}\right)$.

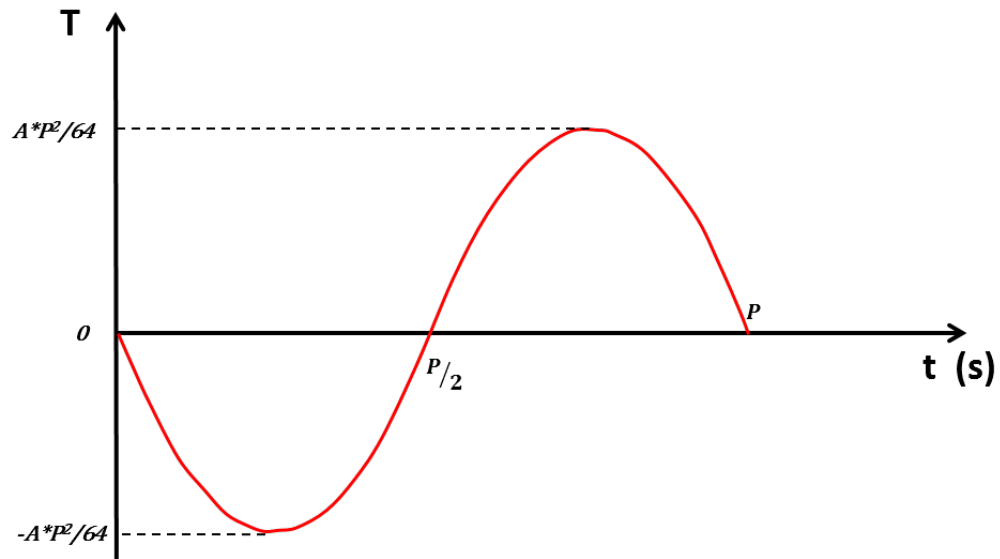


Figure F.5 A cycle of the parabolic wave T with amplitude $\left(\frac{AP^2}{64}\right)$ and period (P)

The last step is to make the amplitude of parabolic wave T match the piston motion amplitude (A) , by multiplying the amplitude by a gain of $\left(\frac{64}{P^2}\right)$. The result is a periodic parabolic input signal X with amplitude (A) and period (P) as shown in Figure F.6.

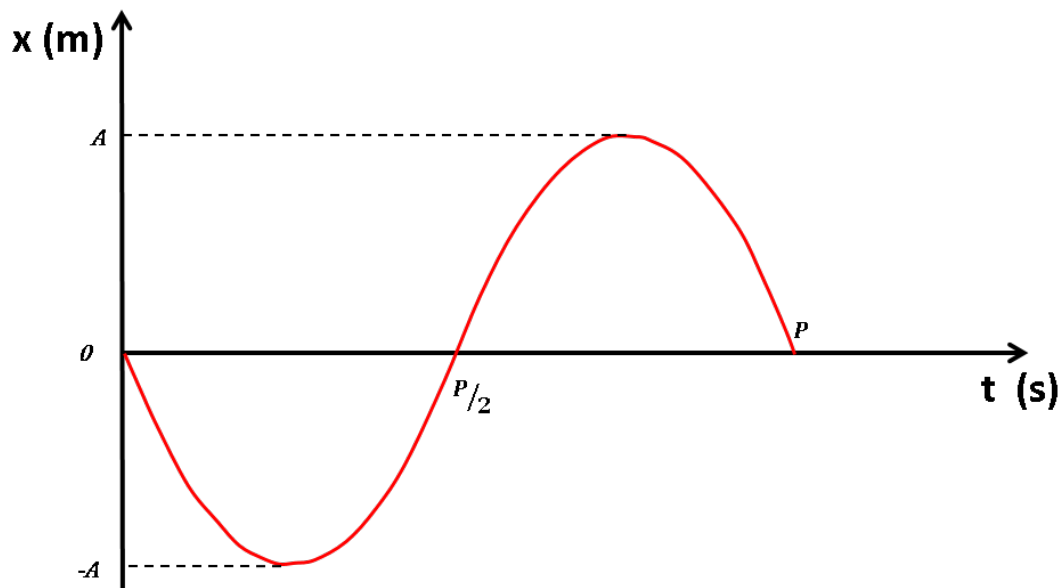


Figure F.6 A cycle of the parabolic wave X with amplitude (A) and period (P)

The Simulink © code to generate the periodic parabolic wave is shown in Figure F.7. With reference to this figure, the square wave of amplitude A is biased with a DC signal $A/2$ and integrated. This signal is then biased by $(A/2 * P/2)/2$ and integrated once more. This signal is multiplied by $\left(\frac{64}{P^2}\right)$ to yield a parabolic displacement curve of amplitude A and frequency (f).

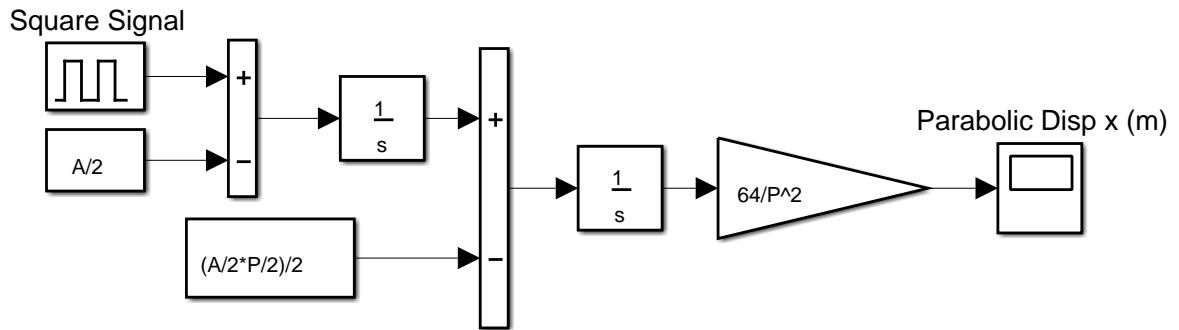


Figure F.7 The Simulink © code to generate the periodic parabolic wave with period P , amplitude A

The parabolic displacement signal generated in Figure F.7 was used as a desired displacement to the closed loop controlled VCHAS systems. By inputting this signal into the VCHAS, the acceleration of the actuator is constant with magnitude:

$$a = \frac{32A}{P^2} = 16Lf^2 \quad (F.4)$$

where A is half of the actuator stroke (L) and P is the period of the input parabolic signal and f is the frequency of the input parabolic signal, and a is the desired acceleration of piston. Please note that details of the derivation of Equation (F.4) was given in Appendix E.

APPENDIX G: ADDITIONAL MODEL VERIFICATION AND VALIDATION RESULTS

In Chapter 4 and Chapter 5, typical model verification and validation results were presented. In this appendix, additional model verification and validation results for VCHAS1 are provided. In addition, additional parabolic curve fitting and sinusoidal curve fitting results are provided.

G.1 Additional Parabolic Curve Fitting

The following figures present curve fitting results of the measured displacement at accelerations of 4.8 m/s^2 , 4.6 m/s^2 , 4.4 m/s^2 , 3.4 m/s^2 , 2.2 m/s^2 , 1.2 m/s^2 , 0.2 m/s^2 and $.01\text{ m/s}^2$. It can be observed that the curve fitting error for all cases is very small giving confidence in the curve fitting approach followed in this thesis.

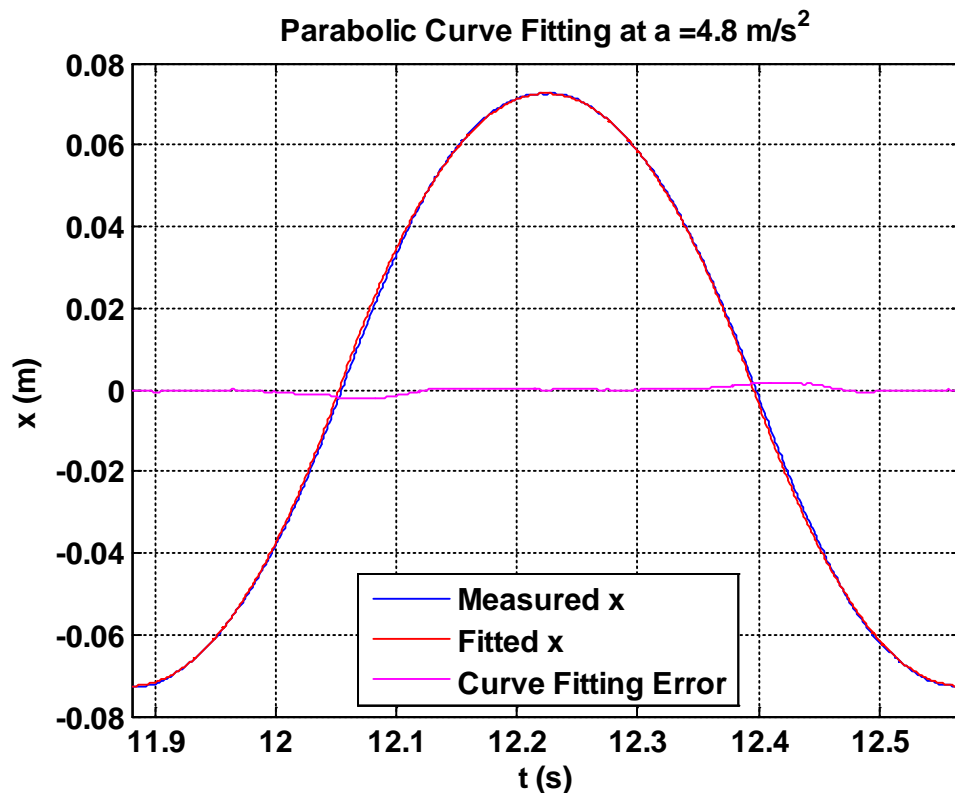


Figure G.1 Parabolic curve fitting of the measured displacement at acceleration = 4.8 m/s^2

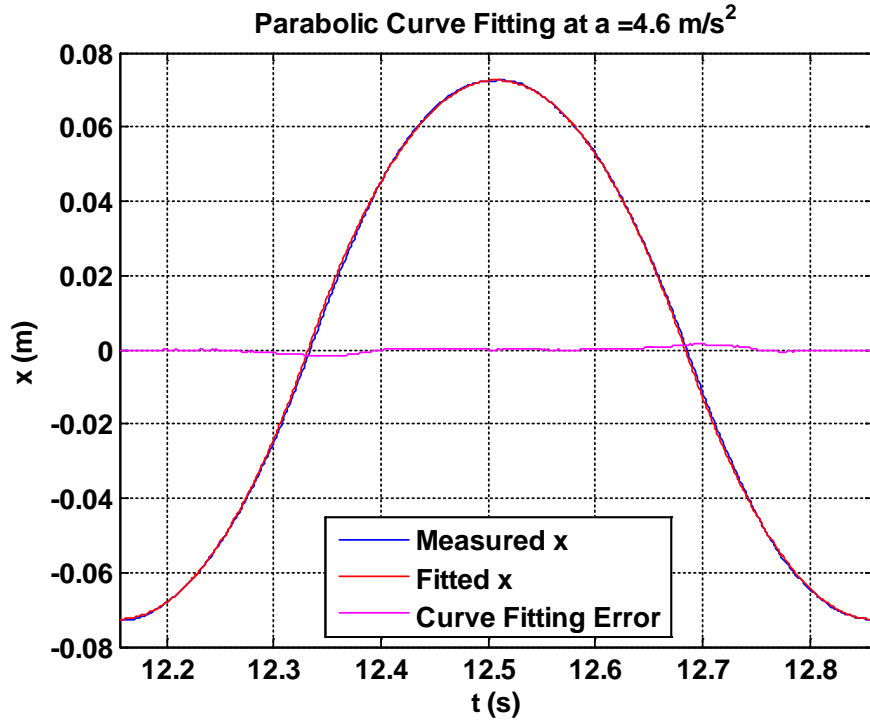


Figure G.2 Parabolic curve fitting of the measured displacement at acceleration = 4.6 m/s^2

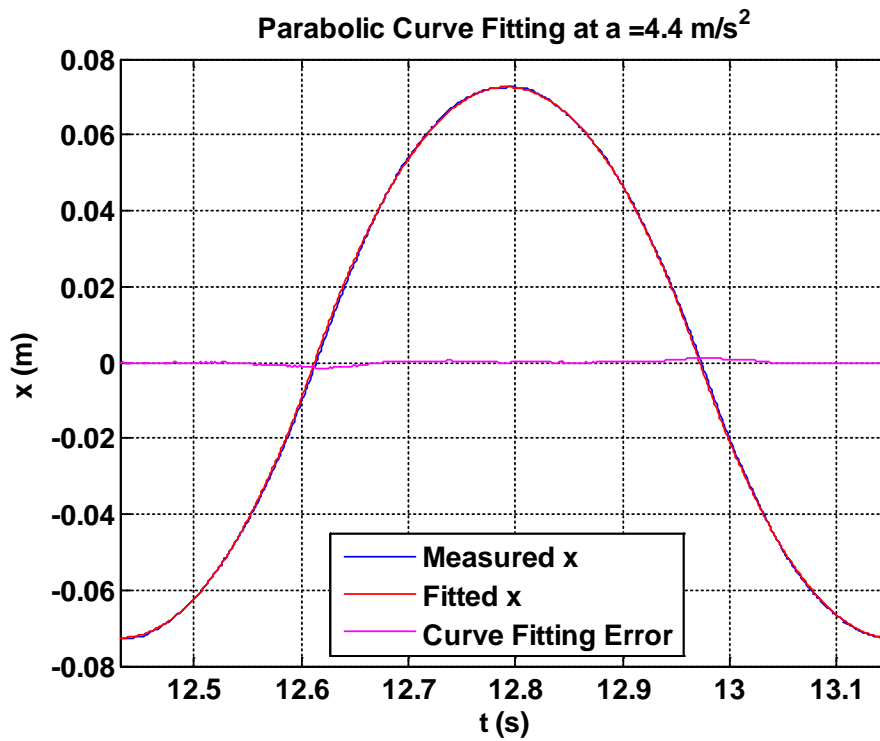


Figure G.3 Parabolic curve fitting of the measured displacement at acceleration = 4.4 m/s^2

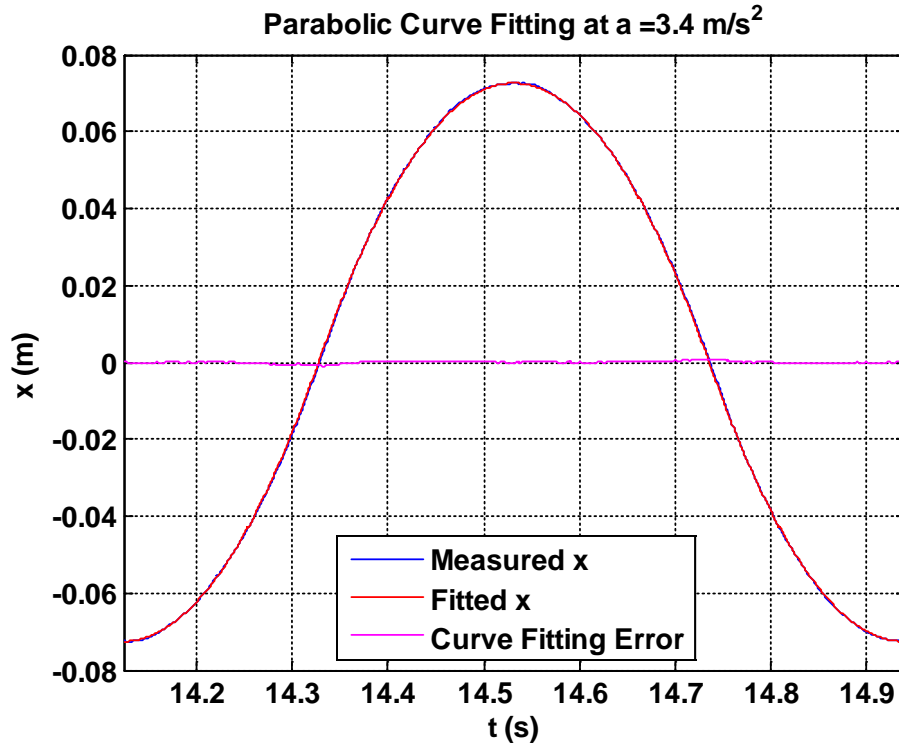


Figure G.4 Parabolic curve fitting of the measured displacement at acceleration = 3.4 m/s^2

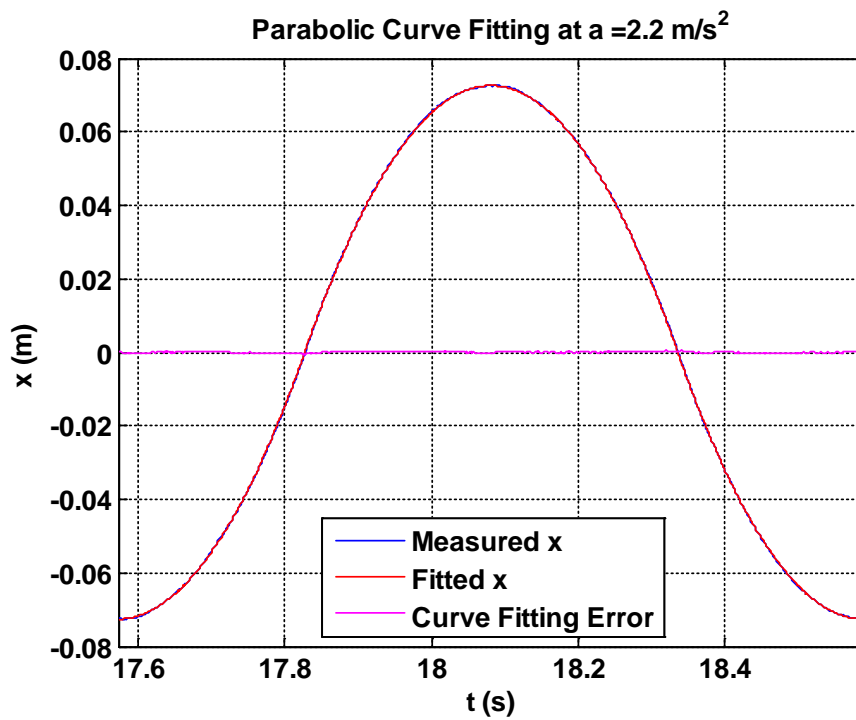


Figure G.5 Parabolic curve fitting of the measured displacement at acceleration = 2.2 m/s^2

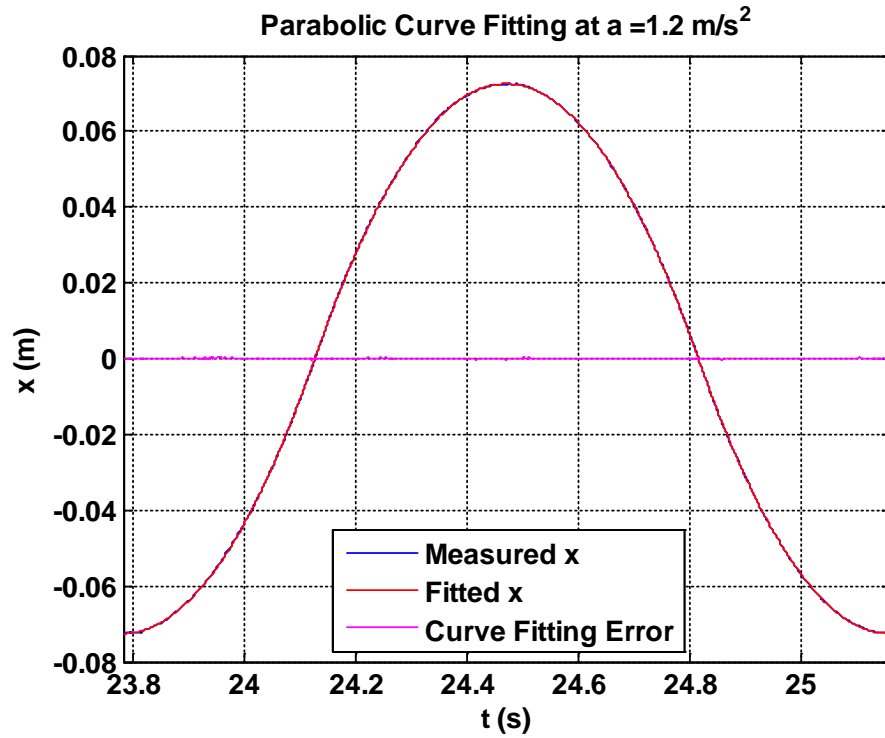


Figure G.6 Parabolic curve fitting of the measured displacement at acceleration = 1.2 m/s^2

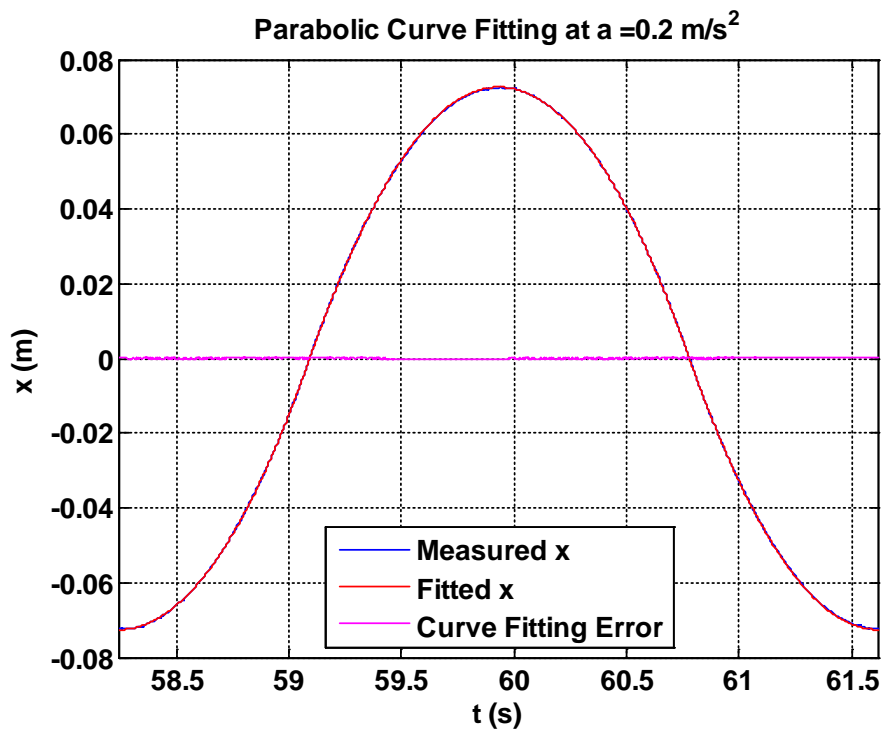


Figure G.7 Parabolic curve fitting of the measured displacement at acceleration = 0.2 m/s^2

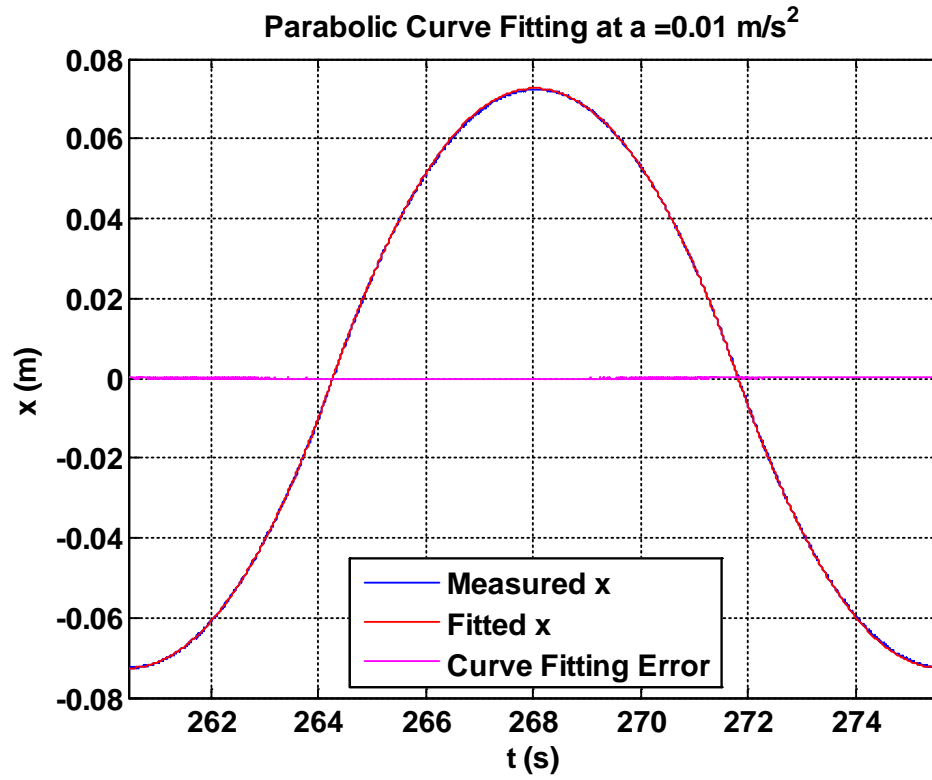


Figure G.8 Parabolic curve fitting of the measured displacement at acceleration = 0.01 m/s^2

G.2 Additional Sinusoidal Curve Fitting

The following figures present sinusoidal curve fitting results of the measured displacement at frequencies of 0.98 Hz, 0.3 Hz, 0.07 Hz, and 0.03 Hz. It can be observed that the curve fitting error for all cases is very small giving confidence in the curve fitting approach followed in this thesis.

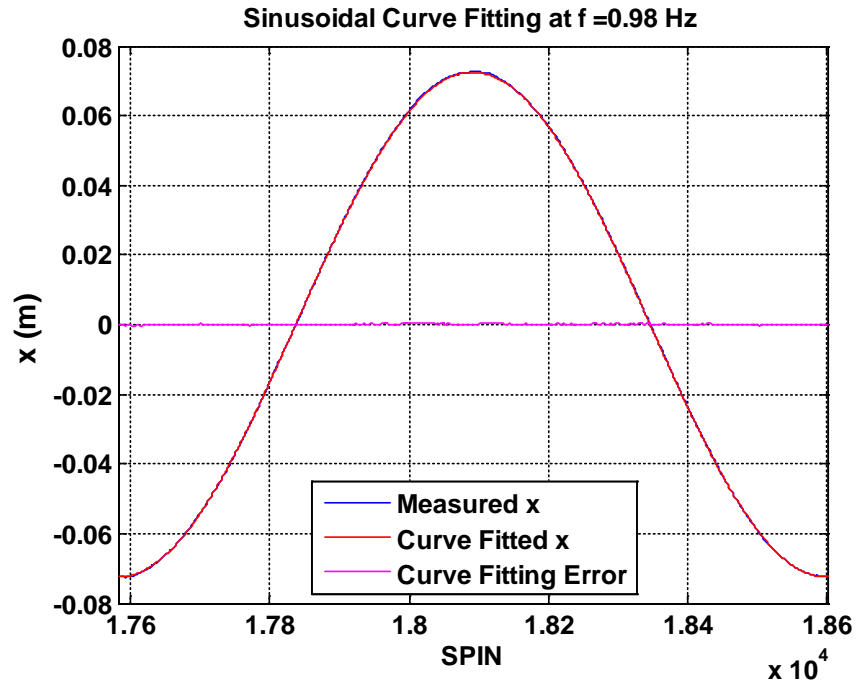


Figure G.9 Sinusoidal curve fitting of the measured displacement at frequency $f = 0.98$ Hz

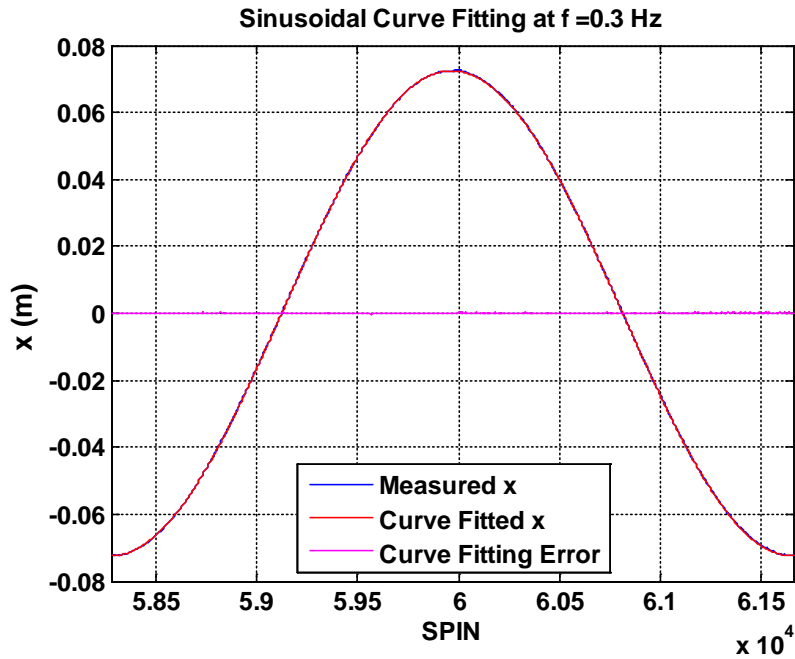


Figure G.10 Sinusoidal curve fitting of the measured displacement at frequency $f = 0.3$ Hz

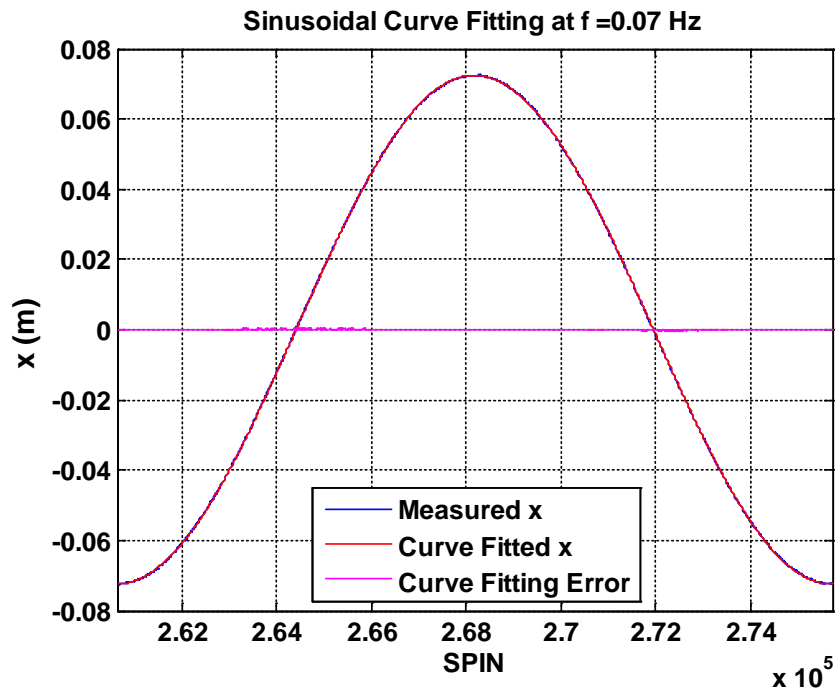


Figure G.11 Sinusoidal curve fitting of the measured displacement at frequency $f = 0.07$ Hz

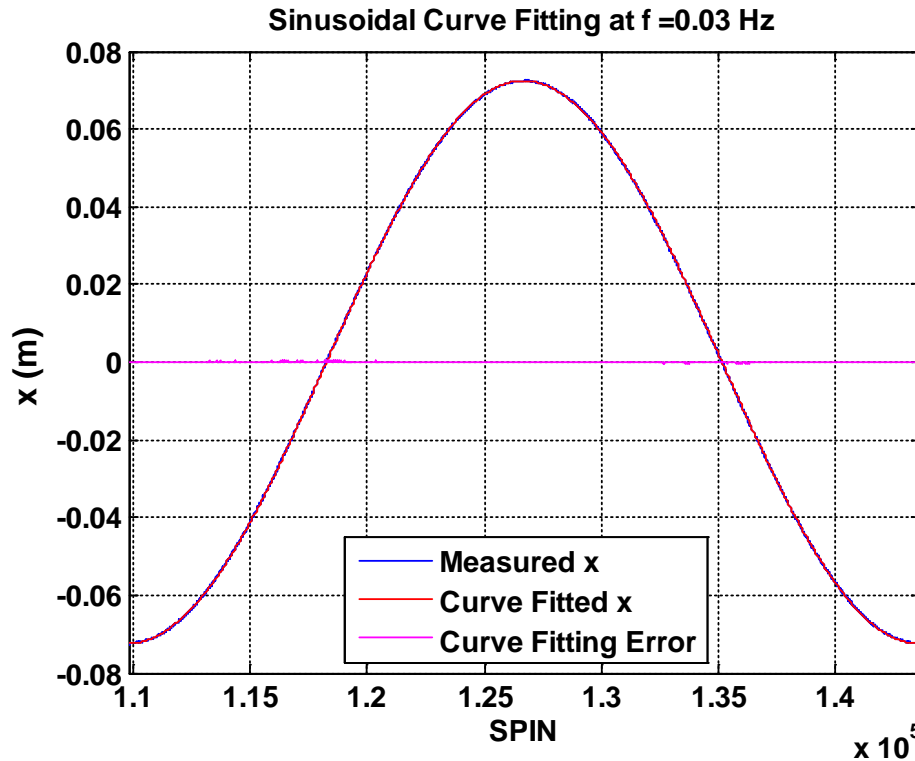
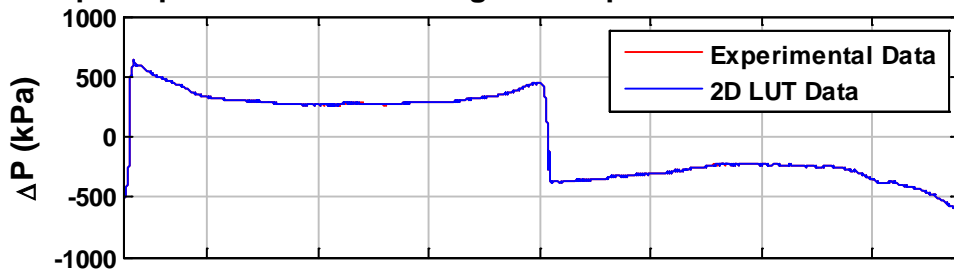


Figure G.12 Sinusoidal curve fitting of the measured displacement at frequency $f = 0.03$ Hz

G.3 Additional Model Verification Results

The following figures present additional model verification results where the 2D LUT data is superimposed on the experimental data and the modelling error is presented for accelerations of 0.01 m/s^2 , 0.2 m/s^2 , 1.2 m/s^2 , 2.2 m/s^2 , 3.4 m/s^2 , 4.4 m/s^2 , 4.6 m/s^2 , and 4.8 m/s^2 . In the figures, it is difficult to distinguish between the experimental curve and the 2D LUT curve since the modelling error is less than 10kPa (1%).

Superimposed 2D LUT Data against Experimental Data at $a=0.01 \text{ m/s}^2$



Model Error (E_r) at $a=0.01 \text{ m/s}^2$

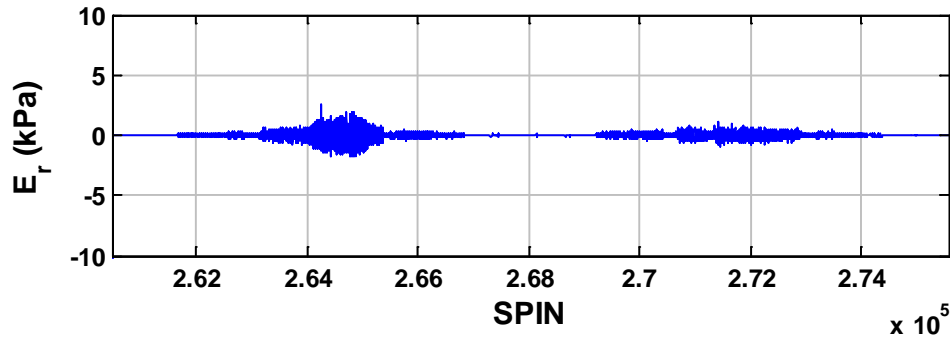
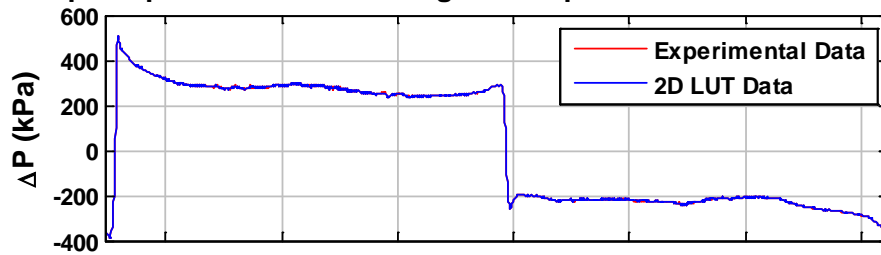


Figure G.13 Model verification of the 2D LUT at $a = 0.01 \text{ m/s}^2$

Superimposed 2D LUT Data against Experimental Data at $a=0.2 \text{ m/s}^2$



Model Error (E_r) at $a=0.2 \text{ m/s}^2$

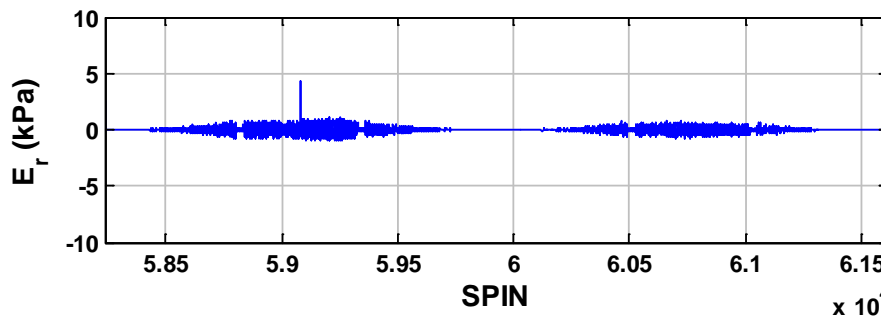
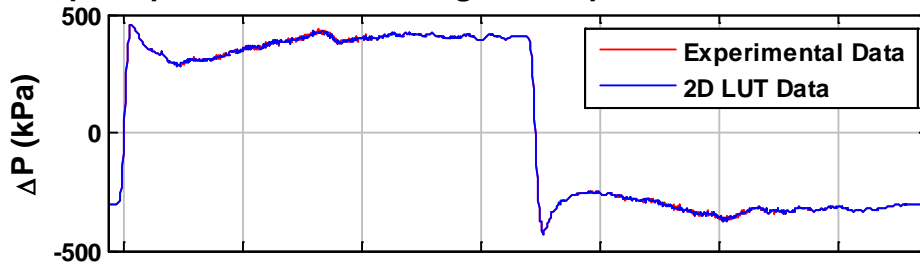


Figure G.14 Model verification of the 2D LUT at $a = 0.2 \text{ m/s}^2$

Superimposed 2D LUT Data against Experimental Data at $a=1.2 \text{ m/s}^2$



Model Error (E_r) at $a=1.2 \text{ m/s}^2$

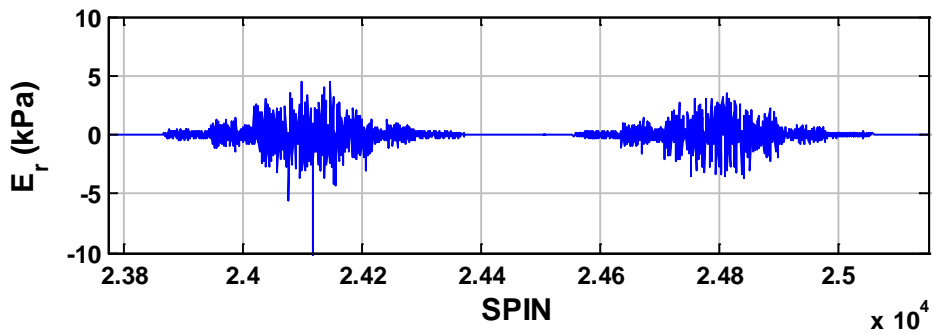
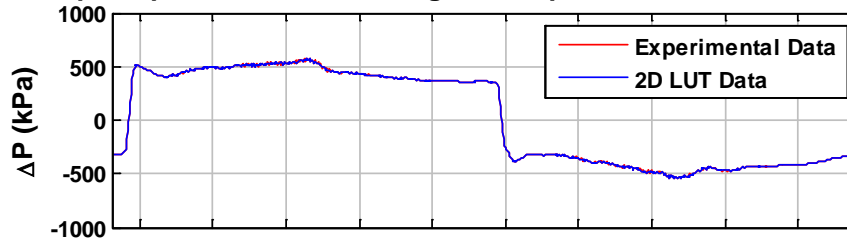


Figure G.15 Model verification of the 2D LUT at $a = 1.2 \text{ m/s}^2$

Superimposed 2D LUT Data against Experimental Data at $a=2.2 \text{ m/s}^2$



Model Error (E_r) at $a=2.2 \text{ m/s}^2$

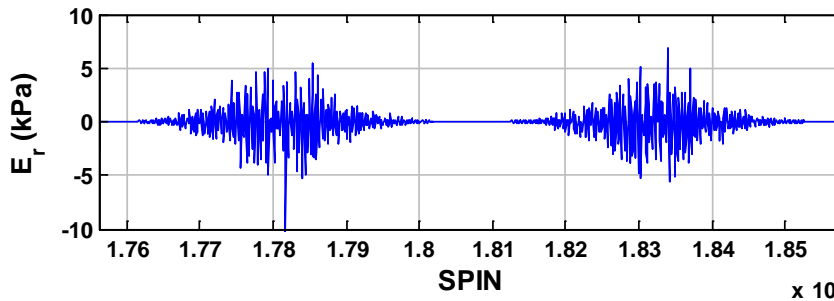


Figure G.16 Model verification of the 2D LUT at $a = 2.2 \text{ m/s}^2$

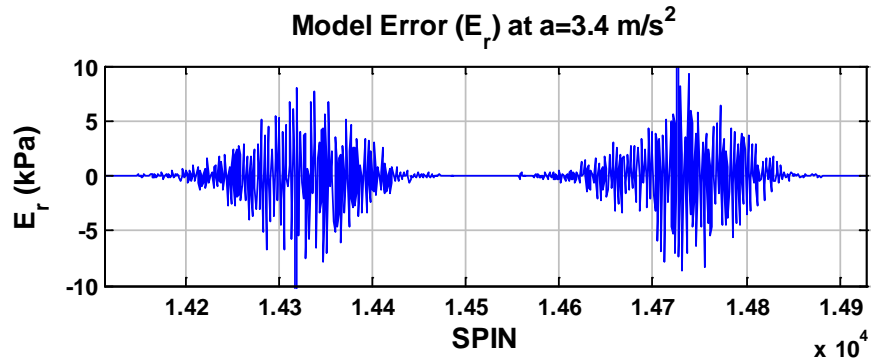
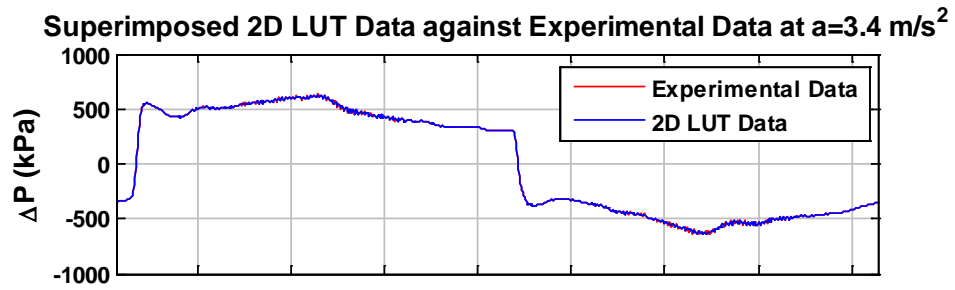


Figure G.17 Model verification of the 2D LUT at $a = 3.4 \text{ m/s}^2$

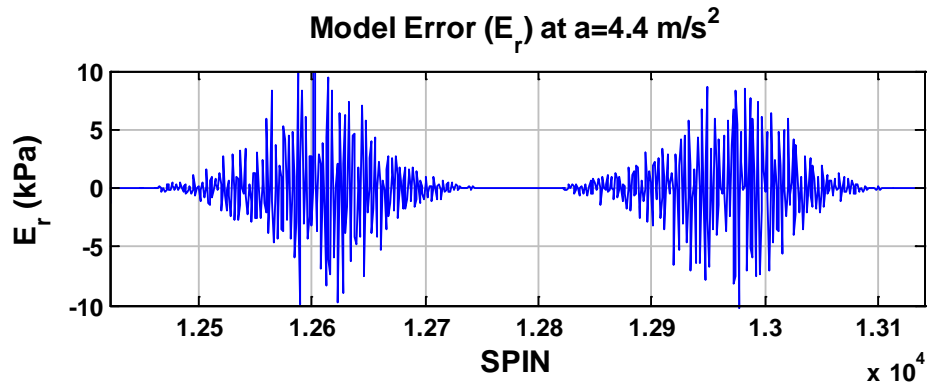
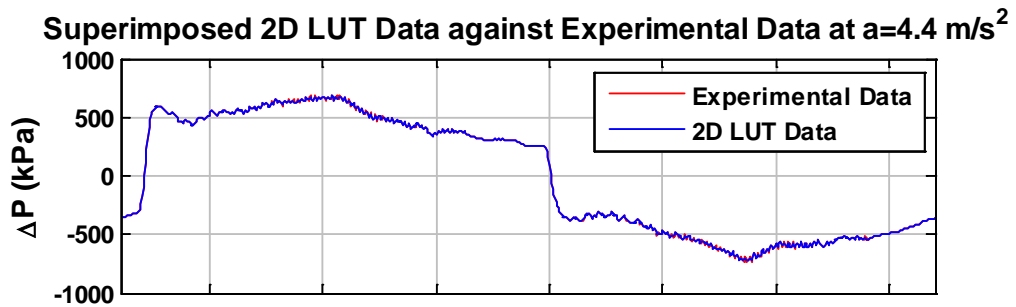


Figure G.18 Model verification of the 2D LUT at $a = 4.4 \text{ m/s}^2$

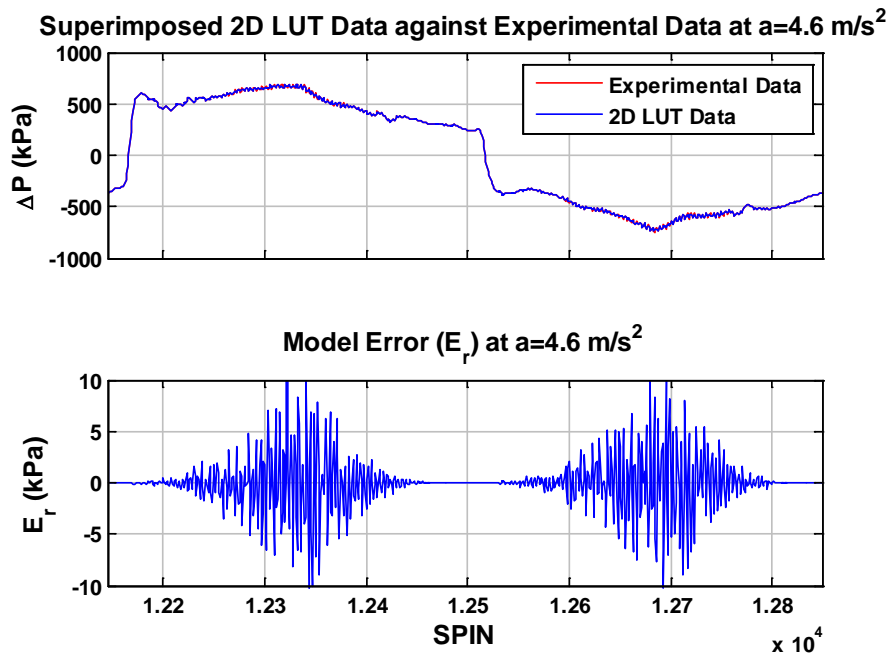


Figure G.19 Model verification of the 2D LUT at $a = 4.6 \text{ m/s}^2$

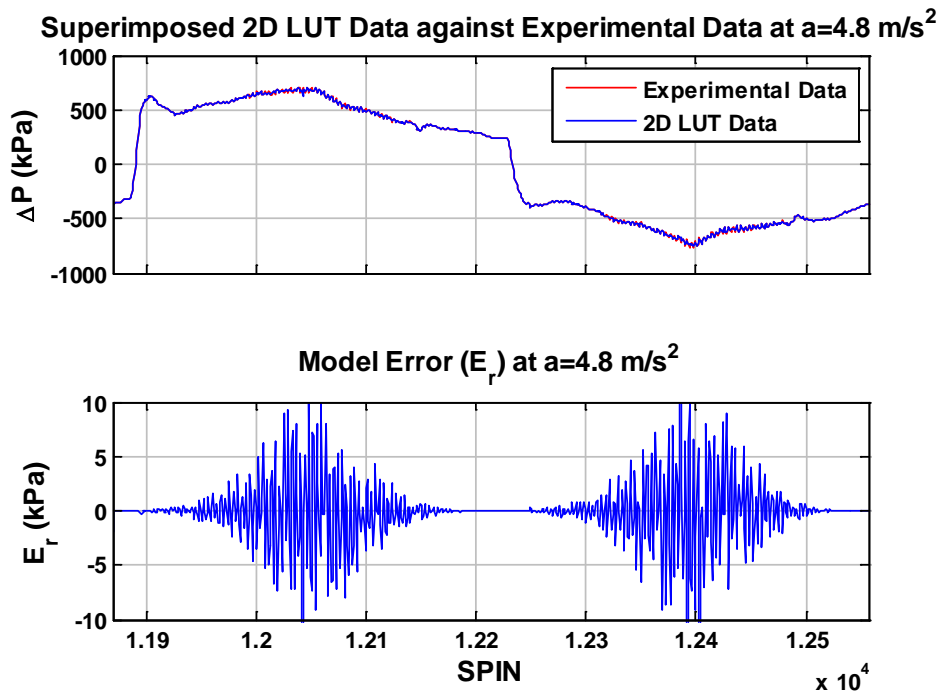


Figure G.20 Model verification of the 2D LUT at $a = 4.8 \text{ m/s}^2$

G.4 Additional Model Validation Results

Figures G.21, G.23, G.25 and G.27 illustrate the 2D LUT model data limitations and Figures G.22, G.24, G.26, and G.28 present the model validation (sinusoidal) results for signal frequencies of 0.03 Hz, 0.07 Hz, 0.3 Hz, and 0.98 Hz. The model validation results for the 2D LUT model and the Stribeck LUT model are included. It can be observed that the model outputs (for model validation regions (from Start Point (Sp) to Point 1, Point 2 to Point 3, and Point 4 to End Point (Ep)) indicated in the Figures G.22, G.24, G.26, and G.28) also follow the experimental results very closely compared to the Stribeck model. All the data (ellipses) fall within the rectangular boxes for all cases (See Figures G.21, G.23, G.25 and G.27). Since 2D LUT data is not available between Point 1 to Point 2, and Point 3 to Point 4, no comparison is possible. The model errors are left blank (removed).

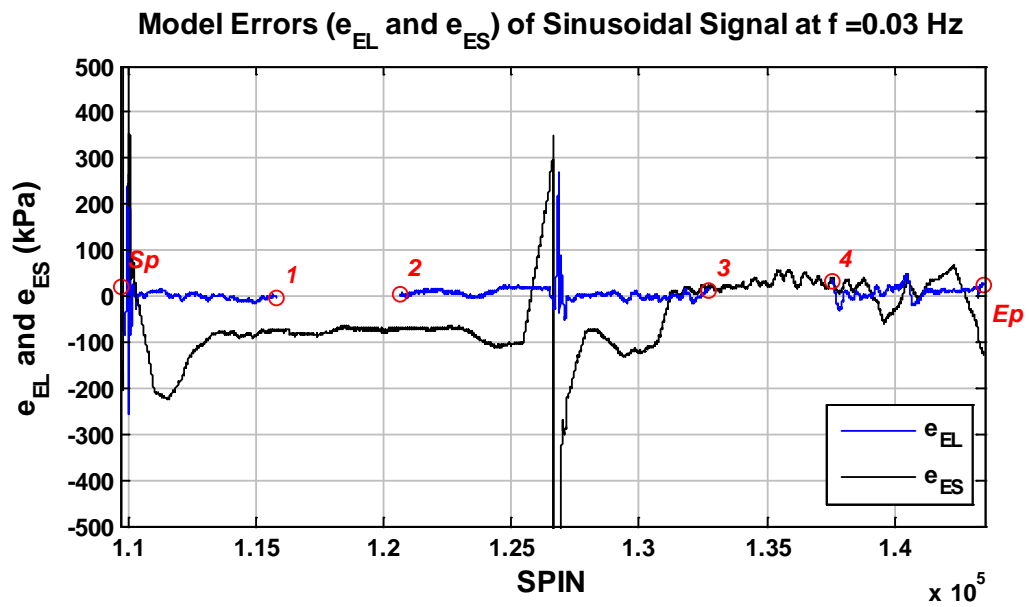
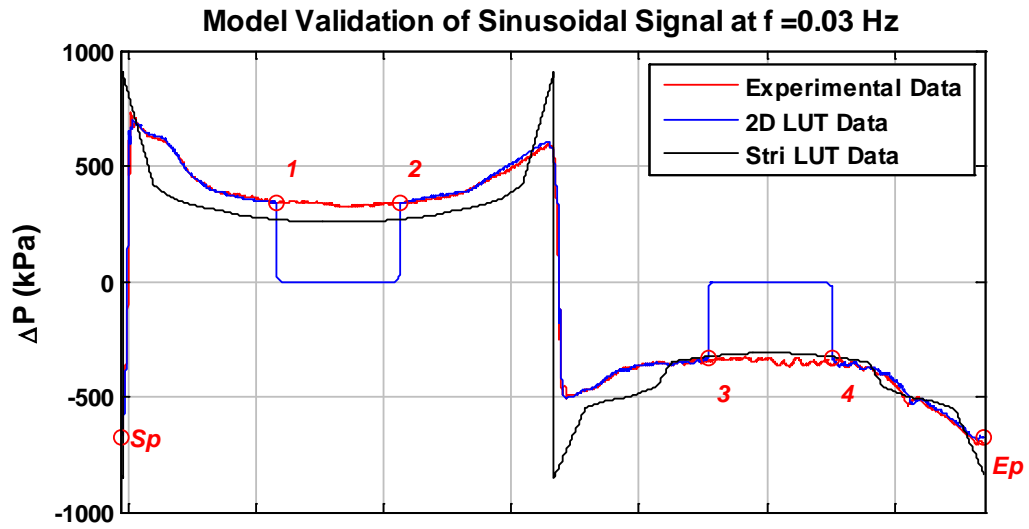


Figure G.22 Model validation of the 2D LUT at frequency $f = 0.03$ Hz. Stri LUT refers to the Stribeck lookup table.

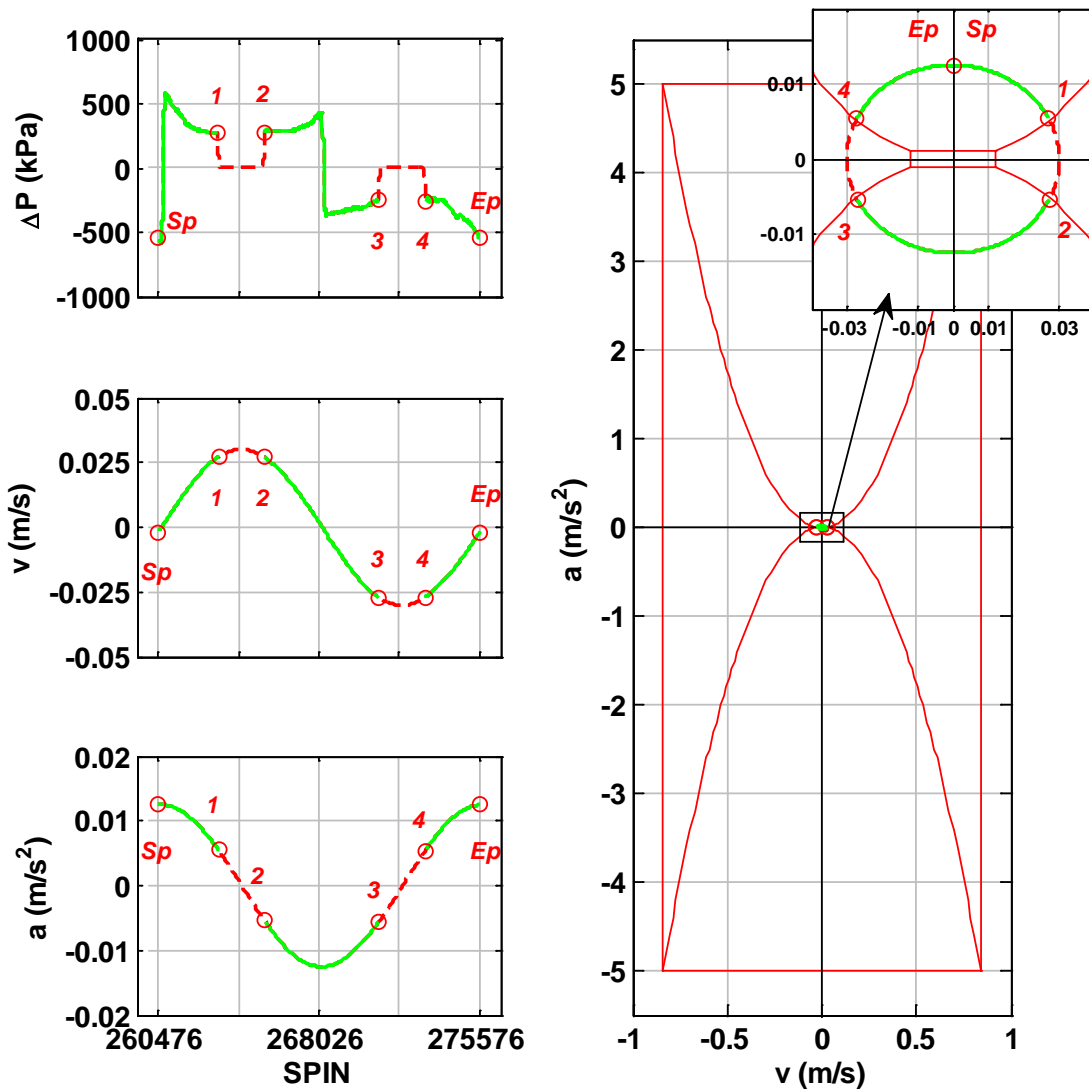


Figure G.23 Sinusoidal signal for model validation at medium frequency $f = 0.07$ Hz. The experimental physical limitations are provided by red lines. The different colors in the elliptical paths of velocity, acceleration and ΔP curves of one cycle represent the model data availability. Derivation of the data ranges is given in Appendix C.2.4. (Red solid: Limitations of 2D LUT; Green: Model validation zone; Red dash: No model data zone).

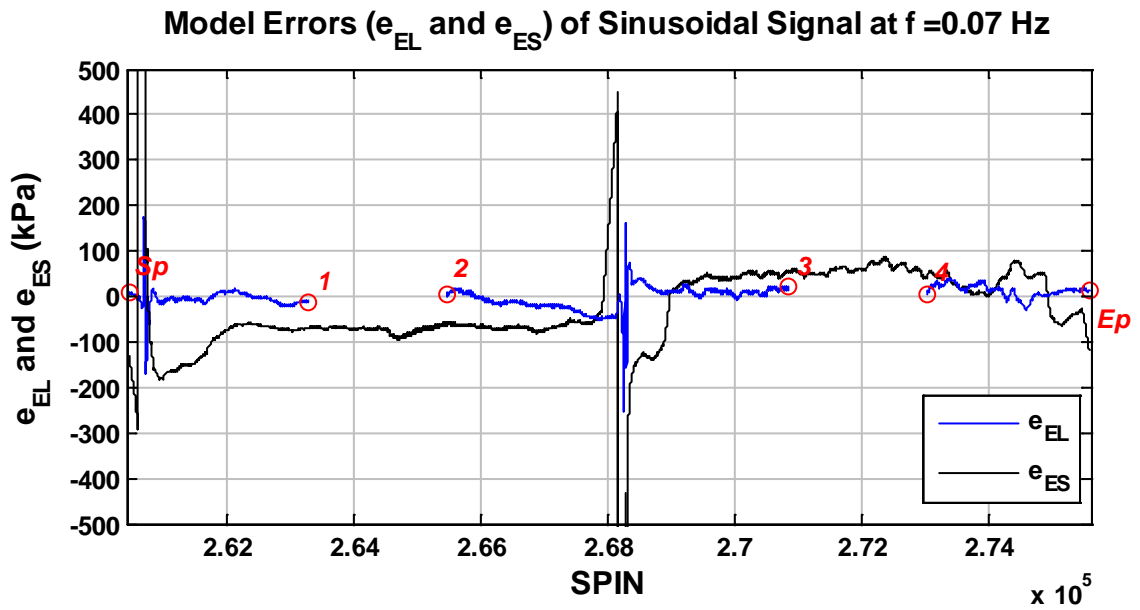
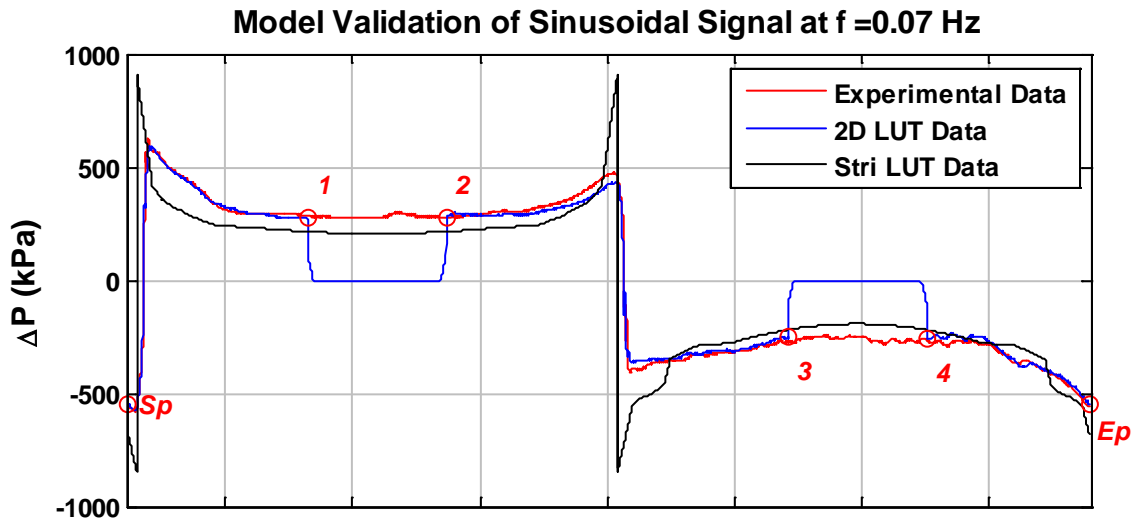


Figure G.24 Model validation of the 2D LUT at frequency $f = 0.07$ Hz. Stri LUT refers to the Stribeck lookup table.

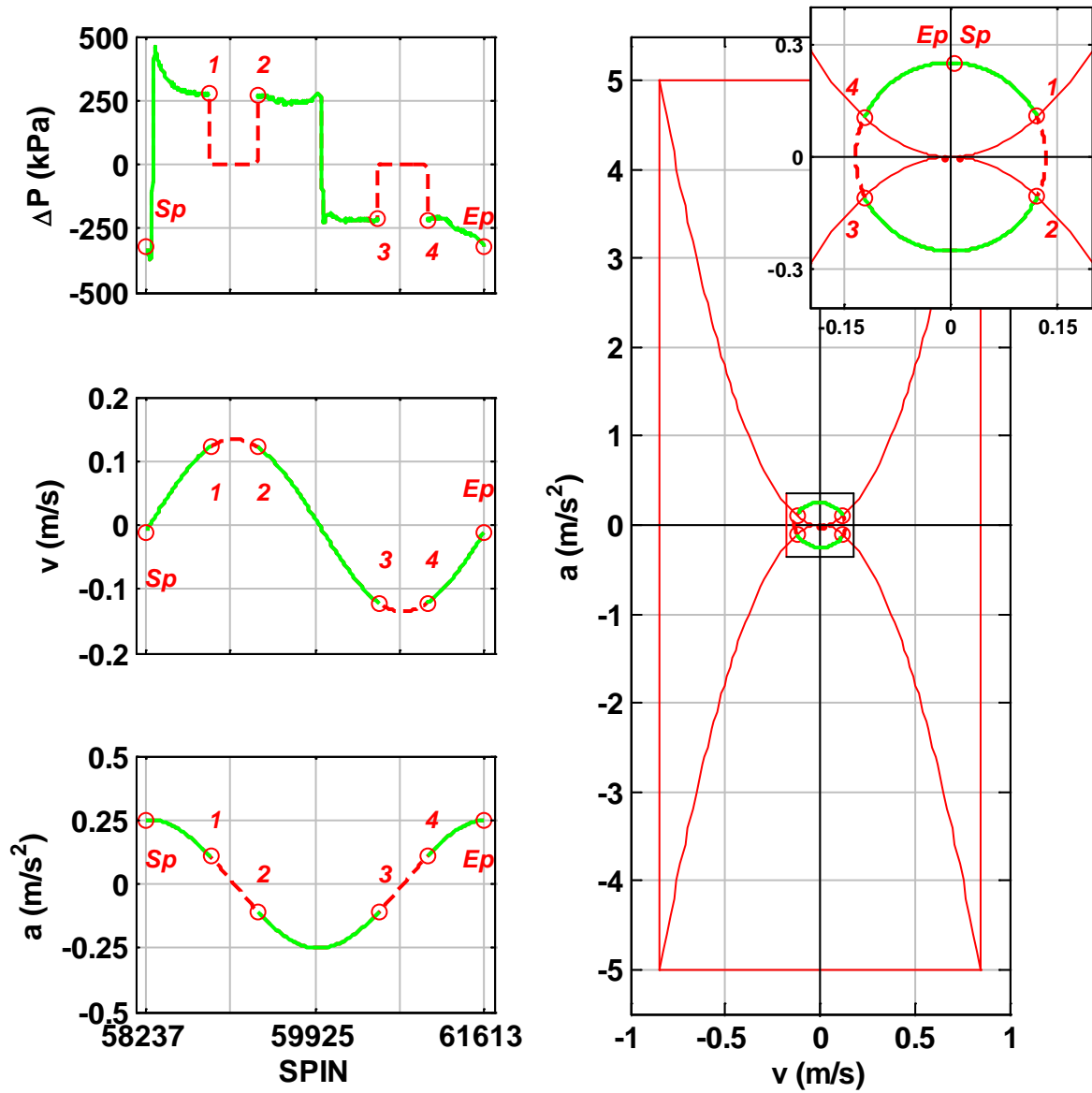


Figure G.25 Sinusoidal signal for model validation at medium frequency $f = 0.3$ Hz. The experimental physical limitations are provided by red lines. The different colors in the elliptical paths of velocity, acceleration and ΔP curves of one cycle represent the model data availability. Derivation of the data ranges is given in Appendix C.2.4. (Red solid: Limitations of 2D LUT; Green: Model validation zone; Red dash: No model data zone).

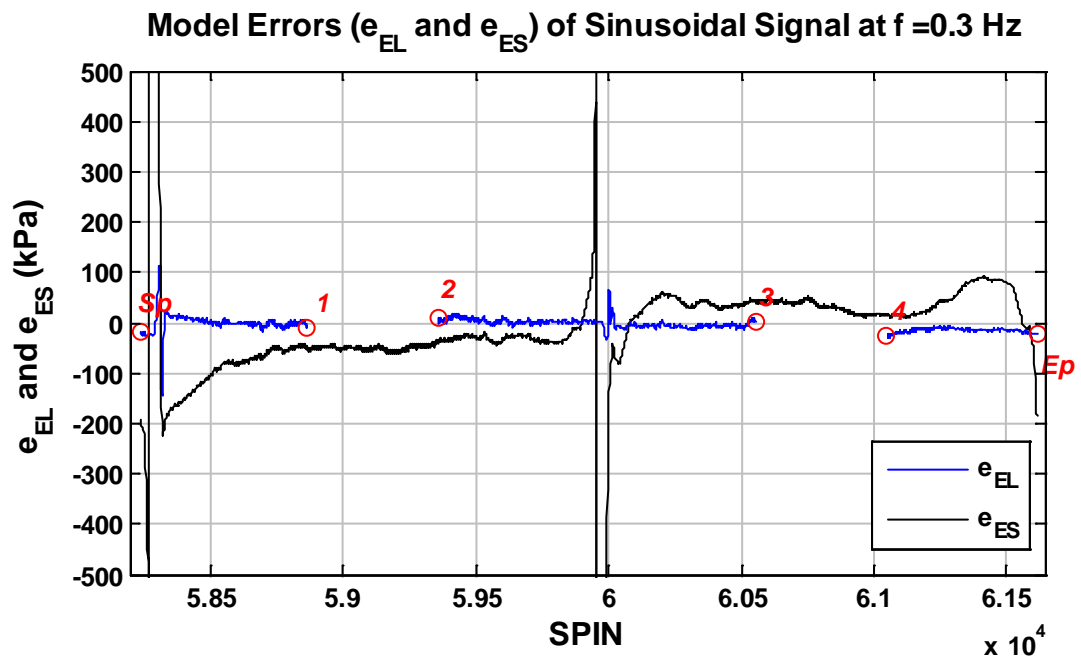
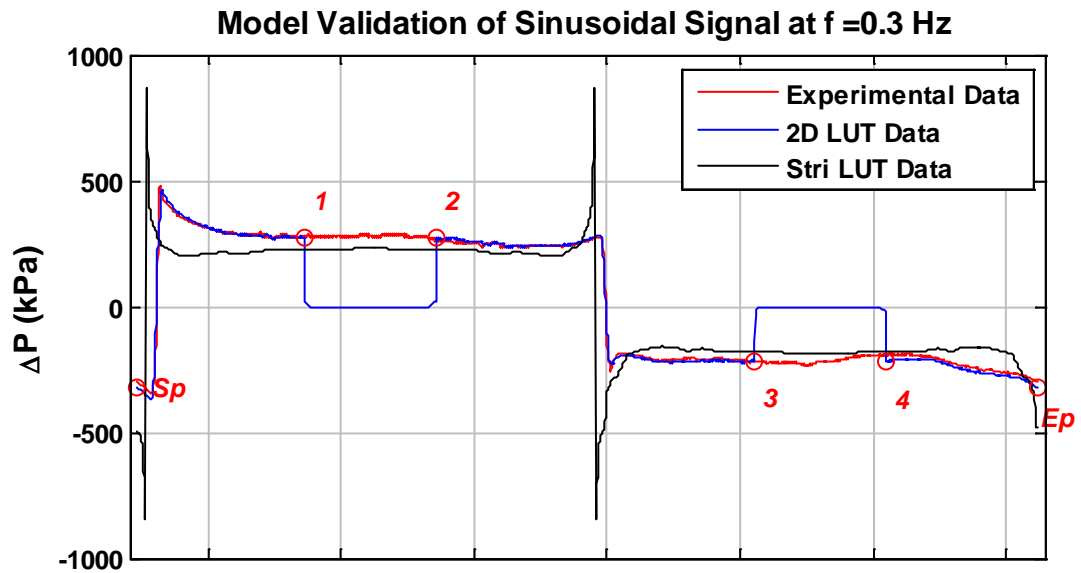


Figure G.26 Model validation of the 2D LUT at frequency $f = 0.3$ Hz. Stri LUT refers to the Stribeck lookup table.

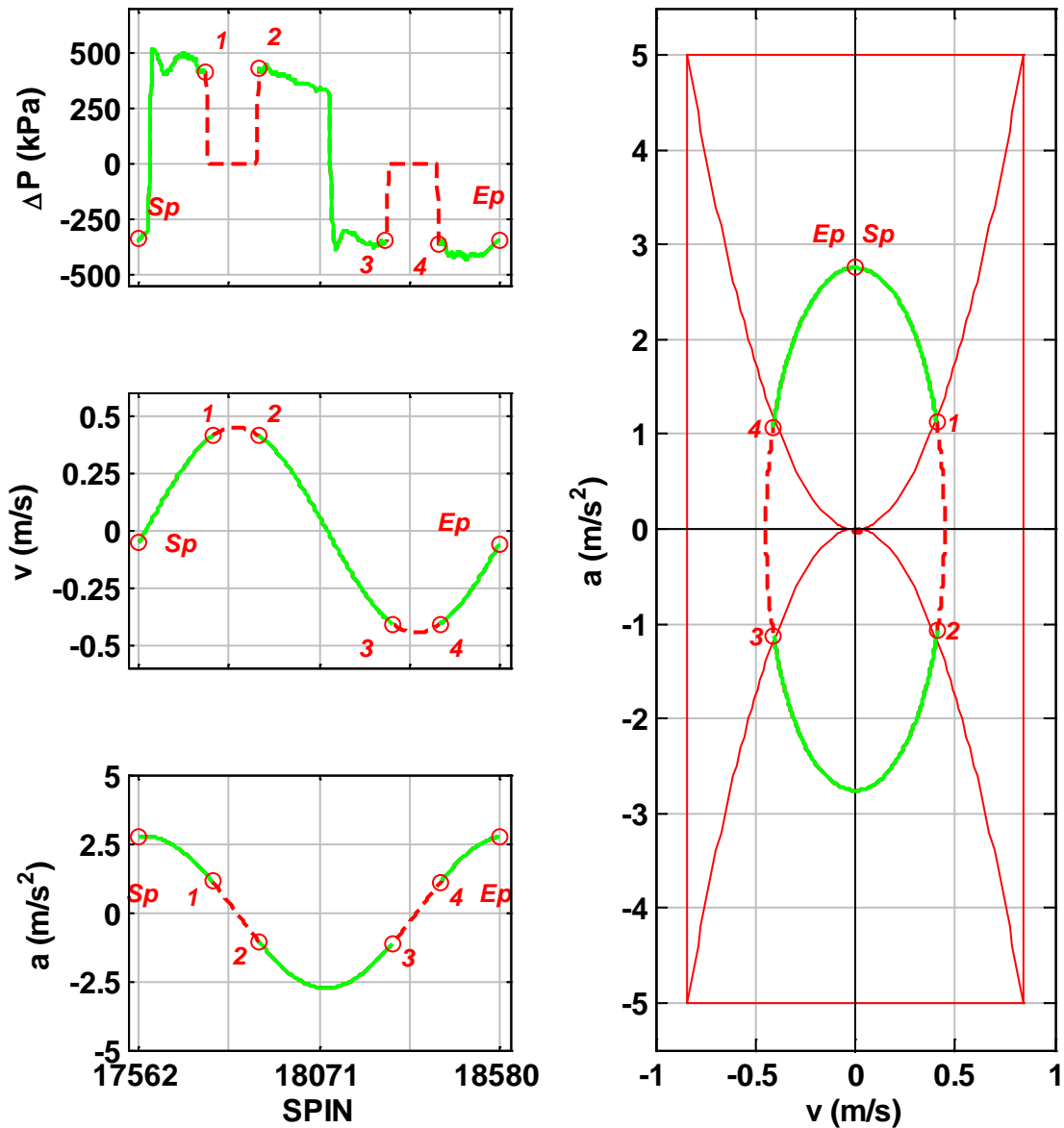


Figure G.27 Sinusoidal signal for model validation at medium frequency $f = 0.98$ Hz. The experimental physical limitations are provided by red lines. The different colors in the elliptical paths of velocity, acceleration and ΔP curves of one cycle represent the model data availability. Derivation of the data ranges is given in Appendix C.2.4. (Red solid: Limitations of 2D LUT; Green: Model validation zone; Red dash: No model data zone).

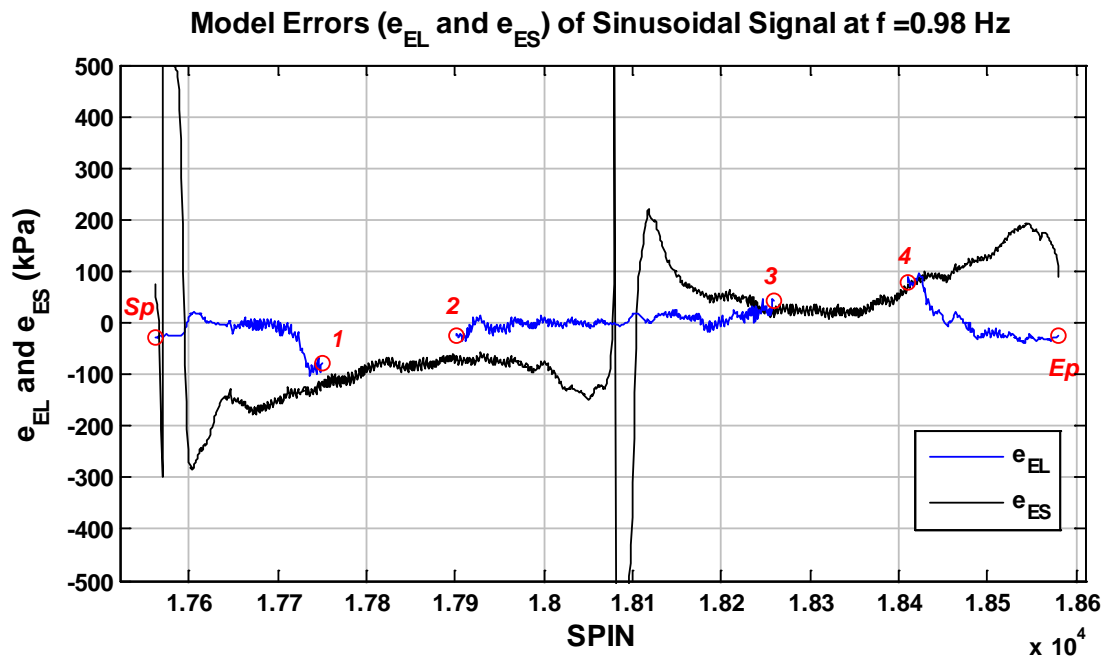
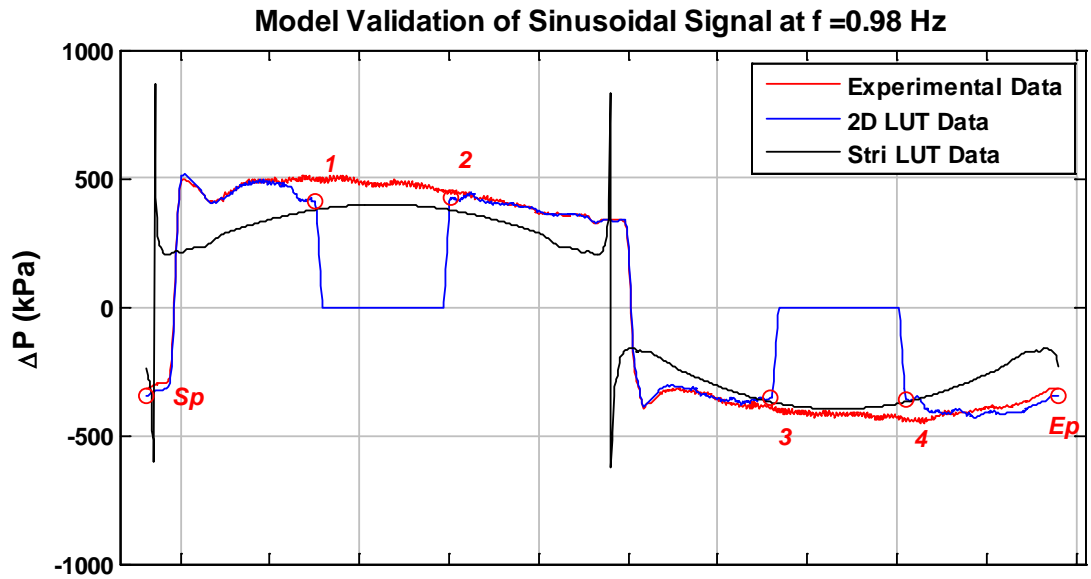


Figure G.28 Model validation of the 2D LUT at frequency $f = 0.98$ Hz. Stri LUT refers to the Stribeck lookup table.

APPENDIX H: EXPERIMENTAL LIMITATION ANALYSIS

In the main body of this thesis, several equations which described the limitations of the 2D LUT modeling and model validation were presented. In this Appendix, a detailed derivation of these equations are presented.

H.1 2D LUT Modeling Limitation Analysis

In Chapter 3, a novel 2D lookup table (2D LUT) model was developed from the experimental data under various acceleration conditions. This section will consider the derivation of the limitations of the model which included the boundary line of the 2D LUT Model, Equation (3.5): $v_{\max_a} = \sqrt{La}$.

As mentioned in Appendix A, for Non-steady state motion with constant acceleration (a), the velocity (v) increases linearly. The piston starts at one end of the cylinder at zero velocity and reaches its maximum velocity at the midpoint of the cylinder. Since the piston travels from the start point to the midpoint of the cylinder, the amplitude of the displacement signal (A) is:

$$A = \left(\frac{1}{2}\right) at_{\max}^2 \quad (\text{H. 1})$$

where t_{\max} is *the* time the piston takes to travel from the start point to the midpoint of the cylinder and a is the acceleration.

From (H.1), t_{\max} can be obtained as follows:

$$t_{\max} = \sqrt{\frac{2A}{a}} \quad (\text{H. 2})$$

Since constant acceleration is assumed, the maximum velocity at the midpoint of the cylinder with acceleration (a) is:

$$v_{\max_a} = at_{\max} \quad (\text{H. 3})$$

Substituting Equation (H.2) into Equation (H.3) yields:

$$v_{\max_a} = a \sqrt{\frac{2A}{a}} \quad (\text{H. 4})$$

which by simplifying Equation (H.4) yields:

$$v_{\max_a} = \sqrt{2Aa} = \sqrt{La} \quad (\text{H. 5})$$

From Equation (H.5), it can be observed that the maximum velocity (v_{\max_a}) of the piston has a nonlinear relationship with constant acceleration (a).

H.2 Model Validation Limitation Analysis

As mentioned in Chapter 4, there were limitations identified in the 2D LUT modeling process and in the model validation. These limitations differ for varying motion conditions. The derivation of some of the limitations are now considered.

H.2.1 The Equation of the Elliptical Curve

This section considers the derivation of Equation (5.10): $\frac{v^2}{v_{\max}^2} + \frac{a^2}{a_{\max}^2} = 1$, for a sinusoidal signal.

A sinusoidal signal was selected for model validation in Chapter 5. From Figure 5.4, it was observed that the velocity and acceleration of the sinusoidal signal varies over one period. The following equations (Equations (H.6) and (H.7)) can be obtained from Equations (5.5) and (5.6) in Chapter 5; that is

$$\frac{v}{A\omega} = \sin(\omega t) \quad (\text{H. 6})$$

$$\frac{a}{A\omega^2} = \cos(\omega t) \quad (\text{H. 7})$$

Using the trigonometric equation,

$$(\sin(\omega t))^2 + (\cos(\omega t))^2 = 1 \quad (\text{H. 8})$$

and substituting Equations (H.6) and (H.7) into Equation (H.8) yields:

$$\left(\frac{v}{A\omega}\right)^2 + \left(\frac{a}{A\omega^2}\right)^2 = 1 \quad (\text{H. 9})$$

Reorganizing Equation (H.9) gives:

$$\frac{v^2}{v_{\max}^2} + \frac{a^2}{a_{\max}^2} = 1 \quad (\text{H. 10})$$

where $v_{\max} = (A\omega)^2$ and $a_{\max} = (A\omega^2)^2$ are the radius of two axis of the ellipse respectively.

H.2.2 Maximum Frequencies

This section considers the derivation of Equation (5.11): $f_{\max_v} = \frac{1}{2\pi} \frac{v_{\max}}{A}$ and Equation

$$(5.12): f_{\max_a} = \frac{1}{2\pi} \sqrt{\frac{a_{\max}}{A}}.$$

The maximum velocities (v_{\max}) and accelerations (a_{\max}) of VCHAS1 and VCHAS2 were presented in Tables 3.3 and 3.4 in Chapter 3, (which defined the physical limitation of the experimental systems). Therefore for a sinusoidal signal, the maximum velocity and acceleration must be less than or equal to the maximum velocities (v_{\max}) and accelerations (a_{\max}) of the experimental system; that is,

$$v_{\sin_max} \leq v_{\max} \quad (\text{H. 11})$$

$$a_{\sin_max} \leq a_{\max} \quad (\text{H. 12})$$

The frequency of the sinusoidal signal is constrained by these limitations. From Equations (5.5) and (5.6) in Chapter 5, the amplitude of velocity and acceleration of the sinusoidal signal can be obtained as follows:

$$v_{\sin_max} = A\omega = 2\pi fA \quad (\text{H. 13})$$

$$a_{\sin_max} = A\omega^2 = (2\pi f)^2 A \quad (\text{H. 14})$$

Substituting Equation (H.13) into Equation (H.11) yields:

$$2\pi fA \leq v_{\max} \quad (\text{H. 15})$$

From Equation (H.15):

$$f \leq \frac{v_{\max}}{2\pi A} \quad (\text{H. 16})$$

Therefore,

$$f_{\max_v} = \frac{1}{2\pi} \frac{v_{\max}}{A} \quad (\text{H. 17})$$

Substituting Equation (H.14) into Equation (H.12) yields

$$(2\pi f)^2 A \leq a_{\max} \quad (\text{H. 18})$$

From Equation (H.16)

$$f \leq \sqrt{\frac{a_{\max}}{(2\pi)^2 A}} \quad (\text{H. 19})$$

and therefore,

$$f_{\max_a} = \frac{1}{2\pi} \sqrt{\frac{a_{\max}}{A}} \quad (\text{H. 20})$$

H.2.3 Intersection Points between the Elliptical ($v - a$) Curve and Boundary Lines

This section considers the derivation of Equation (5.15): $v = A(2\pi f)\sqrt{2(\sqrt{2} - 1)}$ and Equation (5.16): $a = A(2\pi f)^2(\sqrt{2} - 1)$.

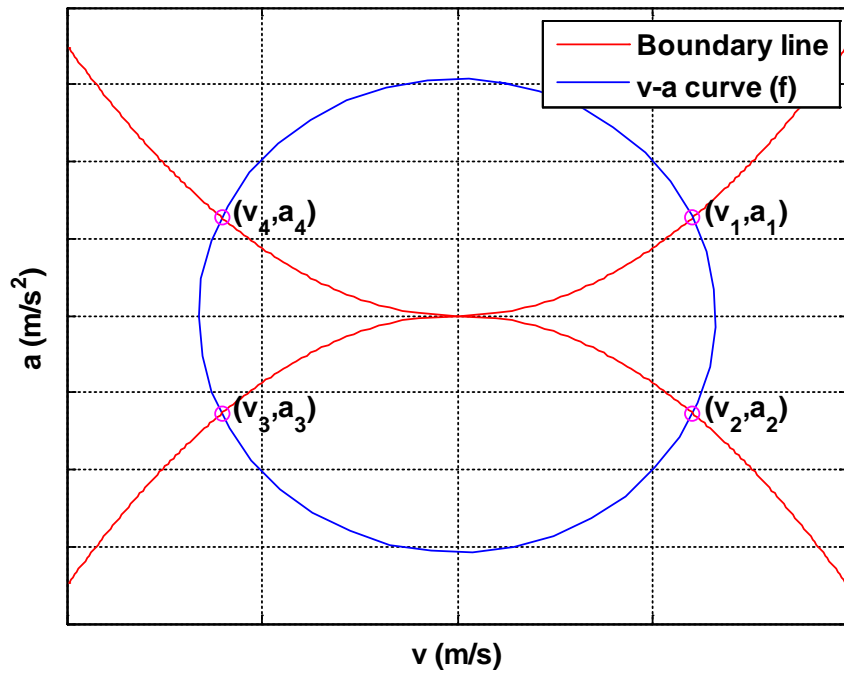


Figure H.1 The four intersection points (in circles) (v_1, a_1) , (v_2, a_2) , (v_3, a_3) , and (v_4, a_4) of the elliptical curve ($v - a$) of the sinusoidal signal and physical limit boundary lines in all quadrants

Consider Figure H.1. The intersection point (v, a) in Quadrant 1 can be obtained as follows:
Substituting Equation (H.5) into Equation (H.9) yields:

$$\left(\frac{\sqrt{2Aa}}{A\omega}\right)^2 + \left(\frac{a}{A\omega^2}\right)^2 = 1 \quad (\text{H. 21})$$

Reorganizing Equation (H.21) yields:

$$a^2 + 2A\omega^2 a - A^2\omega^4 = 0 \quad (\text{H. 22})$$

Therefore, there are 2 roots for the quadratic Equation (H.22):

$$a = \frac{-2A\omega^2 \pm \sqrt{(2A\omega^2)^2 - 4(-A^2\omega^4)}}{2} \quad (\text{H. 23})$$

Simplifying Equation (H.23) yields:

$$a = (-1 \pm \sqrt{2}) A\omega^2 \quad (\text{H. 24})$$

The 2 roots can be listed as follows:

$$a_1 = (-1 + \sqrt{2}) A\omega^2 = A\omega^2 (\sqrt{2} - 1) > 0 \quad (\text{H. 25})$$

$$a_2 = (-1 - \sqrt{2}) A\omega^2 = -A\omega^2 (\sqrt{2} + 1) < 0 \quad (\text{H. 26})$$

It is observed from Equations (H.25) and (H.26) that the first root is positive, and the second root is negative. Since the acceleration is positive in Quadrant 1, the negative root is discarded, thus:

$$a = A(2\pi f)^2(\sqrt{2} - 1) \quad (\text{H. 27})$$

$$v = \sqrt{2Aa} = A\omega \sqrt{2(\sqrt{2} - 1)} = A(2\pi f) \sqrt{2(\sqrt{2} - 1)} \quad (\text{H. 28})$$

The intersection point in Quadrant 1 is therefore:

$$\text{Q1: } (v_1, a_1) = \left(A(2\pi f) \sqrt{2(\sqrt{2} - 1)}, A(2\pi f)^2(\sqrt{2} - 1) \right) \quad (\text{H. 29})$$

Because the intersection points in other Quadrants are symmetrical (Figure H.1), the intersection points in Quadrant 2, 3, and 4 can be obtained as follows:

$$\text{Q2: } (v_2, a_2) = \left(A(2\pi f) \sqrt{2(\sqrt{2} - 1)}, -A(2\pi f)^2(\sqrt{2} - 1) \right) \quad (\text{H. 30})$$

$$\text{Q3: } (v_3, a_3) = \left(-A(2\pi f) \sqrt{2(\sqrt{2} - 1)}, -A(2\pi f)^2(\sqrt{2} - 1) \right) \quad (\text{H. 31})$$

$$\text{Q4: } (v_4, a_4) = \left(-A(2\pi f) \sqrt{2(\sqrt{2} - 1)}, A(2\pi f)^2(\sqrt{2} - 1) \right) \quad (\text{H. 32})$$

H.2.4 Data Range in the Time Domain

The intersection points (v, a) , are obtained in the motion coordinate plane. However, model validation was conducted in the time domain; therefore, the intersection points must be identified in the time domains as well (Figure H.2).

From Equation (H.6), the time can be obtained as follows:

$$t = \frac{1}{\omega} \sin^{-1} \frac{v}{A\omega} \quad (\text{H.33})$$

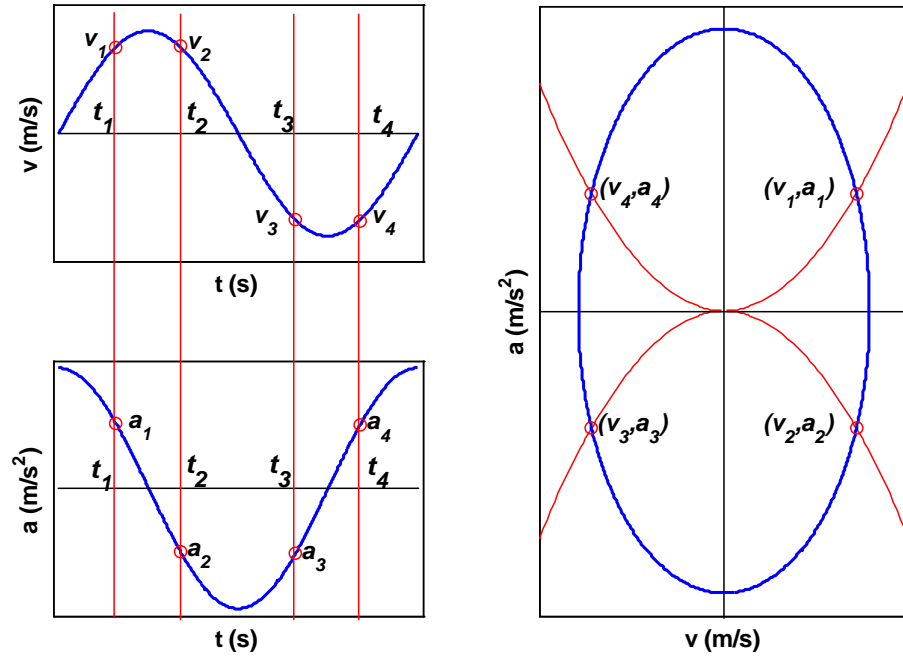


Figure H.2 The four time points t_1, t_2, t_3, t_4 correspond to the four intersection points $(v_1, a_1), (v_2, a_2), (v_3, a_3),$ and (v_4, a_4) of Section H.2.3

Substituting Equation (H.24) into Equation (H.33), the time (t_1) in Quadrant 1 can be obtained as follows:

$$t_1 = \frac{1}{\omega} \sin^{-1} \frac{A\omega \sqrt{2(\sqrt{2}-1)}}{A\omega} = \frac{P}{2\pi} \sin^{-1} \left(\sqrt{2(\sqrt{2}-1)} \right) \quad (\text{H.34})$$

In a similar sense, the time in Quadrants 2, 3 and 4 can be obtained as follows:

$$t_2 = \left(\frac{P}{2} \right) - \frac{P}{2\pi} \sin^{-1} \left(\sqrt{2(\sqrt{2}-1)} \right) \quad (\text{H.35})$$

$$t_3 = \left(\frac{P}{2} \right) + \frac{P}{2\pi} \sin^{-1} \left(\sqrt{2(\sqrt{2}-1)} \right) \quad (\text{H.36})$$

$$t_4 = P - \frac{P}{2\pi} \sin^{-1} \left(\sqrt{2(\sqrt{2}-1)} \right) \quad (\text{H.37})$$

H.2.5 Intersection Points between the Maximum/Minimum Acceleration and Boundary Lines

This section considers the derivation of Equation (5.13): $v = \sqrt{\frac{A^2(2\pi f)^4 - a^2}{(2\pi f)^2}}$.

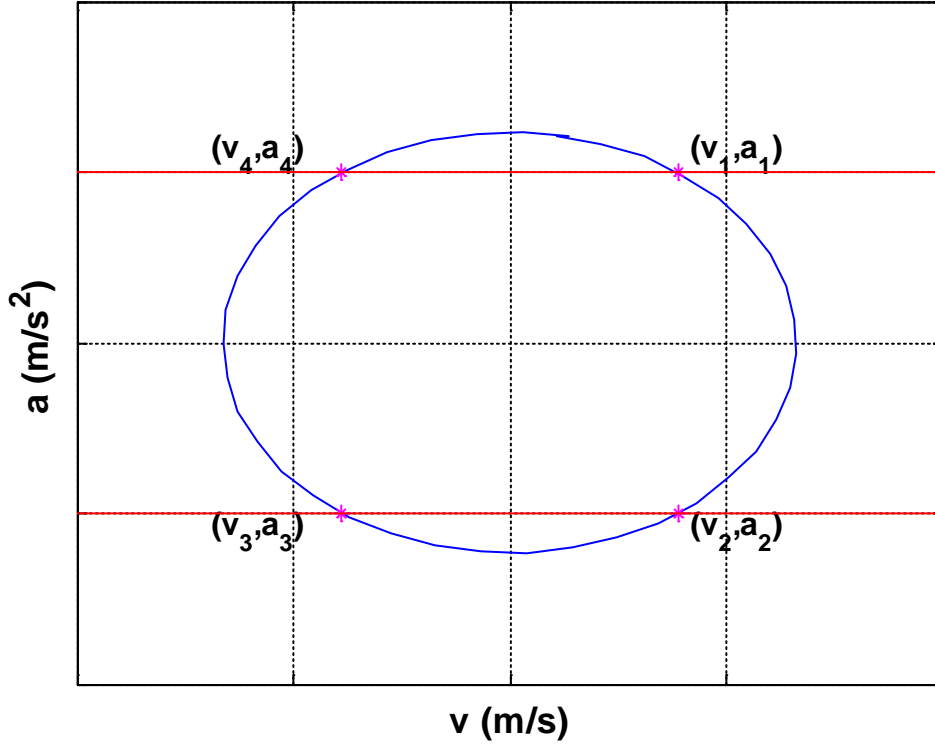


Figure H.3 The four intersection points (in asterisks) (v_1, a_1) , (v_2, a_2) , (v_3, a_3) , and (v_4, a_4) of the elliptical curve $(v - a)$ of the sinusoidal signal and maximum/ minimum acceleration lines in all quadrants

The intersection point (v, a) in Quadrant 1 can be obtained by solving for the root of Equation (H.9) for any given acceleration (a) ; that is

$$v^2 = A^2\omega^2 - \frac{a^2}{A^2\omega^4} A^2\omega^2 \quad (\text{H. 38})$$

$$v = \sqrt{A^2\omega^2 - \frac{a^2}{\omega^2}} = \sqrt{\frac{A^2\omega^4 - a^2}{\omega^2}} = \sqrt{\frac{A^2(2\pi f)^4 - a^2}{(2\pi f)^2}} \quad (\text{H. 39})$$

The intersection point (v, a) in Quadrant 1 is thus:

$$\text{Q1: } (v_2, a_2) = \left(\sqrt{\frac{A^2(2\pi f)^4 - a^2}{(2\pi f)^2}}, a \right) \quad (\text{H. 40})$$

Because the intersection points in the other Quadrants are symmetrical, the intersection points in Quadrants 2, 3, and 4 can be obtained as follows:

$$Q2: (v_2, a_2) = \left(\sqrt{\frac{A^2(2\pi f)^4 - a^2}{(2\pi f)^2}}, -a \right) \quad (H.41)$$

$$Q3: (v_3, a_3) = \left(-\sqrt{\frac{A^2(2\pi f)^4 - a^2}{(2\pi f)^2}}, -a \right) \quad (H.42)$$

$$Q4: (v_4, a_4) = \left(-\sqrt{\frac{A^2(2\pi f)^4 - a^2}{(2\pi f)^2}}, a \right) \quad (H.43)$$

H.2.6 Data Ranges in the Time Domain

The intersection points of Section H.2.5 are obtained in the motion coordinate plane. Model validation is conducted in the time domain; therefore, the intersection points have been identified in the time domain as well (Figure H.4).

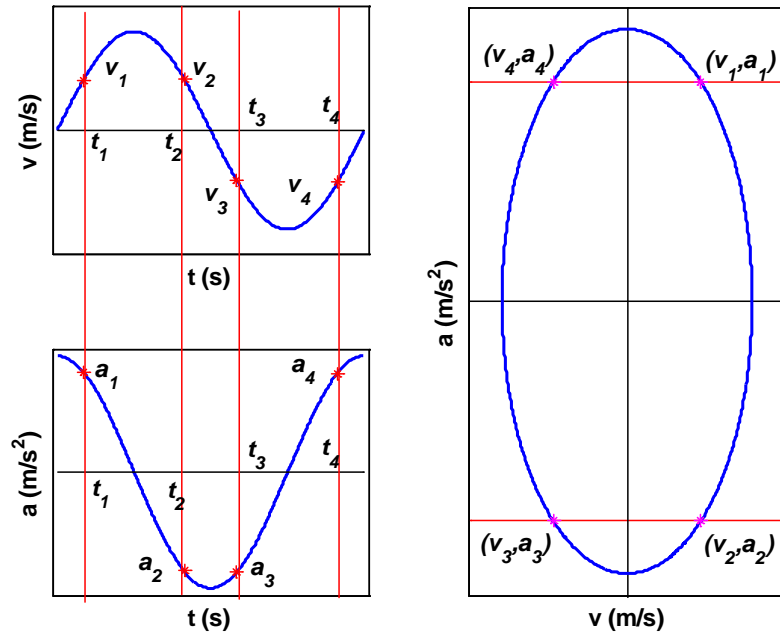


Figure H.4 The four time points t_1, t_2, t_3, t_4 correspond to the four intersection points $(v_1, a_1), (v_2, a_2), (v_3, a_3),$ and (v_4, a_4) of Section H.2.5

If Equation (H.35) is substituted into Equation (H.29), the time (t_1) in Quadrant 1 can be obtained as follows:

$$\begin{aligned}
t_1 &= \frac{1}{\omega} \sin^{-1} \frac{\sqrt{\frac{A^2 \omega^4 - a^2}{\omega^2}}}{A\omega} \\
&= \frac{1}{\omega} \sin^{-1} \sqrt{\frac{A^2 \omega^4 - a^2}{A^2 \omega^4}} = \frac{1}{2\pi} \sin^{-1} \left(\sqrt{1 - \frac{a^2}{A^2 \omega^4}} \right) \quad (\text{H. 44})
\end{aligned}$$

Using a similar approach, the time t_2, t_3, t_4 in Quadrants 2, 3 and 4 can be obtained as follows:

$$t_2 = \left(\frac{P}{2}\right) - \frac{P}{2\pi} \sin^{-1} \left(\sqrt{1 - \frac{a^2}{A^2 \omega^4}} \right) \quad (\text{H. 45})$$

$$t_3 = \left(\frac{P}{2}\right) + \frac{P}{2\pi} \sin^{-1} \left(\sqrt{1 - \frac{a^2}{A^2 \omega^4}} \right) \quad (\text{H. 46})$$

$$t_4 = P - \frac{P}{2\pi} \sin^{-1} \left(\sqrt{1 - \frac{a^2}{A^2 \omega^4}} \right) \quad (\text{H. 47})$$

APPENDIX I: ADDITIONAL 3D VISUALIZATIONS OF THE 2D LUT OF VCHAS1 AND VCHAS2

In Chapter 4, 3D representations of Quadrant 1 (only) and the overall friction (ΔP) characteristics of VCHAS1 and VCHAS2 were given. The top views of these 3D plots were also provided. In this appendix, additional 3D (isometric) representations for the other 3 Quadrants (Quadrants 2, 3 and 4) are presented. Additional isometric, front views and side views of these 3D plots are also provided.

I.1 3D Views of the Other 3 Quadrants

I.1.1 VCHAS1

The isometric 3D views of Quadrants 2, 3, and 4 for VCHAS1 are presented in Figures I.1 through I.3.

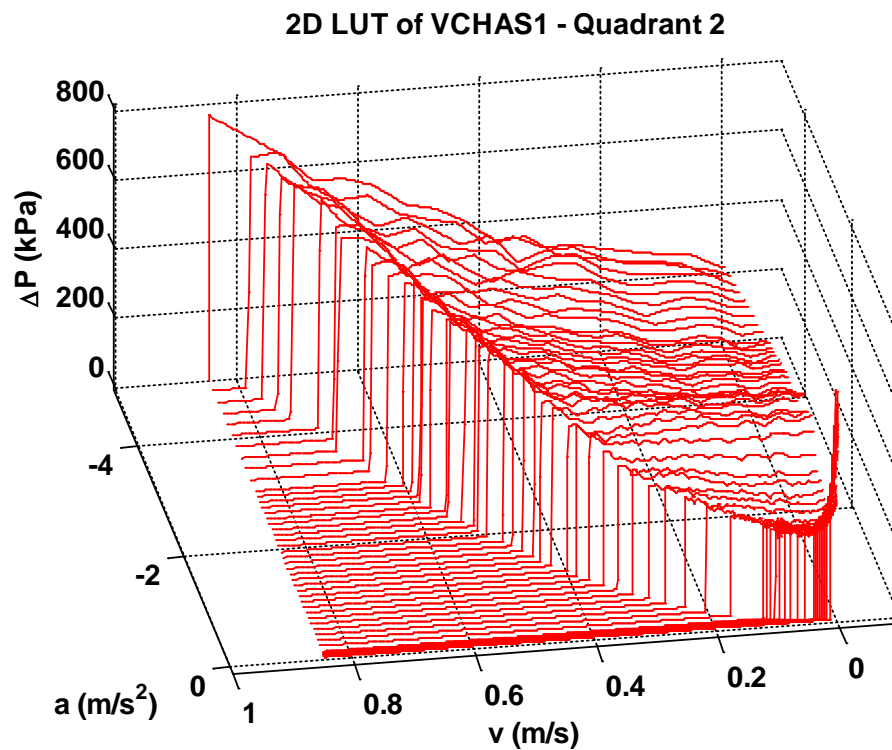


Figure I.1 3D visual plot for Quadrant 2 of VCHAS1

2D LUT of VCHAS1 - Quadrant 3

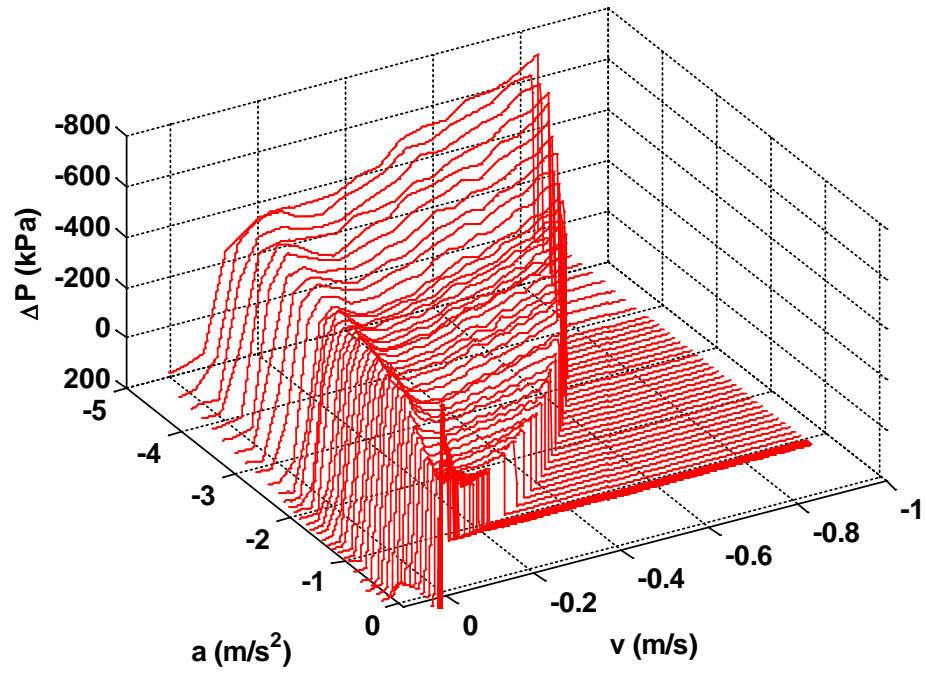


Figure I.2 3D visual plot for Quadrant 3 of VCHAS1 viewing from the bottom up (note, the sign of ΔP (kPa) is negative).

2D LUT of VCHAS1 - Quadrant 4

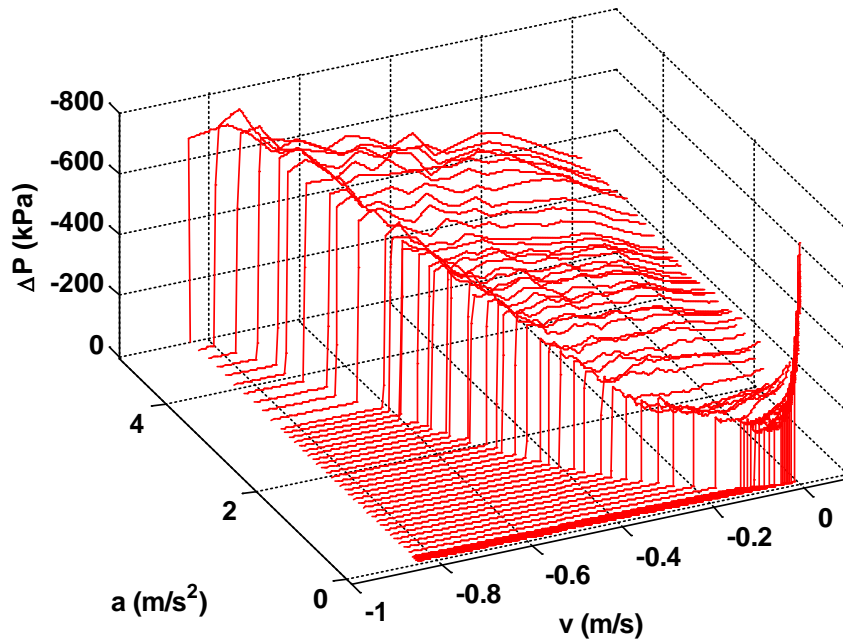


Figure I.3 3D visual plot for Quadrant 4 of VCHAS1 viewing from the bottom up (note, the sign of ΔP (kPa) is negative).

I.1.2 VCHAS2

The isometric 3D views of Quadrants 2, 3, and 4 for VCHAS2 are presented in Figures I.4 through I.6.

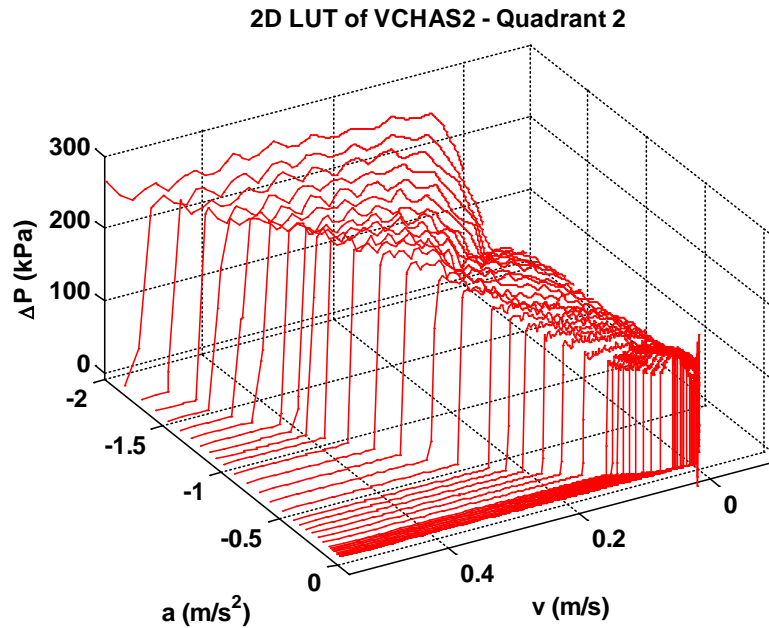


Figure I.4 3D visual plot for Quadrant 2 of VCHAS2.

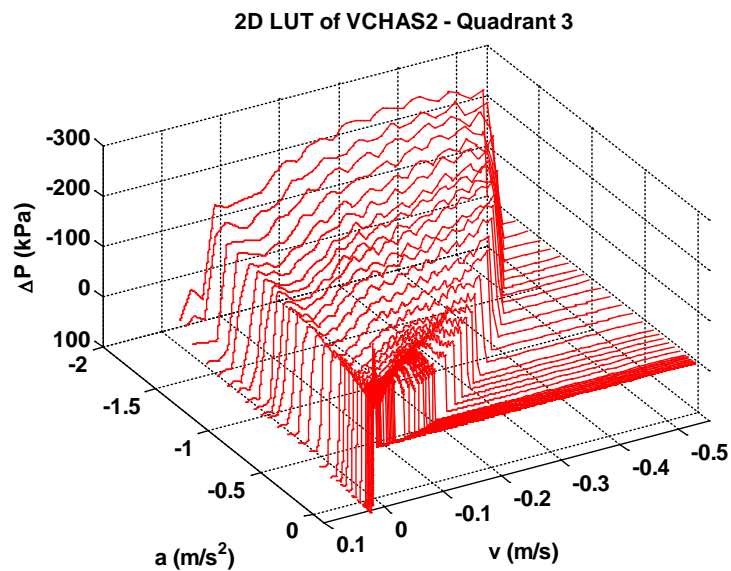


Figure I.5 3D visual plot for Quadrant 3 of VCHAS2 viewing from the bottom up (note, the sign of ΔP (kPa) is negative).

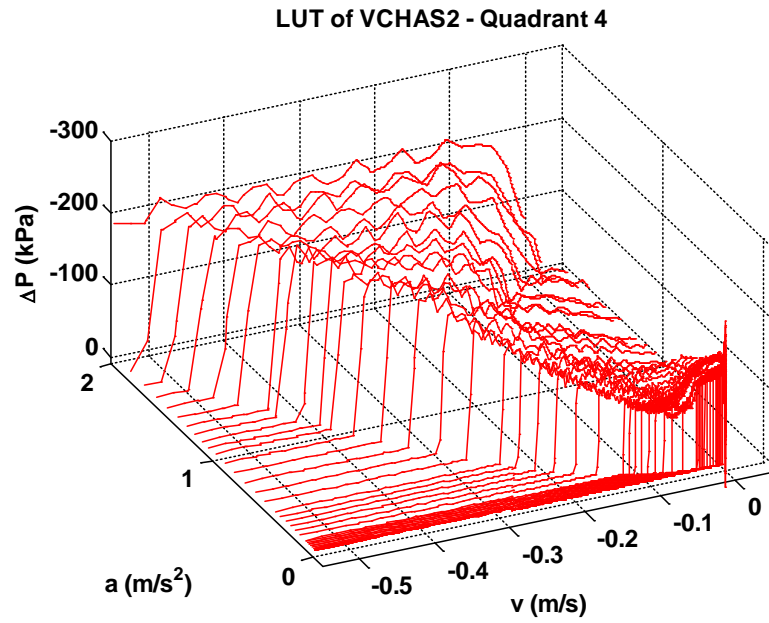


Figure I.6 3D visual plot for Quadrant 4 of VCHAS2 viewing from the bottom up (note, the sign of ΔP (kPa) is negative).

I.2 Alternative Views

Additional front and side views of VCHAS1 & VCHAS2 are presented in this section.

I.2.1 VCHAS1

Additional isometric, front and side views of VCHAS1 are presented in Figures I.7 through I.9.

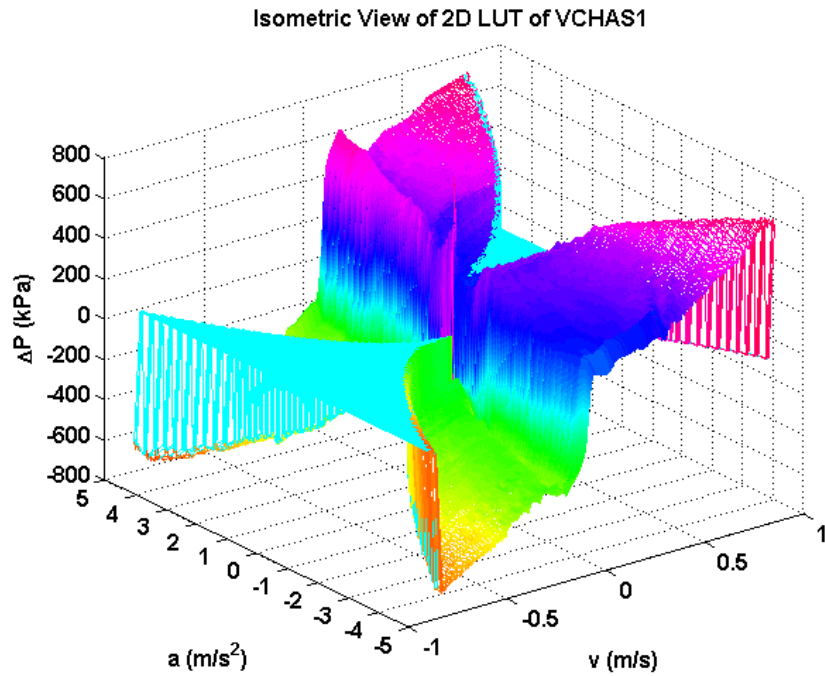


Figure I.7 Isometric View of the 2D LUT of VCHAS1

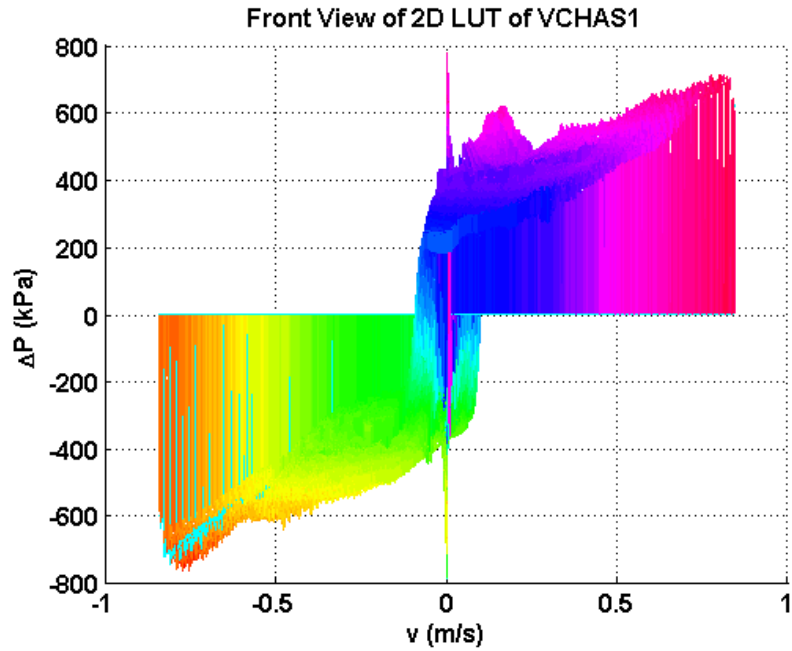


Figure I.8 Front View of the 2D LUT of VCHAS1

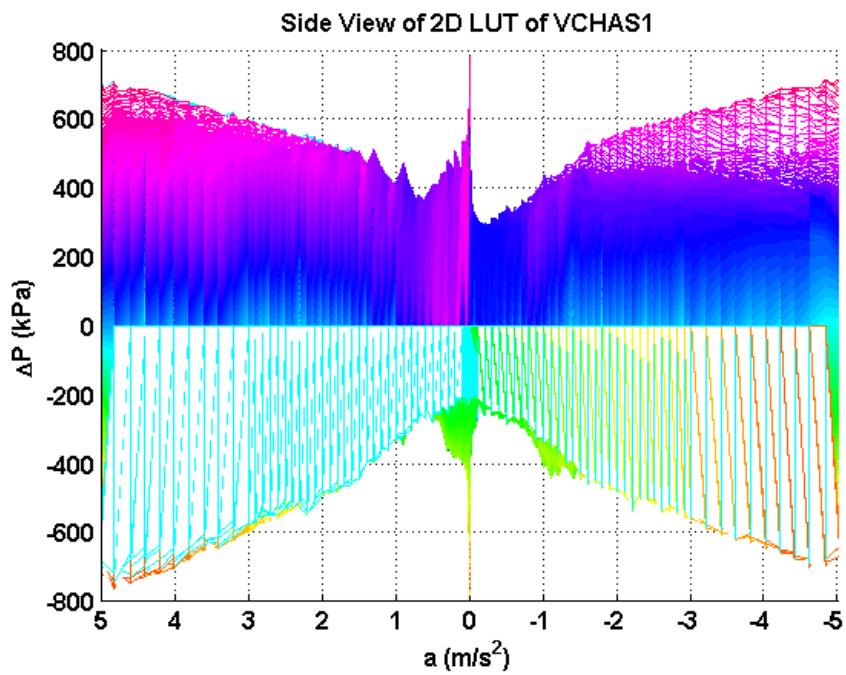


Figure I.9 Side View of the 2D LUT of VCHAS1

I.2.2 VCHAS2

Additional isometric, front and side views of VCHAS2 are presented in Figures I.10 through I.12

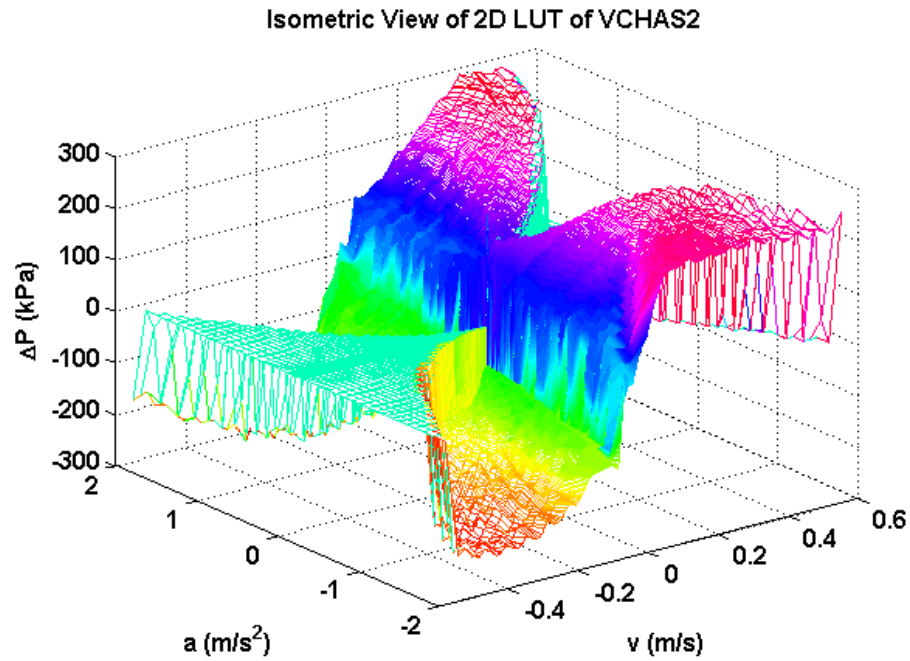


Figure I.10 Isometric view of 2D LUT of VCHAS2

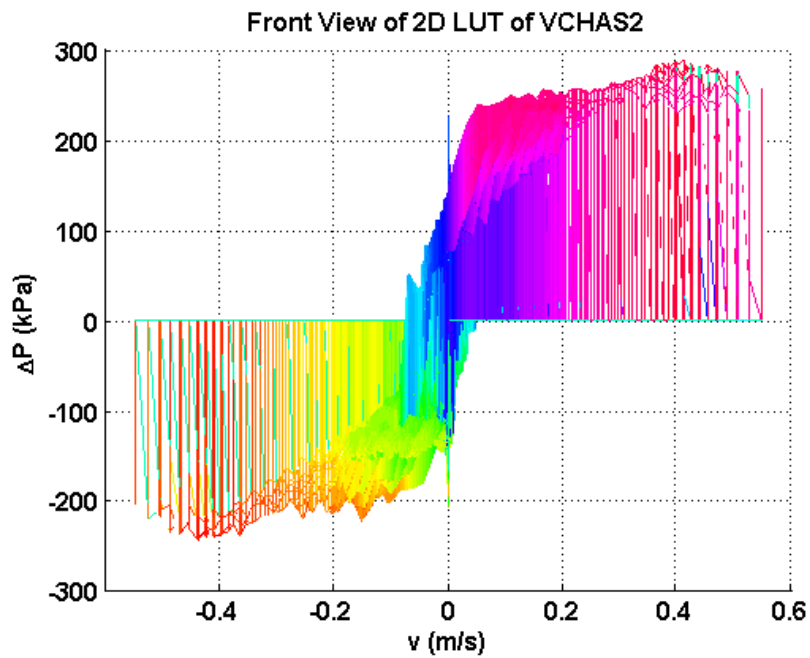


Figure I.11 Front view of the 2D LUT of VCHAS2

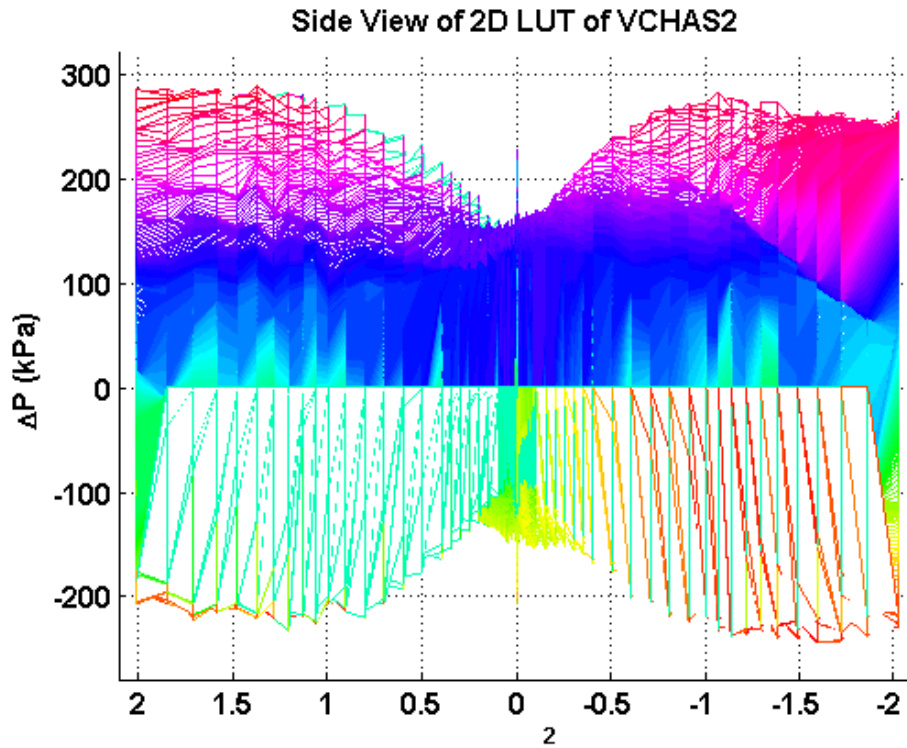


Figure I.12 Side view of the 2D LUT of VCHAS2

APPENDIX J: ALGORITHM FOR DETERMINING THE START POINTS AND END POINTS

In this appendix, the algorithm for determining the start and end points of each quadrant of the selected cycle is discussed.

As mentioned in Chapter 4, a starting point (S_p) on the cycled data was determined by locating the point with the smallest measured value of velocity that was greater than zero. In the algorithm, S_p has to meet the following conditions:

$$v(S_p) \geq 0 \text{ and } v(S_p - 1) \leq 0 \text{ and } v(S_p + 1) > 0 \quad (\text{J.1})$$

Please note that the waveform is presented as a function of the sampling index points. Thus S_p+1 means that the next point is 1 sampling index point unit after S_p . Consider the velocity triangular waveform shown in Figure J.1. The sampling index points (S_p, E_p) represent the start point and end point of a selected cycle. The sampling index points (S_{p1}, E_{p1}), (S_{p2}, E_{p2}), (S_{p3}, E_{p3}), and (S_{p4}, E_{p4}) represent the start points and end points of Quadrant 1, Quadrant 2, Quadrant 3, and Quadrant 4 respectively.

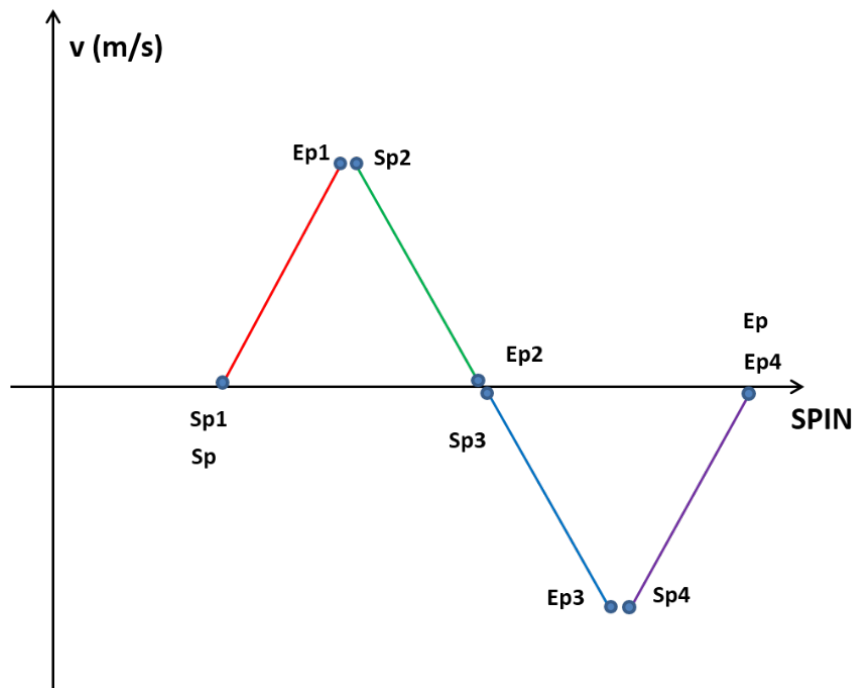


Figure J.1 Start points and end points of each quadrant of a selected cycle

The start point of Quadrant 1 is the same as the start point of the selected cycle:

$$Sp_1 = Sp \quad (J.2)$$

The end point of Quadrant 1 (Ep_1) was chosen to be the maximum discrete value of Quadrant 1. In the algorithm, Ep_1 has to meet the following conditions:

$$v(Ep_1) > v(Ep_1 + 1) \text{ and } v(Ep_1) > v(Ep_1 - 1) \quad (J.3)$$

The start point (Sp_2) of Quadrant 2 would therefore be the next value of velocity that followed the end point (Ep_1).

$$Sp_2 = Ep_1 + 1 \quad (J.4)$$

The end point of Quadrant 2 (Ep_2) was chosen by locating the point with the smallest measured value of velocity that was greater than zero. In the algorithm, Ep_2 has to meet the following conditions:

$$v(Ep_2) \geq 0 \text{ and } v(Ep_2 - 1) \geq 0 \text{ and } v(Ep_2 + 1) < 0 \quad (J.5)$$

The start point (Sp_3) of Quadrant 3 would therefore be the next value of velocity that followed the end point (Ep_2).

$$Sp_3 = Ep_2 + 1 \quad (J.6)$$

The end point of Quadrant 3 (Ep_3) was chosen to be the maximum (negative) discrete value of Quadrant 3. In the algorithm, Ep_3 has to meet the following conditions:

$$v(Ep_3) < v(Ep_3 + 1) \text{ and } v(Ep_3) < v(Ep_3 - 1) \quad (J.7)$$

The start point (Sp_4) of Quadrant 4 would therefore be the next value of velocity that followed the end point (Ep_3).

$$Sp_4 = Ep_3 + 1 \quad (J.8)$$

The end point of Quadrant 4 (Ep_4) was chosen by locating the point with the smallest measured value of velocity that was smaller than zero. In the algorithm, Ep_4 has to meet the following conditions:

$$v(Ep_4) < 0 \text{ and } v(Ep_4 - 1) < 0 \text{ and } v(Ep_4 + 1) \geq 0 \quad (J.9)$$

The end point of the selected cycle is the same as the end point of Quadrant 4:

$$Ep = Ep_4 \quad (J.10)$$